Revista Mexicana de Astronomía y Astrofísica, **61**, 3–13 (2025)

https://doi.org/10.22201/ia.01851101p.2025.61.01.01

DISCOVERY OF 28 OPEN CLUSTERS WITH *GAIA* DR3

W. S. Dias[1] and H. Monteiro[1]

Received June 25 2024; accepted August 26 2024

ABSTRACT

In this work we searched for open clusters in the fields of star-forming regions in the Galaxy using the HDBSCAN applied to the astrometric data from the *Gaia* DR3 catalog. We identified 28 new open clusters, of which the real existence is supported by the membership probability determined from astrometric data and by the presence of cluster sequences in their color-magnitude diagrams, which allows for a reliable isochrone fit. Of the open clusters identified, 3 are younger than 50 Myr, 19 are of intermediate age, and 6 are old clusters. The clusters have apparent radii ranging from 3 to 20 arcmin. For all clusters, we estimate mean proper motion, mean parallax, and fundamental parameters considering the member stars for each cluster. One of the discovered clusters has a distance of 10 kpc and a log(age) $\approx$ 10.1, making it one of the most distant and oldest cataloged open clusters.

RESUMEN

En este trabajo buscamos cúmulos abiertos en regiones de formación estelar en la Galaxia con el algoritmo HDBSCAN aplicado a los datos astrométricos del *Gaia* Catálogo DR3. Identificamos 28 nuevos cúmulos abiertos, cuya existencia real está respaldada por la probabilidad de pertenencia determinada con los datos astrométricos y por la presencia de secuencias de cúmulos en sus diagramas de color y magnitud, lo que permite un ajuste isócrono confiable. De los cúmulos abiertos identificados, 3 tienen edades menores de 50 Myr, 19 son de edad intermedia y 6 son cúmulos antiguos. Los cúmulos tienen radios aparentes entre 3 y 20 minutos de arco. Para todos los cúmulos, estimamos el movimiento propio medio, la paralaje media y los parámetros fundamentales con las estrellas miembros de cada cúmulo. Uno de los cúmulos está a una distancia de 10 kpc y tiene un log(edad) $\approx$ 10,1, con lo cual es en uno de los cúmulos abiertos más distantes y antiguos.

Key Words: open clusters and associations: general

1. INTRODUCTION

Open clusters (OCs) are key objects used to study the structure and dynamics of the Galaxy since their kinematics, distances, and ages can be determined with good precision from the properties of their member stars.

Before the *Gaia* era, the most widely used catalogs of OCs and their fundamental parameters were the New Catalog of Open Clusters and Candidates (Dias et al. 2002) and the Milky Way Star Clusters (Kharchenko et al. 2003), both of which contain about 3 thousand objects.

This scenario changed with the new generation of high precision all-sky astrometric *Gaia* catalogs, which provided data to limiting magnitude about 21, offering an important opportunity to determine the parameters and members of the known open clusters as well as to discover new ones.

Recently, many works have used clustering algorithms, supervised or not, to search for new open clusters and to identify their member stars: He et al. (2022) used the pyUPMASK algorithm (Pera et al. 2021) with the K-means clustering method; Castro-Ginard et al. (2020), Castro-Ginard et al. (2019) and Hao et al. (2022) used DBSCAN (Ester et al. 1996); Cantat-Gaudin & Anders (2020) used the UPMASK procedure (Krone-Martins & Moitinho 2014); Liu & Pang (2019) used the Friend of Friends method; Sim et al. (2019) used Gaussian mixture model and mean-shift algorithms; Jaehnig et al. (2021) used extreme deconvolution Gaussian mixture models; and

[1]UNIFEI, Instituto de Física e Química, Universidade Federal de Itajubá, Brazil.

recently Kounkel & Covey (2019), Kounkel et al. (2020), Hunt & Reffert (2021) and Hunt & Reffert (2023) used HDBSCAN to search for open clusters.

As a direct consequence of the publication of the *Gaia* catalogs and the application of advanced machine learning techniques, currently about 8000 open clusters are known and cataloged (Hunt & Reffert 2023), representing an almost fourfold increase in the number of clusters originally cataloged in our database (Dias et al. 2002). However, according to Hunt & Reffert (2024), the Milky Way contains a total of one hundred thousand open clusters, of which only about 4% have been discovered.

In this context, we have dedicated special attention to the task of a systematic search for previously unknown open clusters, and in this work we present the first results of a search for these objects in the fields from the catalog of star-forming regions in the Galaxy published by Avedisova (2002).

In the next section, we describe the procedures adopted in the search for clusters and the tools used in their analysis. § 3 is dedicated to the presentation of the isochrone fitting procedure to determine distance and age, which indicates that the clusters are real. In § 4 we discuss the results. Finally, in § 5 we give some concluding remarks.

2. CLUSTER SEARCH AND ANALYSIS STRATEGY

In this work we searched for open clusters in the fields of one degree squared centered on the star formation regions provided in the catalog published by Avedisova (2002). Basically we applied the HDBSCAN (Hierarchical Density-Based Spatial Clustering of Applications with Noise) clustering algorithm (Campello et al. 2015, 2013) in two steps, firstly to find all the clusters in each field, and subsequently to estimate the membership for stars in open clusters. These procedures are described below.

2.1. *Searching for Clusters*

The HDBSCAN algorithm is an interesting method for searching for open clusters since it can identify clusters with different shapes and density, being efficient and relatively fast in dealing with large volumes of data, as is the case with the Gaia catalog. Some advantages of the method that make it more robust are its ability to deal with multidimensional data and the fact that it does not require the number of clusters to be initially defined.

As an evolution of the DBSCAN algorithm (Ester et al. 1996) it only requires the definition of the parameters min_cluster_size (minimal size to consider a cluster) and min_samples (primarily controls how tolerant the algorithm is towards noise). The other parameter is the cluster_selection_method used to select the clusters from the cluster tree hierarchy. While EOM (Excess of Mass) method produces clusters with large areas, the leaf method produces small homogeneous clusters.

However, the obtained results from HDBSCAN depend on the data as well as the setup defined to use the algorithm. We refer the reader to the work of Hunt & Reffert (2021) to search for open clusters for a complete description and use of the HDBSCAN algorithm, including tests with different setups and comparisons of their performance with other methods.

In this work we applied the Python code of the HDBSCAN[2] in an unsupervised fashion, to find all the clusters in each field, considering a five-dimensional astrometric space (position in the tangent plane, parallax, and proper motions). We followed the results of Hunt & Reffert (2021) and set the parameters min_cluster_size = 15, min_samples = 80 and method = leaf. We also scaled the data set to have a median of zero and a unit inter−quartile range using a RobustScaler object from scikit−learn (Pedregosa et al. 2011). Clusters with fewer than 15 stars were disregarded in our analyses.

In Figure 1 we present the typical results for this procedure using the field $213.07 - 2.23$ as an example, where four groups were found. In the plot, the member stars of each cluster as originally defined by the algorithm are presented in different colors. In this field three known clusters were found that were colored red for CWNU_1774, green for UBC_212 and cyan for FSR_1077, and one unknown detected open cluster (Dias_21), presented in blue color.

The list of detected clusters was cross-referenced with the most recent publications on new open clusters, as well as with the catalog published by Hunt & Reffert (2023). In this process, we considered as new open cluster candidates those in which the central coordinates differed by more than 5 arcmin, mean proper motion differed by more than 2σ, and mean parallax differed by more than 5σ (to consider large errors for more distant stars) of the known open clusters cataloged.

Subsequently, we used the Aladin Sky Atlas (Bonnarel et al. 2000) which provides tools that help ensure that the member stars of these new candidates did not correspond to members of known clusters, since these new open clusters can be in the same

[2] `https://hdbscan.readthedocs.io/en/latest/`.

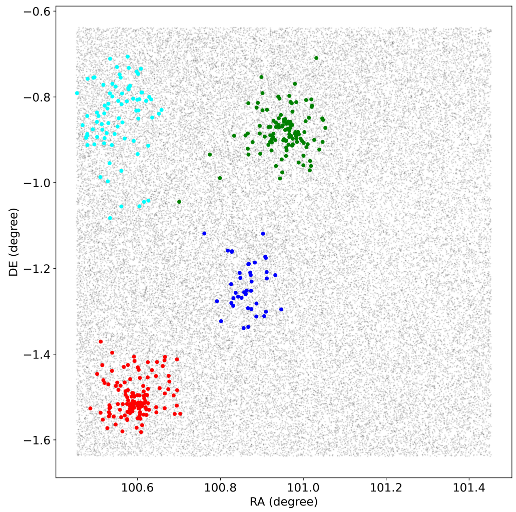

Fig. 1. The sky map with field of one degree centered in the field 213.07 − 2.23 is presented. In the plot, stars members as originally defined by the HDBSCAN algorithm, of each cluster are shown in different colors. In red for CWNU_1774, green for UBC_212 and cyan for FSR_1077. The stars in blue are members of Dias_21, new detected open cluster. The color figure can be viewed online.

field (or close) to known open clusters, as is the case of Dias_21 in the field of the three known clusters as shown in Figure 1.

The candidates listed as uncataloged open clusters had their color-magnitude diagram (CMD) checked by a visual inspection, and only those with a clear typical cluster sequence in the CMD were kept. We selected 28 unknown open cluster candidates and, for each of these cases, performed a more detailed analysis to determine the member stars, to apply the isochrone fit, and to determine their distances and ages.

2.2. *Memberships*

A recent addition to the HDBSCAN library is the introduction of soft clustering[3], which capitalizes on the smoothed density function provided by the condensed tree over the data points. In this approach, cluster labels are not directly assigned to points; rather, each point receives a probability assignment. However, the probability calculations still rely on specified parameters, such as min_cluster_size and min_samples. Here we adopt this probability estimation for the membership of the stars.

Since the results provided by the HDBSCAN algorithm depend on the parameters, we applied the code in a different way to ensure an unbiased membership determination for stars in open clusters. In this approach we use a Monte Carlo method to sample the space of the clustering algorithm, tuning the parameters to capture variations in membership assignment. The clustering algorithm is run 50 times, each time with varying tuning parameters, resulting in a probability estimation distribution for individual stars. Averaging probabilities from the N runs yields a final membership probability for each star. Furthermore, the variance of individual probability estimations is computed and stars that deviate by more than 100% are assigned a probability of zero. This approach eliminates the need for initial assumptions about the HDBSCAN tuning parameters, thus improving the accuracy of the cluster analysis.

The 28 new open clusters candidates were reanalyzed through the HDBSCAN algorithm in this modified fashion, applied to *Gaia* DR3 astrometric data of the stars located in the area delimited by the estimated central coordinates and two times the apparent radius estimated, considering the stars selected from the HDBSCAN applied as described in § 2.1.

3. DISTANCES AND AGES

It is well known that the stars of a real open cluster align along a specific feature, the cluster sequence, in a CMD. This feature is most evident when only stars are included with a sufficiently high membership probability, e.g. as determined by the method described above. Likewise, the stars that form this feature should exhibit an over-density in a 3D plot with proper motion and parallax data, since it is assumed that they occupy a limited volume in space and have similar velocities. In this scenario, a precise isochrone fit to the stars with membership probability greater than 0.51 is a strong indicator for the presence of a real open cluster, and allows to determine its age, extinction, and metallicity. In addition, it yields an estimate of the distance of the cluster, independent of the parallax measurements.

Consequently, the next step in our analysis was to use *Gaia* DR3 G_{BP} and G_{RP} magnitudes to perform an isochrone fit considering the astrometric membership probabilities of the stars derived by the method outlined in § 2.2.

In previous works, we commented on the subjectivity of visual fitting procedures and the dependence of the results on the knowledge of the stellar membership in the analyzed field. Generally, visual isochrone fits do not objectively correspond to the mathematical best fit, for example, using maximum likelihood methods, possibly introducing a bias in

[3]`https://hdbscan.readthedocs.io/en/latest/soft_clustering.html`.

the results. For this reason, we applied the cross-entropy (CE) method to fit theoretical isochrones, as detailed in Monteiro et al. (2017). This approach was previously successfully applied to *Gaia* DR2 data in Dias et al. (2018) and Monteiro & Dias (2019) and to hundreds of clusters using the *Gaia* eDR3 data (Dias et al. 2021) .

The CE method is an iterative statistical procedure where in each iteration the initial sample of the fit parameters is randomly generated using predefined criteria. The code then selects the 10% best fits based on the calculated weighted likelihood values, taking into account the probabilities of astrometric membership. The likelihood function is used to define the objective function, which is then minimized with respect to the parameters. In our code, a prior in A_V is adopted as a normal distribution with μ and variance for each cluster taken from the 3D extinction map produced by Capitanio et al. (2017). The optimization algorithm then minimizes with respect to the parameters. More details can be found in Monteiro et al. (2010) and Monteiro et al. (2017).

Basically, a synthetic cluster is generated using the Padova PARSEC version 1.2S database of stellar evolutionary tracks and isochrones (Bressan et al. 2012), which uses the *Gaia* filter band passes of Evans et al. (2018) and is scaled to the solar metal content with $Z_\odot = 0.0152$. The code scans the following parameter space limits:

- age: from log(age) = 6.60 to log(age) = 10.15;
- distance: from 1 to 25000 parsec;
- A_V: from 0.0 to 5.0 mag;
- $[Fe/H]$: from -0.90 to 0.70 dex

Our code accounts for reddening by including extinction in the generated synthetic cluster, which is then compared to the data through the likelihood function. For each star of the synthetic cluster, we use the A_λ/A_V relations of Monteiro et al. (2020) updated to use the *Gaia* DR3 filter band passes, to obtain the observed photometry for the generated synthetic cluster. In this way, each generated star is reddened according to its color and then compared with the observational data through the likelihood in the optimization process.

4. RESULTS

In this study, we searched for open clusters in 2960 fields of the star formation catalog of Avedisova (2002) using the HDBSCAN algorithm applied to *Gaia* DR3 astrometric data with the tuning parameters described in § 2.1 that allowed us to find 1620 previously cataloged open clusters and 3535 new candidates. Our analysis, including a visual check of the features in the CMD, allowed us to identify 28 new open clusters.

We would like to note that this work did not exhaust the possibilities of searching for open clusters in these fields, since changing the tuning parameters of the HDBSCAN may favor finding clusters with characteristics different from the ones we found. We also chose to provide only the list with the best candidates to avoid introducing noise in the catalogs of known open clusters.

In Figure 2 we show the typical CMD with the membership probabilities of the stars and the optimal isochrone fit determined by the CE optimization algorithm, indicating the reality of the clusters. In the plots, all the stars in the investigated field are presented in light gray, and the member stars are represented by a point color, with the redder color referring to a higher membership probability. The CMDs show the expected characteristics of a field with an open cluster, exhibiting a sequence typical of the presence of an open cluster relatively separate from the sequence of field stars. Note that, as expected, and found by the HDBSCAN in each case, there is a clump of high membership probability stars in the vector proper motion diagram and position in the sky (in this work positions in the tangent plane), with more stars with higher membership closer to the center of the field. The CMDs of all the discovered clusters are shown in Figures 4, 5 and 6.

From a quantitative perspective, these cases exhibit typical errors in the average astrometric parameters, as well as distances and ages, compared to the values reported in the literature, particularly those published in Dias et al. (2021), where we used the same isochrone fitting technique. As expected, the clusters with greater uncertainty in the distance and age parameters present a larger spread in the turn-off and main sequence.

Table 1 summarizes the positions, sizes, and astrometric parameters of these 28 discovered open clusters determined using stars with a membership probability greater than 0.50. The mean radial velocities are provided for 14 clusters using the radial velocity data given in the *Gaia* DR3 catalog. Table 2 provides the results of the fundamental parameters (distance, age, [Fe/H] and A_V) obtained by the isochrone fit given by the mean and standard deviation of the results of ten runs of the fitting procedure, as detailed in last section. In addition to the cluster parameters, all membership probabilities and

TABLE 1

MEAN ASTROMETRIC PARAMETERS FOR 28 DISCOVERED OPEN CLUSTERS

Field	Name	RA_ICRS [deg]	DE_ICRS [deg]	R [arcmin]	N	pmRA [mas yr^{-1}]	e_pmRA [mas yr^{-1}]	pmDE [mas yr^{-1}]	e_pmDE [mas yr^{-1}]	Plx [mas]	e_Plx [mas]	RV [km s^{-1}]	e_RV [km s^{-1}]	NRV
121.37+3.47	Dias_12	9.2993	66.3245	12.681	79	-1.540	0.227	-0.006	0.163	0.159	0.087	-91.057	2.089	2
123.93+1.43	Dias_13	15.0612	64.3680	9.861	54	-1.603	0.228	-0.114	0.114	0.162	0.061	···	···	0
131.86+1.33	Dias_14	33.1042	62.5949	19.458	141	-0.921	0.238	0.092	0.302	0.213	0.056	-60.781	0.830	2
137.69+3.88	Dias_15	45.9315	62.9139	19.751	85	-0.089	0.138	0.056	0.209	0.188	0.050	-33.649	2.538	2
149.59+0.90	Dias_16	61.9305	53.5426	14.053	52	0.116	0.244	0.326	0.121	0.161	0.043	···	···	0
151.63+3.36	Dias_17	66.5584	53.4130	3.394	31	0.108	0.174	-1.044	0.136	0.227	0.070	···	···	0
180.73-2.51	Dias_18	84.2710	26.5927	6.774	43	0.340	0.138	-0.306	0.186	0.220	0.076	-11.718	2.078	2
184.89-1.74	Dias_19	87.7687	23.6001	8.012	49	0.398	0.141	-0.632	0.274	0.197	0.091	···	···	0
203.71+1.18	Dias_20	99.5408	8.2739	17.297	44	-0.167	0.146	-0.377	0.163	0.209	0.049	39.631	1.380	5
213.07-2.23	Dias_21	100.8634	-1.2482	6.837	44	-0.423	0.137	0.534	0.100	0.178	0.051	···	···	0
227.75-0.15	Dias_22	110.0193	-13.3799	11.545	40	-0.647	0.083	0.751	0.097	0.226	0.035	···	···	0
245.93+1.16	Dias_23	120.7232	-28.0161	6.765	35	-1.815	0.130	2.482	0.200	0.192	0.035	47.955	2.839	2
251.88-0.47	Dias_24	122.8776	-34.0747	8.613	45	-2.482	0.092	3.008	0.109	0.167	0.026	96.460	3.521	5
251.52+2.00	Dias_25	124.5981	-32.1535	17.975	66	-2.293	0.222	2.760	0.359	0.160	0.023	76.386	3.494	5
273.89-1.58	Dias_26	140.2921	-52.4072	7.759	40	-3.598	0.222	2.928	0.135	0.115	0.049	···	···	0
292.34-4.88	Dias_27	166.1039	-65.0980	16.645	256	-5.232	0.466	2.062	0.249	0.137	0.057	32.308	1.785	7
293.34-0.86	Dias_28	171.5147	-62.1815	4.021	50	-6.135	0.243	1.207	0.162	0.280	0.040	···	···	0
318.06-0.46	Dias_29	224.3485	-59.3583	14.043	147	-4.748	0.724	-3.380	0.332	0.344	0.054	-27.172	1.566	10
354.99+5.17	Dias_30	258.0942	-30.3556	5.505	32	-3.817	0.287	-5.791	0.301	0.084	0.055	2.528	2.009	3
16.28-2.81	Dias_31	277.6833	-16.1074	8.520	31	-1.179	0.193	-3.047	0.241	0.259	0.056	···	···	0
20.29-1.14	Dias_32	278.2984	-11.9047	8.905	148	-0.304	0.242	-1.854	0.291	0.261	0.079	5.205	5.335	4
22.76-0.25	Dias_33	278.6223	-9.3315	7.998	28	-0.834	0.170	-2.938	0.425	0.327	0.023	-4.218	3.239	2
32.74-0.08	Dias_34	283.1168	-0.4266	4.022	41	-1.626	0.106	-4.295	0.087	0.217	0.032	51.251	1.468	6
26.61-3.98	Dias_35	283.6507	-7.5504	16.807	64	-2.782	0.225	-5.609	0.313	0.147	0.038	···	···	0
54.15+0.17	Dias_36	292.4729	19.0487	3.783	66	-2.595	0.157	-5.523	0.181	0.211	0.065	···	···	0
60.57-0.19	Dias_37	296.4799	24.1809	3.782	44	-1.709	0.102	-4.280	0.116	0.267	0.080	···	···	0
98.51+3.31	Dias_38	324.2194	56.6787	11.981	98	-2.526	0.255	-2.044	0.120	0.103	0.044	···	···	0
98.51+3.31	Dias_39	324.3774	57.0073	9.374	44	-2.466	0.101	-2.185	0.084	0.129	0.035	···	···	0

TABLE 2

RESULTS OF FUNDAMENTAL PARAMETERS OBTAINED FROM THE ISOCHRONE FIT

Field	Cluster	Dist [pc]	e_dist [pc]	logt(age)	e_log(age)	Av [mag]	e_Av [mag]	FeH [dex]	e_FeH [dex]
121.37+3.47	Dias_12	6069	1506	8.939	0.405	4.010	0.395	-0.181	0.063
123.93+1.43	Dias_13	3120	1180	8.770	0.731	3.064	0.349	-0.333	0.101
131.86+1.33	Dias_14	3546	690	8.357	0.494	2.407	0.223	-0.208	0.042
137.69+3.88	Dias_15	6403	1310	9.027	0.218	2.743	0.283	-0.181	0.130
149.59+0.90	Dias_16	3834	760	8.805	0.312	2.616	0.183	-0.361	0.116
151.63+3.36	Dias_17	3137	615	8.225	0.763	2.480	0.220	-0.295	0.034
180.73-2.51	Dias_18	3733	413	8.659	0.238	2.403	0.241	-0.263	0.101
184.89-1.74	Dias_19	5193	557	8.787	0.723	2.545	0.164	-0.269	0.137
203.71+1.18	Dias_20	4678	761	8.882	0.197	2.197	0.187	-0.304	0.097
213.07-2.23	Dias_21	4295	225	7.730	0.209	1.973	0.058	-0.227	0.088
227.75-0.15	Dias_22	3504	236	8.327	0.430	1.614	0.118	-0.206	0.074
245.93+1.16	Dias_23	5563	545	9.210	0.292	1.246	0.305	-0.183	0.053
251.88-0.47	Dias_24	5769	705	8.179	0.863	1.676	0.225	-0.194	0.121
251.52+2.00	Dias_25	4626	286	7.885	0.416	1.356	0.096	-0.262	0.056
273.89-1.58	Dias_26	5246	1649	8.519	0.456	2.777	0.504	-0.149	0.231
292.34-4.88	Dias_27	6346	878	9.476	0.228	2.072	0.201	-0.088	0.066
293.34-0.86	Dias_28	3489	696	6.969	0.444	2.889	0.139	0.083	0.079
318.06-0.46	Dias_29	2457	373	8.070	0.754	4.064	0.111	0.156	0.031
354.99+5.17	Dias_30	10691	3453	10.022	0.216	2.056	0.506	0.195	0.061
16.28-2.81	Dias_31	3966	788	9.052	0.216	2.838	0.177	0.217	0.078
20.29-1.14	Dias_32	4783	240	8.823	0.055	4.050	0.101	0.332	0.062
22.76-0.25	Dias_33	3537	455	8.667	0.569	3.956	0.121	0.342	0.106
32.74-0.08	Dias_34	3077	655	8.414	0.259	4.039	0.101	0.409	0.131
26.61-3.98	Dias_35	5539	1074	9.577	0.049	1.425	0.063	0.219	0.074
54.15+0.17	Dias_36	3893	555	7.007	0.689	3.633	0.106	0.102	0.069
60.57-0.19	Dias_37	2903	774	8.951	0.761	3.709	0.404	0.074	0.049
98.51+3.31	Dias_38	6826	1583	8.962	0.101	2.897	0.225	-0.178	0.111
98.51+3.31	Dias_39	5181	1027	8.611	0.621	2.782	0.313	-0.246	0.036

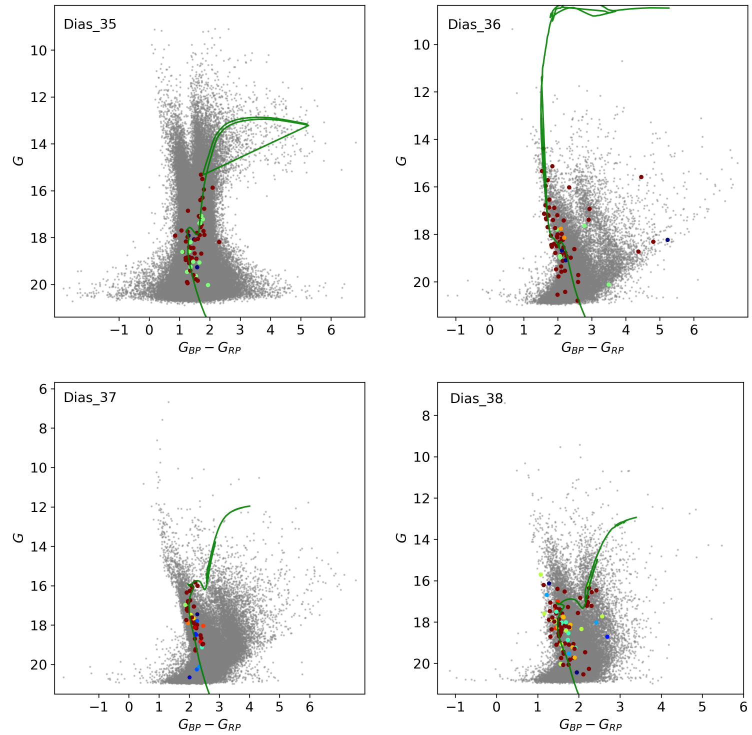

Fig. 2. Color-magnitude diagram with isochrone fitted for some of the discovered clusters studied. The color is proportional to the astrometric membership, where more red means a higher membership probability. The gray points correspond to field stars. The CMDs of all clusters in the sample are shown in Appendix. The color figure can be viewed online.

individual stellar data are also made electronically available.

5. DISCUSSION

The superposition of known open clusters in their projections on the sky can occur with some frequency, especially in regions rich in stars and clusters. However, depending on the situation, the identification of new clusters can be obscured by a denser open cluster in the field, as for example discussed by Hunt & Reffert (2023) for the case of HSC_2382 in the field of IC_ 2662, as well as new star clusters discovered in the field of the open cluster NGC_5999 by Ferreira et al. (2019), and around NGC_6649 by Gao (2024).

In this work, five discovered clusters are located in the field of known open clusters. Our investigation of the cross-match with the clusters published in Hunt's catalog, as well as the mean astrometric parameters and distance and age estimated from the isochrone fit, ensure that this is not a rediscovery of the same known open cluster. The new clusters in the same field of known clusters are the following: Dias_22 is about 13 arcmin from Haffner_6, Dias_23 is 12 arcmin from UBC_640, Dias_31 is 19 arcmin from Ruprecht_171, Dias_32 16 arcmin from Ruprecht_143 and Dias_34 is situated about 8 arcmin from the center of HSC_320.

Dias_38 and Dias_39 are two OCs found in the same investigated field with angular separation of 20 arcmin. In Figure 3 the sky map and the CMD of the investigated field 98.51 + 3.31 of one degree square are given with the 98 and 44 member stars of OC Dias_38 and Dias_39 superimposed in green and blue, respectively. As can be seen in Table 1 there is no significant difference in the astrometric parameters, but according to the results of our isochrone fit, over-plotted on the CMD in Figure 3, the clusters have about the same age. However, Dias_38 is about 1500 pc more distant than Dias_39. Unfortunately, we did not find members with determined radial velocity that would be useful for determining the Galactic orbits of the objects. This could be an interesting case for checking the possibility that the two are binary clusters. We understand that these cases need further confirmation.

Finally, we point out that Dias_30 is the older and more distant open cluster candidate of the sample and it is also among the oldest and most dis-

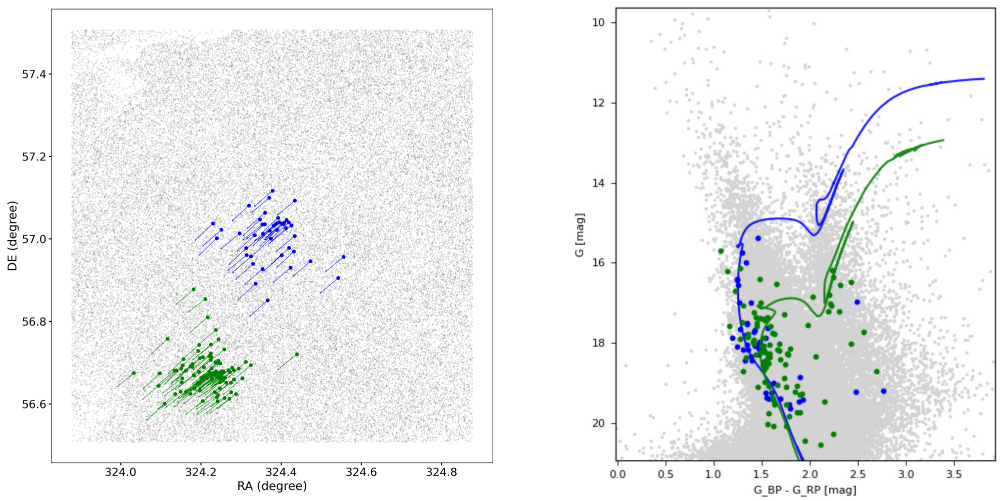

Fig. 3. Sky map and color-magnitude diagram of the stars in the field $98.51+3.31$ with the member stars of the clusters Dias_38 and Dias_39 plotted in green and blue, respectively. The length of the vectors are presented in arbitrary units. The isochrones in the CMD are those with results given in the Table 2. The color figure can be viewed online.

tant in the list of known open clusters. The CMD, presented in Figure 5, shows that the members selected by the HDBSCAN algorithm turn away from the main sequence towards the giant branch. The absence of a defined main sequence due to possible members beyond the limiting magnitude of the *Gaia* DR3 catalog results in poor parameter estimates by our code. However, we opted to maintain this new candidate in our list, since it is at the limit of detection of the Gaia DR3 data.

6. CONCLUSIONS

This paper presents the first results of the ongoing project to search for open clusters using a clustering algorithm applied to Gaia data. We report 28 new open clusters in our Galaxy discovered by applying the HDBSCAN algorithm to *Gaia* DR3 data in fields of star formation from the catalog published by Avedisova (2002).

We determined the astrometric membership probability of the stars in each field using the HDBSCAN algorithm applied in a variational fashion, which eliminates the need for initial assumptions about the tuning parameters of the method.

For all clusters, we determined mean proper motions and parallaxes, as well as the fundamental parameters (d, $\log(t)$, A_V) and [Fe/H]), using our non-subjective multidimensional global optimization tool to fit theoretical isochrones to *Gaia* DR3 photometric data.

We were able to obtain the mean radial velocity for 14 open clusters using radial velocity data published in the *Gaia* DR3 catalog.

Surprisingly, we found Dias_30 among the oldest and most distant in the list of the known open clusters in the Galaxy, making it an interesting case to be investigated further with deep data such as Euclid, LSST and ELT.

Finally, the results of this work indicate that there is still work to be done on open cluster discovery. Although the need for automated searches is evident, the use of clustering algorithms has not yet been exhausted as, depending on the technique, OCs with different characteristics are detected. Even HDBSCAN deserves to be tested with different tuning parameters in the search, mainly due to its efficiency and speed.

We thank the referee for the valuable suggestions that improved the quality of the paper. W.S.Dias is Bolsista FAPEMIG - CNPq - Brasil (processo BPQ-06608-24) and acknowledges FAPESP (fellowship 2024/15923-1) and CNPq (fellowship 310765/2020-0). H. Monteiro would like to thank FAPEMIG grants APQ-02030-10 and CEX-PPM-00235-12. This research was performed using the facilities of the Laboratório de Astrofísica Computacional da Universidade Federal de Itajubá (LAC-UNIFEI). This work has made use of data from the European Space Agency (ESA) mission *Gaia* (`http://www.cosmos.esa.int/Gaia`), processed by the *Gaia* Data Processing and Analysis Consortium (DPAC, `http://www.cosmos.esa.int/web/Gaia/dpac/consortium`). We employed catalogs from CDS/Simbad (Strasbourg) and Digitized Sky Survey images from the Space Telescope Science Institute (US Government grant NAG W-2166).

APPENDIX

Color-magnitude diagram with isochrone fitted for the discovered clusters.

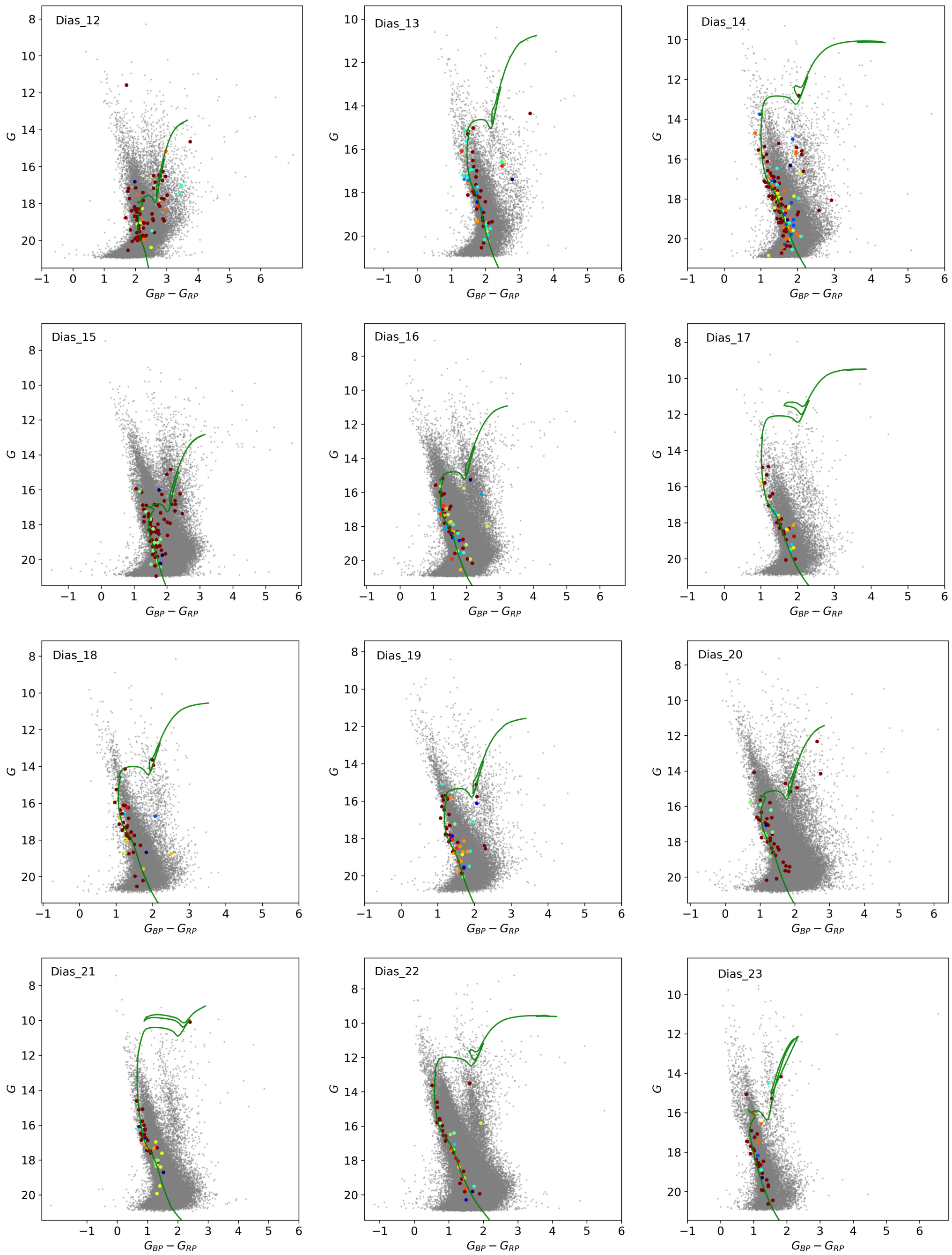

Fig. 4. Color-magnitude diagram with isochrone fitted for the discovered clusters studied. The color is proportional to the astrometric membership, where more red means higher membership probability. The gray points correspond to field stars. The color figure can be viewed online.

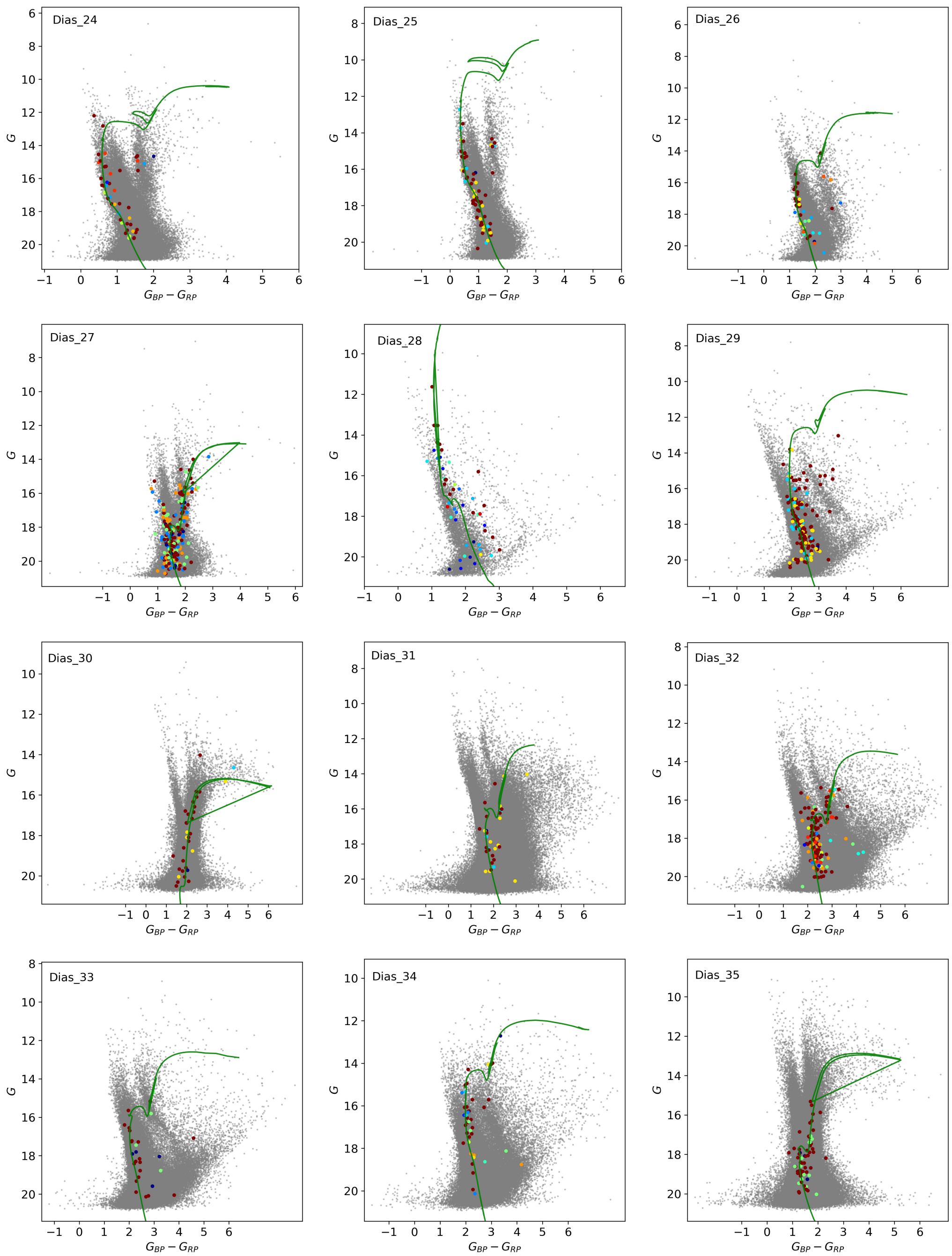

Fig. 5. Same as Figure 4. The color figure can be viewed online.

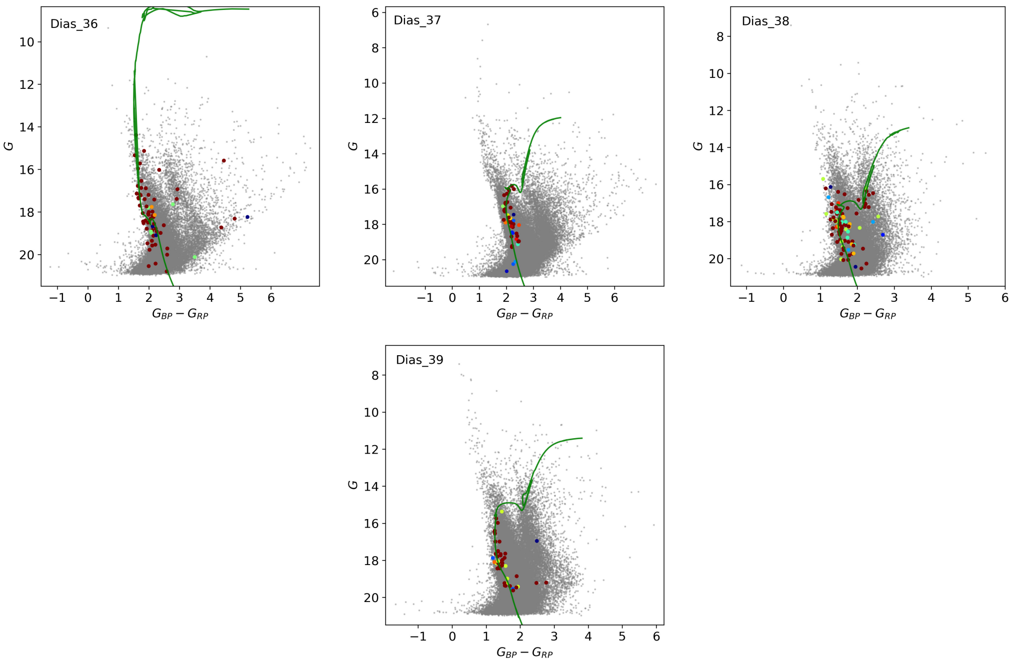

Fig. 6. Same as Figure 4. The color figure can be viewed online.

REFERENCES

Avedisova, V. S. 2002, ARep, 46, 193, https://doi.org/10.1134/1.1463097

Bonnarel, F., Fernique, P., Bienaymé, O., et al. 2000, A&AS, 143, 33, https://doi.org/10.1051/aas:2000331

Bressan, A., Marigo, P., Girardi, L., et al. 2012, MNRAS, 427, 127, https://doi.org/10.1111/j.1365-2966.2012.21948.x

Campello, R. J. G., Moulavi, D., & Sander, J. 2013, in Advances in Knowledge Discovery and Data Mining - 17th Pacific-Asia Conference, PAKDD, ed. J. Pei, V. Tseng, L. Cao, H. Motoda, & G. Xu, 160-172, https://doi.org/10.1007/978-3-642-37456-2_14

Campello, R. J. G. B., Moulavi, D., Zimek, A., & Sander, J. 2015, ACM Transactions on Knowledge Discovery from Data (TKDD), 10, 1, https://doi.org/10.1145/2733381

Cantat-Gaudin, T. & Anders, F. 2020, A&A, 633, 99, https://doi.org/10.1051/0004-6361/201936691

Capitanio, L., Lallement, R., Vergely, J. L., Elyajouri, M., & Monreal-Ibero, A. 2017, A&A, 606, 65, https://doi.org/10.1051/0004-6361/201730831

Castro-Ginard, A., Jordi, C., Luri, X., et al. 2020, A&A, 635, 45, https://doi.org/10.1051/0004-6361/201937386

Castro-Ginard, A., Jordi, C., Luri, X., Cantat-Gaudin, T., & Balaguer-Núñez, L. 2019, A&A, 627, 35, https://doi.org/10.1051/0004-6361/201935531

Dias, W. S., Alessi, B. S., Moitinho, A., & Lépine, J. R. D. 2002, A&A, 389, 871, https://doi.org/10.1051/0004-6361:20020668

Dias, W. S., Monteiro, H., Lépine, J. R. D., et al. 2018, MNRAS, 481, 3887, https://doi.org/10.1093/mnras/sty2341

Dias, W. S., Monteiro, H., Moitinho, A., et al. 2021, MNRAS, 504, 356, https://doi.org/10.1093/mnras/stab770

Ester, M., Kriegel, H.-P., Sander, J., & Xu, X. 1996, in Proc. of 2nd International Conference on Knowledge Discovery and Data Mining (KDD-96), 226

Evans, D. W., Riello, M., De Angeli, F., et al. 2018, A&A, 616, 4, https://doi.org/10.1051/0004-6361/201832756

Ferreira, F. A., Santos, J. F. C., Corradi, W. J. B., Maia, F. F. S., & Angelo, M. S. 2019, MNRAS, 483, 5508, https://doi.org/10.1093/mnras/sty3511

Gao, X. 2024, MNRAS, 527, 1784, https://doi.org/10.1093/mnras/stad3358

Hao, C. J., Xu, Y., Wu, Z. Y., et al. 2022, A&A, 660, 4, https://doi.org/10.1051/0004-6361/202243091

He, Z., Li, C., Zhong, J., et al. 2022, ApJS, 260, 8, https://doi.org/10.3847/1538-4365/ac5cbb

Hunt, E. L. & Reffert, S. 2021, A&A, 646, 104, https://doi.org/10.1051/0004-6361/2020239341

__________. 2023, A&A, 673, 114, https://doi.org/10.1051/0004-6361/202346285

__________. 2024, arXiv e-prints, arXiv:2403.05143, https://doi.org/10.1051/0004-6361/202348662

Jaehnig, K., Bird, J., & Holley-Bockelmann, K. 2021, ApJ, 923, 129, https://doi.org/10.3847/1538-4357/ac1d51

Kharchenko, N. V., Pakulyak, L. K., & Piskunov, A. E. 2003, ARep, 47, 263, https://doi.org/10.1134/1.1568131

Kounkel, M. & Covey, K. 2019, AJ, 158, 122, https://doi.org/10.3847/1538-3881/ab339a

Kounkel, M., Covey, K., & Stassun, K. G. 2020, AJ, 160, 279, https://doi.org/10.3847/1538-3881/abc0e6

Krone-Martins, A. & Moitinho, A. 2014, A&A, 561, 57, https://doi.org/10.1051/0004-6361/201321143

Liu, L. & Pang, X. 2019, ApJS, 245, 32, https://doi.org/10.3847/1538-4365/ab530a

Monteiro, H. & Dias, W. S. 2019, MNRAS, 487, 2385, https://doi.org/10.1093/mnras/stz1455

Monteiro, H., Dias, W. S., & Caetano, T. C. 2010, A&A, 516, 2, https://doi.org/10.1051/0004-6361/200913677

Monteiro, H., Dias, W. S., Hickel, G. R., & Caetano, T. C. 2017, NewA, 51, 15, https://doi.org/10.1016/j.newast.2016.08.001

Monteiro, H., Dias, W. S., Moitinho, A., et al. 2020, MNRAS, 499, 1874, https://doi.org/10.1093/mnras/staa2983

Pedregosa, F., Varoquaux, G., Gramfort, A., et al. 2011, Journal of Machine Learning Research, 12, 2825, http://jmlr.org/papers/v12/pedregosa11a.html

Pera, M. S., Perren, G. I., Moitinho, A., Navone, H. D., & Vazquez, R. A. 2021, A&A, 650, 109, https://doi.org/10.1051/0004-6361/202040252

Sim, G., Lee, S. H., Ann, H. B., & Kim, S. 2019, JKS, 52, 145, https://doi.org/10.5303/JKAS.2019.52.5.145

Wilton S. Dias: UNIFEI, Instituto de Física e Química, Universidade Federal de Itajubá, Av. BPS 1303 Pinheirinho, 37500-903 Itajubá, MG, Brazil (wiltonsdias@yahoo.com.br).

Héktor Monteiro: UNIFEI, Instituto de Física e Química, Universidade Federal de Itajubá, Av. BPS 1303 Pinheirinho, 37500-903 Itajubá, MG, Brazil (hmonteiro@unifei.edu.br).

Revista Mexicana de Astronomía y Astrofísica, **61**, 15–28 (2025)

https://doi.org/10.22201/ia.01851101p.2025.61.01.02

ABSOLUTE ELEMENTS FOR THE NEAR CONTACT ECLIPSING BINARY V878 HERCULIS

R. H. Nelson[1,2,3], K. B. Alton,[2], M. R. Kendurkar[3], and K. Stępień[4]

Received July 7 2024; accepted September 9 2024

ABSTRACT

New radial velocity (RV) and light curve (LC) data for the eclipsing binary V878 Her have been simultaneously modeled with the Wilson-Devinney code (WD2003). Two distinct LC datasets were investigated: one was from the Transiting Exoplanet Survey Satellite (TESS) while the others were acquired from a ground-based observatory in Canada. Supporting spectroscopic data were acquired using the 1.83-m Plaskett Telescope at the Dominion Astrophysical Observatory (DAO) between 2009-2020. Potential progenitors of this near contact binary (NCB) were evaluated using an evolutionary model derived from cool close binaries. It is argued that V878 Her is not in the thermal relaxation oscillation (TRO) phase but, instead, it is a first timer, i.e. in a state of contact binary formation. Its most probable ZAMS progenitor had masses equal to about 1.7 and 0.6 $M_{\odot}$ with an orbital period of nearly 1.6 days.

RESUMEN

Hemos modelado simultáneamente nuevas curvas de velocidad radial y de luz para la binaria eclipsante V878 Her con el código Wilson-Devinney (WD2003). Se investigaron dos conjuntos de datos distintos para las curvas de luz. Uno proviene del "Transiting Exoplanet Survey Satellite (TESS)" mientras que los otros se adquirieron en un observatorio terrestre en Canadá. Datos espectroscópicos de apoyo se adquirieron con el telescopio Plaskett de 1.83-m en el Dominion Astrophysical Observatory (DAO) entre 2009-2020. Se evaluaron los posibles progenitores de esta binaria casi en contacto (NCB) mediante un modelo evolutivo para binarias cerradas frías. Argumentamos que 878 Her no está en la fase de relajamiento de oscilaciones térmicas (TRO) sino que está justo en proceso de formación de la binaria en contacto. Su progenitor más probable en la ZAMS tuvo masas de aproximadamente 1.7 and 0.6 $M_{\odot}$ y un período orbital de cerca de 1.6 días.

Key Words: stars: binaries: eclipsing — stars: binaries: spectroscopic — stars: evolution — stars: fundamental parameters — stars: imaging

1. INTRODUCTION

Near contact binaries (NCBs) have been identified as a separate class of binaries by Shaw (1990) who distinguished two types of NCBs: V1010 Oph type and FO Vir type. Yakut & Eggleton (2005) suggested the names SD1 and SD2 for NCBs of V1010 Oph and FO Vir type, respectively. SD1 binaries consist of primaries filling their critical Roche lobes and transfering matter through the Lagrangian point L1 to slightly oversized (by a factor of ≈ 1.2) secondaries whereas SD2 binaries resemble short period Algol-type variables. We will use the designations SD1 and SD2 herein.

After finding evidence for variability from photographic plates, Kaiser (1994) confirmed that V878 Her (aka SAO 46698, BD-49 2630, TYC 3516-0047-1, and TIC 188766090) was variable using photoelectric detection. The first linear ephemeris was reported in another study (Kaiser et al. 1996) which

[1]Mountain Ash Observatory, 1393 Garvin Street, Prince George, BC, Canada, V2M 3Z1.
[2]Desert Blooms Observatory, 70 Summit Ave., Cedar Knolls, NJ, 07927, USA.
[3]Guest investigator, Dominion Astrophysical Observatory, 5071 W Saanich Rd, Victoria, BC V9E 2E7, Canada.
[4]Warsaw University Observatory, Al. Ujazdowskie 4, 00-478 Warszawa, Poland.

described this system as a "thermally decoupled binary of W UMa or near contact (NCB) type". Later on Bloomer & Ngwele (1999) produced new CCD-derived light curves in V- and R-passbands from which newly derived light elements showed no significant changes compared to those reported earlier by Kaiser et al. (1996). A spectroscopic study (Popper 1996) indicated that V878 Her was close to type F5. Cross correlation of positional data found in the SuperWASP and ROSAT archives indicated that the location of this variable star was coincident with an X-ray source (Norton 2007) thereby suggesting significant stellar coronal activity (Rosner et al. 1985; Hartman & Noyes 1987). Hoffman et al. (2008) classified V878 Her as a β Lyrae type candidate based on light curve data from the Northern Sky Variability Study (NSVS). Other than times-of-minima which have been sporadically published over the past 45 years, no definitive characterization of this eclipsing binary system has been found in the literature. Herein, new radial velocity data simultaneously modeled with multi-bandpass light curves have resulted in a far more robust physical, geometric and evolutionary characterization of V878 Her.

2. SECULAR PERIOD ANALYSIS

A combination of photographic, photoelectric and ccd-derived times-of minimum published between 1978 and 2022 are summarized in Table 1. An eclipse timing difference (ETD) plot (aka "O-C diagram") was initially seeded using the eclipse elements taken from the International Variable Star Index (`https://www.aavso.org/vsx/index.php?view=detail.top\&oid=186067`). After updating the linear ephemeris (equation 1) using near-term (2017-2021) timings it was apparent that a change in the ETD residuals could be established (Figure 1) that was best fit with a quadratic expression (equation 2).

$$MinI(HJD) = 2\,459\,363.7562(7) + 0.5294714(5)\cdot E. \tag{1}$$

$$\begin{aligned} ETD = \quad & 0.00416 \pm 1.3000\cdot 10^{-3} + \\ & 1.5397 \pm 2.4283\cdot 10^{-7}E - \\ & 1.3457 \pm 0.0883\cdot 10^{-10}E^2\,. \end{aligned} \tag{2}$$

Since the quadratic term coefficient ($Q = -1.3457 \pm 0.0883$) is negative, this result would suggest that the orbital period has been decreasing at the rate:

$$dP/dt = 2Q/P = 0.016 \pm 0.001\ s\cdot y^{-1}. \tag{3}$$

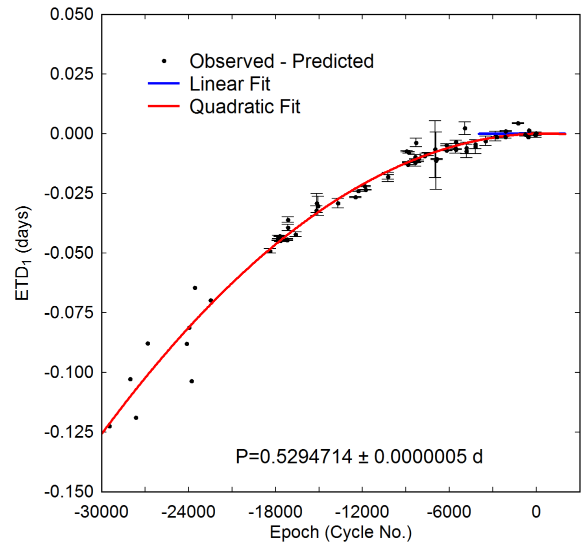

Fig. 1. V878 Her. Eclipse timing difference (ETD) plot generated using the eclipse elements from equation 1. Significant scatter observed during earlier epochs is attributed to ToM values estimated from photographic plates. The color figure can be viewed online.

Period change defined by a parabolic relationship is often attributed to angular momentum loss (AML) due to magnetic stellar wind or by mass transfer (Stępień 1995; Stępień 2006; Qian 2001, 2003; Li et al. 2019). Ideally the net effect is a decreasing orbital period when AML dominates. The orbital period can also decrease when conservative mass transfer from the more massive to its less massive binary partner is the dominant process. In contrast, separation of the binary pair increases when conservative mass transfer from the less massive to its more massive cohort occurs, or when spherically symmetric mass loss from either body (e.g. a wind but not magnetized) takes place. In mixed situations (e.g. mass transfer from less massive star, together with AML) the orbit evolution depends on which process prevails (Alton & Stępień 2018).

3. EFFECTIVE TEMPERATURE ESTIMATION

Interstellar extinction was estimated using the dust maps originally generated by Schlegel et al. (1998) and then later adjusted by Schlafly & Finkbeiner (2011). A mean value for $T_{\rm eff1}$ (6300 ± 138 K) was adopted from multiple surveys including 2MASS (6272 K) using J, K and H transforms to the Johnson-Cousins photometric system (Warner 2007), Gaia DR2 (6274 K), Gaia DR3 (6262 K), UCAC4 (6175 K), TESS (6181 K) and that estimated from $(V - R_{\rm c})_{\rm o}$ at MAO (6440 K). Accordingly, the spectral type of the primary star would likely range between F6 and F7, or close to F8 as reported by Ren et al. (2020).

4. PHOTOMETRIC OBSERVATIONS

Between April 16, 2013 and May 7, 2014 a total of 277 science frames in V, 276 in R_c and 276 in the I_c passbands were taken at Mountain Ash Observatory (MAO) in Prince George, BC, Canada. The imaging equipment included a 33-cm $f/4.5$ Newtonian telescope coupled with an SBIG ST-10XME ccd camera which were installed on a Paramount ME mount. Image calibration was performed using standard dark subtraction and flat fielding (CCD-Soft Version 5.00.210). Three comparison stars used during ensemble aperture photometry (MPO Canopus v10.7.12.9) are listed in Table 1 along with their J2000 coordinates (Gaia EDR3; Gaia Collaboration (2021)) and magnitudes (APASS-DR9; Henden et al. (2009)). Comparison star differences were constant to within ≈0.01 magnitude, with no apparent systematic variation.

Primarily designed to detect very small brightness changes from a host star during an exoplanet transit, the TESS Mission (Ricker et al. 2015; Caldwell 2020) also provides a rich source of light curve data for many more traditional variable stars. The TESS CCD detector bandpass ranges between 600-1000 nm and is centered near Cousins I band (I_c). The first imaging campaign in the vicinity of V878 Her started on April 16, 2020 and ran every 2 min through May 12, 2020. Another group of images were then similarly acquired between May 14, 2020 and June 8, 2020. Since light curves from this second group exhibited some obvious changes in amplitude (probably due to change in spot size or location) we chose to only evaluate those light curve data acquired between April 16 and May 12, 2020. Raw flux readings were processed by the TESS Science Processing Operations Center (TESS-SPOC) to remove long term trends using so-called Co-trending Basis Vectors (CBVs). These results identified as "Presearch Data Conditioning Simple Aperture Photometry" (PDCSAP) flux are usually cleaner data than the SAP flux.

5. SPECTROSCOPIC OBSERVATIONS

Starting in April, 2009 and ending on August 29, 2020 a total of 22 medium-resolution (R≈10,000) spectra were acquired at the Dominion Astrophysical Observatory (DAO) in Victoria, British Columbia, Canada using the 1.83-m Plaskett Telescope. The spectrograph, fitted with a 2118Yb grating (1800 lines/mm and blazed at 500 Angstroms), produced a reciprocal dispersion approximating 10 Å/mm. The wavelength range (5000 to 5250 Å) was chosen to include the strong iron absorption lines at 5167.48 and 5171.59 Å. Spectra from an iron-argon lamp taken immediately before and after each stellar spectra were used for wavelength calibration. RV standard stars were selected from the 1986 Astronomical Almanac (Section H42-2), many of which were also listed as suitable IAU radial velocity standard stars (Stefanik et al. 1999). These have been proven to be extremely reliable and consistent with the results achieved in over 20 publications using the same 1.83-m Plaskett Telescope. In general, stars were selected near in spectral type (and luminosity class) to the target stars (typically A-F, luminosity class V) and as bright as possible. Typical exposures of standards (running from magnitude 2.0 to 8.0) on a 1.5-2 meter class optical telescope run from a few seconds to perhaps 10 or 20 min. Windows software RaVeRe, written by the first author, and available on his website (Nelson 2013), was used for detrending and reduction of the spectral data. The radial velocities were determined by the Broadening Functions (BF) routine (Ruciński (1969); Ruciński (1992); Ruciński (2004); Nelson (2010)) as implemented in the Windows-based application Broad (Nelson 2013); details regarding this procedure are provided in Nelson (2010). The elements used for all phasing are given in equation 1. A log of observations ($RV_{1,2}$) corrected for Heliocentric Julian Date (HJD) is presented in Table 2; each RV uncertainty estimate is derived from the standard deviation of values from multiple comparison stars. The calibrated one-dimensional spectra, sorted by phase, are presented in Figure 2. To disentangle the components, Gaussian profile curve fitting was employed according to Nelson (2020). Representative broadening peaks are illustrated at phase 0.323 (Figure 3) and phase 0.706 (Figure 4).

6. LIGHT CURVE ANALYSES

V878 Her light curve morphology is consistent with eclipsing variables identified as near contact binary stars (NCBs). Shaw (1994) classified these systems based upon their short orbital periods (<1 d), tidal interactions, and facing surfaces that are less than 0.1 orbital radii apart. Light curves from some semi-detached classical Algols and β Lyrae type eclipsing binary systems appear similar to those exhibited by NCBs. However, one distinguishing difference is the effective temperature ($T_{\rm eff}$) of the more massive component defined herein as the primary star. Compared to NCBs which typically feature a

TABLE 1

V878 HER TIMES OF MINIMUM (ToM), MEASUREMENT UNCERTAINTY, EPOCH AND ECLIPSE TIMING DIFFERENCES (ETD) USED TO CALCULATE LINEAR AND QUADRATIC EPHEMERIDES

ToM (HJD-2400000)	Err	Cycle No.	ETD	Ref.	ToM (HJD-2400000)	Err	Cycle No.	ETD	Ref.
43759.5820	nr	-29471	-0.1224	1	54932.5981	0.0002	-8369	-0.0119	14
44512.5100	nr	-28049	-0.1027	1	54933.3945	0.0010	-8367.5	-0.0097	14
44733.8130	nr	-27631	-0.1188	1	54971.5224	0.0018	-8295.5	-0.0037	14
45161.6570	nr	-26823	-0.0877	1	55045.3760	0.0004	-8156	-0.0114	15
46590.7000	nr	-24124	-0.0880	1	55275.1686	0.0000	-7722	-0.0094	16
46669.5980	nr	-23975	-0.0812	1	55321.7629	0.0005	-7634	-0.0086	17
46757.4680	nr	-23809	-0.1035	1	55396.4184	0.0006	-7493	-0.0085	15
46879.8150	nr	-23578	-0.0644	1	55662.4798	0.0119	-6990.5	-0.0065	18
47466.4640	nr	-22470	-0.0697	1	55695.5670	0.0120	-6928	-0.0113	19
49637.5821	0.0009	-18369.5	-0.0491	1	55725.7476	0.0003	-6871	-0.0106	20
49917.6769	0.0001	-17840.5	-0.0447	1	56077.3202	0.0002	-6207	-0.0070	21
49922.7073	0.0002	-17831	-0.0443	1	56082.3525	0.0004	-6197.5	-0.0047	21
49927.7383	0.0006	-17821.5	-0.0432	1	56398.9750	0.0020	-5599.5	-0.0061	22
49983.5979	0.0002	-17716	-0.0429	1	56416.1822	0.0000	-5567	-0.0067	23
50001.5979	0.0003	-17682	-0.0449	1	56418.8298	0.0002	-5562	-0.0064	22
50251.5088	0.0003	-17210	-0.0445	2	56422.8038	0.0006	-5554.5	-0.0034	22
50251.5090	0.0004	-17210	-0.0443	2	56750.5524	0.0026	-4935.5	0.0023	24
50291.4891	0.0014	-17134.5	-0.0393	2	56799.5203	0.0024	-4843	-0.0059	24
50291.4924	0.0011	-17134.5	-0.0360	2	56808.5199	0.0028	-4826	-0.0073	24
50573.4298	0.0009	-16602	-0.0421	3	57131.5003	0.0019	-4216	-0.0044	25
51323.4360	0.0020	-15185.5	-0.0322	4	57137.5883	0.0029	-4204.5	-0.0054	25
51338.7938	0.0040	-15156.5	-0.0290	5	57499.4844	0.0019	-3521	-0.0030	25
51386.4451	0.0040	-15066.5	-0.0302	4	57855.5559	0.0021	-2848.5	-0.0010	26
52118.4404	0.0020	-13684	-0.0291	6	57915.6505	0.0002	-2735	-0.0014	27
52743.7486	0.0003	-12503	-0.0266	7	58228.5682	0.0005	-2144	-0.0013	28
52859.1761	0.0002	-12285	-0.0239	8	58246.8374	0.0002	-2109.5	0.0011	29
53088.9686	0.0002	-11851	-0.0220	9	58688.4198	0.0002	-1275.5	0.0044	30
53115.4406	0.0002	-11801	-0.0235	8	58962.4166	0.0008	-758	-0.0003	31
53932.4204	0.0009	-10258	-0.0181	10	59061.4267	0.0000	-571	-0.0013	32
53941.4214	0.0019	-10241	-0.0181	11	59069.3688	0.0000	-556	-0.0013	32
54628.4214	0.0003	-8943.5	-0.0073	12	59090.0208	0.0000	-517	0.0013	32
54669.4497	0.0001	-8866	-0.0130	13	59321.3980	0.0010	-80	-0.0005	33
54683.4818	0.0002	-8839.5	-0.0119	13	59330.3990	0.0010	-63	-0.0005	33
54701.4879	0.0003	-8805.5	-0.0078	13	59330.3994	0.0007	-63	-0.0001	34
54928.3621	0.0015	-8377	-0.0121	14	59363.7563	0.0003	0	0.0001	35

nr: not reported

1. Kaiser et al. (1996); 2. Agerer & Huebscher (1997); 3. Agerer & Hübscher (1999); 4. Agerer et al. (2001)
5. Bloomer & Ngwele (1999); 6. Agerer & Hübscher (2002); 7. Dvorak (2004); 8. Krajci (2005)
9. Nelson (2005); 10. Hübscher et al. (2006); 11. Hübscher & Walter (2006); 12. Bràt et al. (2008)
13. Yilmaz et al. (2009); 14. Hübscher et al. (2010); 15. Hübscher & Monninger (2011); 16. Nagai (2011)
17. Diethelm (2010); 18. Hübscher et al. (2012); 19. Paschke (2011); 20. Diethelm (2011)
21. Liakos et al. (2014); 22. Nelson (2014); 23. Nagai (2014); 24. Hübscher & Lehmann (2015)
25. Hübscher (2017); 28. Pagel (2018b); 26. Pagel (2018a); 27. Samolyk (2017)
29. Nelson (2019); 30. Pagel (2020); 31. Pagel (2021); 32. Nagai (2021)
33. Paschke (2021); 34. Pagel (2022); 35. Nelson (2022)

late F spectral type component along with a cooler (G-K spectral type) companion, β Lyrae and Algol-like binaries usually include at least one massive (O, B and A spectral type) constituent. Depending on the evolutionary status of each pair, Roche lobe overflow (RLOF) in all three cases may lead to mass transfer by the donor and mass gain by the accretor.

Roche-lobe modeling of light curve data acquired at MAO (Figure 5) and TESS (Figure 6) was initially performed with *PHOEBE* 0.31a (Prša & Zwit-

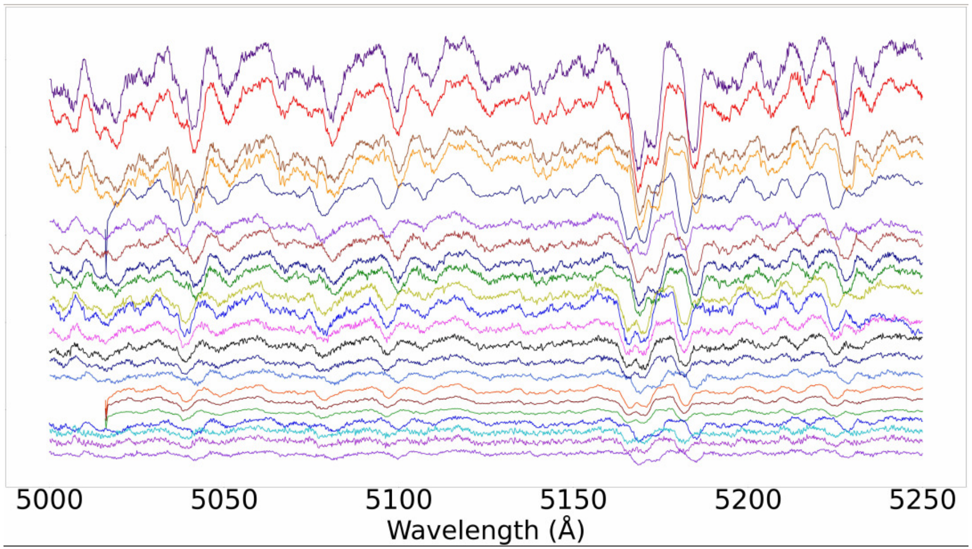

Fig. 2. V878 Her spectra sorted by phase (Table 3) and offset for clarity. The vertical scale is arbitrary. The color figure can be viewed online.

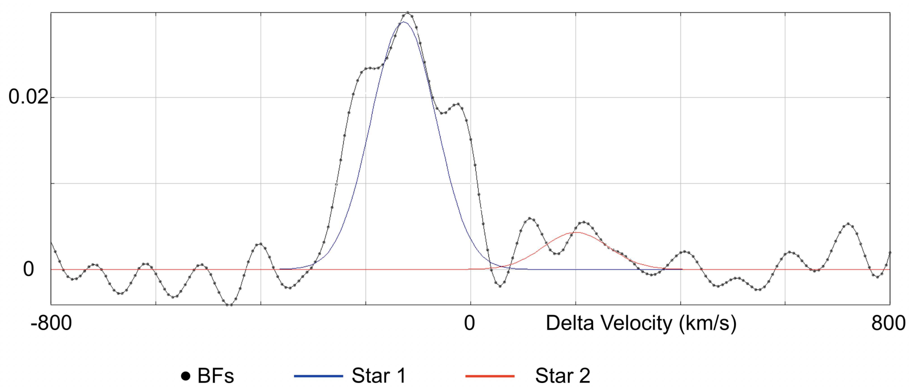

Fig. 3. Broadening function for V878 Her at phase 0.323 and the fitted Gaussian profiles. The standard spectrum is from HD 126053 while the target spectrum was the mid-value (n=7) obtained on HJD 2456761.0290. The color figure can be viewed online.

ter 2005) and then refined using *WDwint56a* (Nelson 2009). Both programs feature a graphical interface to the Wilson-Devinney WD2003 code (Wilson & Devinney 1971; Wilson 1979, 1990). *WDwint56a* incorporates Kurucz's atmosphere models (Kurucz 1993) that are integrated over VR_cI_c passbands. Based on the assumption that V878 Her is an NCB system, Roche-lobe modeling proceeded using Mode 5 for an Algol-like semi-detached binary where the secondary star fills the Roche lobe. Other modes (overcontact and semi-detached with primary star filling the Roche lobe) never improved light curve simulation as defined by the model residual mean square errors. Since the effective temperature

TABLE 2

V878 HER AND 3 COMPARISON STARS FOR ENSEMBLE APERTURE PHOTOMETRY

Object	RA (J2000)	Dec (J2000)	V-mag	$(B-V)$
V878 Her	17:24:25.278	+49:38:37.26	9.92	0.522
GSC 3516-0810	17:25:40.521	+49:33:25.70	10.32	1.18
GSC 3516-0710	17:25:57.766	+49:33:27.00	10.62	1.13
GSC 3516-0361	17:26:03.191	+49:35:47.90	11.28	0.979

TABLE 3

LOG OF DAO OBSERVATIONS AND RESULTS

Mid-time HJD-2400000	Exposure (s)	Phase at Mid-exp	RV_1 (km·s^{-1})	RV_1 err (km·s^{-1})	RV_2 (km·s^{-1})	RV_2 err (km·s^{-1})
54925.8980	2400	0.361	-115.64	6.5	112.09	11.21
54927.8954	2498	0.134	-90.74	6.15	135.92	9.75
54927.9435	3600	0.225	-114.84	6.73	173.48	15.07
54927.9977	3600	0.327	-99.92	3.54	143.95	9.29
55668.9429	1800	0.730	65.10	3.98	-240.85	3.35
56403.8551	1940	0.738	57.26	12.5	-240.28	9.53
56404.9559	3600	0.817	73.29	6.91	-251.13	18.24
56405.9400	3600	0.676	55.75	3.95	-222.60	3.2
56407.8898	3600	0.358	-119.12	2.13	147.51	4.71
56761.0290	1235	0.323	-150.64	3.79	179.61	3.1
56765.9727	3600	0.660	55.16	5.88	-219.35	11.02
56766.0108	2799	0.732	66.25	3.93	-244.69	2.27
57493.9813	1800	0.630	30.26	2.31	-193.36	3.3
57504.8839	720	0.221	-117.84	3.41	147.36	6.7
57504.9509	700	0.348	-125.42	13.64	57.81	11.45
57995.7647	700	0.334	-127.71	3.51	138.97	6.65
58008.7406	700	0.841	67.19	3.65	-243.50	2.27
58234.0069	700	0.296	-132.41	8.64	180.19	5.98
58241.9784	700	0.351	-121.90	2.25	153.16	5.98
58241.9870	700	0.367	-108.80	5.88	150.16	11.25
58597.9718	700	0.706	71.14	9.79	-224.91	8.88
59100.7570	700	0.303	-102.86	3.46	168.78	5.84

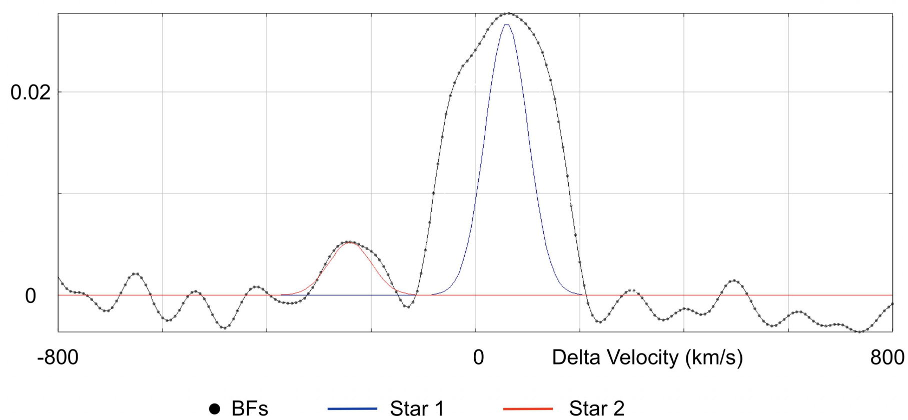

Fig. 4. Broadening function for V878 Her at phase 0.706 and the fitted Gaussian profiles. The standard spectrum is from HD 126053 whereas the program spectrum was the mid-value (n=5) acquired on HJD 2458597.9718. The color figure can be viewed online.

of the primary was estimated to be 6300 K, internal energy transfer to the stellar surface is driven by convective (<7200 K) rather than by radiative processes (Bradstreet & Steelman 2004). Therefore, bolometric albedo ($A_{1,2}$=0.5) was assigned according to Ruciński (1969) while the gravity darkening coefficient ($g_{1,2}$=0.32) was adopted from Lucy (1967). Logarithmic limb darkening coefficients (x_1, x_2, y_1, y_2) were interpolated (van Hamme 1993) following any change in effective temperature during model fit optimization by differential corrections (DC). All but the temperature of the more massive star ($T_{\rm eff1}$),

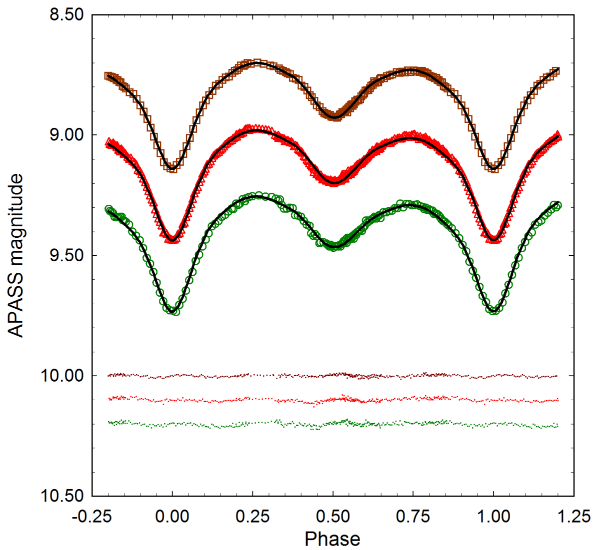

Fig. 5. V878 Her light curves from MAO (2013-2014) superimposed with W-D Roche model simulations (solid black lines). Plotted are, top to bottom: I_c, R_c and V. At the bottom of the figure, the model fit residuals are provided in the same order as the light curves. The color figure can be viewed online.

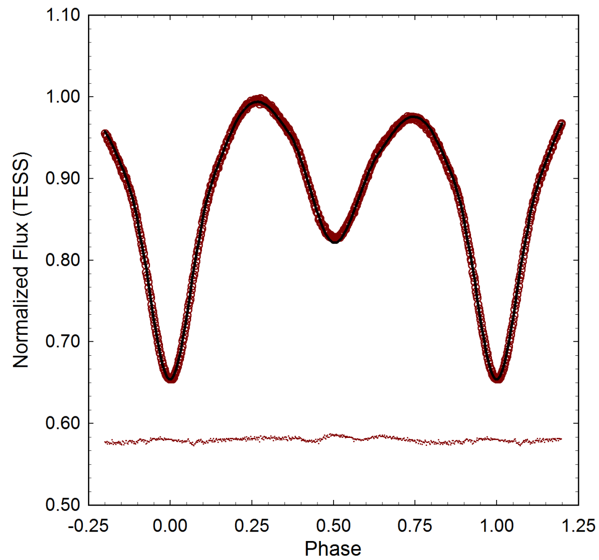

Fig. 6. Peak normalized V878 Her light curve and the Roche lobe modeling results from the TESS Mission (April 16–May 12, 2020). At the bottom of the figure, the differences between the observed and simulated light curve fits are plotted with a fixed offset (0.4). The color figure can be viewed online.

$A_{1,2}$ and $g_{1,2}$ were allowed to vary during DC iterations. In general, the best fits for $T_{\rm eff2}$, i, q and Roche potentials (Ω_1, Ω_2) were collectively refined (method of multiple subsets) by DC using the multi-bandpass light curve data until a simultaneous solution was found. It should be noted that V878 Her did not require any third light correction (l_3=0) to improve W-D model fits. Light curve data acquired at MAO between 2013 and 2014 (Figure 5) and from the TESS satellite (Figure 6) in 2020 exhibited obvious asymmetry during quadrature (Max I>Max II). This so-called "O'Connell effect" (O'Connell 1951), posits the presence of a star spot leading to surface inhomogeneity. In this case the addition of a large hot spot positioned near the neck region of the secondary star provided the best fit light curve simulations. This persistent feature found in light curves acquired between 2013-2020 is consistent with magnetospheric accretion resulting from mass transfer onto the secondary star and the predicted orbital period decrease over time. The properties of V878 Her position this star into the category of SD1 binaries. Detection of X-rays coincident with the location of V878 Her (Norton 2007) suggests that the high energy physics normally associated with mass transfer in an NCB (Shaw 1994) is consistent with the putative location of a hot spot in the neck region. Final models using the TESS and land-based light curves provided similar effective temperatures for the secondary where $T_{\rm eff2}$=4243 and 4391 K, respectively. These values correspond more closely to spectral class K5-K6 (Pecaut & Mamajek 2013).

The remaining W-D model fit parameters from the MAO and TESS datasets (Table 3), differ only slightly including the spot size and location which might be expected to change in the time interval between the two datasets. If we assume the hot spot on the secondary star results from conservative mass transfer, the amount of material lost by the donor primary can be estimated according to Kwee (1958):

$$dm/dt = m\left[\frac{q}{3P(1-q^2)}\right]dP/dt. \tag{4}$$

where

$$m = M_1 + M_2 \; and \; q = M_2/M_1. \tag{5}$$

Based on the combined mass of the primary (1.55 $M_\odot$) and secondary (0.69 $M_\odot$) stars (Table 4), conservative mass transfer is estimated to be $1.44 \pm 0.129 \cdot 10^{-7}$ $M_\odot \cdot$y^{-1}. This value falls well within the range (0.13-2.79$\cdot 10^{-7}$ $M_\odot \cdot$y^{-1}) reported by Zhu et al. (2009) for other NCBs of SD1 type. Assuming that accretion onto the secondary was continuous between 1978 and 2021 (Table 2), nearly 2.1 times the Earth's mass was transferred.

TABLE 4

WILSON-DEVINNEY PARAMETERS FOR THE BEST-FIT V878 HER LIGHT CURVE SOLUTION

WD Quantity[a]	TESS	MAO
$T_{\rm eff1}$ (K)[b]	6300 (138)	6300 (138)
$T_{\rm eff2}$ (K)	4243 (93)	4391 (96)
q (m_2/m_1)	0.442 (1)	0.443 (2)
Ω_1	2.763 (1)	2.766 (4)
Ω_2	2.763 (1)	2.766 (4)
i°	69.05 (3)	68.75 (16)
a ($R_\odot$)	3.60 (7)	3.51 (07)
V_γ (km·s^{-1})	-29.4 (1.7)	-29.2 (1.3)
$A_{\rm S} = T_{\rm S}/T_\star$[c]	1.18 (1)	1.17 (1)
$\Theta_{\rm S}$(spot co-latitude)[c]	89.6 (4)	93.9 (1.8)
$\phi_{\rm S}$ (spot longitude)[c]	23.2 (8)	47.3 (1.6)
$r_{\rm S}$ (angular radius)[c]	34.3 (2)	34.5 (7)
$L_1/(L_1{+}L_2)_{\rm V}$[d]	···	0.940 (1)
$L_1/(L_1{+}L_2)_{\rm R_c}$	···	0.915 (1)
$L_1/(L_1{+}L_2)_{\rm I_c}$	···	0.894 (1)
$L_1/(L_1{+}L_2)_{\rm TESS,\ I_c}$	0.911 (11)	···
r_1 (pole)	0.4244 (1)	0.4241 (8)
r_1 (point)	0.5820 (342)	0.5739 (209)
r_1 (side)	0.4591 (2)	0.4515 (10)
r_1 (back)	0.4793 (2)	0.4788 (12)
r_2 (pole)	0.2902 (1)	0.2904 (1)
r_2 (point)	0.4170 (1)	0.4172 (1)
r_2 (side)	0.3027 (1)	0.3029 (1)
r_2 (back)	0.3353 (1)	0.3355 (1)

[a]All uncertainty estimates for q, $\Omega_{1,2}$, i, $r_{1,2}$, and L_1 from $WDwint56a$ (Nelson 2013)
[b]Fixed with no error during DC
[c]Secondary spot parameters in degrees ($\Theta_{\rm P}$, $\phi_{\rm P}$ and $r_{\rm P}$); $A_{\rm P}$ equals the spot temperature ($T_{\rm S}$) divided by star temperature, T_*
[d]L_1 and L_2 refer to scaled luminosities of the primary and secondary stars, respectively

7. SPECTROSCOPIC ANALYSES

Stand alone radial velocity observations fit with a sine curve model are plotted in Figure 7 and yielded the following values: $K_1 = -101.7 \pm 4.3$ km·s^{-1}, $K_2 = 219.5 \pm 2.4$ km·s^{-1}, $RV_\gamma = -34.4 \pm 5.0$ km·s^{-1}(systemic velocity). When modeled without any light curve data, the spectroscopic mass ratio ($q_{\rm sp}$=M_2/M_1) was determined to be 0.464 ± 0.040. Given the inherent precision of the TESS satellite-based photometric observations, we adopted the physical and geometric parameters obtained following simultaneous Roche-type light curve modeling (WD2003) with the RV data. This produced the following estimates for M_1 (1.55 ± 0.18 $M_\odot$), M_2 (0.69 ± 0.23 $M_\odot$), R$_1$ (1.62 ± 0.03 $R_\odot$), R$_2$ (1.12 ± 0.02 $R_\odot$), $q_{\rm WD}$=0.442 ± 0.001, L_1 (3.75 ± 0.36 $L_\odot$), and L_2 (0.37 ± 0.04 $L_\odot$). The mass ratio (0.442 ± 0.001) derived from modeling the combined curves (RV+TESS-LC) is negligibly different from the spectroscopically determined mass ratio (0.443 ± 0.002) calculated from the multi-bandpass (VR_cI_c) light curves acquired at MAO.

In the present dataset, each RV estimate is the mean of values obtained from eight different standards; uncertainty is simply the standard deviation of the group. WD2003 parameter values with associated uncertainty following Roche-lobe modeling are listed in Table 3. These are formal statistical values known to be smaller than total uncertainty since systematic experimental errors cannot be readily determined. Spatial representations of V878 Her rendered with Binary Maker 3 (Bradstreet & Steelman 2004) are illustrated in Figure 8.

8. EVOLUTIONARY ANALYSIS OF V878 HER

8.1. *General Considerations*

Evolutionary status of NCBs has been a matter of debate since their identification as a separate group of variables, particularly in connection with W UMa type binaries. Lucy (1976) developed a model of a cool contact binary in which both components oscillate around a marginal thermal equilibrium remaining in contact for a part of the cycle and in a semidetached configuration for the rest. The model was called Thermal Relaxation Oscillations (TRO) theory. Following the theory, candidates for the broken contact binaries were sought and SD1 binaries seemed to be natural choice (Lucy & Wilson 1979; Eggleton 2006). However, several authors considered these binaries as “first timers” i.e. semidetached binaries that are coming into first-time contact (Shaw 1994; Hilditch et al. 1998). Others noticed several problems with SD1 binaries being TRO oscillators, like a systematic difference between masses and angular momenta of SD1 and W UMa binaries. Some suggested that only a fraction of SD1 binaries can be first timers while the others are TRO oscillators. The problem then arises how to distinguish one from another (van Hamme et al. 2001; Yakut & Eggleton 2005).

A thorough discussion of the properties of NCBs of both groups and a comparison with W UMa type binaries was carried out by Stępień & Kiraga (2013). The authors demonstrated that not only the mean values of period, component masses and angular momentum but also their distributions are distinctly different from the corresponding features of W UMa stars. In contrast, the distributions of both groups

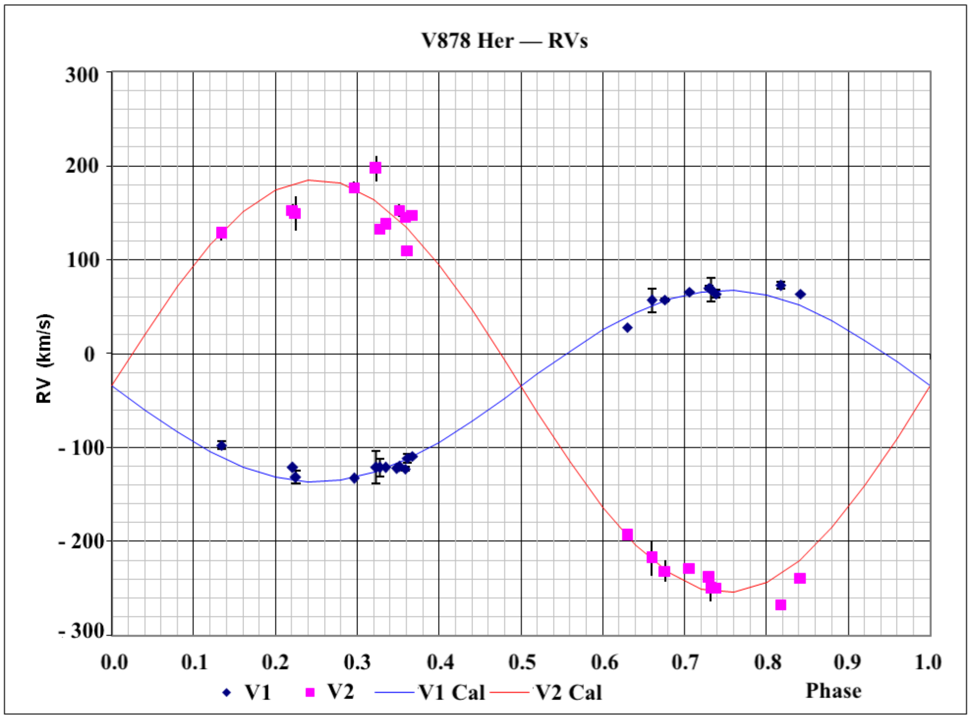

Fig. 7. Observed V878 Her radial velocities with W-D solution using photometric data from the TESS Mission. Since the computed curves from the MAO and TESS datasets were visually identical, only one *RV* plot is presented. The color figure can be viewed online.

of NCBs, i.e. SD1 and SD2, are similar to each other indicating generic connection between them. In conclusion the authors support the early hypothesis developed by Shaw (1994) according to which SD1 binaries are formed from close detached binaries when the more massive binary fills its critical Roche lobe and transfers matter to the secondary until the original secondary becomes a more massive component, passing through the contact configuration. The mass transfer still goes on and the binary assumes an SD2 configuration. Later, an A type W UMa binary or short period Algol is formed depending on the amount of angular momentum left in the system. In considering the evolution of the progenitor of V878 Her we adopt the above scenario.

If SD1 binaries cannot be considered as TRO oscillators, the basic prediction of the theory is not confirmed. In fact, even assuming that SD1 *are* TRO oscillators, they can explain only the most massive and the longest period tails of W UMa star distributions. An overwhelming majority of W UMa stars have periods, masses and angular momenta substantially lower than SD1 binaries and we do not observe any semi-detached binaries within these ranges.

To solve the problem, an alternative evolutionary model of cool contact binaries has been developed by one of us (Stępień 2006, 2009, 2011). The model assumes that the binaries are past mass transfer in case A (Kippenhahn & Weigert 1967) with the mass ratio reversal and each component separately remains in thermal equilibrium. The present secondary is the more advanced evolutionary former primary and the present primary is very little evolved former secondary which gained hydrogen rich matter from its companion. The evolution of the progenitor of a contact binary can be divided into three phases: an initial detached binary tightens its orbit due to the angular momentum loss via a magnetic wind and at the same time the more massive component expands evolutionary. The first phase comes to end when the primary fills its Roche lobe and starts transferring matter to its companion. The second phase correspond to the rapid mass transfer until mass ratio reversal and the third phase describes a final evolution of a binary until coalescence of both components. The basic assumptions and equations of the model, i.e. the expression for binary angular momentum, Kepler's Third Law, the approximate expression for Roche-lobe sizes, as well as those describing mass

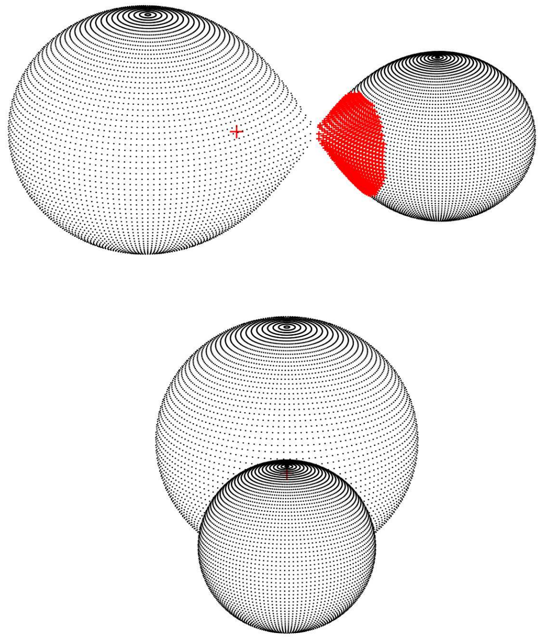

Fig. 8. Roche surface potentials and spatial representations of V878 Her from the TESS mission (April 16–May 12, 2020). The hot spot (top) located in the neck region showed little sign of changing between 2013 and 2020 suggesting a sustained period of mass transfer and accretion onto the secondary star. This is consistent with the orbital period secular analysis (Figure 1). The bottom figure depicts the partial eclipse ($i \simeq 69°$) as seen from our vantage point. The color figure can be viewed online.

and angular momentum losses due to the magnetized wind are described elsewhere (Stępień et al. 2017). Evolutionary models of single stars PARSEC (Bressan et al. 2012) are used to approximate the evolution of both components at each time step. While this approximation is satisfactory for the first and third phase when each component is in thermal equilibrium, it is poorly satisfied during the rapid mass exchange when both components are out of thermal equilibrium. Unfortunately, SD1 binaries seem to be exactly in this phase, as observations indicate, which means that the computed values of the stellar parameters during that phase should be treated as approximate.

A series of evolutionary models for V878 Her progenitors has been calculated from zero-age main sequence (ZAMS) through the Roche lobe overflow (RLOF) till the near contact phase. Details of the mass transfer following RLOF are described by Stępień & Kiraga (2013). Right after RLOF the more massive component transfers mass on its thermal time scale or even faster, depending on values of the binary parameters (Sarna & Fedorova 1989; Ge et al. 2010). After about 0.1 $M_\odot$ is transferred, the secondary swells and approaches its Roche lobe. When its radius is very close to the size of the Roche lobe, the secondary does not accept all transferred mass and a fraction of this matter returns to the primary after encircling the secondary. The mass transfer rate drops and is determined now by the rate at which the secondary tends to shrink trying to regain thermal equilibrium.

We assume that V878 Her is just in the phase when the secondary approaches its Roche lobe. In the result we stop calculations when 0.1 $M_\odot$ is transferred to the secondary past RLOF.

8.2. *Results of Calculations*

NCBs present a serious difficulty for spectroscopic observations. As Shaw (1994) noted, contrary to contact systems where comparable surface brightnesses of both components result in a moderate contrast of their luminosities, a substantial difference in temperatures of NCB components makes this contrast reach a factor of the order of 10 or even 100. This is why so few NCBs have measured radial velocity curves and quite often with a rather low accuracy. This is also the case of V878 Her that results in significant uncertainties of the observed values of the component masses. To allow for this uncertainty we computed a series of models with masses from the range given by error limits.

Our basic model is supposed to reproduce the best estimates of masses $M_1 = 1.55 M_\odot$ and $M_2 = 0.69 M_\odot$ together with orbital parameters as given in Table 4. Its initial, ZAMS values turned out to be $M_1 = 1.659 M_\odot$, $M_2 = 0.597 M_\odot$ and $P = 1.57$ day. After 1.26 Gyr the more massive component reaches RLOF and the binary parameters are as follows: $M_1 = 1.645 M_\odot$, $M_2 = 0.594 M_\odot$, $R_1 = 2.051 R_\odot$, $R_1 = 0.578 M_\odot$ and $P = 0.708$ day. The radius of the primary at this moment expanded to 0.65 of the value reached by a star of this mass at the terminal main sequence. The secondary is still very little evolved so its radius is close to its ZAMS value. The core luminosities of both stars are $L_1 \approx 11 L_\odot$ and $L_2 \approx 0.07 L_\odot$. After additional 10^7 years about 0.1 $M_\odot$ is transferred from the primary to the secondary. The resulting parameters are now: $M_1 = 1.545 M_\odot$, $M_2 = 0.694 M_\odot$ and $P = 0.529$ day. The values of stellar radii resulting directly from the computations are unreliable because the calculations do not allow for deviations from thermal equilibrium; so we simply assume that they are close to radii of both Roche lobes, i.e. $R_1 \approx 1.62 R_\odot$ and $R_2 \approx 1.12 R_\odot$. The core luminosities are not expected to change significantly compared to the RLOF phase as the rapid mass transfer hardly influences the interior of stars. Note that they differ significantly from the presently observed values $L_1 \approx 3.75 L_\odot$ $L_2 \approx 0.37 L_\odot$. It is so because a fraction of the core luminosity of the primary is converted into the potential energy of expanding layers and also transferred to the secondary.

When calculating models with masses deviating from the best adopted values by one standard error we kept the orbital period and mass ratio fixed. Both quantities are determined with sufficiently high accuracy to neglect their possible deviations. This, together with the requirement that both masses are within one error from the adopted values, means that the minimum component masses are $M_1 = 1.37 M_\odot, M_2 = 0.61 M_\odot$ and the maximum allowed masses are $M_1 = 1.73 M_\odot, M_2 = 0.76 M_\odot$. The low mass model is reproduced satisfactorily by an initial ZAMS binary with $M_1 = 1.49 M_\odot, M_2 = 0.51 M_\odot$ and $P = 1.95$ day. After 1.8 Gyr the primary fills its Roche lobe and RLOF begins with the following binary parameters: $M_1 = 1.472 M_\odot, M_2 = 0.505 M_\odot$, $P = 0.752$ day, and after another 10^7 years the model binary resembles the present variable with the parameters $M_1 = 1.367 M_\odot, M_2 = 0.60 M_\odot$, $P = 0.527$ day. Similarly, the ZAMS high mass model has $M_1 = 1.835 M_\odot, M_2 = 0.670 M_\odot$, $P = 1.28$ day, after 8.5×10^8 years at the RLOF the masses and the orbital period are $M_1 = 1.826 M_\odot, M_2 = 0.666 M_\odot$, $P = 0.670$ day, whereas after additional 10^7 years these values are $M_1 = 1.733 M_\odot, M_2 = 0.759 M_\odot$, $P = 0.530$ day.

It follows from the model computations that a progenitor of V878 Her was a detached binary with the initial period of 1.5 day (possibly, between 1.3 and 2 days),in a good agreement with the results of Stępień (2011) who argued that the initial (ZAMS) binary period distribution has a cutoff around 1.5-2 days. The initial mass ratio was $q_{init} = 0.36$ (0.34 or 0.37 for the minimum and maximum mass models, respectively). Mass transfer began at RLOF when the primary radius was equal to about 2/3 of the TAMS radius and the binary was about 1 Gyr old. The primary was massive enough to have a radiative envelope hence the mass transfer to the secondary made its radius shrink. However, the low value of q resulted in even stronger shrinking of the primary's Roche lobe. In effect, the mass transfer rate should have quickly risen from thermal to dynamical (Sarna & Fedorova 1989; Nelson & Eggleton

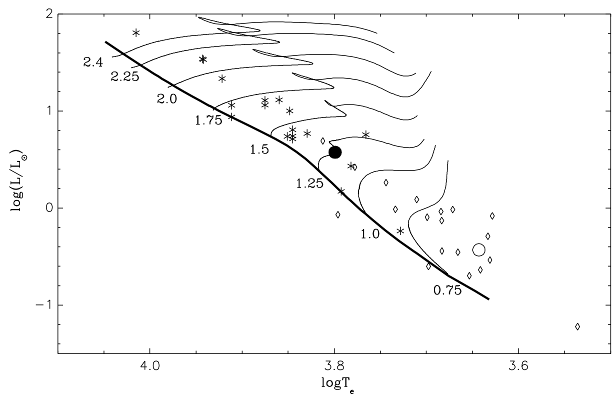

Fig. 9. Positions of the V878 Her components (primary - filled circle, secondary - open) shown among other NCBs of SD1-type from Tian & Chang (2020), with asterisks denoting primaries and diamonds - secondaries. Evolutionary tracks of stars with indicated masses and solar (Z=0.014) metallicity, together with the isochrone of 10^8 years (thick solid line), mimicking ZAMS, are taken from PARSEC models (Bressan et al. 2012).

2001; Ge et al. 2010) until the secondary filled its Roche lobe. But the observations show the opposite: while the theoretical thermal rate at RLOF, given by $\dot{M}_{th} = 3.3 \times 10^{-8} RL/M = 4.7 \times 10^{-7}\ M_\odot$/year, the observed rate is equal to only $1.44 \times 10^{-7}\ M_\odot$/year, i.e. three times lower. The expected thermal mass transfer rate is somewhat lower after 0.1 of the solar mass has been transferred but it is still significantly higher than observed, not to mention about the dynamical rate which is orders of magnitude higher. The low observed mass transfer rate supports the evolutionary model of the mass transfer presented by Stępień & Kiraga (2013) that assumes that in the late phase of rapid mass transfer, when the secondary is almost touching its Roche lobe, the net mass transfer rate decreases as the increasing fraction of the mass flux returns to the primary. The secondary ultimately accepts matter at the rate dictated by its thermal time scale after a contact system is formed.

Figure 9 shows the positions of both components from V878 Her on the HR diagram, as compared to other NCBs of SD1-type analysed in a recent paper by Tian & Chang (2020). It should be stressed, however, that the apparent temperatures and luminosities of NCBs do not necessarily reflect their true evolutionary status due to significant modification of the parameters by mass transfer between the components.

9. CONCLUSIONS

New radial velocity and light curve data for V878 Her, a near contact partially eclipsing binary, have been simultaneously analysed with the Wilson-Devinney (WD2003) code. There were two separate LC datasets: One was from the TESS space satellite and the other from a land-based (MAO) observatory. The *RV* data alone yielded results for K_1 (101.7 ± 4.3 km·s^{-1}), K_2 (219.5 ± 2.4 km·s^{-1}), RV_γ (-34.4 ± 5 km·s^{-1}), and $q_{\rm sp}$ ($0.464 \pm$ 0.040). A more rigorous analysis (Wilson 1990) was obtained by simultaneously modeling the TESS light curve data and the *RV* observations from DAO. This resulted in the best estimates for M_1 (1.55 ± 0.18 $M_\odot$), M_2 (0.69 ± 0.23 $M_\odot$), R_1 (1.62 ± 0.03 $R_\odot$), R_2 (1.12 ± 0.02 $R_\odot$), $q_{\rm WD}$ (0.442 ± 0.001), L_1 (3.75 ± 0.36 $L_\odot$), and L_2 (0.37 ± 0.04 $L_\odot$). Simultaneous analysis with the MAO data yielded similar parameter values but often with greater uncertainties.

Evolutionary calculations indicate that the age of V878 Her is around 1 Gyr. Its progenitor was a detached binary with ZAMS component masses $M_1 \approx 1.66 M_\odot$, $M_2 \approx 0.6 M_\odot$ and initial orbital period $P \approx 1.6$ days. The presently observed mass transfer rate is significantly lower than expected from TRO theory and implies that V878 Her is a first timer which will change into a contact system in the future.

This research has made use of the SIMBAD database operated at Centre de Données astronomiques de Strasbourg, France. This work also presents results from the European Space Agency (ESA) space mission Gaia. Gaia data are being processed by the Gaia Data Processing and Analysis Consortium (DPAC). Funding for the DPAC is provided by national institutions, in particular those participating in the Gaia MultiLateral Agreement (MLA). The Gaia mission website is https://www.cosmos.esa.int/gaia while the Gaia archive website is https://archives.esac.esa.int/gaia. This paper also makes use of data obtained from the Mikulski Archive for Space Telescopes (MAST) at the Space Telescope Science Institute. STScI is operated by the Association of Universities for Research in Astronomy, Inc., under NASA contract NAS5-26555. Support to MAST for these data is provided by the NASA Office of Space Science via grant NAG5-7584 and by other grants and contracts. It is a pleasure to thank the staff members at the DAO (David Bohlender, Dmitry Monin) for their usual splendid help and assistance. The diligence and dedication shown by all associated with these organizations is very much appreciated.

REFERENCES

Alton, K. B. & Stępień, K. 2018, AcA, 68, 449, https://doi.org/10.32023/0001-5237/68.4.7
Agerer, F. & Huebscher, J. 1997, I.B.V.S., 4472, 1
Agerer, F. & Hübscher, J. 1999, I.B.V.S., 4711, 1
Agerer, F., Dahm, M., & Hübscher, J. 2001, I.B.V.S., 5017, 1
Agerer, F. & Hübscher, J. 2002, I.B.V.S., 5296, 1
Bloomer, R. H. & Ngwele, I. R. 1999, I.B.V.S., 4754, 1
Bradstreet, D. H. & Steelman, D. P. 2004, BInary Maker 3, Contact Software (http://www.binarymaker.com)
Bràt, L., Šmelcer, L., Kuèáková, H., et al. 2008, O.E.J.V.S, 094, 1
Bressan, A., Marigio, P., Girardi, L., et al. 2012, MNRAS, 427, 127, https://doi.org/10.1111/j.1365-2966.2012.21948.x
Caldwell, D. A. 2020, RNAAS, 4, 201, https://doi.org/10.3847/2515-5172/abc9b3
Diethelm, R. 2010, I.B.V.S., 5945, 1
_________. 2011, I.B.V.S., 5992, 1
Dvorak, S. W. 2004, I.B.V.S., 5502, 1
Eggleton, P. P. 1996, ASPC 90, The origins, evolution, and destinies of binary stars in clusters, ed. E. F. Milone and J. -C. Mermilliod, 257
Gaia Collaboration, Brown, A. G. A., Vallenari, A., et al. 2021, A&A, 649, 1, https://doi.org/10.1051/0004-6361/202039657
Ge, H., Hjellming, M. S., Webbink, R. F., Chan, X. & Han, Z. 2010, ApJ, 717, 72, https://doi.org/10.1088/0004-637X/717/2/724
Hartmann, L. W. & Noyes, R. W. 1987, ARA&A, 25, 271, https://doi.org/10.1146/annurev.aa.25.090187.001415
Henden, A. A., Welch, D. L., Terrell, D., & Levine, S. E. 2009, AAS, 41, 669
Hilditch, R. W., Bell, S. A., Hill, G., & Harries, T. J. 1998, MNRAS, 296, 100, https://doi.org/10.1046/j.1365-8711.1998.01299.x
Hoffman, D. I., Harrison, T. E., Coughline, J. L., et al. 2008, AJ, 136, 1067, https://doi.org/10.1088/0004-6256/136/3/1067
Hübscher, J., Paschke, A., & Walter, F. 2006, I.B.V.S., 5731, 1
Hübscher, J. & Walter, F. 2006, I.B.V.S., 5761, 1
Hübscher, J., Lehmann, P. B., Menninger, G., Steinbach, H.-M., & Walter, F. 2010, I.B.V.S., 5918, 1
Hübscher, J. & Monninger, G. 2011, I.B.V.S., 5959, 1
Hübscher, J., Lehmann, P. B., & Walter, F. 2012, I.B.V.S., 6010, 1
Hübscher, J. & Lehmann, P. B. 2015, I.B.V.S., 6149, 1
Hübscher, J. 2017, I.B.V.S., 6196, 1
Kaiser, D. H. 1994, I.B.V.S., 4119, 1

Kaiser, D. H., Lubcke, G. & Williams, D. B. 1996, I.B.V.S., 4284, 1

Kippenhahn, R. & Weigert, A. 1967, ZA, 65, 251

Krajci, T. 2005 I.B.V.S., 5592, 1

Kurucz, R. L. 1993, in Light Curve Modelling of Eclipsing Binary Stars, ed. E. F. Milone (New York, NY: Springer), 93

Kwee, K. K. 1958, Bulletin of the Astronomical Institutes of the Netherlands, 14, 131

Li, K., Xia, Q.-Q, Liu, J-Z. et al. 2019, RAA, 19, 147, https://doi.org/10.1088/1674-4527/19/10/147

Liakos, A., Gazeas, K. & Nanouris, N. 2014, I.B.V.S., 6095, 1

Lucy, L. B. 1967, ZA, 65, 89

Lucy, L. B. 1976, ApJ, 205, 208, https://doi.org/10.1086/154265

Lucy L. B. & Wilson, R. E. 1979, ApJ, 231, 502, https://doi.org/10.1086/157212

Nagai, K. 2011, Var. Star Bulletin, 51, 5

_________. 2014, Var. Star Bulletin, 56, 4

_________. 2021, Var. Star Bulletin, 69, 7

Nelson, R. H. 2005, I.B.V.S., 5602, 1

_________. 2009, WDWint56a: Astronomy Software by Bob Nelson (https://www.variablestarssouth.org/bob-nelson)

_________. 2010, in The Alt-Az Initiative: Telescope, Mirror, & Instrument Developments, ed. R. M. Genet, J. M. Johnson, & V. Wallen (Collins Foundation Press)

_________. 2013, Software by Bob Nelson, http://binaries.boulder.swri.edu/binaries/

_________. 2014, I.B.V.S., 6092, 1

_________. 2019, I.B.V.S., 6262, 1

_________. 2020, NewA, 77, 101362, https://doi.org/10.1016/j.newast.2020.101362

_________. 2022, OEJV, 226, 1, https://doi.org/10.5817/OEJV2022-0226

Nelson, C. A. & Eggleton, P. P. 2001, ApJ, 552, 664, https://doi.org/10.1086/320560

Norton, A. J., Wheatley, P. J., West, R. G., et al. 2007, 2007, A&A, 467, 785, https://doi.org/10.1051/0004-6361:20077084

O'Connell, D. J. K. 1951, PRCO, 2, 85

Pagel, L. 2018a, I.B.V.S., 6244, 1

_________. 2018b, BAV Journal, 31, 17

_________. 2020, BAV Journal, 33, 17

_________. 2021, BAV Journal, 52, 14

_________. 2022, BAV Journal, 60, 21

Paschke, A. 2011, O.E.J.V.S., 142, 1

_________. 2021, BAV Journal, 55, 5

Pecaut, M. J. & Mamajek, E. E. 2013, ApJS, 208, 9, https://doi.org/10.1088/0067-0049/208/1/9

Popper, D. M. 1996, ApJS, 106, 133, https://doi.org/10.1086/192331

Prša & Zwitter. 2005, AJ, 628, 426, https://doi.org/10.1986/430591

Qian, S. 2001, MNRAS, 328, 635, https://doi.org/10.1046/j.1365-8711.2001.04931.x

Qian, S. 2003, MNRAS, 342, 1260, https://doi.org/10.1046/j.1365-8711.2003.06627.x

Ren, J. -J., Raddi, R., Rebassa-Mansergas, A., et al. 2020, ApJ, 905, 38, https://doi.org/10.3847/1538-4357/abc017

Ricker, G. R., Winn, J. N., Vanderspek, R., et al. 2015, JATIS, 1, 014003

Rosner, R., Golub, L., & Vaianna, G. S. 1985, ARA&A, 23, 413, https://doi.org/10.1146/annurev.aa.23.090185.02213

Ruciński, S. M. 1969, AcA, 19, 245

_________. 1992, AJ, 104, 1968, https://doi.org/10.1086/116372

_________. 2004, IAUS 215, Stellar Rotation, ed. A. Maeder & P. Enenes (San Francisco, CA: ASP), 17

Samolyk, G. 2017, JAVSO, 45, 215

Sarna, M. J. & Fedorova, A. V. 1989, A&A, 208, 111

Schlegel, D. J., Finkbeiner, D. P., & Davis, M. 1998, ApJ, 500, 525, https://doi.org/10.1086/305772

Schlafly, E. F. & Finkbeiner, D. P. 2011, ApJ, 737, 103, https://doi.org/10.1088/0004-637X/737/2/103

Shaw, J. S. 1990, in Active Close Binaries, ed. C. Ibanglou, (Dordrecht: Kluwer Academic Publishers), 241

Shaw, J. S. 1994, MmSAI, 65, 95

Stefanik, R. P., Latham, D. W., & Torres, G. 1999, ASPC 185, Precise Stellar Radial Velocities, ed. J. B. Hearnshaw & C. D. Scarfe, 354

Stępień, K. 1995, MNRAS, 274, 1019, https://doi.org/10.1093/mnras/274.4.1019

_________. 2006, AcA, 56, 199

_________. 2009, MNRAS, 397, 857, https://doi.org/10.1111/j.1365-2966.2009.14981.x

_________. 2011, AcA, 61, 139

Stępień, K. & Kiraga, M. 2013, AcA, 63, 239

Stępień, K., Pamyatnykh, A. A., & Rozyczka, M. 2017, Astr. Ap., 597, 87, https://doi.org/10.1051/0004-6361/201629511

Tian, X.-M. & Chang, L.-F. 2020, PASA, 37, 31, https://doi.org/10.107/pasa.2020.22

van Hamme, W. 1993, AJ, 106, 2096https://doi.org/10.1086/116788

van Hamme, W., Samec, R. G., Gothard, N. W., et al. 2001, AJ, 122, 3436, https://doi.org/10.1086/324110

Warner, B. D. 2007, MPBu, 34, 113

Wilson, R. E. 1979, ApJ, 234, 1054, https://doi.org/10.1086/157588

_________. 1990, ApJ, 356, 613, https://doi.org/10.1086/168867

Wilson, R. E. & Devinney, E. J. 1971, ApJ, 166, 605, https://doi.org/10.1086/150986

Yakut, K. & Eggleton, P. P. 2005, ApJ, 629, 1055, https://doi.org/10.1086/431300

Yilmaz, M., Basturk, O., Alan, N., et al. 2009, I.B.V.S., 5887, 1

Zhu, L. Y., Qian, S. B., Zola, S., & Kreiner, J. M. 2009, ApJ, 137, 3574, https://doi.org/10.1088/0004-6256/137/3/3574

DOI: https://doi.org/10.22201/ia.01851101p.2025.61.01.02

K. B. Alton and R. H. Nelson: Desert Blooms Observatory, 70 Summit Ave., Cedar Knolls, NJ, 07927, USA.

M. R. Kendurkar and R. H. Nelson: Guest investigator, Dominion Astrophysical Observatory, 5071 W Saanich Rd, Victoria, BC V9E 2E7, Canada.

R. H. Nelson: Desert Blooms Observatory, 70 Summit Ave., Cedar Knolls, NJ, USA (mail@underoakobservatory.com).

K. Stępień: Warsaw University Observatory, Al. Ujazdowskie 4, 00-478 Warszawa, Poland.

Revista Mexicana de Astronomía y Astrofísica, **61**, 29–47 (2025)

https://doi.org/10.22201/ia.01851101p.2025.61.01.03

GX 301-2 PRE-PERIASTRON AND APASTRON FLARES WITH *MAXI*

Á. Torregrosa[2], J. J. Rodes-Roca[1,2], J. M. Torrejón[1,2], G. Sanjurjo-Ferrín[2], T. Mihara[3], M. Nakajima[4], and M. Sugizaki[5]

Received July 10 2024; accepted October 2 2024

ABSTRACT

The bright high-mass X-ray binary GX 301-2 exhibits two periodic flare episodes along its orbit which are produced when the neutron star is close to the apastron and periastron passages. Time-resolved spectra were extracted and several models applied to describe all of them. The best description was obtained with a blackbody continuum modified by the Fe K-shell absorption edge, absorbed by a large column density on the order of 10^{23} cm^{-2} and, if present, a Fe Kα fluorescent emission line. Three of the nine apastron flares were as bright as the pre-periastron flare and two of them coincided with spin-up episodes of the neutron star. This fact points to the presence of a transient disc around the neutron star as it passes through the apastron that increases the accretion process. The size of the emitting region on the neutron star surface showed some variability but quite consistent with a hot spot.

RESUMEN

GX 301-2 presenta dos fulguraciones periódicas que se producen cuando la estrella de neutrones se encuentra cerca de los pasos por el apoastro y el periastro. Se extrajeron los espectros con resolución en fase orbital y la mejor descripción de todos ellos se obtuvo con un continuo de cuerpo negro modificado por el umbral de absorción de la capa K del Fe, absorbido por una gran columna de hidrógeno (10^{23} cm^{-2}) y, si estaba presente, una línea de emisión fluorescente del Fe Kα. Tres de las nueve fulguraciones en el apoastro fueron tan brillantes como la fulguración del preperiastro y dos de ellas coincidieron con episodios de aumento del período de la pulsación de la estrella de neutrones. Este hecho apunta a la presencia de un disco transitorio alrededor del objeto compacto en su paso por el apoastro. El tamaño de la región de emisión indica una mancha caliente en la superficie del objeto compacto.

Key Words: pulsars: individual: GX 301–2 — supergiants — X-rays: binaries

1. INTRODUCTION

GX 301−2 (also known as 4U 1223−62) is an X-ray pulsar whose rapid variability in the high-energy X-ray flux was discovered by McClintock et al. (1971) and Lewin et al. (1971). The neutron star moves in an eccentric orbit ($e = 0.462$) with an orbital period of 41.5 days (Sato et al. 1986) around the early B-type companion, Wray 15-977 (BP Cru). Its spin period of ≈ 685 s was discovered by White et al. (1976) and long-term frequency history shows a complex behavior spinning up and down on different timescales, as it can be seen in the *Fermi*/GBM Accreting Pulsars Program (Finger et al. 2009; Malacaria et al. 2020). The X-ray light curve shows a regular strong peak which is due to the pre-periastron passage of the neutron star. At this orbital phase, the compact object not only accretes matter from the dense stellar wind but is further enhanced by the material in the circumstellar disc around the compact object, which in turns powers the X-ray emission. Besides this strong flare,

[1]Department of Physics, Systems Engineering and Signal Theory, University of Alicante, 03080 Alicante, Spain.
[2]University Institute of Physics Applied to Sciences and Technologies, University of Alicante, 03080 Alicante, Spain.
[3]MAXI team, Institute of Physical and Chemical Researh (RIKEN), 2-1 Hirosawa, Wako, Saitama 351-0198, Japan.
[4]Nihon University School of Dentistry at Matsudo 2-870-1 Sakae-cho Nishi, Matsudo-shi, Chiba 271-8587, Japan.
[5]Science and Engineering, Kanazawa University, Kakuma, Kanazawa, Ishikawa 920-1192, Japan.

evidence of a second though much weaker periodic flare near apastron passage was discovered by Pravdo et al. (1995). However, it is not always detectable (Pravdo & Ghosh 2001). Spherically symmetric stellar wind models fail to describe both column density and luminosity data. Nevertheless, adding a gas stream which is not spherically distributed around the optical companion, improves the description of the data producing strong peaks in both column density and luminosity data (Stevens 1988; Leahy 1991; Haberl 1991a).

The spectral classification of Wray 15-977 is B1 Ia+ hypergiant (Kaper et al. 1995), confirmed by the spectra taken with the high-resolution Ultraviolet and Visual Echelle Spectrograph on the Very Large Telescope (Kaper et al. 2006). Model atmosphere fits to high-resolution optical spectra gave a radius $R_\star = 62\,R_\odot$, a mass $M_\star = \left(43^{+10}_{-4}\right)\,M_\odot$, an effective temperature $T_{\rm eff} = 18\,000$ K and a luminosity $L_\star = 5\times10^5\,L_\odot$. This luminosity corresponds to a distance $D = 3$ kpc, proposed by Kaper et al. (2006) on the basis of the Na I D interstellar lines. The European Space Agency (ESA) mission Gaia[6] Early Data Release 3 (GEDR3) has been used to find the distance to GX 301-2 , $D = \left(3.55^{+0.18}_{-0.16}\right)$ kpc. It is known as "photogeometric" distance and has been determined by using the parallax measure, BR-RP colour and the source's G-band magnitude (Bailer-Jones et al. 2021).

GX 301–2 has been observed by most X-ray observatories such as *Tenma* (Leahy 1991), *EXOSAT* (Haberl 1991a), *ASCA* (Saraswat et al. 1996; Endo et al. 2002), *RXTE* (Mukherjee & Paul 2004), *BeppoSAX* (La Barbera et al. 2005), *Chandra* (Watanabe et al. 2003) and *Suzaku* (Suchy et al. 2012). Focusing the study of the spectrum on the [0.3–10.0] keV energy band, the X-ray continuum spectra are usually described by three components: (i) an extremely absorbed power law; (ii) a scattered high absorbed power law; and (iii) an absorbed thermal component with a temperature of 0.8 keV. Moreover, the residuals between the spectrum and the continuum model show a number of emission lines depending on the X-ray observatory and the orbital phase of the observation. In addition, the iron complex at 6.4 keV was fully resolved by *Chandra* detecting the Compton shoulder of the iron Kα line at 6.24 keV (Watanabe et al. 2003).

The source GX 301−2 was observed with the *XMM-Newton* observatory on August 14th, 2008 (MJD 54 692.11–54 692.88, ObsID 0555200301), and on July 12th, 2009 (MJD 55 024.103–55 024.643, ObsID 0555200401). Both observations were taken during the pre-periastron flare. As a result of the high flux at this orbital phase ≈ 0.91, the *EPIC/MOS* CCD cameras were turned off to provide more telemetry for the *EPIC/PN* instrument, which was operated in modified timing mode, and a medium filter was used. In this timing mode the lower energy threshold of the instrument is increased to 2.8 keV to avoid telemetry drop outs due to the brightness of the source. The orbital-phase averaged spectra of both observations were extracted and described with several models. After trying different models, we found that the best continuum model that could fit both spectra significantly well was a hybrid model, combining thermal and non-thermal components. A component is called thermal when radiation is produced as a consequence of the thermal motion of the plasma particles (for instance, blackbody radiation). Otherwise, the emitted radiation is non-thermal (for instance, non-thermal inverse-Compton emission) (Giménez-García et al. 2015). The [2.8–10.0] keV energy spectrum was fitted using a model of the form:

$$F(E) = tbnew \times po + tbnew \times bbody + GL, \qquad (1)$$

where *tbnew*[7], in terms of XSPEC, is a new version of the Tübingen-Boulder interstellar medium absorption model which updates the absorption cross sections and abundances (Wilms et al. 2000); *po* is a typical photon power law whose parameters include a dimensionless photon index (Γ) and the normalisation constant (K), the spectral photons keV^{-1} cm^{-2} s^{-1} at 1 keV; *bbody* corresponds to a simple blackbody model incorporating the temperature $kT_{\rm bb}$ in keV and the normalisation *norm*, defined as L_{39}/D^2_{10}, where L_{39} is the source luminosity in units of 10^{39} erg s^{-1} and D^2_{10} is the distance to the source in units of 10 kpc; and *GL* indicates the Gaussian functions added to describe the emission lines. Therefore, the power-law component is interpreted in terms of inverse Compton-scattering by hot electrons of a seed radiation field, while the blackbody radiation is a foot-print of hot-spots on the NS surface. The total absorption column comprises the contribution from the interstellar medium and from the medium local to the source. The latter is by far the most dominant, and can be used to probe stellar wind structures or the presence of matter surrounding the compact object (i.e. accretion stream, accretion disc).

[6]https://www.cosmos.esa.int/gaia

[7]https://pulsar.sternwarte.uni-erlangen.de/wilms/research/tbabs/

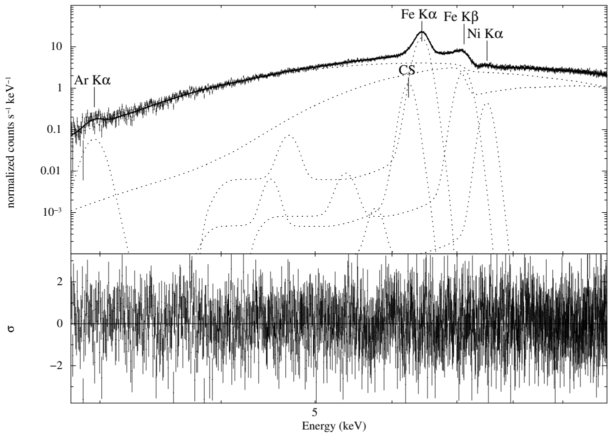

Fig. 1. *XMM-Newton* with ID 0555200301 (2008) orbital phase averaged spectrum of GX 301-2 in the (2.8–10.0) keV band. *Top panel*: data and best-fit model described by equation (1). *Bottom panel* shows the residuals between the spectrum and the model. Spectral parameters can be found in Table 1 (third column).

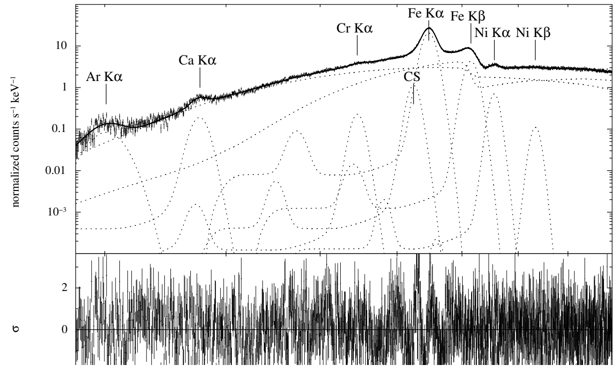

Fig. 2. *XMM-Newton* with ID 0555200401 (2009) orbital phase averaged spectrum of GX 301-2 in the (2.8–10.0) keV band. *Top panel*: data and best-fit model described by equation (1). *Bottom panel* shows the residuals between the spectrum and the model. Spectral parameters can be found in Table 1 (fourth column).

The best-fit parameters for the overall spectra of GX 301-2 and the corresponding uncertainties are summarized in Table 1 where it is also included the equivalent width (EW) of the Gaussian emission lines. Figures 1 and 2 show the data, the best-fit model described by equation (1), and the corresponding residuals.

The Gaussian emission lines were located at Ar Kα, Fe Kα, Fe Kβ, and Ni Kα, fluorescent line energies in the two *XMM-Newton* observations; meanwhile, the Gaussian emission lines located at Ca Kα, Cr Kα, and Ni Kβ fluorescent line energies were only detected in the *XMM-Newton* observation from 2009. Moreover, the Fe Kα showed residuals when fitted with a single Gaussian and an additional Compton Shoulder was also included (Watanabe et al. 2003). The *XMM-Newton* observation from 2009 was also analysed by Fürst et al. (2011). They used different continuum models to fit this spectrum but they also added the same Gaussian emission lines used in this work. The *XMM-Newton* observation from 2008 was also studied by Roy et al. (2024). To describe this spectrum, these authors fitted a model as previously used by Fürst et al. (2011) and identified the same Kα emission lines, included the Compton Shoulder, and Fe Kβ, but Ni Kβ was not detected.

The size of emitting region on the NS surface was obtained from the *bbody* component by the equation:

$$R_{\rm bb}({\rm km}) = 3.04\times10^4\,\frac{D\sqrt{F_{\rm bb}}}{T_{\rm bb}^2}, \tag{2}$$

where D is the distance to the source in kpc, $F_{\rm bb}$ is the unabsorbed flux in erg s^{-1} cm^{-2} in the energy range [2.8–10.0] keV and $T_{\rm bb}$ is the temperature in keV. Taking into account the distance to the source given by *GEDR3* $d(kpc) = 3.55^{+0.18}_{-0.16}$ it has been found that the radius of the emission region is consistent with a hot spot on the NS surface: from the 2008 observation, the calculated flux was $F_{\rm bb} = \left(1.40^{+0.17}_{-0.20}\right)\times10^{-9}$ erg s^{-1}cm^{-2} and gave a radius $R_{\rm bb} = 0.41^{+0.10}_{-0.08}$ km, and from the 2009 observation, $F_{\rm bb} = \left(8.1^{+1.6}_{-0.9}\right)\times10^{-10}$ erg s^{-1}cm^{-2} and $R_{\rm bb} = 0.27^{+0.07}_{-0.06}$ km, respectively.

The intrinsic bolometric X-ray luminosity can be expressed through the unabsorbed X-ray flux of the source as:

$$L_{\rm X} = 4\,\pi\,D^2\,F_{\rm no\_abs}, \tag{3}$$

where $L_{\rm X}$ is the X-ray luminosity, D is the distance to the source and $F_{\rm no\_abs}$ is the unabsorbed flux in the [2.8–10.0] keV energy band. The observed $F_{\rm no\_abs}$ for the 2008 and 2009 observations were $\left(6.9^{+0.8}_{-1.0}\right)\times10^{-9}$ erg s^{-1}cm^{-2} and $\left(5.3^{+1.0}_{-0.6}\right)\times10^{-9}$ erg s^{-1}cm^{-2}, respectively, corresponding to X-ray luminosities of $L_{\rm X_{2008}} = (1.1\pm0.3)\times10^{37}$ erg s^{-1} and $L_{\rm X_{2009}} = \left(8.1^{+2.4}_{-1.6}\right)\times10^{36}$ erg s^{-1}.

In Table 1, *norm* represents the blackbody normalisation and is related to the luminosity of the X-ray source and the distance $\left(L_{39}/D_{10}^2\right)$. Matching this expression with the values of luminosities and distance to the source, the results were 0.08 ± 0.10 and $0.06^{+0.08}_{-0.07}$ from the 2008 and 2009 observations, respectively, which is consistent with the fit values taking the uncertainties into account.

TABLE 1

BEST-FIT MODEL PARAMETERS FOR THE AVERAGED SPECTRA[a]

Component	Parameter	Value (ID 0555200301)	Value (ID 0555200401)
tbnew	N_H^1 [10^{22} atoms cm^{-2}]	191^{+19}_{-9}	183^{+12}_{-10}
	N_H^2 [10^{22} atoms cm^{-2}]	$42.2^{+1.1}_{-1.0}$	$53.3^{+2.2}_{-1.7}$
Power law	Photon index Γ	1.2 ± 0.3	$1.03^{+0.13}_{-0.12}$
	norm [keV^{-1} s^{-1} cm^{-2}]	$0.7^{+0.7}_{-0.3}$	$0.40^{+0.14}_{-0.10}$
bbody	kT [keV]	$3.14^{+0.21}_{-0.11}$	3.37 ± 0.22
	norm [L_{39}/D_{10}^2]	$0.041^{+0.005}_{-0.006}$	$0.026^{+0.005}_{-0.002}$
Ar Kα	Line E [keV]	2.96 ± 0.04	3.013 ± 0.012
	σ [keV]	$0.005^{+0.010}_{-0.005}$	$0.092^{+0.021}_{-0.018}$
	EW [keV]	$0.11^{+0.06}_{-0.03}$	$0.82^{+0.09}_{-0.07}$
	norm [10^{-5} ph s^{-1} cm^{-2}]	$2.8^{+1.5}_{-0.7}$	$4.7^{+0.5}_{-0.4}$
Ca Kα	Line E [keV]		3.756 ± 0.008
	σ [keV]		$0.021^{+0.018}_{-0.021}$
	EW [keV]		0.094 ± 0.009
	norm [10^{-5} ph s^{-1} cm^{-2}]		$6.4^{+0.6}_{-0.6}$
Cr Kα	Line E [keV]		$5.463^{+0.021}_{-0.015}$
	σ [keV]		0.01 (frozen)
	EW [keV]		$0.0117^{+0.0023}_{-0.0022}$
	norm [10^{-5} ph s^{-1} cm^{-2}]		$8.1^{+1.6}_{-1.5}$
Compton Shoulder	Line E [keV]	6.24 (frozen)	6.24 (frozen)
	σ [keV]	0.01 (frozen)	0.01 (frozen)
	EW [keV]	$0.0207^{+0.0024}_{-0.0021}$	$0.0163^{+0.0011}_{-0.0007}$
	norm [10^{-4} ph s^{-1} cm^{-2}]	$7.7^{+0.9}_{-0.8}$	$4.5^{+0.3}_{-0.2}$
Fe Kα	Line E [keV]	$6.4388^{+0.0017}_{-0.0009}$	$6.4698^{+0.0007}_{-0.0004}$
	σ [keV]	$0.0462^{+0.0019}_{-0.0022}$	$0.0503^{+0.0008}_{-0.0009}$
	EW [keV]	$0.528^{+0.005}_{-0.006}$	0.701 ± 0.003
	norm [10^{-2} ph s^{-1} cm^{-2}]	$1.159^{+0.012}_{-0.014}$	1.016 ± 0.005
Fe Kβ	Line E [keV]	$7.121^{+0.005}_{-0.004}$	$7.1518^{+0.0019}_{-0.0012}$
	σ [keV]	$0.063^{+0.006}_{-0.007}$	$0.056^{+0.002}_{-0.003}$
	EW [keV]	0.134 ± 0.005	0.223 ± 0.003
	norm [10^{-3} ph s^{-1} cm^{-2}]	$2.49^{+0.09}_{-0.10}$	$2.64^{+0.03}_{-0.04}$
Ni Kα	Line E [keV]	$7.513^{+0.015}_{-0.018}$	$7.558^{+0.003}_{-0.012}$
	σ [keV]	0.03 ± 0.03	$0.00^{+0.03}_{-0.00}$
	EW [keV]	0.027 ± 0.005	0.0422 ± 0.0023
	norm [10^{-4} ph s^{-1} cm^{-2}]	$4.0^{+0.8}_{-0.7}$	4.03 ± 0.22
Ni Kβ	Line E [keV]		8.33 ± 0.04
	σ [keV]		$0.03^{+0.07}_{-0.03}$
	EW [keV]		0.008 ± 0.003
	norm [10^{-5} ph s^{-1} cm^{-2}]		9 ± 3
χ^2_r		χ^2/(d.o.f.) = 1531/1420 = 1.1	χ^2/(d.o.f.) = 1711/1412 = 1.2

[a]Parameters for equation (1). Observations ID 0555200301 (third column) and 0555200401 (fourth column). EW represents the equivalent width of the emission line. Uncertainties are given at the 90% confidence limit and d.o.f is degrees of freedom.

DOI: https://doi.org/10.22201/ia.01851101p.2025.61.01.03

An intense Fe Kα emission line (EW $\approx$ [0.5, 0.7] keV) with a global hydrogen column above 10^{24} cm^{-2} has been found in the analysis and it is compatible with Leahy et al. (1988, 1989), and Fürst et al. (2011) who found in this X-ray region a strong emission line Fe Kα visible together with a hydrogen column above 10^{24} cm^{-2}.

The flux ratio between the Fe Kα and Fe Kβ allowed us to derive that the ionisation state of iron varied from Fe XII-XIII (Fe Kβ/Fe Kα = $0.215^{+0.010}_{-0.011}$) in the 2008 observation to Fe > XIV (Fe Kβ/Fe K$\alpha = 0.260^{+0.004}_{-0.005}$) in 2009 observation. These results pointed out that only mildly ionised iron was present in the plasma (Fürst et al. 2011).

TABLE 2

EPHEMERIS DATA USED FOR *MAXI*/GSC 'S TIMING CALCULATIONS

$T_{0,\mathrm{periastron\_passage}}$ (MJD)	48802.79 ± 0.12
P_{orb} (d)	41.498 ± 0.002 (Koh et al. 1997)

On the other hand, the flux ratio between Ni Kα and Ni Kβ (Ni Kβ/Ni K$\alpha = 0.23 \pm 0.09$) was slightly consistent with measurements in solid state metals within errors (Han & Demir 2009) in the 2009 observation.

The results mentioned above show a slightly different values between parameters from one observation to the other. In order to further study these differences, the pre-periastron flare has been analysed in the long term to find how the spectral parameters evolve with time. In addition, GX 301-2 also shows a periodic near-apastron flare with lower intensity than the pre-periastron flare and it is also included in this long term analysis. For such studies, it is also very convenient to have spectra measured at different orbital phases with uniform phase coverage. The characteristics of the *Monitor of All Sky X-ray Image* (*MAXI*), moderate energy resolution and all-sky coverage, are well suited for elaborate studies of the orbital phase resolved spectra of bright X-ray sources. The process which was used to obtain the data is explained in § 2.

Observations, data and timing analysis are described in § 2, *MAXI*/GSC spectral analyses for the pre-periastron and near-apastron flares are discussed in § 3, and § 4 contains the summary of the main results.

2. TIMING ANALYSIS

The orbital phase of the pre-periastron flare has been divided into three sections to perform the spectral analysis. To define them the *MAXI*/GSC (2.0–20.0) keV light curve with a time bin of 0.02 days[8] has been folded using the ephemeris from Koh et al. (1997), which are reported in Table 2, and a circular orbit has been assumed because we wanted to have an approximation of the results. Figure 3 shows the light curve folded over the GX 301-2 orbital period where three sections have been identified by vertical lines: I pre-flare, II flare and III post-flare. As a consequence of the low intensity level, only one section has been used to define the near-apastron flare at the [0.20–0.70] orbital phase range. For each orbit, the Modified Julian Dates (MJDs) for every orbital

[8] `http://maxi.riken.jp/pubdata/v7lrkn/J1226-627/index.html`

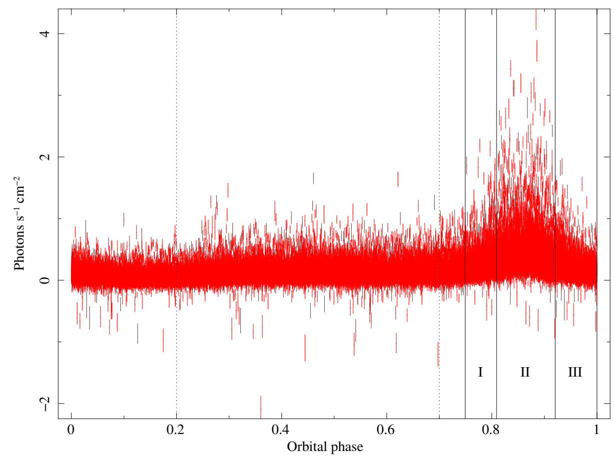

Fig. 3. Folded and background subtracted light curve in the (2.0–20.0) keV energy range. The light curve was folded over the orbital period and binned into ≈ 450 phase bins. The selection criteria for the apastron flare from MAXI data were: orbital phase range = [0.20–0.70] and (2-20) keV flux > 0.5 photons cm^{-2} s^{-1}. The color figure can be viewed online.

phase range of the pre-periastron flare have been calculated. For each section, data were accumulated over ten consecutive orbits to extract spectra with acceptable signal-to-noise ratio. As an example, Table 3 summarizes MJDs of the first ten orbits for pre-flaring, flaring and post-flaring, which were used as good time intervals (GTIs) to extract the spectra. One possible implication of the circular orbit assumption is that the MJDs would be affected by the approach of the orbit and there could be inaccuracies that could affect the conclusions obtained. However, the spectra are consistent from one set to the next one (see Figures 9-11) and this indicates that the assumption of a circular orbit is useful for the system GX 301-2 when analysing the pre-periastron flare.

Figure 4 shows a comparison between spectra obtained by accumulating ten orbits (top spectra) and spectra obtained by accumulating five orbits (bottom spectra).

In the context of *MAXI*/GSC data, the passbands often used are called "soft" (2.0–4.0) keV, "medium" (4.0–10.0) keV, and "hard" (10–20.0) keV bands. To search for pre-periastron and near-apastron changes in the X-ray emission, light curves in the (2.0–4.0) keV, (4.0–10.0) keV, (10–20.0) keV and (5.7–7.5) keV (iron complex emission lines) energy bands were extracted and analysed using *Astropy*, a collection of software packages which are included in *Python* (Astropy Collaboration et al. 2022). In each of these light curves a *Lomb-Scargle* periodogram (Press & Rybicki 1989) was applied and

TABLE 3

FIRST TEN ORBITS: PRE-FLARE, FLARE AND POST-FLARE

Pre-flare (≈[0.7493, 0.8090])	Flare (≈[0.8090, 0.9205])	Post-flare (≈[0.9205, 0.9984])
$MJD_i - MJD_f$	$MJD_i - MJD_f$	$MJD_i - MJD_f$
55141.582121−55144.056111	55144.056111−55148.686661	55148.686661−55151.921117
55183.080121−55185.554111	55185.554111−55190.184661	55190.184661−55193.419117
55224.578121−55227.052111	55227.052111−55231.682661	55231.682661−55234.917117
55266.076121−55268.550111	55268.550111−55273.180661	55273.180661−55276.415117
55307.574121−55310.048111	55310.048111−55314.678661	55314.678661−55317.913117
55349.072121−55351.546111	55351.546111−55356.176661	55356.176661−55359.411117
55390.570121−55393.044111	55393.044111−55397.674661	55397.674661−55400.909117
55432.068121−55434.542111	55434.542111−55439.172661	55439.172661−55442.407117
55473.566121−55476.040111	55476.040111−55480.670661	55480.670661−55483.905117
55515.064121−55517.538111	55517.538111−55522.168661	55522.168661−55525.403117

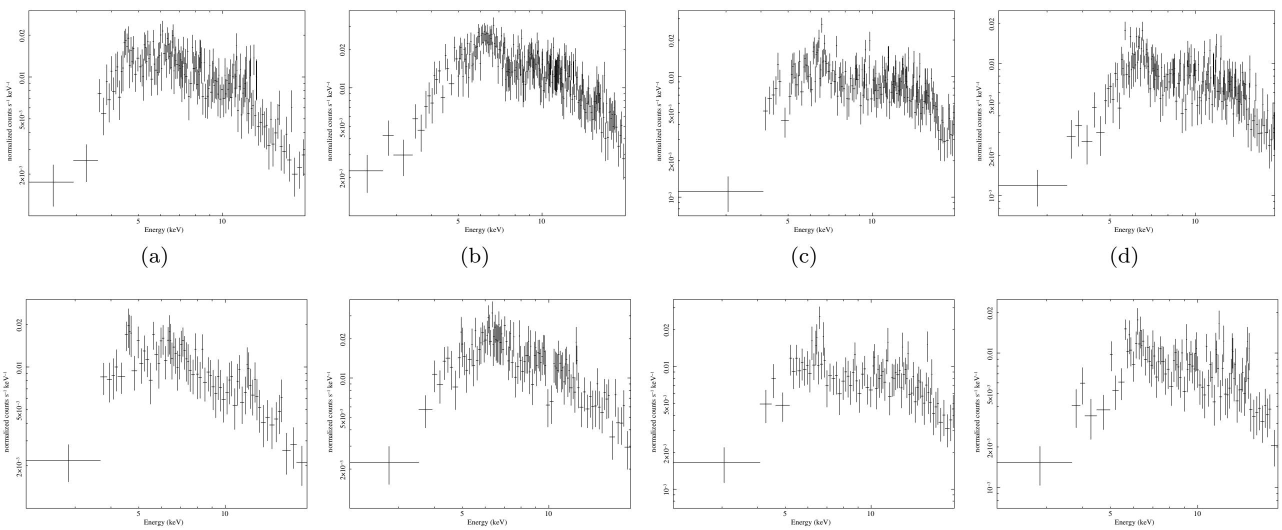

(a) (b) (c) (d)

(e) (f) (g) (h)

Fig. 4. MAXI/GSC spectra of GX 301-2 in the (2.0–20.0) keV band. (a) and (e): pre-flare, third extraction. (b) and (f) pre-flare, ninth extraction. (c) and (g): post-flare, fifth extraction. (d) and (h): post-flare, eighth extraction. Spectra (a)−(d) correspond to the accumulation of ten orbits. Spectra (e)−(h) correspond to the accumulation of five orbits. Units of the x-axis: Energy (keV). Units of the y-axis: normalized counts s^{-1} keV^{-1}.

the error in the period is approximately the area where the peak is at the 90% of its value. It was apparent that the light curves were similar to each other and, in this work, only the periodogram of the light curve (4–10) keV is shown (see Figure 5). As can be seen from Figure 5, the highest peak (power ≈ 0.084) is at (41.4±0.5) days which corresponds to the rotational period of the binary system determined by Koh et al. (1997). The second peak (power ≈ 0.055) in the power density spectrum at ≈20.7 days is potentially a harmonic of the orbital period.

The hardness ratio is a specially useful tool to quantify and characterise the source spectrum. Therefore, simple hardness ratio (hard/medium) and fractional difference hardness ratio (medium−soft)/(medium+soft) have been calculated using the weighted average over 150 bins and plotted in Figures 6 and 7, respectively. The weighting factor here for computing the average HR is the error weighted average, where the errors have been calculated with the general method of using formulas for propagating errors. Both graphs show that the ratios continue to oscillate around the average, with no clear trend.

Figure 8 shows the pulse frequency history of GX 301-2 observed with *Fermi*/GBM Accreting Pulsars Program[9] (Malacaria et al. 2020). Every two

[9]http://gammaray.nsstc.nasa.gov/gbm/science/pulsars

DOI: https://doi.org/10.22201/ia.01851101p.2025.61.01.03

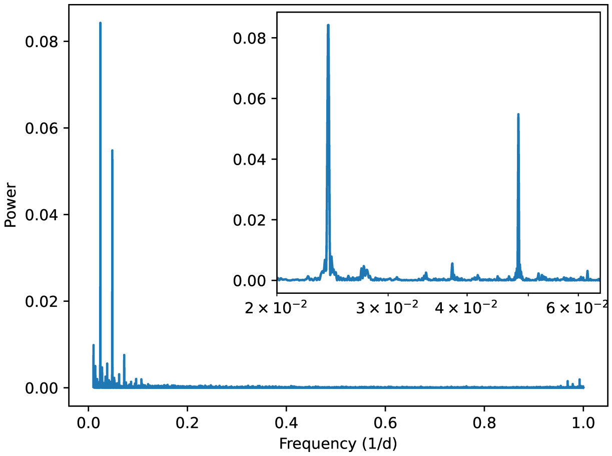

Fig. 5. Lomb-Scargle periodogram of the (4.0–10.0) keV light curve. The plot on the right top corner has been added to show only lower frequencies where the peaks lie. The color figure can be viewed online.

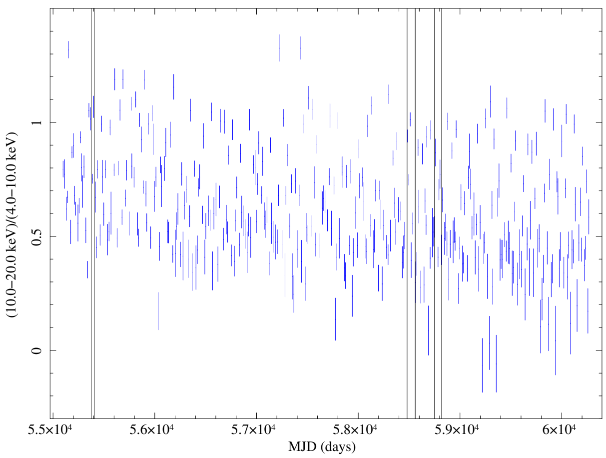

Fig. 6. Hardness ratio $hard/medium = (10.0 - 20.0\ \text{keV})/(4.0 - 10.0\ \text{keV})$ using weighted average. The spin-up episodes are indicated by two vertical lines: (a) from MJD 55375 to 55405, (b) from MJD 58480 to 58560 and (c) from MJD 58750 to 58820. The color figure can be viewed online.

vertical lines on this plot represent a spin-up episode in the history of observations of the source, which have been associated with the formation of a transient accretion disc (Koh et al. 1997; Nabizadeh et al. 2019). Two of these irregular spin-up episodes can be related to the apastron passages (see § 3.2).

3. SPECTRAL ANALYSIS

3.1. *Pre-periastron Flare Spectra*

The spectra were obtained using the *MAXI*/GSC on-demand process[10]; all of them

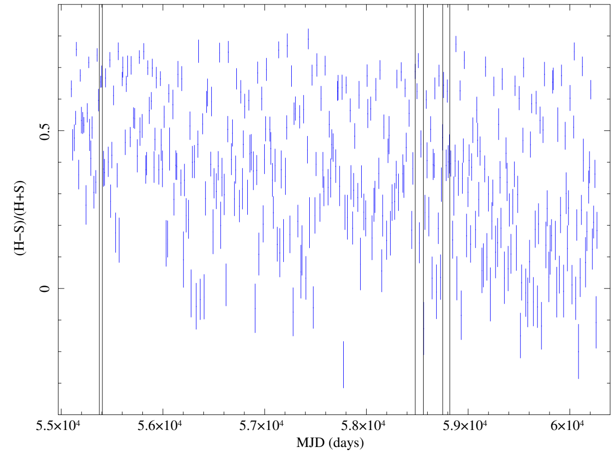

Fig. 7. Hardness curve (medium − soft)/(medium + soft) using weighted averages. The spin-up episodes are indicated by two vertical lines: (a) from MJD 55375 to 55405, (b) from MJD 58480 to 58560 and (c) from MJD 58750 to 58820. The color figure can be viewed online.

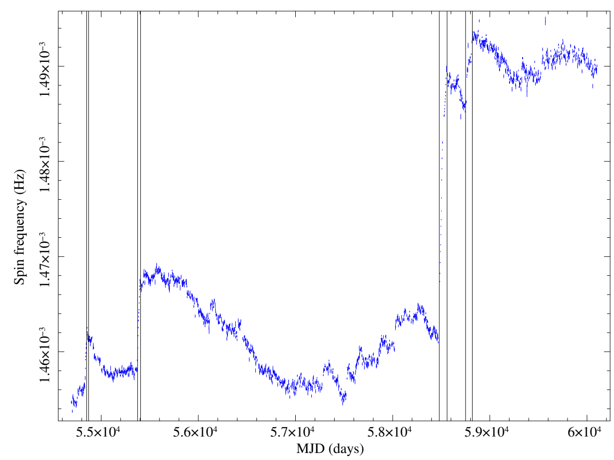

Fig. 8. Spin frequency versus the MJD for the system GX 301-2 using the data from *Fermi*/GBM . There are four spin-up episodes which are indicated by two vertical lines: (a) from MJD 54850 to 54870, (b) from MJD 55375 to 55405, (c) from MJD 58480 to 58560 and (d) from MJD 58750 to 58820. The color figure can be viewed online.

were analysed and modelled with the XSPEC (Arnaud 1996) package and the energy range used for spectral fitting was (2.0–20.0) keV. Both phenomenological and physical models commonly applied to accreting X-ray pulsars have been tested. Models with power law components have been developed to HMXBs, such as Cen X-3 (Ebisawa et al. 1996) and GX 301-2 (Fürst et al. 2011; Ji et al. 2021). First of all, traditional models like power law with a high energy cut-off or with a Fermi-Dirac cut-off were explored. Although these

[10] `http://maxi.riken.jp/mxondem`

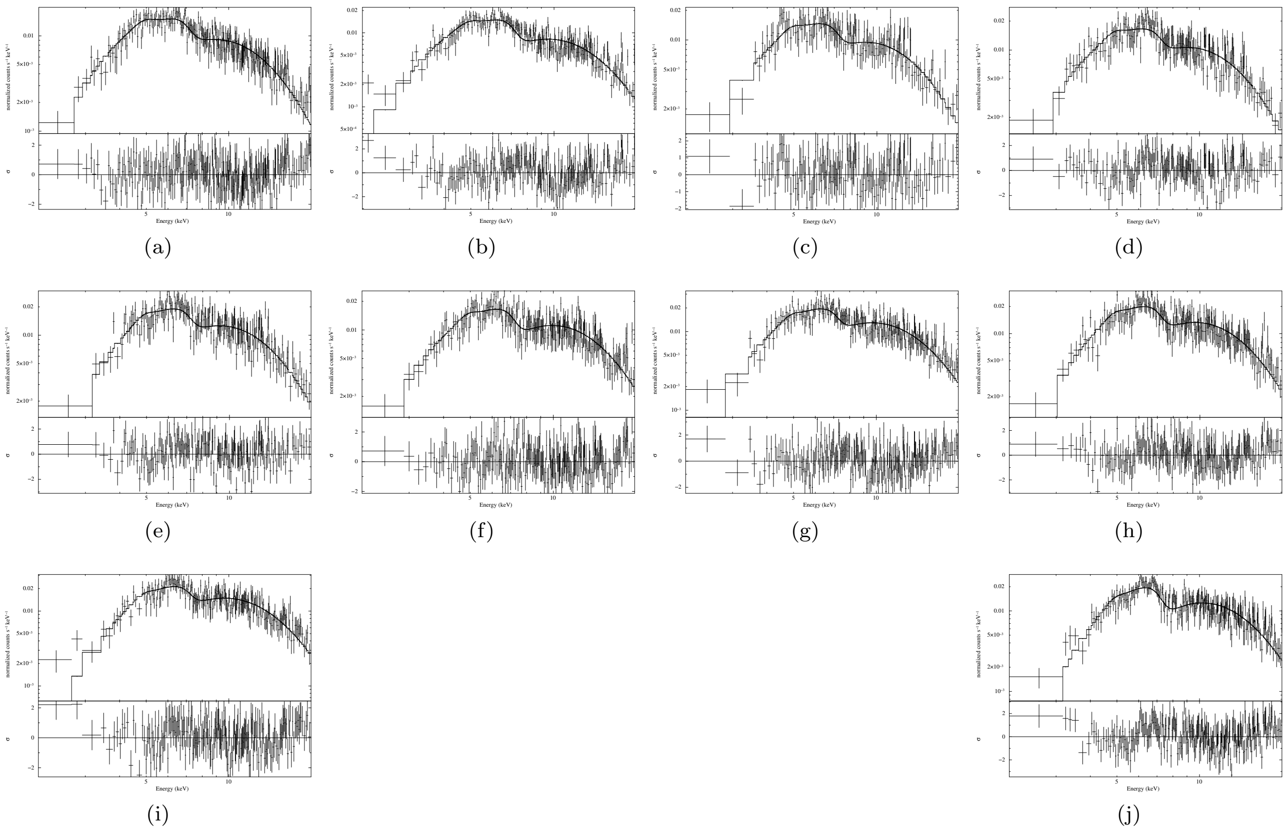

Fig. 9. *MAXI*/GSC spectra of GX 301-2 in the (2.0–20.0) keV band corresponding to the pre-flare (≈[0.7493, 0.8090]), model defined by equation (6). The same orbital phase range was accumulated in groups of ten consecutive orbits to obtain each spectrum. Units of the x-axis: Energy (keV). Units of the y-axis: Normalized counts s^{-1} keV^{-1}.

models reasonably well reproduce the observed flare spectra between (2.0–20.0) keV ($\chi^2_r = [0.96 - 1.32]$), they cannot offer a good statistical and/or physical solution for all spectra because the parameters of the high energy cut-off and the photon index ($\Gamma = [-0.3, 0.6]$) could not be constrained well. As the principal aim is to describe with a consistent model all spectra these models were rejected. Then, the orbital phase-averaged spectra were described using a simple model with two power laws described by equations (4) and (5). A fast charged particle traversing a region containing a strong magnetic field will change direction because the magnetic field exerts a force perpendicular to the direction of motion. Because the velocity vector changes, the charged particle is accelerated and consequently emits electromagnetic energy, called synchroton radiation. Observed polarisation in the radiation is usually a proof of synchrotron emission (Giménez Cañete & Castro Tirado 2005). The usual spectra form can be described by a power law $F(E) = B\,E^{-\Gamma}$, where B represents a constant and Γ is the photon index. The more positive the value of the Γ, the softer is the spectrum. The scattering of X-rays by interstellar dust softens the spectrum by E^{-2} relative to the source spectrum, and soft X-rays are scattered more strongly than hard X-rays. In the energy range (0.1–10) keV, the main interaction between X-rays and matter is the photoelectric effect, whose cross-section varies with energy as $\approx Z^3\,E^{-3}$. Consequently, absorption is greatest at low energies and in high-Z materials. Thus, the energy spectra have been fitted by two power-law components, where each photon index indicates the source spectrum and the scattering or absorption spectrum, respectively. Initially, the orbital phase-resolved spectra were fitted with a composite model of two absorbed power laws:

$$F(E) = tbnew \times B\,E^{-\gamma} + tbnew \times B\,E^{-(\gamma+2.0)} + GL, \quad (4)$$

$$F(E) = tbnew \times BE^{-\gamma} + tbnew \times BE^{-(\gamma+3.0)} + GL. \quad (5)$$

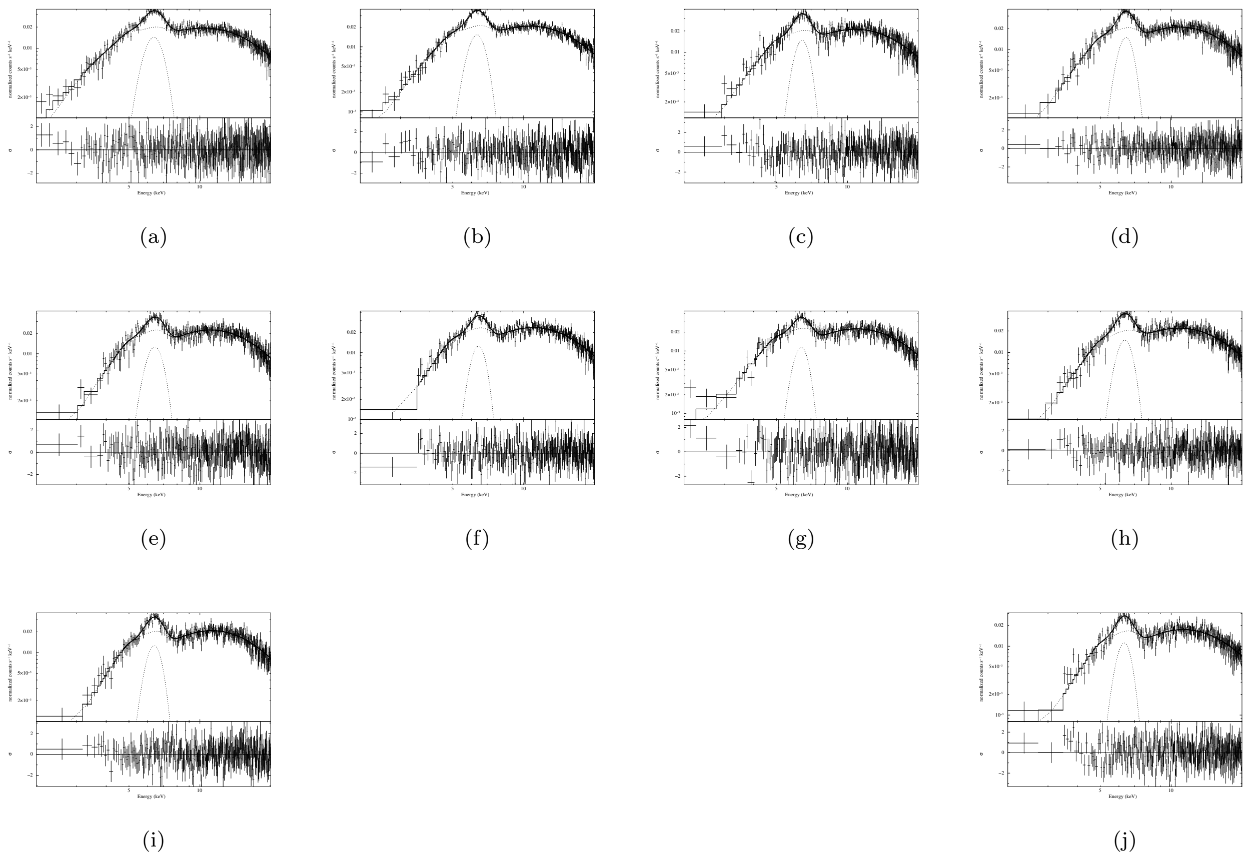

Fig. 10. *MAXI*/GSC spectra of GX 301-2 in the (2.0–20.0) keV band corresponding to the flare (≈[0.8090, 0.9205]), model defined by equation (6). The same orbital phase range was accumulated in groups of ten consecutive orbits to obtain each spectrum. Units of the x-axis: Energy (keV). Units of the y-axis: normalized counts s^{-1} keV^{-1}.

Although both models described above fitted the averaged spectra between (2.0–20.0) keV with a similar statistical confidence (equation 4, $\chi_r^2 = [0.86\text{–}1.10]$; equation 5, $\chi_r^2 = [0.89\text{–}1.18]$), they could not offer a consistent astrophysical solution to all the resolved spectra. For example, in the flare spectra N_H^2 values were above 200×10^{22} cm^{-2} in eight spectra (equation (4), $N_H^2 \approx \left(231 - 10^6\right) \times 10^{22}$ cm^{-2}; equation (5), $N_H^2 \approx \left(266 - 10^6\right) \times 10^{22}$ cm^{-2}), which were not consistent with the N_H values $(10 - 80) \times 10^{22}$ cm^{-2} obtained in the *MAXI*/GSC analysis of Islam & Paul (2014).

During flare episodes the surface temperature of the neutron star can reach several million degrees and, therefore, it will emit blackbody radiation with photons in the X-ray range. The blackbody component has been used to describe the soft energy band spectra of HMXBs like Cen X-3 using data from *XMM-Newton* (Sanjurjo-Ferrín et al. 2021) and *MAXI*/GSC (Torregrosa et al. 2022). The overall *MAXI*/GSC spectra of the source was modelled with an absorbed *bbody* component. The spectral shape showed evidence for an Fe K-shell absorption edge at ≈ 7.1 keV (Saraswat et al. 1996; Endo et al. 2002; Ji et al. 2021); therefore, an edge component fixed at this energy was added. The following model was applied to describe all observational data:

$$F(E) = tbnew \times bbody \times edge + GL, \qquad (6)$$

where the Gaussian line was also included to account for the iron fluorescent emission line at ≈6.4 keV, if present. The model gave a good statistical description (pre-flare, $\chi_r^2 = 0.91 - 1.22$; flare, $\chi_r^2 = 0.89 - 1.07$; post-flare, $\chi_r^2 = 0.85 - 1.18$). In Figures 9-11 the ten *MAXI*/GSC spectra for each preperiastron section, the best-fitting model, and residuals to the best-fitting model are shown.

Some spectra showed a low-energy excess below ≈4.0 keV as can be seen in Figure 9, images (b), (c), (g), (i) and (j); Figure 10, image (g); and Figure 11,

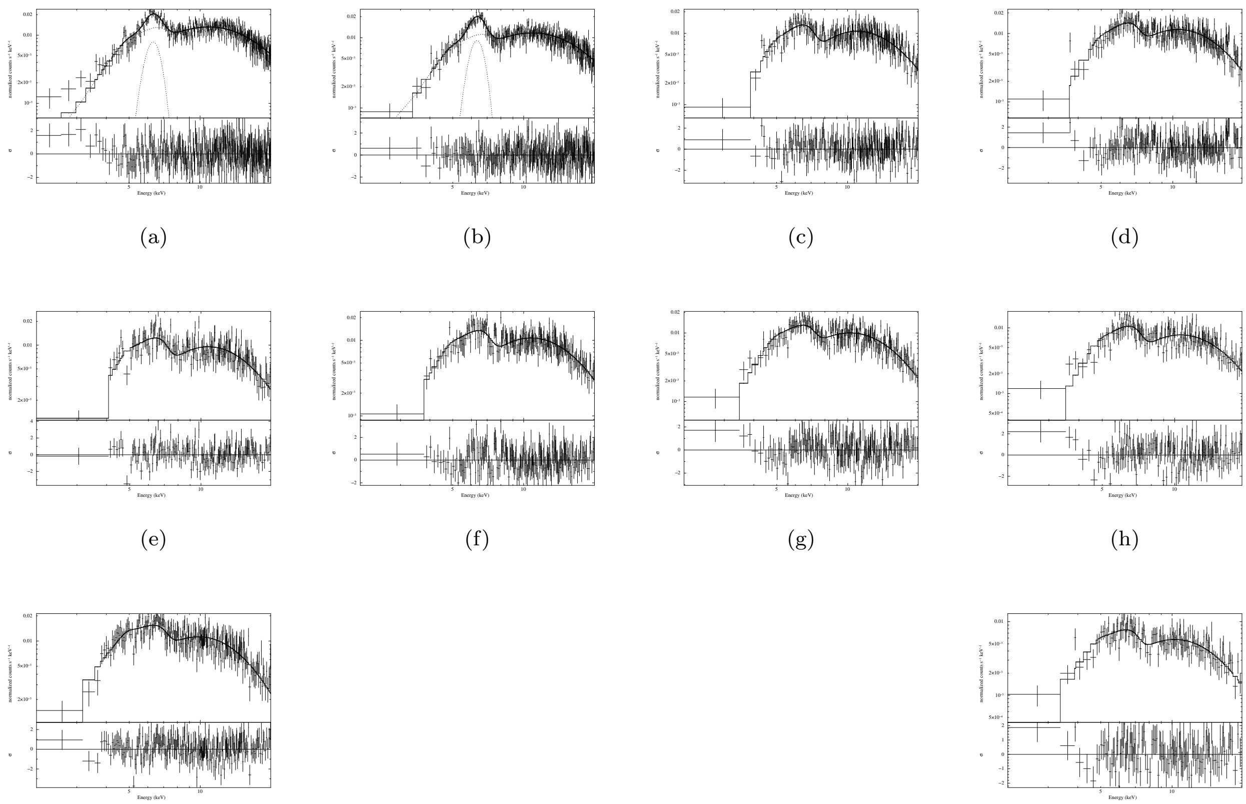

(a) (b) (c) (d)

(e) (f) (g) (h)

(i) (j)

Fig. 11. *MAXI*/GSC spectra of GX 301-2 in the (2.0–20.0) keV band corresponding to the post-flare (≈[0.9205, 0.9984]), model defined by equation (6). The same orbital phase range was accumulated in groups of ten consecutive orbits to obtain each spectrum. Units of the x-axis: Energy (keV). Units of the y-axis: Normalized counts s^{-1} keV^{-1}.

images (g), (h) and (j). This soft excess could be produced by a transitory structure in the line of sight because it was not a permanent effect in all X-ray spectra. Therefore, a possible explanation may be the presence of a transitory disc which enhances the accretion of matter. X-ray pulsars such as GX 301-2 tend to be spinning up because the accreted material from the optical star has an angular momentum which is eventually transferred to the compact object. The higher the X-ray luminosity, the more material is accreted by the pulsar, and therefore the faster it will spin. The strongest spin-up event of GX 301-2 so far (between 2018 December and 2019 March) pointed to an accretion due to both direct accretion from the stellar wind and a temporary accretion disc (Nabizadeh et al. 2019). This scenario was also supported by the observations taken with the *Insight-Hard X-ray Modulation Telescope* during the initial part of this spin-up episode (Liu et al. 2021). On the other hand, the low-energy excess could also be explained by scattering in the gas stream around the neutron star and in the stellar wind of the B-type companion star (Saraswat et al. 1996).

Figures 12 to 19 show the evolution of the best-fit model parameters during the pre-periastron and apastron passages. In Figures 13-19 filled black squares represent the pre-flare parameter values, filled red triangles the flare parameter values, and open blue circles the post-flare parameter values.

Taking the uncertainties into account, the results for the *bbody* normalisation (Figure 12) obtained with XSPEC (open blue circles) are consistent with the values obtained using L_{39}/D_{10}^2 (filled red squares).

The radius of the emission zone (Figure 13) is of the order of 1 km, which is consistent with a hot spot on the NS surface and with the results of *XMM-Newton* data. The temperature of the blackbody (kT in keV, Figure 14) has a constant value between (3.0–3.5) keV in the pre-flare spectra, but it is en-

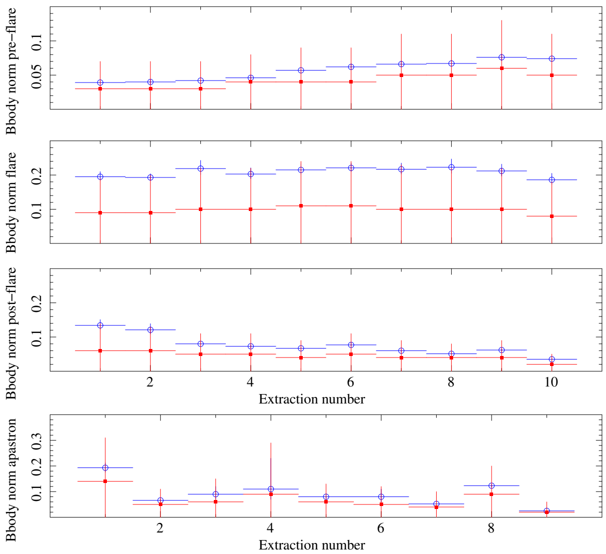

Fig. 12. Evolution of the *bbody* norm for the pre-periastron flare and apastron outbursts versus the extraction number (*MAXI*/GSC data, model defined by equation 6). *Top panel*: pre-flare. *Second panel*: flare. *Third panel*: post-flare. *Bottom panel*: apastron outbursts. Filled red squares: bbody norm calculated by using L_{39}/D_{10}^2. Open blue circles: *bbody* norm fit value. The color figure can be viewed online.

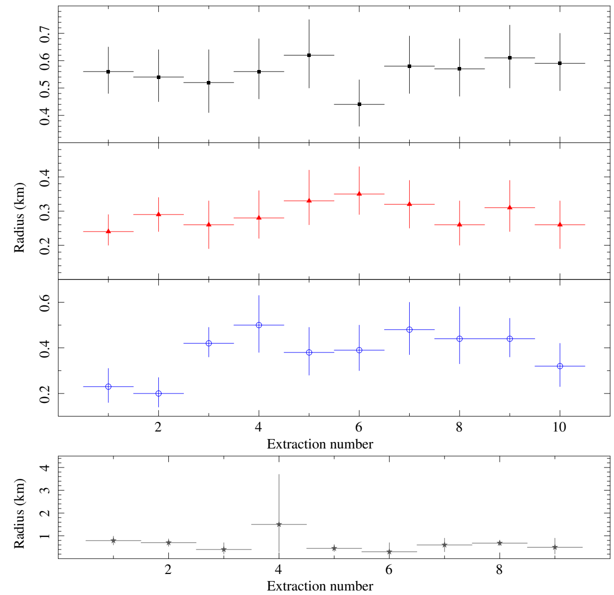

Fig. 13. Evolution of the radius of the emission zone for the pre-periastron flare and apastron outbursts versus the extraction number (*MAXI*/GSC data, model defined by equation 6). Filled black squares: pre-flare. Filled red triangles: flare. Open blue circles: post-flare. Filled dark grey stars: apastron outbursts. The color figure can be viewed online.

hanced in the sixth extraction, which is reflected in a drop of the emission radius (Figure 13). In the flare spectra, it is enhanced in the (5.5–6.5) keV range indicating an increase in the accretion rate which is reflected in a higher X-ray luminosity compared to pre- and post-flare. In the post-flare the temperature is approximately constant, (3.8–4.1) keV, between the third and the tenth extraction, but there is a large increase in the first and second extractions with a value ≈ 6.0 keV which is reflected in a clear decrease of the emission zone between $\approx$ (0.2–0.3) km.

In the flare the unabsorbed flux (Figure 15) has no significant evolution in the fitting energy range (2.0–20.0) keV, showing that the accretion rate is quite stable. The unabsorbed fluxes show opposite trends between the pre-flare (the flux increases) and the post-flare (the flux decreases) showing that the accretion rate has a different behaviour along the pre-periastron passage. A possible explanation for this would be that the absorbing matter is located in the line of sight between the observer and the neutron star in the post-flare ($N_H \gtrsim 2 \times 10^{23}$ cm^{-2}) and away from the line of sight in the pre-flare ($N_H < 2 \times 10^{23}$ cm^{-2}). Thus, it is confirmed that the distribution of circumstellar matter around the compact object is rather inhomogeneous during the pre-periastron passage (Saraswat et al. 1996; Islam & Paul 2014).

The X-ray luminosity (Figure 16) is consistent with a constant value ($L_{\rm X} \approx 1.3 \times 10^{37}$ erg s^{-1}) in the flare spectra (which agrees with the observations ID 0555200301 and ID 0555200401 from *XMM-Newton*) and is greater than in the pre-flare ($L_{\rm X} = [4-7] \times 10^{36}$ erg s^{-1}) and in the post-flare ($L_{\rm X} = [3-8] \times 10^{36}$ erg s^{-1}) spectra. This scenario, in which the wind mass-loss rate is insufficient to power the source entirely, indicates that an additional mechanism is needed to give the neutron star the fuel it needs. Wind-fed HMXBs are powered by accretion of the radiatively driven wind of the luminous component on the compact object with typical X-ray luminosities $\approx 10^{36}$ erg s^{-1} (see Martínez-Núñez et al. 2017; Kretschmar et al. 2019, for instance), i.e. one order of magnitude smaller than observed in the flare event. A possible mechanism for enhancing the X-ray emission is thought to be the presence of a gas stream trailing the neutron star (Saraswat et al. 1996; Islam & Paul 2014). Another cause could be that an accretion disc has formed around the neutron star (Nabizadeh et al. 2019; Liu et al. 2021) or a combination of both possibilities (Saraswat et al. 1996). Spin-up episodes are usually characterised by an increase in X-ray lumi-

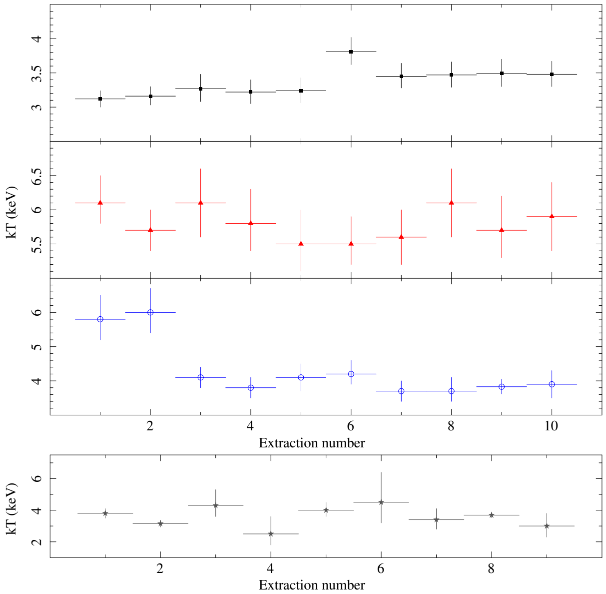

Fig. 14. Evolution of the bbody temperature for the pre-periastron flare and apastron outbursts versus the extraction number (*MAXI*/GSC data, model defined by equation 6). Filled black squares: pre-flare. Filled red triangles: flare. Open blue circles: post-flare. Filled dark grey stars: apastron outbursts. The color figure can be viewed online.

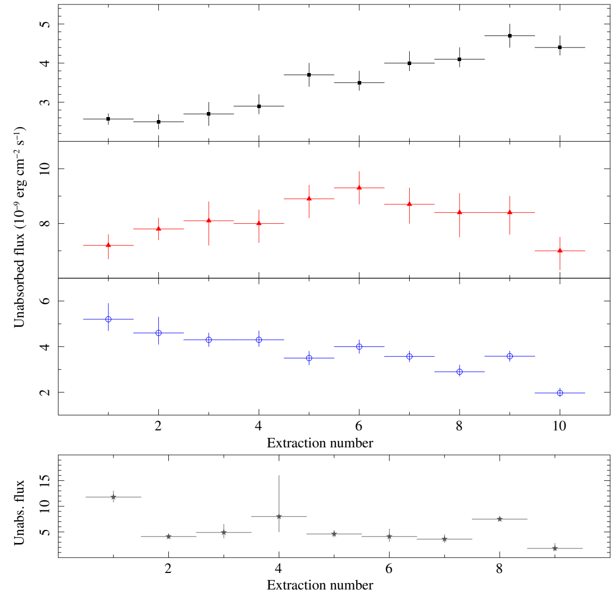

Fig. 15. Evolution of the unabsorbed flux for the pre-periastron flare and apastron outbursts (in units of $10^{-9}\,\mathrm{erg\,cm^{-2}\,s^{-1}}$) versus the extraction number (*MAXI*/GSC data, model defined by equation 6). Filled black squares: pre-flare. Filled red triangles: flare. Open blue circles: post-flare. Filled dark grey stars: apastron outbursts. The color figure can be viewed online.

nosity, associated with an enhancement of the accreted matter as a consequence of the formation of a temporary accretion disc around the neutron star (Nabizadeh et al. 2019; Manikantan et al. 2023).

This source is seen through a column density in the range $N_H = [10-40] \times 10^{22}$ cm^{-2}, and all X-rays below $[2-3]$ keV are absorbed. At these column densities a feature due to the K edge of Fe at 7.1 keV should be present. Figure 17 shows the optical depth of the iron edge ($\tau_{\rm Kedge}$) best-fit parameter that lies in the range $[0.3-0.8]$. This represents an ionisation state of nearly neutral iron Fe I-V (if values reported by Saraswat et al. 1996; Endo et al. 2002; Ji et al. 2021, are taken into account).

The long-term averaged spectra in the flare section present a fluorescent iron emission line energy consistent with the Fe Kα line and a constant value of $\approx (6.35 \pm 0.08)$ keV, as can be seen in Figure 18, top panel, which implies an ionisation state of iron up to Fe XVII. It was only detected in the first two spectra in the post-flare section and it was totally absent in the pre-flare section. However, Islam & Paul (2014) performed an orbital phase-resolved spectral analysis of GX 301-2 and they reported that the iron emission line was detected in all the orbital phases. The fitted values of the line width, the equivalent width and the intensity of the Fe Kα emission line are plotted in Figure 18: second, third and bottom panels, respectively.

If the emission line luminosity is produced by a thin spherical shell of matter, i.e. a shell of gas surrounding a point source of continuum radiation with uniform ionisation, composition and density, the line equivalent width should be proportional to the column density (Kallman et al. 2004; Torrejón et al. 2010) $EW_{\rm line}({\rm keV}) \simeq 0.3\,N_H\left(10^{24}\ {\rm cm}^{-2}\right)$. The absorbing component varies in the range $\approx [10-30] \times 10^{22}$ cm^{-2} (see second panel from the top of Figure 19), which implies an equivalent width of Fe Kα in the range $EW_{\rm line} \approx [30-90]$ eV. On the other hand, for an isotropic surrounding cosmic fluorescing plasma, Inoue (1985) obtained a relationship between the expected equivalent width of the iron Kα line and the hydrogen column density as $EW_{\rm expected}({\rm eV}) = 100\,N_H\left(10^{23}\ {\rm cm}^{-2}\right)$ which is valid for $N_H < 10^{24}$ cm^{-2} and a photon index of the power-law spectrum of 1.1 (see also Endo et al. 2002, for example). They also concluded that GX 301-2 corresponds to this case and, therefore, $EW_{\rm line} \approx [100-300]$ eV. However, *MAXI*/GSC observations gave equivalent widths of the iron emission line in the range $EW_{\rm line} \approx [600-1100]$ eV, which implies large deviations from the linear correlation. The largest value of the equivalent width

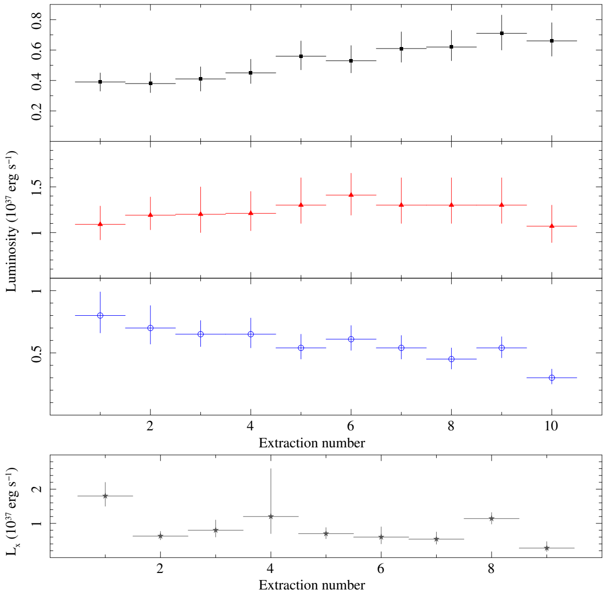

Fig. 16. Evolution of the luminosity for the pre-periastron flare and apastron outbursts versus the extraction number (*MAXI*/GSC data, model defined by equation 6). Filled black squares: pre-flare. Filled red triangles: flare. Open blue circles: post-flare. Filled dark grey stars: apastron outbursts. The color figure can be viewed online.

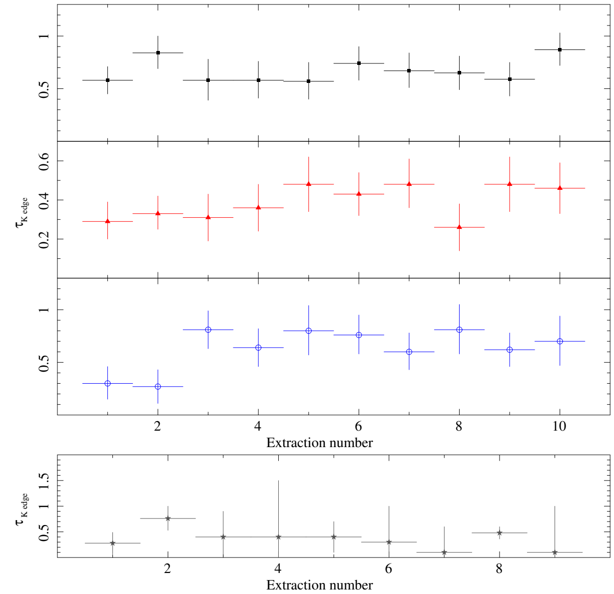

Fig. 17. Evolution of the optical depth of the edge for the pre-periastron flare and apastron outbursts versus the extraction number (*MAXI*/GSC data, model defined by equation 6). Filled black squares: pre-flare. Filled red triangles: flare. Open blue circles: post-flare. Filled dark grey stars: apastron outbursts. The color figure can be viewed online.

was obtained with the smallest column density. The fact that the Fe Kα is not a single line but a superposition of different Kα lines of differently strongly ionised iron together with the Compton shoulder at $\approx$6.24 keV and the wind speed could explain the large equivalent widths found in this study (Watanabe et al. 2003; Fürst et al. 2011; Ji et al. 2021). Taking the uncertainties into account, the best-fit parameters in the pre-periastron orbital phase are consistent with previous studies (Islam & Paul 2014; Manikantan et al. 2023). As a consequence, during the pre-periastron passage the fluorescent iron emission line is not emitted from a spherically symmetric distribution of matter surrounding the neutron star. Although this study has focused on flare episodes, a very small part of the orbit, these results are consistent with those obtained by Islam & Paul (2014).

Figure 20 shows the equivalent width of the Fe Kα against the absorption column density during the pre-periastron passage compared with the theoretical predictions for an isotropically distributed gas and for a spherical shell of gas surrounding the source. In fact, it seems that there is a moderate anti-correlation between them during the pre-periastron passage and a Pearson correlation coefficient $r = -0.63$ was found. This result is in contrast to other studies, such as Makino et al. (1985), Endo et al. (2002), Fürst et al. (2011), Ji et al. (2021), where they found a linear correlation between these two parameters which suggests that the accretion material near the neutron star is spherically distributed. Nevertheless, Ji et al. (2021) also found deviations from this linear correlation when the column density was higher than 1.7×10^{24} cm^{-2}. They pointed out that this could be due to the formation of an accretion disc.

In Figure 21 the intensity of the Fe Kα emission line is shown versus the unabsorbed flux of the source in the [2-20] keV energy band (left plot) and the optical depth of the iron K-edge absorption versus the equivalent width of the iron Kα line (right plot). A moderate linear correlation (Pearson correlation coefficient $r = 0.63$) can be seen, which should be consistent with the expected line intensities for the hydrogen column densities derived from the model described by equation 6 (see fig.6b in Haberl 1991b, where the incident spectrum was assumed to be a power-law with photon index $\Gamma = 0.55$). In contrast, from the plot $\tau_{\rm edge}$ versus EW, an anticorrelation relationship (Pearson correlation coefficient $r = -0.75$) seems to be present between these parameters during the pre-periastron passage. The solid line represents the linear fit found by Ji et al. (2021) where they suggested that the re-

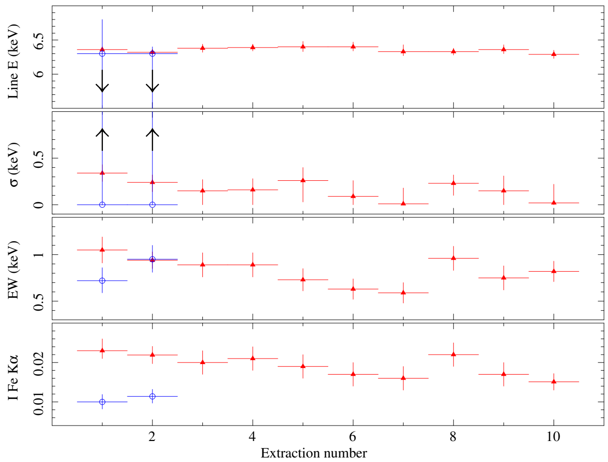

Fig. 18. The parameters of the Fe Kα emission line versus the extraction number (*MAXI*/GSC data, model defined by equation 6). *Top panel*: line energy. *Second panel*: line width. *Third panel*: equivalent width. *Bottom panel*: intensity. The unit of the line flux I is photons s^{-1} cm^{-2}. Filled red triangles: flare. Open blue circles: post-flare. The color figure can be viewed online.

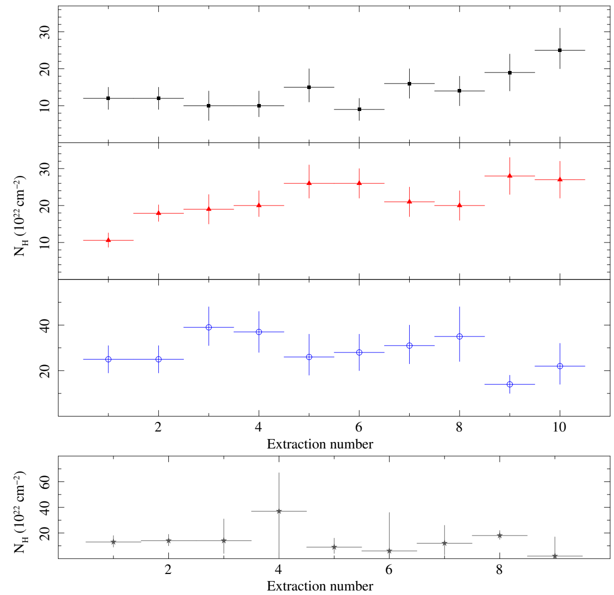

Fig. 19. Evolution of the column density for the pre-periastron, flare, and apastron outbursts versus the extraction number (*MAXI*/GSC data, model defined by equation 6). Filled black squares: pre-flare. Filled red triangles: flare. Open blue circles: post-flare. Filled dark grey stars: apastron outbursts. The color figure can be viewed online.

processed material reached an optical depth of unity for EW $\approx$ 400 eV (see also Torrejón et al. 2010, where they also found a linear correlation).

3.2. *Apastron Flare Spectra*

The folded light curve of GX 301-2 shows two flare-like features at binary orbital phases $\approx$ 0.26, i.e. before apastron passage (Haberl 1991b; Saraswat et al. 1996), and at $\approx$ 0.45 near-apastron passage (as can be seen in Figure 3, see also Pravdo et al. 1995; Pravdo & Ghosh 2001, for instance). In general, periodic near-apastron outbursts show lower intensity than the pre-periastron flare, although X-ray emission can sometimes be as low as $\approx 10^{36}$ erg s^{-1}, i.e. it cannot be distinguished from the baseline X-ray intensity along the orbit. Thus, the criterion to identify an apastron outburst was that the unabsorbed X-ray flux was greater than $\approx 2\times10^{-9}$ erg s^{-1}cm^{-2}. The orbital phase of the apastron outbursts was also obtained with the parameters reported by Koh et al. (1997). Then, the Good Time Intervals (GTIs) were derived and the corresponding MJDs are listed in the caption of Figure 22. Finally, the spectra were extracted following the process explained in § 3.1.

In this analysis, all apastron spectra were fitted with the same model used for the pre-periastron flare spectra. The range of the χ_r^2 values was $[0.7-1.2]$ for all fits. Nevertheless, it should be noted that no Gaussian component has been included here because the fluorescent iron emission line was not detected by

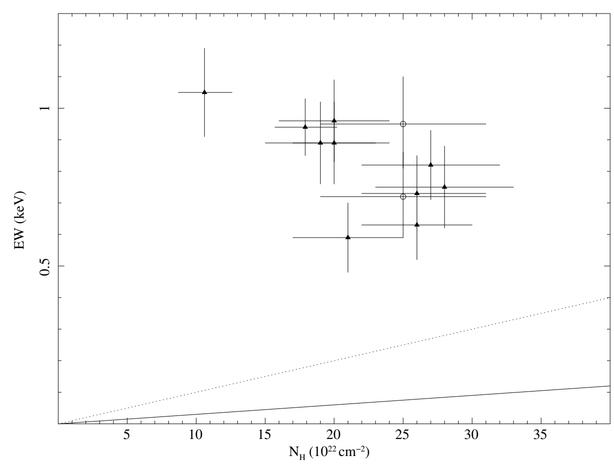

Fig. 20. Variability of the equivalent width as a function of the column density (also known as the curve of growth). Filled black triangles: flare. Open black circles: post-flare. The dotted line represents the relation for an isotropic surrounding cosmic fluorescing plasma, $EW_{\rm expected}(\rm eV) = 100\,N_H\left(10^{23}\ \rm cm^{-2}\right)$ (Inoue 1985). The solid line shows the relation for the luminosity produced by a thin spherical shell of matter $EW_{\rm line}(\rm keV) \simeq 0.3\,N_H\left(10^{24}\ \rm cm^{-2}\right)$ (Kallman et al. 2004; Torrejón et al. 2010).

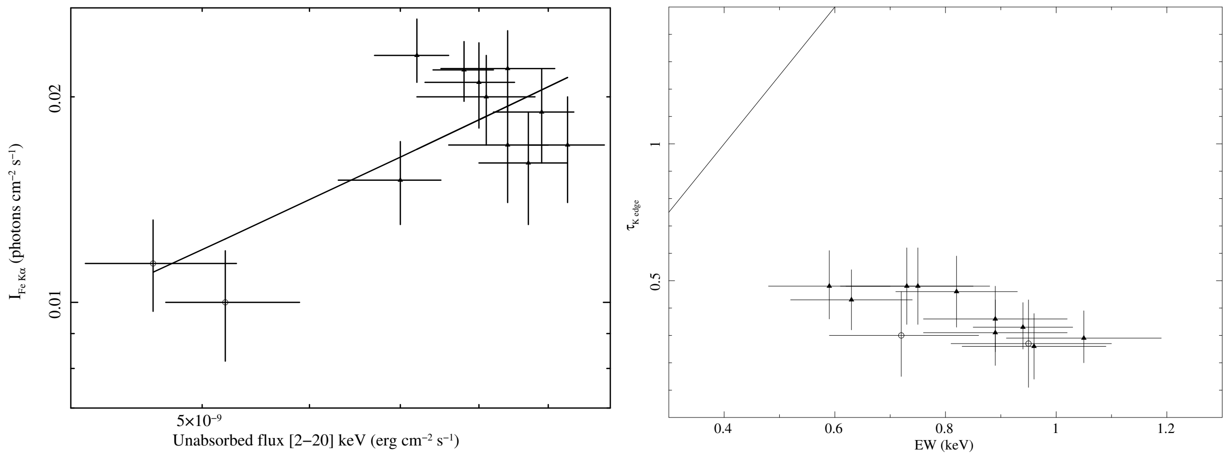

(a) (b)

Fig. 21. *Left panel*: Log-log plot of the Fe Kα intensity as a function of the unabsorbed flux in the (2-20) keV energy band. The solid line represents a linear fit. *Right panel*: Plot of the optical depth of the iron K-edge absorption as a function of the equivalent width of the iron Kα line (in keV). The solid line is the linear fit found by Ji et al. (2021). An apparent anti-correlation can be seen during the pre-periastron passage. The larger the EW of the Fe Kα, the smaller the optical depth of the iron K-edge absorption. Filled black triangles: flare. Open black circles: post-flare.

TABLE 4

SELECTED FIT PARAMETERS FROM APASTRON FLARE SPECTRA

Extraction Number	MJDs [Orbital Phase]	$R_{\rm bb}$ (km)	$K_{\rm bb}$ $[L_{39}/D^2_{10}]$	Bbody norm fit value	$L_{X(2.0-20.0\_{\rm keV})}$ $\left(10^{37}{\rm erg\,s^{-1}}\right)$
1	55376.5−55380.5 [0.41–0.51]	$0.79^{+0.20}_{-0.19}$	$0.14^{+0.17}_{-0.15}$	$0.193^{+0.019}_{-0.017}$	$1.8^{+0.4}_{-0.3}$
2	55710.0−55713.0 [0.45–0.52]	$0.70^{+0.17}_{-0.16}$	$0.05^{+0.06}_{-0.05}$	$0.066^{+0.007}_{-0.006}$	$0.63^{+0.14}_{-0.11}$
3	55870.0−55873.0 [0.30–0.37]	$0.4^{+0.3}_{-0.2}$	$0.06^{+0.09}_{-0.07}$	$0.09^{+0.03}_{-0.02}$	$0.8^{+0.3}_{-0.2}$
4	56163.5−56164.5 [0.38–0.40]	$1.5^{+2.2}_{-1.2}$	$0.09^{+0.20}_{-0.13}$	$0.11^{+0.12}_{-0.04}$	$1.2^{+1.4}_{-0.5}$
5	57285.0−55288.0 [0.40–0.47]	$0.45^{+0.17}_{-0.14}$	$0.06^{+0.07}_{-0.06}$	$0.080^{+0.012}_{-0.010}$	$0.70^{+0.18}_{-0.15}$
6	57454.0−57457.0 [0.47–0.55]	$0.3^{+0.4}_{-0.3}$	$0.05^{+0.07}_{-0.06}$	$0.08^{+0.03}_{-0.02}$	$0.6^{+0.3}_{-0.2}$
7	58029.5−58041.5 [0.34–0.63]	0.6 ± 0.3	$0.04^{+0.06}_{-0.05}$	$0.052^{+0.014}_{-0.010}$	$0.54^{+0.21}_{-0.15}$
8	58480.5−58495.5 [0.21–0.57]	0.68 ± 0.11	$0.09^{+0.11}_{-0.09}$	0.123 ± 0.006	$1.14^{+0.18}_{-0.16}$
9	59119.0−59122.0 [0.60–0.67]	$0.5^{+0.4}_{-0.3}$	$0.02^{+0.04}_{-0.03}$	$0.025^{+0.014}_{-0.007}$	$0.28^{+0.19}_{-0.10}$

MAXI/GSC. Figure 22 shows the data, the absorbed blackbody modified by the iron K-edge absorption best-fit model (top panels), and the residuals for the model (bottom panels). The best-fit model parameters are plotted in Figures 12-17 and 19, bottom panels.

The unabsorbed fluxes and the derived radii of the blackbody emission region are shown in Figures 15 and 13, respectively. The results for the radii are consistent with a hot spot on the NS surface (Sanjurjo-Ferrín et al. 2021; Torregrosa et al. 2022) (see Table 4, Column 3).

Using the definition of the *bbody normalisation* $K_{\rm bb} = L_{39}/D^2_{10}$, we have derived its value in the nine spectra (see Table 4, Column 4). These values are consistent with those obtained from fitting the model $F(E) = tbnew \times bbody \times edge$, taking the uncertainties into account (see Figure 12, bottom panel).

The first apastron outburst spectrum observed by *MAXI*/GSC is shown in Figure 22 (a) whose X-ray luminosity, see Table 4, Column 6, $\left(L_{X({\rm a})} \approx 2 \times 10^{37}\right)$ was unusually brighter than that of pre-periastron flare (see Figure 16 and compare second and bottom panels). This flare was also detected by *Fermi*/GBM and could be associated with a rapid spin-up episode of GX 301-2 (Finger et al. 2010). According to the long-term light curve obtained with *Fermi*/GBM , rapid spin-up began on June 23, 2010 (MJD 55 370.84) and finished on July 22, 2010 (MJD 55 399.07), as can be seen in Figure 8. Pulse timing measurements for the interval June 23.8-July 22.1 showed a spin-up fre-

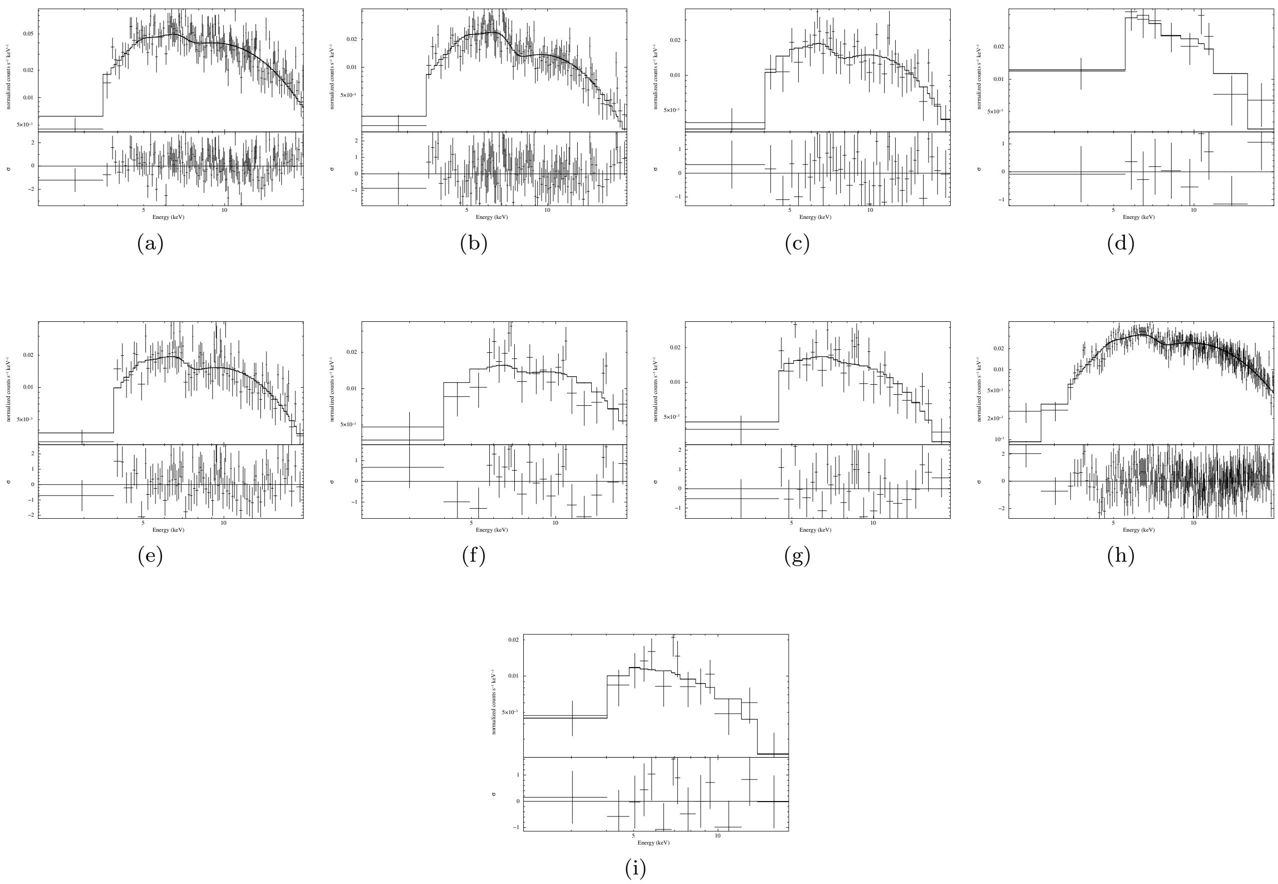

Fig. 22. *MAXI*/GSC spectra of GX 301-2 in the [2.0–20.0] keV band corresponding to the apastron flare. MJDs from left to right for each spectrum: (a) [55376.5−55380.5], (b) [55710.0−55713.0], (c) [55870.0.0−55873.0], (d) [56163.5−56164.5], (e) [57285.0−57288.0], (f) [57454.0−57457.0], (g) [58029.5−58041.5], (h) [58480.5−58495.5] and (i) [59119.0−59122.0]. Units of the x-axis: Energy (keV). Units of the y-axis: Normalized counts s^{-1} keV^{-1}.

quency rate of $\dot{\nu}_{\rm spin} = (3.89 \pm 0.08) \times 10^{-12}$ Hz/s, giving a spin-up time scale of $\approx$ 12 yr. This extracted spectrum covered only 1/7 of the spin-up episode with an spin-up frequency rate of $\dot{\nu}_{\rm spin} = (6.21 \pm 0.21) \times 10^{-12}$ Hz/s. The following apastron flare with an X-ray luminosity similar to the preperiastron flare is shown in Figure 22 (d) and was not associated with any significant changes in the spin period of the neutron star (the spin frequency decreased from $\nu_1 = (1.46861 \pm 0.00017) \times 10^{-3}$ Hz on MJD 55 611.1160 to $\nu_2 = (1.46818 \pm 0.00018) \times 10^{-3}$ Hz on MJD 55 616.9968). The last one studied in this work corresponded to the eighth extraction, Figure 22 (h), where the source presented a new rapid spin-up event (Abarr et al. 2020; Liu et al. 2021; Manikantan et al. 2023). In this case, during the observation the spin frequency increase from $\nu_1 = (1.467459 \pm 0.000011) \times 10^{-3}$ Hz on MJD 58 485.1001 to $\nu_2 = (1.472308 \pm 0.000007) \times 10^{-3}$ Hz on MJD 58 494.9950 at a rate of $\dot{\nu}_{\rm spin} = (5.75 \pm 0.02) \times 10^{-12}$ Hz/s, which is near to the spin frequency increase over 18 days (MJD 58 485.1001–58 502.9107) $\dot{\nu}_{\rm spin} = (5.70 \pm 0.02) \times 10^{-12}$ Hz/s. Then, the spin frequency rose over 24 days (MJD 58 502.9107–58 553.1933) at a rate of $\dot{\nu}_{\rm spin} = (2.37 \pm 0.18) \times 10^{-12}$ Hz/s.

Another rapid spin-up episode seen with *Fermi*/GBM from MJD 54 830.9617 to MJD 54 855.1007 showed a spin-up frequency rate of $\dot{\nu}_{\rm spin} = (2.97 \pm 0.12) \times 10^{-12}$ Hz/s (Finger et al. 2010). Moreover, similar spin-up events were detected with the Burst And Transient Source Experiment (BATSE) and reported by Koh et al. (1997); Bildsten et al. (1997). They found a spin frequency growth over 23 days at a rate of $\dot{\nu}_{\rm spin} = 4.5 \times 10^{-12}$ Hz/s and over 15 days at a rate of $\dot{\nu}_{\rm spin} = 3.0 \times 10^{-12}$ Hz/s.

The rest of the apastron flares shown in Figures 22 (b), (c), (e), (f), (g) and (i) had an X-ray emission slightly lower than pre-periastron flares which were not associated with any significant changes in the spin period of the neutron star. From MJD 55 708.9521 to MJD 55 714.8995, the spin-up rate was $\dot{\nu}_{\rm (b)} = (1.1 \pm 0.6) \times 10^{-12}$ Hz/s; from MJD 55 860 to 55 875 only two pulse timing measurements were taken, MJD 55 871.1393 and 55 873.1066, which gave a spin-down rate of $\dot{\nu}_{\rm (c)} = (-1.9 \pm 1.4) \times 10^{-12}$ Hz/s; from MJD 57 265.2712 to MJD 57 290.7870, the spin-up rate was $\dot{\nu}_{\rm (e)} = (9.8 \pm 0.8) \times 10^{-13}$ Hz/s (although this time interval had a gap without measurements MJD 57 273–57 286); from MJD 57 449.0139 to 57 458.9447 the spin-down rate was $\dot{\nu}_{\rm (f)} = (-1.1 \pm 0.3) \times 10^{-12}$ Hz/s; from MJD 58 028.9070 to MJD 58 036.7733, the spin-up rate was $\dot{\nu}_{\rm (g)} = (1.0 \pm 0.7) \times 10^{-12}$ Hz/s (but before and after there was a gap of 10 days without pulse measurements); and from MJD 59 117.1258 to MJD 59 121.0794, the spin-up rate was $\dot{\nu}_{\rm (g)} = (2.4 \pm 1.1) \times 10^{-12}$ Hz/s.

As far as it is known from the rapid spin-episodes in GX 301-2 , during the apastron passage the source becomes as bright as a pre-periastron flare, as a consequence of the formation of a transitory accretion disc. Thus, the mass transfer from the companion star to the neutron star is a rather irregular process during this orbital phase (see X-ray luminosities in Table 4). The strongest events show that the material is accreted from the stellar wind, possibly from a gas stream (Leahy & Kostka 2008) and probably through a temporary accretion disc (Koh et al. 1997; Nabizadeh et al. 2019; Abarr et al. 2020; Liu et al. 2021; Manikantan et al. 2023). However, the fourth apastron flare [see extraction number 4 in Table 4 and Figure 22 (d)] did not show a spin-up of the neutron star and no transitory disc was formed. Therefore, the material should be accreted by the stellar wind and possibly from a gas stream.

It should be noted that the fluorescence iron emission line at ≈6.4 keV has not been detected in any spectrum of the apastron flare. Sensitive X-ray observatories such as *ASCA* (Endo et al. 2002), *XMM-Newton* (Giménez-García et al. 2015), and *Chandra* (Torrejón et al. 2010) detected and resolved the iron line complex in GX 301-2 . In contrast, *MAXI*/GSC does not have enough sensitivity to distinguish between a weak, broad iron Kα emission line and a bright X-ray continuum (Rodes-Roca et al. 2015; Torregrosa et al. 2022). Nevertheless, other long-term orbital phase resolved spectroscopy studies reported the presence of the Fe Kα line in all orbital phases (Islam & Paul 2014; Manikantan et al. 2023).

4. SUMMARY AND CONCLUSIONS

The main goal of the current study was to determine the long-term variation of GX 301-2 in the pre-periastron and apastron flares. The Good Time-Intervals corresponding to these orbital phases were generated using the orbital ephemeris from Koh et al. (1997).

The main results can be summarise as follows:

– From the analysis of the *MAXI*/GSC (4.0–10.0) keV light curve, we have estimated the orbital period of the binary system, $P_{\rm orb} = 41.4 \pm 0.5$ days, being in agreement with the best value derived by Koh et al. (1997).

– Two variations of the model *tbnew* × *po* + *tbnew* × *po* + *GL* have been applied to find if there was elliptical polarisation due to synchrotron radiation. This model was not able to describe all *MAXI*/GSC data properly.

– The size of the emitting region on the neutron star surface in the pre-periastron and apastron flares obtained using the *bbody normalisation* (see Figure 13 and Table 4) was compatible with a hot spot. The temperature of the blackbody is in the range [5.1–6.7] keV during the pre-periastron flare and two post-flare, but lower than 5.0 keV in the rest of the spectra. It was not clear if there is a connection between the high temperature of the blackbody and the detection of the iron Kα line.

– The X-ray luminosity during the pre-periastron flare was compatible with a constant value ($L_{\rm X} \approx 1.3 \times 10^{37}$ erg s^{-1}) indicating an accretion rate quite regular from the stellar wind and a gas stream trailing the neutron star (Leahy & Kostka 2008). This mass transfer model would also explain the X-ray luminosities obtained in the pre-flare ($L_{\rm X} = [4-7] \times 10^{36}$ erg s^{-1}), in the post-flare ($L_{\rm X} = [3-8] \times 10^{36}$ erg s^{-1}) and in most of the apastron flares ($L_{\rm X} = [3-8] \times 10^{36}$ erg s^{-1}). However, two of the strongest apastron flares had an X-ray luminosity comparable to the pre-periastron flare during rare spin-up events. It is believed that a certain amount of angular momentum should be transported through the formation of an accretion disc at this orbital phase (Nabizadeh et al. 2019; Abarr et al. 2020; Manikantan et al. 2023). At least one of the largest apastron flares (extraction number 4 in Table 4) was not related to a spin-up episode and, therefore, it is

DOI: https://doi.org/10.22201/ia.01851101p.2025.61.01.03

quite likely that a transient accretion disc did not form. Consequently, it remains unknown why only some apastron flares spin up the X-ray source and on what this depends.

– The curve of growth showed a moderate anti-correlation between the equivalent width of Fe Kα and the column density, and clear deviations from spherically distributed absorbing matter (Kallman et al. 2004; Islam & Paul 2014; Giménez-García et al. 2015; Ji et al. 2021) in the pre-periastron flare. On the other hand, a moderate correlation between the unabsorbed X-ray flux and the intensity of Fe Kα was found, which could be consistent with the expected values corresponding to the hydrogen column densities in the pre-periastron flare (see Figure 6b in Haberl 1991b).

– The optical depth of the K-edge absorption was moderately anti-correlated to the equivalent width of Fe Kα, and clearly deviated from the linear correlation reported by Ji et al. (2021) (see also the result obtained by Torrejón et al. 2010).

This research made use of MAXI data provided by RIKEN, JAXA and MAXI team. JJRR acknowledges the support by the Matsumae International Foundation Research Fellowship No14G04, and also thanks the entire MAXI team for their collaboration and hospitality in RIKEN. We would like to thank particularly T. Mihara and S. Nakahira for invaluable assistance in analysing MAXI data. GSF, JMT & JJRR acknowledge the financial support from the MCIN with funding from the European Union NextGenerationEU (PRTR-C17.I01) and Generalitat Valenciana Proj. (Athena-XIFU-UA), ref. ASFAE/2022/002. This work has made use of data from the European Space Agency (ESA) mission Gaia (https://www.cosmos.esa.int/gaia), processed by the Gaia Data Processing and Analysis Consortium (DPAC, https://www.cosmos.esa.int/web/gaia/dpac/consortium). Funding for the DPAC has been provided by national institutions, in particular the institutions participating in the Gaia Multilateral Agreement. We thank the anonymous referee for the constructive comments that helped us to improve the manuscript.

REFERENCES

Abarr, Q., Baring, M., Beheshtipour, B., et al. 2020, ApJ, 891, 70, https://doi.org/10.3847/1538-4357/ab672cz

Arnaud, K. A. 1996, ASPC 101, Astronomical Data Analysis and Systems, ed. G. H. Jacoby & J. Barnes, 17

Astropy Collaboration, Price-Whelan, A. M., Lim, P. L., et al. 2022, ApJ, 935, 167, https://doi.org/10.3847/1538-4357/ac7c74

Bailer-Jones, C. A. L., Rybizki, J., Fouesneau, M., Demleitner, M., & Andrae, R. 2021, AJ, 161, 147, https://doi.org/10.3847/1538-3881/abd806

Bildsten, L., Chakrabarty, D., Chiu, J., et al. 1997, ApJS, 113, 367, https://doi.org/10.1086/313060

Ebisawa, K., Day, C. S. R., Kallman, T. R., et al. 1996, PASJ, 48, 425, https://doi.org/10.1093/pasj/48.3.425

Endo, T., Ishida, M., Masai, K., et al. 2002, ApJ, 574, 879, https://doi.org/10.1086/341060

Finger, M. H., Beklen, E., Narayana Bhat, P., et al. 2009, arXiv:0912.3847, https://doi.org/10.48550/arXiv.0912.3847

Finger, M. H., Camero-Arranz, A., Wilson-Hodge, C., & Jenke, P. 2010, ATel, 2712, 1

Fürst, F., Suchy, S., Kreykenbohm, I., et al. 2011, A&A, 535, 9, https://doi.org/10.1051/0004-6361/201117665

Giménez Cañete, A. & Castro Tirado, A. 2005, Astronomía X (Equipo Sirius), Madrid

Giménez-García, A., Torrejón, J. M., Eikmann, W., et al. 2015, A&A, 576, 108, https://doi.org/10.1051/0004-6361/201425004

Haberl, F. 1991a, A&A, 252, 272

_________. 1991b, ApJ, 376, 245

Han, I. & Demir, L. 2009, PhRvA, 80, 052503, https://doi.org/10.1103/PhysRevA.80.052503

Inoue, H. 1985, SSSRv, 40, 317, https://doi.org/10.1007/BF00212905

Islam, N. & Paul, B. 2014, MNRAS, 441, 2539, https://doi.org/10.1093/mnras/stu756

Ji, L., Doroshenko, V., Suleimanov, V., et al. 2021, MNRAS, 501, 2522, https://doi.org/10.1093/mnras/staa3788

Kallman, T. R., Palmeri, P., Bautista, M. A., Mendoza, C., & Krolik, J. H. 2004, ApJS, 155, 675, https://doi.org/10.1086/424039

Kaper, L., Lamers, H. J. G. L. M., Ruymaekers, E., van den Heuvel, E. P. J., & Zuiderwijk, E. J. 1995, A&A, 300, 446

Kaper, L., van der Meer, A., & Najarro, F. 2006, A&A, 457, 595, https://doi.org/10.1051/0004-6361:20065393

Koh, D. T., Bildsten, L., Chakrabarty, D., et al. 1997, ApJ, 479, 933, https://doi.org/10.1086/303929

Kretschmar, P., Fürst, F., Sidoli, L., et al. 2019, NewAR, 86, 101546, https://doi.org/10.1016/j.newar.2020.101546

La Barbera, A., Segreto, A., Santangelo, A., Kreykenbohm, I., & Orlandini, M. 2005, A&A, 438, 617, https://doi.org/10.1051/0004/6361:20041509

Leahy, D. A. 1991, MNRAS, 250, 310, https://doi.org/10.1093/mnras/250.2.310

Leahy, D. A. & Kostka, M. 2008, MNRAS, 384, 747, https://doi.org/10.1111/j.1365-2966.2007.

12754.x

Leahy, D. A., Matsuoka, M., Kawai, N., & Makino, F. 1989, MNRAS, 236, 603, https://doi.org/10.1093/mnras/236.3.603

Leahy, D. A., Nakajo, M., Matsuoka, M., et al. 1988, PASJ, 40, 197

Lewin, W. H. G., McClintock, J. E., Ryckman, S. G., & Smith, W. B. 1971, ApJ, 166, 69, https://doi.org/10.1086/180741

Liu, J., Ji, L., Jenke, P. A., et al. 2021, MNRAS, 504, 2493, https://doi.org/10.1093/mnras/stab938

Makino, F., Leahy, D. A., & Kawai, N. 1985, Space Sci. Rev., 40, 421, https://doi.org/10.1007/BF00179851

Malacaria, C., Jenke, P., Roberts, O. J., et al. 2020, ApJ, 896, 90, https://doi.org/10.3847/1538-4357/ab855c

Manikantan, H., Paul, B., Roy, K., & Rana, V. 2023, MNRAS, 520, 1411, https://doi.org/10.1093/mnras/stad037

Martínez-Núñez, S., Kretschmar, P., Bozzo, E., et al. 2017, Space Sci. Rev., 212, 59, https://doi.org/10.1007/s11214-017-0340-1

McClintock, J. E., Ricker, G. R., & Lewin, W. H. G. 1971, ApJ, 166, 73, https://doi.org/10.1086/180742

Mukherjee, U. & Paul, B. 2004, A&A, 427, 567, https://doi.org/10.1051/0004-6361:20034407

Nabizadeh, A., Mönkkönen, J., Tsygankov, S. S., et al. 2019, A&A, 629, 101, https://doi.org/10.1051/0004-6361/201936045

Pravdo, S. H., Day, C. S. R., Angelini, L., et al. 1995, ApJ, 454, 872, https://doi.org/10.1086/176540

Pravdo, S. H. & Ghosh, P. 2001, ApJ, 554, 383, https://doi.org/10.1086/321350

Press, W. H. & Rybicki, G. B. 1989, ApJ, 338, 277, https://doi.org/10.1086/167197

Rodes-Roca, J. J., Mihara, T., Nakahira, S., et al. 2015, A&A, 580, 140, https://doi.org/10.1051/0004-6361/201425323

Roy, K., Manikantan, H., & Paul, B. 2024, MNRAS, 527, 2652, https://doi.org/10.1093/mnras/stad3395

Sanjurjo-Ferrín, G., Torrejón, J. M., Postnov, K., et al. 2021, MNRAS, 501, 5892, https://doi.org/10.1093/mnras/staa3953

Saraswat, P., Yoshida, A., Mihara, T., et al. 1996, ApJ, 463, 726, https://doi.org/10.1086/177285

Sato, N., Nagase, F., Kawai, N., et al. 1986, ApJ, 304, 241, https://doi.org/10.1086/164157

Stevens, I. R. 1988, MNRAS, 232, 199, https://doi.org/10.1093/mnras/232.1.199

Suchy, S., Fürst, F., Pottschmidt, K., et al. 2012, ApJ, 745, 124, https://doi.org/10.1088/0004-637X/745/2/124

Torregrosa, Á., Rodes-Roca, J. J., Torrejón, J. M., Sanjurjo-Ferrín, G., & Bernabéu, G. 2022, RMxAA, 58, 355, https://doi.org/10.22201/ia.01851101p.2022.58.02.15

Torrejón, J. M., Schulz, N. S., Nowak, M. A., & Kallman, T. R. 2010, ApJ, 715, 947, https://doi.org/10.1088/0004-637X/715/2/947

Watanabe, S., Sako, M., Ishida, M., et al. 2003, ApJ, 597, 37, https://doi.org/10.1086/379735

White, N. E., Mason, K. O., Huckle, H. E., Charles, P. A., & Sanford, P. W. 1976, ApJ, 209, 119, https://doi.org/10.1086/182281

Wilms, J., Allen, A., & McCray, R. 2000, ApJ, 542, 914, https://doi.org/10.1086/317016

DOI: https://doi.org/10.22201/ia.01851101p.2025.61.01.03

T. Mihara: MAXI team, Institute of Physical and Chemical Researh (RIKEN), 2-1 Hirosawa, Wako, Saitama 351-0198, Japan.

M. Nakajima: Nihon University School of Dentistry at Matsudo 2-870-1 Sakae-cho Nishi, Matsudo-shi, Chiba 271-8587, Japan.

J. J. Rodes-Roca and J. M. Torrejón: Department of Physics, Systems Engineering and Signal Theory, University of Alicante, 03080 Alicante, Spain.

M. Sugizaki: Science and Engineering, Kanazawa University, Kakuma, Kanazawa, Ishikawa 920-1192, Japan.

Á. Torregrosa, J. J. Rodes-Roca, J. M. Torrejón and G. Sanjurjo-Ferrín: University Institute of Physics Applied to Sciences and Technologies, University of Alicante, 03080 Alicante, Spain (aat34@alu.ua.es).

Revista Mexicana de Astronomía y Astrofísica, **61**, 49–63 (2025)

https://doi.org/10.22201/ia.01851101p.2025.61.01.04

PHOTOMETRIC LIGHT CURVE SOLUTION OF FOUR SHORT PERIOD K-SPECTRAL TYPE ECLIPSING BINARY SYSTEMS

H. Aceves[1], R. Michel[1], L. Altamirano-Dévora[1,5], F. Acerbi[2], C. Barani[3], and M. Martignoni[4]

Received March 12 2024; accepted October 8 2024

ABSTRACT

The filtered B, V, R and I light curves of four short period ($P < 0.25$d) eclipsing binary systems are presented and analysed; two having $P \approx 0.22$d, close to the short period limit for contact binaries (CBs). New ephemerides are provided. No third light was found necessary in any case, and one or more spots were introduced to account for asymmetries in the light curves. Two systems belong to the W sub-type of the W-UMa CBs and a third one to the A sub-type of the W-UMa type CBs. The last one is a semi-detached binary with a large temperature difference between the components and a low mass ratio $q = 0.191$. All components of the binaries are of the K spectral type, and the secondary of the semi-detached binary is of the M spectral type. Absolute parameters of the components were calculated using different evolutionary diagrams. Interestingly, two target have estimated total masses that are smaller than the lower mass limit known for CBs.

RESUMEN

Se analizan curvas de luz en los filtros B, V, R e I para cuatro binarias eclipsantes de periodo corto ($P < 0.25$d); dos con $P \approx 0.22$d, cercano al límite de periodo corto de binarias de contacto (CBs). Se proveen nuevas efemérides. No se encontró necesaria una tercera luz en ningún caso, y se requirieron una o dos manchas para explicar las asimetrías en las curvas de luz. Dos sistemas pertenecen al subtipo W de las W-UMa CBs y una tercera al subtipo A del tipo W-UMa. El último sistema es una binaria semi-desligada con una diferencia de temperaturas grande entre sus componentes y una razón baja de masa $q = 0.191$. Todos los componentes de las binarias son del tipo espectral K, y la secundaria de la binaria semi-desligada es del tipo espectral M. Se calculan parametros absolutos usando distintos diagramas evolutivos. Interesantemente, dos binarias presentan masas totales estimadas menores que el límite inferior en masa conocido para CBs.

Key Words: stars: fundamental parameters — stars: individual: 2MASS J09344360+4208318 (V0443 UMa, Gaia ID 814599066616791552), 2MASS J10054868+2332408, 2MASS J11393492+4128139, 2MASS J16091958+3532114 — techniques: photometric

1. INTRODUCTION

Among contact binaries (CBs) systems of spectral type K some have short periods, close to the cut-off period ($P \approx 0.22$d), according to the period-colour relation for contact binaries (Zhu et al. 2015). Moreover, as argued by Liu et al. (2023), the study of these late-type systems could provide fundamental information for understanding the nature of A and W sub-type binaries and the structure and evolution of W-UMa systems. K type binaries generally belong to the W subclass of W-UMa binaries and are in shallow contact, so they are good targets for testing the thermal relaxation oscillation (TRO) theory (Lucy 1976; Lucy & Wilson 1979; Flannery 1976; Robertson & Eggleton 1977; Yakut & Eggleton 2005 and Li et al. 2008).

The TRO theory predicts that binaries evolve in alternating cycles of contact and semi-detached

[1]Instituto de Astronomía, UNAM. Ensenada, México.
[2]Independent researcher.
[3]Independent researcher.
[4]Stazione Astronomica Betelgeuse, Magnago, Italy.
[5]FIAD-UABC, Ensenada, México.

phases with mass exchange between the components until the system reaches a high degree of contact and the binary merges into a single rapidly rotating star (Stępień 2011; Tylenda et al. 2011; Zhu et al. 2016; Liao et al. 2017).

In this work we obtain new high quality terrestrial data on four eclipsing binaries and provide photometric light curve solutions for all of them. As well, absolute elements are estimated using empirical relations from the literature. The paper is divided into nine sections. In §2 a brief description of the discovery and some published data of the systems are stated, and in §3 our new observations and ephemeris are indicated. § 4 presents our synthetic light curve solutions and in §5 estimates of absolute elements are provided. In §6 interstellar absorption parameters are given, while in §7 the stability parameter of our CBs are computed, and in §8 estimates of the energy transfer between the components of our CBs are enunciated. In §9 general remarks about our systems and final comments are presented.

2. HISTORY OF THE SYSTEMS

The system 2MASS J09344360+4208318 (hereafter J09344360), with α_{2000} = 09h 34m 43.60s and δ_{2000} = +42d 08m 31.8s, was identified as a variable star by Lohr et al. (2013) during a search in the SuperWASP (Wide Angle Search for Planets) photometric survey archive (Pollacco et al. 2006) for eclipsing binaries with very short orbital periods ($P < 20,000$s or ≈ 0.2315d). They found a period of 19201.57s (0.2222404d) and suggested a negative $\mathrm{d}P/\mathrm{d}t$ value of -0.095 ± 0.023. The shape of the light curve and the differences in primary and secondary eclipse depths suggest that J09344360 could be a detached or semi-separated system not in thermal contact (Lohr et al. 2013). In the 82^{nd} list of variable stars, J09344360 was assigned the name V0443 UMa (Kazarovets et al. 2019). The system was observed during the low-resolution spectra survey of the Large Sky Area Multi-Object Fiber Spectroscopic Telescope (LAMOST) (Cui et al. 2012; Zhao et al. 2012) and included by Qian et al. (2020) in his catalogue of new stellar atmospheric parameters, assigning to it the EW type, the spectral type $K5$ and a temperature of 4465K.

Binary 2MASS J10054868+2332408 (hereafter J10054868), with α_{2000} = 10h 05m 48.68s and δ_{2000} = +23d 32m 40.8s, was found to be a variable of EW type with a short period of 0.2223 days by the Télescope à Action Rapide pour les Objets Transitoires, TAROT (Damerdji et al. 2007); the amplitude of variation was indicated to be 0.55 mags and the system to be of the EB/EW contact binary type. Subsequently, the system was observed in the Catalina surveys (Drake et al. 2014) and assigned a $P = 0.222324$d (19208.79s) and the W-UMa type of variability. Marsh et al. (2017) published a catalogue of 9380 W-UMa systems using the Catalina Real-Time Transient Survey Variables Sources Catalogue (Drake et al. 2014), in which our target is listed with a 0.5mags amplitude of variation and, from an empirical relationship, a temperature of $T = 4757$K for the primary component. Again, Qian et al. (2020) included J10054868 in their catalogue of new stellar atmospheric parameters, assigning to it the EW type, the period of variation $P = 0.2223243$d (19208.82s), the spectral type $K3$ and the temperature $T = 4852$K. The system was included in a long list of contact binaries selected from the Northern Catalina Sky Survey (Marsh et al. 2017) by Sun et al. (2020), who derived its relative properties using a self-developed automatic Wilson-Devinney code.

Binary 2MASS J11393492+4128139 (hereafter J11393492), with α_{2000} = 11h 39m 34.89s and δ_{2000} = +41d 28m 14.4s), was first observed by the Catalina surveys (Drake et al. 2014) with a period of $P = 0.238544$d (20610.20s) and a W-UMa type of variability. It was included in the catalogue of Marsh et al. (2017), with an amplitude of variability of 0.166 mag. and a temperature $T = 4234$K of the primary component.

Our fourth binary 2MASS J16091958+3532114 (hereafter J16091958), with α_{2000} = 16h 09m 19.58s and δ_{2000} = +35d 32m 11.4s, was reported as a variable star by the Robotic Optical Transient Search Experiment I (ROTSE-I) survey (Akerlof et al. 2000) with a period of $P = 0.247641$d and an amplitude of variation of 0.666 mag. Subsequently, the system was observed by the Catalina surveys (Drake 2014) and assigned a period of $P = 0.247632$d (21395.40s), a W-UMa type of variability, and an amplitude of variations of 0.47 mag. In the catalogue of Marsh et al. (2017), this target is listed with an amplitude of the variations of 0.483 mag and a temperature $T = 5545$K for the primary component. Also for this system, Sun et al. (2020) derived its relative properties using a self-developed automatic Wilson-Devinney code.

3. OBSERVATIONS AND NEW EPHEMERIS

Our observations follow the same general procedures used in earlier related works on binaries by our research group (Barani et al. 2022, Michel et al. 2023), and which we describe next.

Observations were done at the San Pedro Mártir Observatory (Mexico) with the 0.84-m f/15 Ritchey-

TABLE 1

LOG OF THE OBSERVATIONS

Target	UT Obs Date	ObsTime (h)	FWHM (pixels)	exp$B$ (s)	exp$V$ (s)	exp$R$ (s)	exp$I$ (s)	err$B$ (mmag)	err$V$ (mmag)	err$R$ (mmag)	err$I$ (mmag)
J09344	2022-03-21	6.44	6.7	60	40	25	25	7.6	5.6	4.5	3.5
	2023-03-25	6.23	3.9	60	40	25	25	5.8	4.5	3.6	2.8
	2023-03-28	7.11	3.6	60	40	25	25	5.8	4.5	3.6	2.8
J10054	2023-03-26	7.22	5.5	60	40	25	25	6.7	5.4	4.5	3.6
J11393	2022-03-16	4.04	4.8	80	40	30	30	22.4	14.3	8.5	5.4
	2022-04-15	3.17	3.7	40	20	15	15	24.5	14.6	9.8	5.8
	2023-03-27	9.11	3.4	60	40	25	25	11.7	9.5	7.6	4.5
J16091	2022-03-22	4.25	3.7	40	20	15	15	8.1	8.5	6.7	5.5
	2022-05-14	7.92	3.2	40	20	15	15	7.2	8.3	6.6	5.2
	2022-06-25	2.74	3.8	40	20	15	15	7.7	8.5	7.2	5.6

Chretien telescope, the Mexman filter-wheel and the *Marconi 5* CCD detector (an e2v CCD231-42 2k chip with 15×15 μm^2 pixels, gain of 2.2 e$^-$/ADU and readout noise of 3.6 e$^-$). The field of view was $9.7' \times 9.7'$ and a binning of 2×2 was employed during all the observations.

A log of the observations is shown in Table 1. FWHM is the average FWHM in binned pixels of the measured stars for the whole night. The typical differential magnitude errors (the quadratic addition of the magnitude errors of the variable and reference star) are also shown. Also the exposure times in seconds in each observed band are provided.

All the images were processed using IRAF[6] routines. Images were bias subtracted and flat field corrected before the instrumental magnitudes were computed with the standard aperture photometry method using an aperture of 1.5 times the average FWHM of the night.

The field stars were also calibrated in the $UBVRI$ system with the help of Landolt's photometric standards (Landolt 2009). Based on this information we were able to choose comparison stars with colors similar to the variables, making differential extinction corrections negligible:

1. For J09344360, star 2MASS J10381377 + 3219597: $U = 15.046, B = 15.051, V = 14.429, R = 14.054, I = 13.694$, was employed
2. For J10054868, star 2MASS J19493362 + 3141488: $U = 14.041, B = 13.008, V = 11.773, R = 11.121, I = 10.545$ was used.
3. For J11393492, star 2MASS J07334403 + 3024524 $U = 19.624, B = 18.355, V = 16.933, R = 16.079, I = 15.282$ was chosen.
4. For J16091958, star 2MASS J00000000 + 1111111 $U = 19.624, B = 18.355, V = 16.933, R = 16.079, I = 15.282$ was selected.

From our observations we determined the apparent magnitude m_v in quadrature for J09344360 while for J10054868 we calculated the V magnitude using equations (23) of Fukugita et al. (1996). All the obtained light curves are shown in Figures 2 and 3 .

Times of minima were determined from the light curves of our binaries and new ephemeris were determined, such values are shown in Table 2. Any part of the data used here can be provided upon request.

4. SYNTHETIC LIGHT CURVE SOLUTION

To derive the parameters of the systems considered here, the photometric light curves were analysed using the latest version of the Wilson-Devinney (W-D) code (Wilson & Devinney 1971; Wilson 1990; Wilson 1994; Wilson & van Hamme 2016) using its user-friendly interface written in Python, `PyWD2015` (Güzel & Özdarcan 2020). `PyWD2015` does not change the original W-D functionality, but only provides a convenient interface for the DC and LC programs. Some useful tools in `PyWD2015` facilitate the technical aspects of the modelling process, as well as the iterative visualisation of the results.

For the light curve analysis we used the well-known procedure called "q–search". This procedure requires to set some parameters fixed in `PyWD2015` and others free (variable), with a range of fixed mass ratios ($q = m_2/m_1$). A first look at the light curves of our systems clearly shows that they exhibit continuous changes in light, suggesting the behavior of W-UMa systems and the use of `Mode 3` of the Wilson-Devinney code.

The analysis in `Mode 3` requires as fixed parameters the gravity darkening coefficients $g_1 = g_2$, set to 0.32 (Lucy 1967), the bolometric albedos

[6] IRAF is distributed by the National Optical Observatories, operated by the Association of Universities for Research in Astronomy, Inc., under cooperative agreement with the National Science Foundation.

TABLE 2

TIMES OF MINIMA AND NEW EPHEMERIS

Target	HJD	Epoch	O-C	Error	Source	New ephemerid
J09344360	2454368.4008	-8848	-0.0010	0.0177	[1]	HJD2456334.7872(11) 0d.22224067(10)
	2454368.5113	-8847.5	-0.0016	0.012	[1]	
	2456334.7850	0	-0.0022	-	[2]	
	2457505.7758	5269	0.0026	0.0099	[3]	
	2457505.8912	5269.5	0.0069	0.0208	[3]	
	2459659.7290	14961	-0.0008	0.0018	[5]	
	2459659.8389	14961.5	-0.0020	0.0026	[5]	
	2460028.7609	16621.5	0.0005	0.0021	[5]	
	2460028.8708	16622	-0.0007	0.0019	[5]	
	2460031.7596	16635	-0.0011	0.0016	[5]	
	2460031.8711	16635.5	-0.0007	0.0022	[5]	
J10054868	2454118.1421	-8539.5	-0.0003	-	[1]	HJD 2456016.6796(5) 0d.2223246(1)
	2454118.2534	-8539	-0.0001	-	[1]	
	2456016.6810	0	0.0014	-	[2]	
	2457484.1350	6600.5	-0.0001	0.0107	[3]	
	2457484.2451	6601	-0.0011	0.0112	[3]	
	2460029.7656	18050.5	0.0005	0.0003	[5]	
	2460029.8760	18051	-0.0003	0.0003	[5]	
J11393492	2457307.5748	-0.5	0.0017	-	[3]	HJD 2457307.6923 (23) 0d.2385424(3)
	2457307.6906	0	-0.0017	-	[3]	
	2459654.9491	9840	0.0000	-	[5]	
	2460030.6501	11415	-0.0033	-	[5]	
	2460030.7775	11415.5	0.0049	-	[5]	
	2460030.8902	11416	-0.0017	-	[5]	
J16091958	2457506.4766	0	0.0010	0.0011	[4]	HJD 2457506.4656(27) 0d.2476461(4)
	2457548.9457	171.5	-0.0012	-	[3]	
	2459660.8713	8699.5	-0.0011	0.0020	[5]	
	2459661.0022	8700	0.0060	0.0018	[5]	
	2459713.7396	8913	-0.0052	0.0011	[5]	
	2459713.8676	8913.5	-0.0010	0.0023	[5]	
	2459755.8461	9083	0.0015	0.0011	[5]	

[1] SWASP. [2] AAVSO VSX. [3] ASAS. [4] OEJV 179. [5] This paper.

$A_1 = A_2 = 0.5$ (Ruciński 1973), and the limb darkening coefficients of the components interpolated from the square–root law tables of Claret & Bloemen (2011).

The free parameters in `Mode 3` are the temperature of the secondary component T_2, the inclination of the system i, the dimensionless potentials of the components $\Omega_{1,2}$ and the luminosity of the primary L_1. Here, the estimated temperature T_1 used for J09344360 and J10054868 were the effective temperatures obtained from LAMOST spectroscopy, which is reliable for AFGK stars (Ren et al. 2016). For J11393492 and J16091958 the average temperature for T_1 from different sources was used.

Convergence of the calculation was achieved as a contact system (`Mode 3`) for J10054868, J11393492 and J16091958. However, using `Mode 3`, we were unable to find convergence for J09344360. We therefore switched to `Mode 2`, which does not use any constraint on the potentials $\Omega_{1,2}$ (Leung & Wilson 1977), to test for a semi-detached configuration solution in `PyWD2015`. After a few iterations, the solution converged on `Mode 4` –a semi-detached configuration with star 1 filling its Roche lobe. In this mode, Ω_1 is fixed by the code to the appropriate value of the mass ratio q so that the primary component fills its Roche lobe exactly, and Ω_2 is one of the adjustable parameters. The different calculation modes offered by the W-D code are described in Wilson & van Hamme (2016).

The behavior of the q-search procedure, where the mean residual for the input data Σ is plotted against the value of the mass ratio q, is shown in Figure 1. The value of q corresponding to the minimum value of Σ was therefore included in the list of adjustable parameters and a more detailed analysis was carried out.

The presence of a third light was not found in any of the systems studied here, or its value was negligible. However, there is a further point that needs to be considered regarding J09344360 (V0443) as pointed out by the referee of this work.

The data from the Gaia mission (Gaia Collaboration et al. 2018) shows the existence of star Gaia ID 814599066616791552 (hereafter Gaia 552) only 0.7 arc seconds away from J09344360. This source

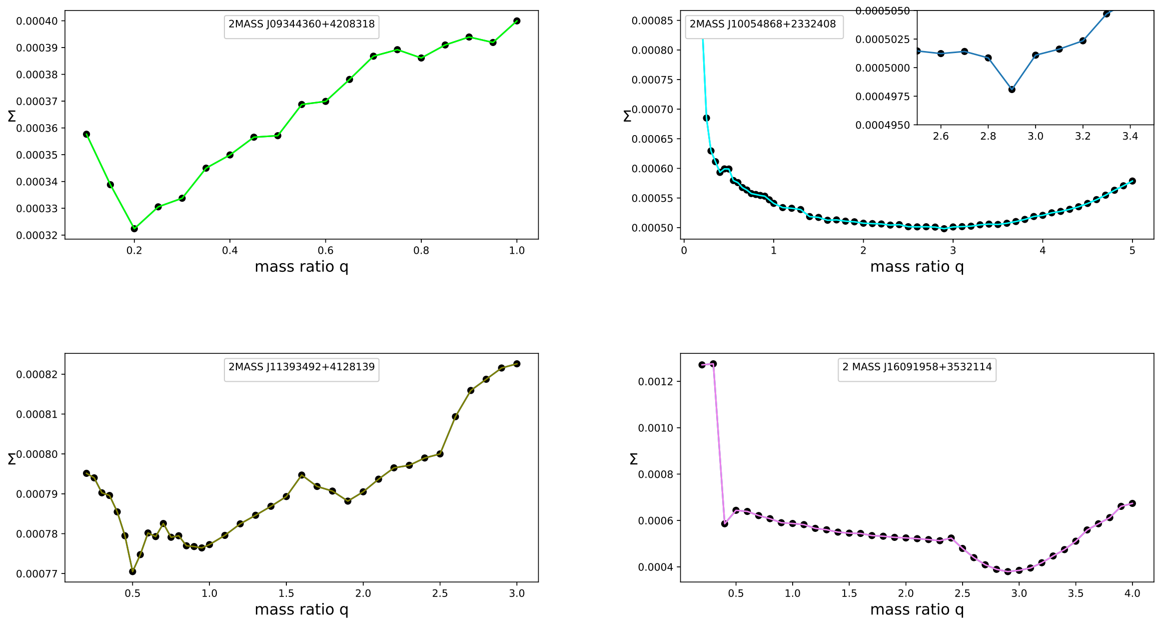

Fig. 1. Relation Σ, the mean residuals for input data, versus mass-ratio q as provided by the `PyWD2015` code. The colour figure can be viewed online.

is highlighted as non-variable and in the Gaia DR3 catalogue it is found to have a very similar magnitude and color to the average magnitude and color of J09344360. Specifically, the average G-band magnitude in Gaia is $G = 13.94$ mag for J09344360, and for Gaia 552 is $G = 14.07$ mag. Also, since the G-band time series of J09344360 is available from the Gaia DR3 catalogue, we used the Gaia light curve of J09344360 and the Gaia magnitude of Gaia 552 to evaluate the effect of this source on J09344360.

The above is necessary because the observing site of our measurements is the San Pedro Mártir Observatory (México) that has a seeing, with values measured using the DIMM, ranging from 0.48 to 0.81 arc seconds as the median value, and from 0.6 to 0.7 arc seconds as the mean value (Michel et al. 2003). All this precludes us from detecting accurate data for Gaia 552.

Now, given that it was not possible to distinguish the Gaia 552 source from J09344360 in our images, we proceeded to transform Gaia 552 luminosity into the $BVRI$ bands using the polynomials proposed by Carrasco and Bellazzini.[7]

This transformation of magnitudes allow us, by knowing the average brightness of J09344360 from Gaia measurements and our own, influenced by the luminosity of Gaia 552, to calculate the values -at each color- that are to be subtracted from our measurements to neutralize the Gaia 552-induced luminous effect. The new data obtained are used to obtain the parameters of J09344360 reported here.

In the light curves of the three contact systems the so-called O'Connell effect, different heights of the maxima, is visible (O'Connell 1951). This effect is generally attributed to the presence of a hot or cool spot on one or both components of the system. Hence in our calculations the spot parameters, co-latitude θ, longitude ψ, angular radius γ, and the temperature factor T_s/T_* have been treated as free parameters in `PyWD2015`.

Table 3 shows the results of our W-D work sessions. Note that for systems with mass ratio $q > 1$, the reciprocal value of q (q_{inv}) was used, as is generally accepted. The final fit of the observed points is shown in Figure 2 and Figure 3. Graphical representations of the systems are shown in Figure 4, using the `Binary Maker 3.0` software (Bradstreet & Steelman 2002).

5. ESTIMATES OF THE ABSOLUTE ELEMENTS

The absolute parameters of the systems presented here were estimated using the Gaia DR3 distance value (Gaia Collaboration et al. 2018).

We did not use the parallax value since all systems have a RUWE value (Renormalised Unit Weight Error) relatively high according to Lindegren

[7] `https://gea.esac.esa.int/archive/documentation/GEDR3/Data_processing/chap_cu5pho/cu5pho_sec_photSystem/cu5pho_ssec_photRelations.html`.

TABLE 3

LIGHT CURVE SOLUTIONS OF OUR FOUR SYSTEMS. ERRORS ARE THOSE OBTAINED FROM THE W-D CODE

Parameter	J09344360	J10054868	J11393492	J16091958
$i(^{\circ})$	68.994±0.683	71.982±0.212	51.644±0.806	85.688±0.406
T_1 (K)	4465(fxd)	4850(fxd)	4150(fxd)	5255(fxd)
T_2 (K)	3462±27	4528±9	3934±11	5045±5
$\Omega_1 = \Omega_2$		6.380±0.030	2.913±0.022	6.413±0.006
Ω_1	2.221(fxd)			
Ω_2	2.331±0.045			
q	0.191±0.009	2.923±0.022	0.510±0.009	2.896±0.001
$1/q$		0.342		0.345
f	0%	21.70%	0.45%	10.50%
f_2	0.051%			
L_{1B}	0.993±0.003	0.372±0.004	0.635±0.043	0.322±0.001
L_{1V}	0.987±0.003	0.348±0.004	0.636±0.037	0.310±0.001
L_{1R}	0.975±0.003	0.328±0.003	0.634±0.032	0.303±0.001
L_{1I}	0.953±0.003	0.315±0.002	0.638±0.024	0.294±0.001
L_{2B}	0.010±0.001	0.577±0.008	0.023±0.001	0.640±0.010
L_{2V}	0.016±0.001	0.594±0.010	0.024±0.001	0.653±0.011
L_{2R}	0.024±0.001	0.609±0.001	0.026±0.001	0.670±0.014
L_{2I}	0.040±0.001	0.628±0.014	0.028±0.001	0.669±0.015
L_{3BVRI}	0	0	0	0
Primary				
r(pole)	0.490±0.004	0.281±0.001	0.411±0.002	0.276±0.001
r(side)	0.534±0.005	0.294±0.001	0.436±0.003	0.288±0.001
r(back)	0.556±0.004	0.334±0.001	0.465±0.003	0.324±0.001
Secondary				
r(pole)	0.202±0.019	0.454±0.002	0.304±0.007	0.449±0.001
r(side)	0.208±0.021	0.489±0.003	0.318±0.008	0.482±0.001
r(back)	0.224±0.029	0.518±0.005	0.351±0.013	0.510±0.001
Residual	0.00032406	0.00050008	0.00076165	0.00037905
Lat_{spot}		10°3.4±1.3	30°.3±1.1	51°.7±1.2
$Long_{spot}$		120°.7±1.1	110°.5±1.6	72°.1±0.9
Radius		20°.8±0.45	28°.2±0.93	20°.5±0.66
T/F		0.97±0.06	0.87±0.09	1.23±0.10
Component		1	1	1
Lat_{spot}		90°.6±1.2		
$Long_{spot}$		181°.1±1.2		
Radius		17°.3±0.51		
T/F		0.94±0.03		
Component		2		

(2018); see Table 5. In particular J09344360 and J11393492 have a RUWE value of ≈ 2.

For J09344360 the distance value was missing in the Gaia DR3 catalog and therefore the absolute parameters were estimated using the following relations:

(a) Period-Mass ($P-M_1$) relation obtained from the absolute parameter estimates of 118 systems using the parallax method from Gaia DR3 (Poro et al. 2022),

$$M_1 = (2.924 \pm 0.075)P + (0.147 \pm 0.029) \ .$$

(b) Orbital period-semimajor axis (P-a) relation as suggested by Poro et al. (2024), obtained from the study of 414 contact systems with $P < 0.7$ days from Latković et al. (2021),

$$a = 5.914^{+0.272}_{-0.298}\, P + 0.372^{+0.113}_{-0.114} \ .$$

Subsequently, knowing the mass ratio q, the fractional radii $r_{1,2}$ and the temperatures of the components of J09344360, the values of the absolute radii and luminosities $R_{1,2}$ and $L_{1,2}$ were obtained from the well-known formula $R_{1,2} = a \times r_{mean}$ and the Stefan-Boltzmann law.

For the other systems knowing the distance we calculated: the visual absolute magnitude M_v, the bolometric magnitude M_{bol}, the total luminosity L_{tot} and the individual luminosities $L_{1,2}$ using the following equations:

$$M_v = m_v - 5 \log d + 5 - A_v \ ,$$

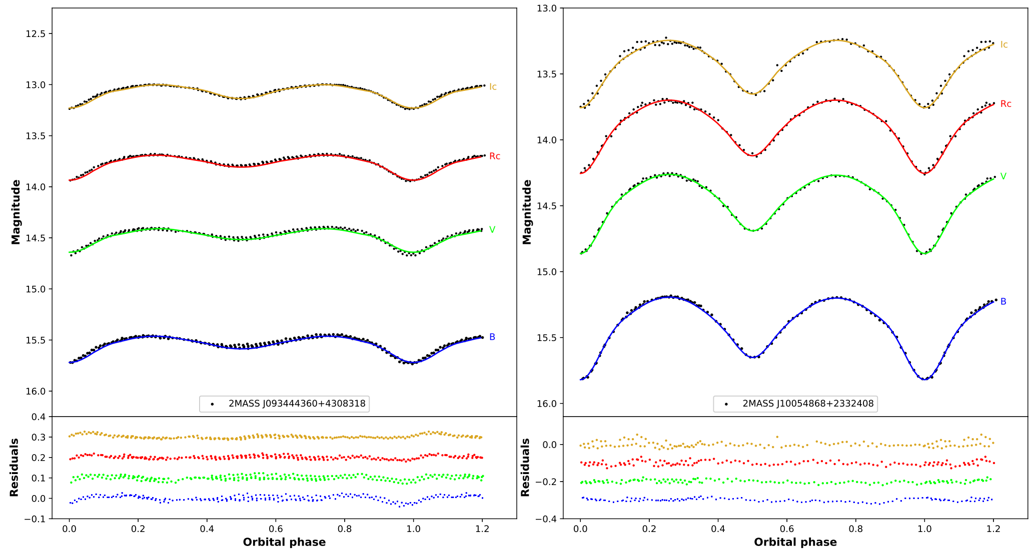

Fig. 2. CCD light curves of 2MASS J09344360+4208318 and 2MASS J10054868+2332408. Points are the original CCD observations and lines are the theoretical fits with the surface spot/s contribution. The residuals are shown at the bottom of each panel, arbitrarily shifted for clarity. The colour figure can be viewed online.

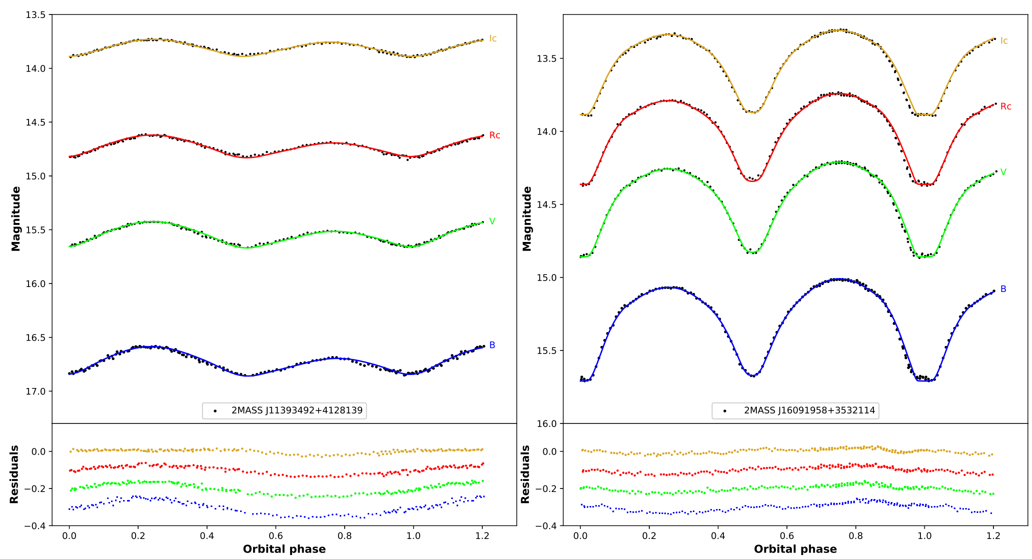

Fig. 3. The same of Figure 2 but for 2MASS J11393492+4128139 and 2MASS J16091958+3532114. The colour figure can be viewed online.

where m_v is the V magnitude, d the distance in parsec and A_v the interstellar absorption; $M_{bol} = M_v + BC$, where BC is the star's bolometric correction as interpolated from the Pecaut & Mamajek (2013) tables;

$$\log(L_{tot}/L_{\odot}) = 0.4 \times (4.74 - M_{bol})\,;$$

$L_1 = L_{tot}/c$, $c = L_{2V}/L_{1V}$, and $L_2 = L_{tot} - L_1$.

The temperatures of the first and second components of the systems are known, so we obtained their radii $R_{1,2}$, the semi-axis a, and the total mass of the systems from Kepler's third law as follows:

$$R_{1,2}[\mathrm{R}_{\odot}] = L_{1,2}[\mathrm{L}_{\odot}]^{1/2}/T_{1,2}[\mathrm{T}_{\odot}]^2\ ,$$

where $T_{\odot} = 5771.8$K, and

$$a = R_1/r_{1mean}\,;$$

$$M_{tot} = 0.0134\,(a^3/P^2)\,.$$

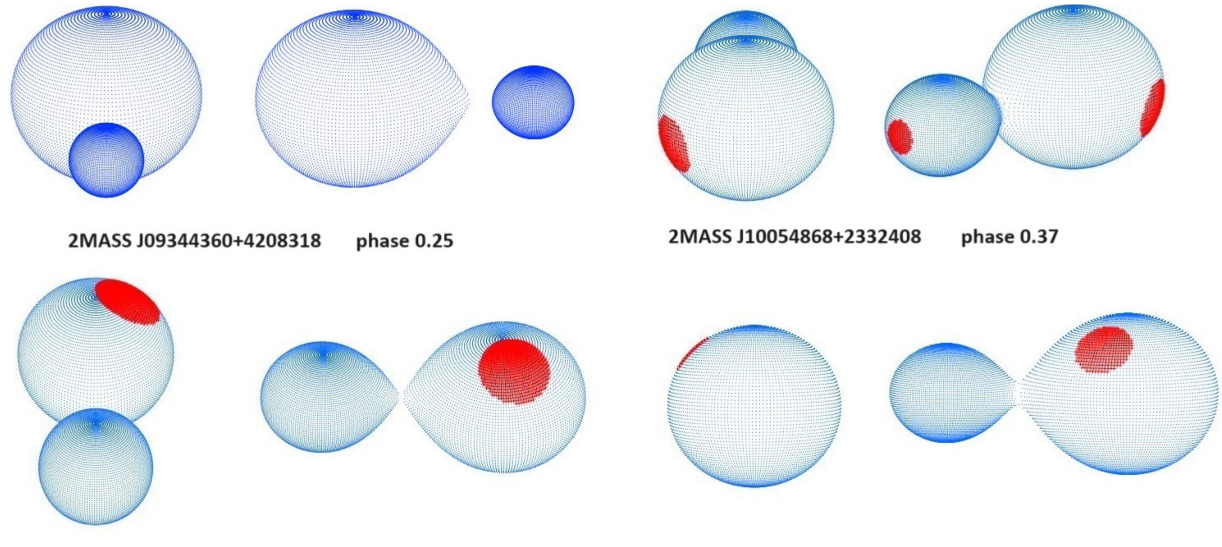

Fig. 4. The 3D view of the stars. Left at the primary minimum, right with the spot/s visible. The colour figure can be viewed online.

TABLE 4

ABSOLUTE ELEMENTS VALUES FOR ALL THE SYSTEMS

Target	$M_1(\mathrm{M}_\odot)$	$M_2(\mathrm{M}_\odot)$	$R_1(\mathrm{R}_\odot)$	$R_2(\mathrm{R}_\odot)$	$L_1(\mathrm{L}_\odot)$	$L_2(\mathrm{L}_\odot)$	$M_{tot}(\mathrm{M}_\odot)$
J09344360	0.797±0.003	0.153±0.008	0.888±0.011	0.356±0.039	0.283±0.007	0.016±0.004	0.949
J10054868	1.125±0.190	0.385±0.089	0.840±0.044	0.561±0.016	0.267±0.026	0.157±0.009	1.510
J11393492	0.418±0.190	0.213±0.100	0.868±0.075	0.189±0.070	0.202±0.035	0.008±0.071	0.631
J16091958	0.659±0.090	0.228±0.032	0.758±0.011	0.481±0.026	0.335±0.007	0.159±0.022	0.887
	J_0	$\log J_0$	J_{lim}	$\log J_{lim}$	Spec. type	$\log \rho_1(\mathrm{gr/cm^3})$	$\log \rho_2(\mathrm{gr/cm^3})$
J09344360	9.29^{50}	50.97	2.47^{51}	50.97	K5 + M3	0.34	0.81
J10054868	2.74^{51}	51.44	4.26^{51}	51.63	K3 + K4-5	0.54	0.39
J11393492	7.74^{50}	50.89	1.01^{51}	51.00	K7 + K9	0.42	0.63
J16091958	1.18^{51}	51.07	1.70^{51}	51.23	K0 + K2	0.48	0.31

Note: Spectral types are according to Pecaut & Mamajek (2013).

Using the value of the mass ratio from the Wilson-Devinney analysis, we obtained the masses M_1 and M_2, and therefore all the physical parameters of the systems under study, whose values are shown in Table 4.

6. INTERSTELLAR ABSORPTION

For the calculation of A_v we used the NASA & IPAC Galactic Dust Reddening and Extinction maps[8]obtaining the total interstellar absorption in the photometric V band value of the color excess $E\infty(B-V)$ from Schlafly & Finkbeiner (2011) and Schlegel et al. (1998).

[8]The NASA&IPAC Extragalactic Database (NED) is funded by the National Aeronautics and Space Administration and operated by the California Institute of Technology.

Subsequently the value of the total interstellar absorption in the V band up to the distance d was calculated via the well known Bahcall & Soneira (1980) relation:

$$A_d(b) = A_\infty(b)[1 - \exp(-d \sin b/H)]\,, \tag{1}$$

where H is the scale height for the interstellar dust, which is adopted to be 125 pc (Marshall et al. 2006); values are shown in Table 5.

7. STABILITY PARAMETER

The Flannery (1976) stability parameter $\Im$ for mass exchange in a contact binary system can be defined as follows:

$$\Im = \ln\left[\frac{R_p(0.38 + 0.2\log q)}{R_s(0.38 - 0.2\log q)}\right]\,, \tag{2}$$

TABLE 5

TOTAL INTERSTELLAR ABSORPTION

Target	b	d	RUWE	A_v
J09344360	47.506	365.61	1.990	0.036
J10054868	52.570	399.60	1.002	0.090
J11393492	69.443	411.45	2.037	0.057
J16091958	47.361	540.02	0.983	0.055

where R_p is the radius of the primary and R_s is the radius of the secondary.

If $\Im = 0$, there is no mass transfer; if $\Im > 0$, an unbalanced pressure gradient will force gas from the primary to the secondary, and vice versa if $\Im < 0$.

In the cases studied here we get $\Im= 0.74$ for J09344360 and $\Im = 1.21$ for J11393492, so there is mass transfer from the primary to the secondary. The opposite ($\Im < 0$) is true for J10054868 and J16091958 where we get $\Im = -0.90$ and -0.95 respectively.

8. ENERGY TRANSFER IN OUR BINARIES

One of the characteristics of the secondary components of contact binary systems is that they are brighter and larger than their zero-age main sequence (ZAMS) counterparts (Struve 1948).

In fact, as far as our target systems are concerned we show their radii and luminosity data in Table 6, in comparison to their main sequence analog and, as observed, the secondaries display such behavior.

According to the studies of Wang (1994), Csizmadia & Klagyivik (2004) and Jiang et al. (2009), we can estimate the energy transfer parameter β and the luminosity transfer from primary to secondary ΔL as, respectively:

$$\beta = \frac{L_{1,obs}}{L_{1,ZAMS}} = \frac{1+q^{4.6}}{1+q^{0.92}X(T_2/T_1)^4}, \qquad (3)$$

and

$$\Delta L = (1-\beta)XL_1\,, \qquad (4)$$

where X is the relative temperature difference parameter $(T_1 - T_2)/T_1$.

Therefore the percentage of the intrinsic luminosity of the primary that is transferred to the secondary during the energy transfer process can be estimated with the previous relationships in equations (3) and (4).

Furthermore, we can calculate the effects of the energy transfer on the secondary, for example, the increase in luminosity ΔL_2 (Yang & Liu 2001) and the decrease in radius R_2 to become a main sequence star, in terms of the logarithm of $\mathrm{d}R_2/R_{2,ZAMS}$ (Jiang et al. 2009). The estimates of these quantities are displayed in Table 7.

9. DETAILS ON THE SYSTEMS AND FINAL REMARKS

9.1. *Common Features*

The common features of our systems can be summarised in a few relevant points:

(1) The four systems studied here, although with some differences among them that will be explained later, belong to the late spectral type K and, with their short periods, are good targets for testing the thermal relaxation oscillation (TRO) theory (Lucy 1976; Lucy & Wilson 1979; Flannery 1976; Robertson & Eggleton 1977; Yakut & Eggleton 2005 and Li et al. 2008), and are of great interest for the study of the structure and evolution of eclipsing binaries (Acerbi et al. 2022). The TRO model predicts that binaries evolve in a cycle around the marginal contact state, oscillating between contact-semidetached-contact states and exhibiting alternate EW and EB light curves (Zhu et al. 2010).

(2) In addition, the three systems close to the short period limit of 0.22 days are ultra-short period binaries (USPBs) (Rucinski 1992; Rucinski 2007). These binaries are important objects for studying the period cut-off phenomenon (Liu et al. 2014; Li et al. 2019). Although many studies have been conducted on the period distribution of close binaries, the values of the period limit and the period cut-off are still open questions. However, thanks to the use of data from several photometric surveys, Qian et al. (2020) recently proposed a new period cut-off value of 0.15 days and concluded that the maximum of the period distribution of close binaries is about 0.31 days. The same conclusion was reached by Latković et al. (2021) who found the maximum of the period distribution to be close to 0.3 days.

(3) The low degree of contact is another common feature of the four binary systems studied here, which is a well-known feature of K-type systems.

9.2. *J09344360*

This binary is a short-period ($P \approx 0.22$d) formally semi-detached system (Figure 5, left), as also argued by Lohr et al. (2013), in which the primary component fills its Roche lobe while the secondary is a little inside it ($f = 0.051$).

The stability parameter ($\Im = 0.74$) suggests that there is currently mass transfer between the components.

TABLE 6

SECONDARIES OF CBs AND THEIR ZAMS COUNTERPARTS

Target	$R_2(\mathrm{R}_\odot)$	$R_{2,ZAMS}(\mathrm{R}_\odot)$	$L_2(\mathrm{L}_\odot)$	$L_{2,ZAMS}(\mathrm{L}_\odot)$
J10054868	0.840	0.381	0.267	0.018
J11393492	0.189	0.225	0.008	0.004
J16091958	0.758	0.239	0.267	0.005

TABLE 7

TRANSFER ENERGY PARAMETERS

Target	β	ΔL	ΔL_2	$\log \mathrm{d}R_2/R_{2,ZAMS}$
J10054868	0.785	0.034	0.245	-0.152
J11393492	0.729	0.055	0.006	-0.374
J16091958	0.764	0.038	0.332	-0.156

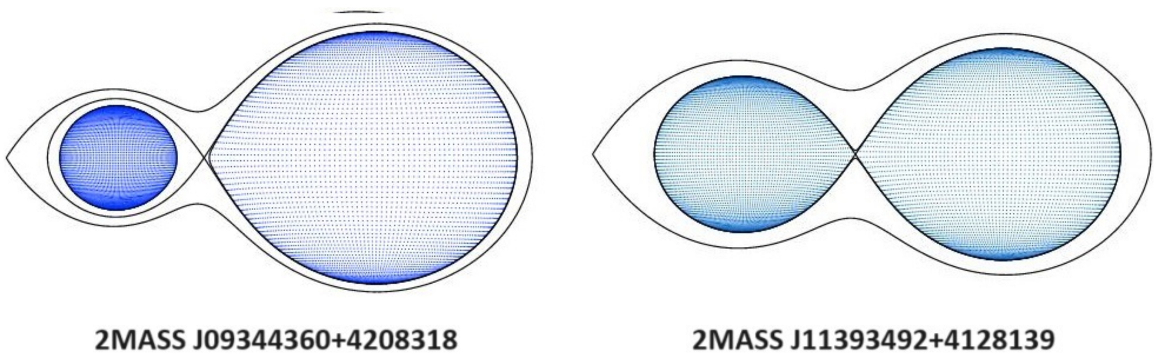

Fig. 5. The configuration of the components of 2MASS J09344360+4208318 (V0443 UMa) and 2MASS J11393492+4128139 in the orbital plane is shown. The colour figure can be viewed online.

The later spectral type of the components ($K5 + M3$) is indicative of an old formed system that has probably experienced more than one TRO cycle and is now in a slightly semi-detached state far from thermal stability ($\Delta T \approx 1000$K).

With the current extreme mass ratio of $q = 0.191$, it is likely that this system may be at the beginning of a new phase of contact binary evolution, as suggested by its position in the heat diagram of Figure 7 near the outer edge of the lower (red) boundary.

The location of the secondary component in the $\log M - \log L$ diagram (Figure 6) and the total mass of the system ($M_{tot} = 0.95\mathrm{M}_\odot$), slightly below the lower mass limit of 1.0-1.2$\mathrm{M}_\odot$ for the known contact binaries Stępień (2006), suggests that it has lost mass during the TRO cycles and may imply a later evolutionary stage.

9.3. *J10054868, J11393492 and J16091958*

All three systems are contact binaries with short periods ($P \approx 0.22$-0.25 d) and in which the temperature of the components suggests a spectral type K.

J11393492 is an A-subtype contact system while J10054868 and J16091958 are W-subtype contact systems. It is worth noticing that it is somewhat strange to find a spectral K type in A-subtype contact systems. Late spectral type systems generally belong to the W-subtype of W UMa contact binaries, although it is possible to find exceptions to this in the literature, as ES Cep (Zhu et al. 2014), 2MASS J11201034-2201340 (Hu et al. 2016), AP UMi (Awadalla et al. 2016), NSV 395 (Samec et al. 2016), ROTSE J135349.8+305205 and 1SWASP J150957.5-115308 (Barani et al. 2022). The mass ratio of J11393492 is $q = 0.51$ and from the W-D analysis a shallow filling value of $f = 4.5$ (Figure 5,

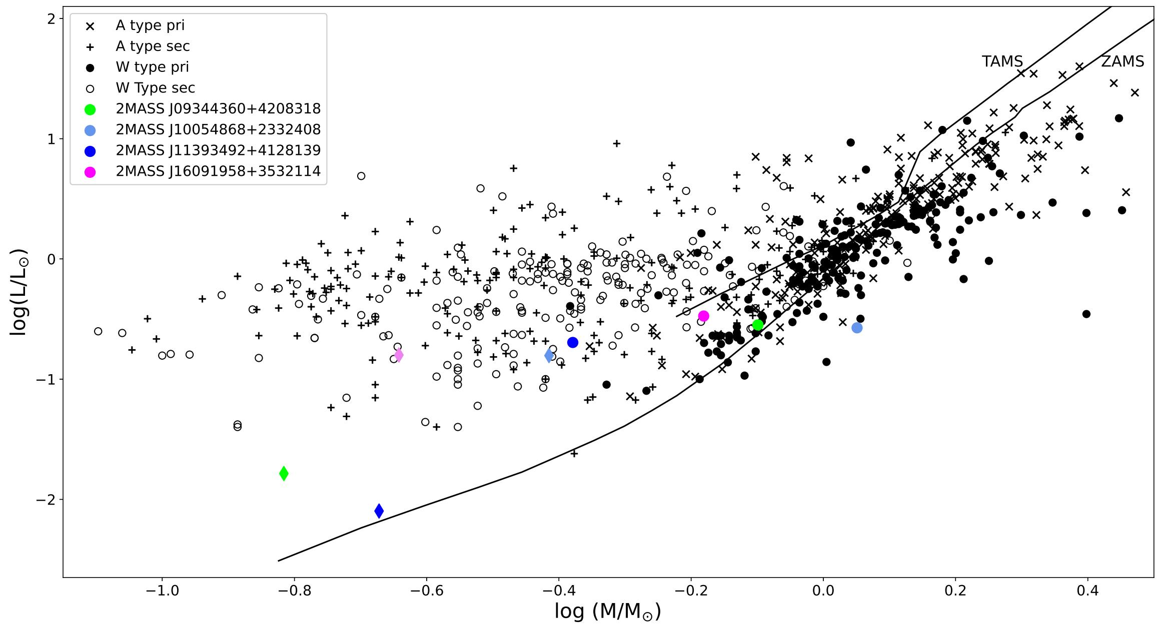

Fig. 6. Location of the components of our systems on the logarithmic Mass-Luminosity diagram. The primaries are marked with circles and the secondaries with diamonds. The sample of W UMa type systems was obtained from a compilation of Latković et al. (2021). Zero Age Main Sequence (ZAMS) and Terminal Age Main Sequence (TAMS) are taken from Girardi et al. (2000) for the solar chemical composition. The colour figure can be viewed online.

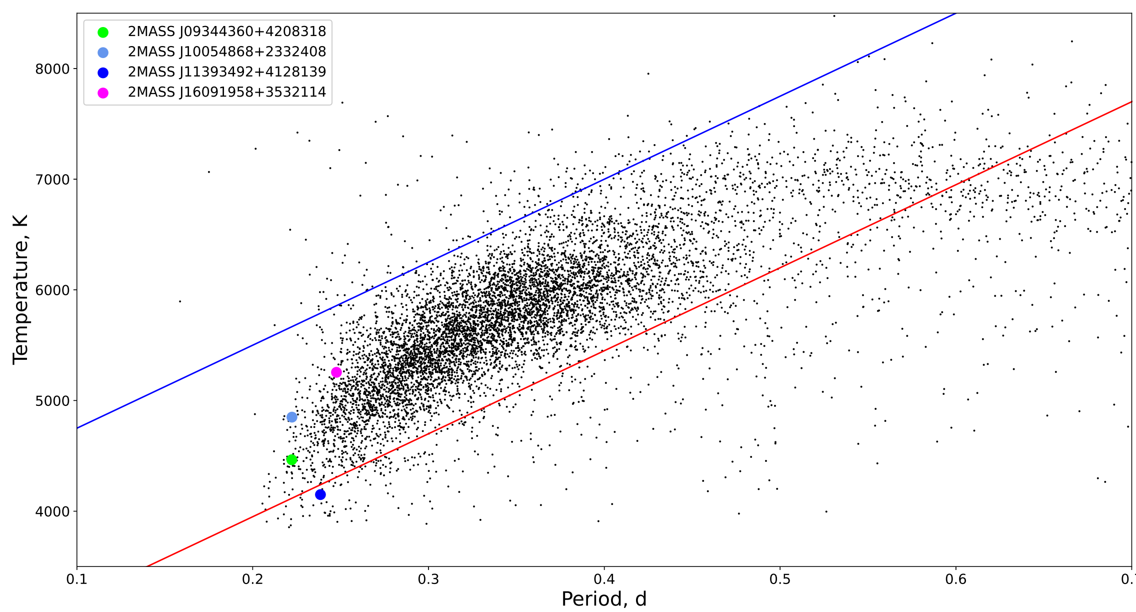

Fig. 7. Correlation between orbital period and temperature based on parameters of 8510 contact binaries from Qian et al. (2020). The red and blue lines are the boundaries of normal EWs. Systems near the red border are marginal contact systems, while those close to the blue border are deep contact ones. The colour figure can be viewed online.

right) was found, despite that it is in good thermal contact with only $\Delta T = 216$K. A cool spot, generally associated with magnetic activity such as solar magnetic spots (Mullan 1975), was added to the primary component to account for the asymmetries in its light curve (Figure 4).

The stability parameter is positive ($\Im = +1.21$), so we currently have a mass transfer from the primary to the secondary component of the system.

J10054868 and J16091958 show common features that are the good thermal contact between their components, the shallow fill-out and the presence of spot(s) (Table 3). While for J16091958 the hot spot is produced by the impact of mass transferred from the secondary to the primary component, which is supported by the value of the Flannery parameter ($\Im = -0.90$), for J10054868 a cool spot, possibly caused by magnetic activity, was required on the component to account for the discrepancies in the light curve.

The relative properties of both the systems were derived by Sun et al. (2020) using a self-developed automatic Wilson-Devinney code. With respect to J10054868, the more obvious difference between their solution and ours is that we obtain a W-subtype, whereas Sun et al. (2020) obtain an A- subtype W UMa.

It is however known (e.g. van Hamme (1982), Lapasset & Claria (1986)) that sometimes both A and W configurations can reproduce well the photometric light curve, and the right choice between the two solutions can be obtained only having a spectral mass ratio.

For our two systems, after starting the two solutions with very similar temperatures of the primary component, we obtained encouraging similar results with those of Sun et al. (2020) with only minor differences in the mass ratio q of about 1/3, theirs smaller than ours. A luminosity $L_{1\odot}$ for J10054868 twice as large was obtained here; they obtain a luminosity for J16091958 1/3 larger than our result.

It is also necessary to note that during their solutions Sun et al. (2020), did not consider the effect of starspots, while we have found two cool spots on the components for J10054868 and one cool spot on the primary component of J16091958. This is probably the reason of such discrepancy.

Figure 6 shows the positions of the components of our systems in the $\log M - \log L$ diagram where they are located with other W UMa systems from the Latković et al. (2021). The ZAMS and TAMS lines are calculated from Girardi et al. (2000).

The position of the components of J10054868 is among the other primaries and secondaries of the sample, while the primary components of J11393492 and J16091958 are near the TAMS, implying that they have evolved away from the main sequence. These results are due to the mass and energy exchange between the binary components and their internal evolutionary transformations. The secondary components deviate significantly from ZAMS, like the majority of the secondaries of other W UMa systems, meaning that they are little evolved (J11393492) or evolved (J16091958) stars and this may be due to the energy transfer from the more massive component to the less massive one during their evolutionary process (Li et al. 2008).

From the heat map shown in Figure 7 it is possible to observe that both current systems are located inside the boundaries for normal EW systems, with similar positions between the red and blue lines that are the boundaries of the normal EW systems. The position of J11393492 in this Figure 7 is slightly below the red line, and in the $\log M - \log J_0$ (Figure 8) is close to the line that separates the contact from the detached region. The latter suggests that the system, with its filling factor close to zero and the almost equal temperature of its components, is either at the end or at the beginning of the contact phase, as predicted by the TRO theory. The small mass ratios, $q \approx 0.34$ for both J10054868 and J16091958, their low fill-out value, 21.7% and 10.5% respectively, the almost equal temperature of the components, and their position in the contact region of the $\log M - \log J_0$ diagram (Figure 8) suggest that they are approaching the final evolutionary stage of contact binaries. The total estimated masses for J11393492 $M_{tot} = 0.63\mathrm{M}_\odot$ and of J16091958 $M_{tot} = 0.89\mathrm{M}_\odot$ are below the lower mass limit of $1.0 - 1.2\mathrm{M}_\odot$ for known contact binaries (Stępień 2006).

This work has made use of data from the European Space Agency (ESA) mission Gaia,[9] and processed by the Gaia Data Processing and Analysis Consortium (DPAC).[10] Our new observations were carried out at the Observatorio Astronómico Nacional on the Sierra San Pedro Mártir (OAN-SPM), Baja California, México, which is operated by the Universidad Nacional Autónoma de México (UNAM). This work has made use of data from the International Variable Star Index (VSX) database (operated at AAVSO Cambridge, Massachusetts, USA), as well as of the AAVSO Photometric All-Sky Survey (APASS) funded by the Robert Martin Ayers Sci-ences Fund. Also, use has been made of the VizieR catalogue access tool, the SIMBAD database, operated at CDS, Strasbourg, France. The original description of the VizieR service was published in

[9] `https://www.cosmos.esa.int/gaia`.

[10] `https://www.cosmos.esa.int/web/gaia/dpac/consortium`.

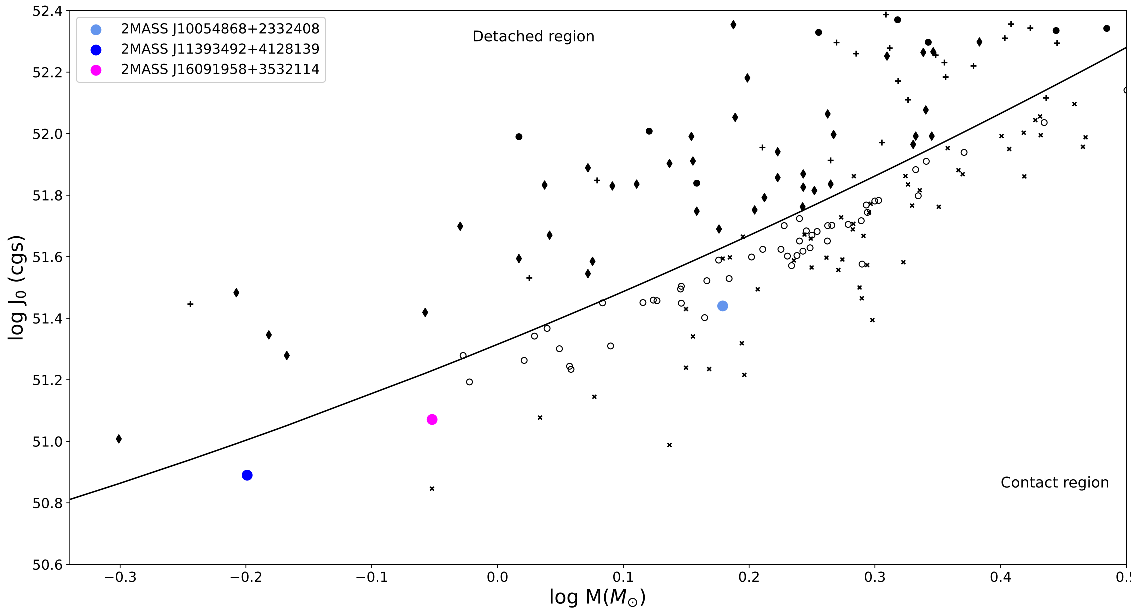

Fig. 8. Position of the three contact systems in the log $M_\odot$ − log J_0 diagram. Symbols are described in Figure 1 of the original paper of Eker et al. (2006). The colour figure can be viewed online.

A&AS 143, 23. Use of the NASA/IPAC Extragalactic Database (NED), which is founded by the National Aeronautics and Space Administratrion and operated by the California Institute of Technology, has been made. We would like to thank the anonymous referee for her/his useful comments which have improved the quality of this paper, and in particular for calling our attention to the presence of a companion to J09344360, as detected by GAIA, and suggestions on how to consider such effect. We also thank Dr. Gisella Clementini (INAF, Bologna) for her helpful suggestions and clarifications regarding GAIA observations on J09344360.

REFERENCES

Acerbi, F., Barani, C., & Popov, V. 2022, NewA, 97, 101873, https://doi.org/10.1016/j.newast.2022.101873

Akerlof, C., Amrose, S., Balsano, R., et al. 2000, AJ, 119, 1901, https://doi.org/10.1086/301321

Awadalla, N. S., Hanna, M. A., Ismail, M. N., et al. 2016, JKAS, 49, 65, https://doi.org/10.5303/JKAS.2016.49.3.065

Bahcall, J. N. & Soneira, R. M. 1980, ApJS, 44, 73, https://doi.org/10.1086/190685

Barani, C., Martignoni, M., Michel, R., Acerbi F., Aceves H., Popov V. 2022, RMxAA, 58, 237, https://doi.org/10.22201/ia.01851101p.2022.58.02.06

Bradstreet, D. H. & Steelman, D. P. 2002, AAS, 201, 1124

Claret, A. & Bloemen, S. 2011, A&A, 529, 75, https://doi.org/10.1051/0004-6361/201116451

Cui, X.-Q., Zhao, Y.-H., Chu, Y.-Q., et al. 2012, RAA, 12, 1197, https://doi.org/10.1088/1674-4527/12/9/003

Csizmadia, S. & Klagyivik, P. 2004, A&A, 426, 1001, https://doi.org/10.1051/0004-6361:20040430

Damerdji, Y., Klotz, A., & Boër, M. 2007, AJ, 133, 1470, https://doi.org/10.1086/511747

Drake, A. J., Graham, M. J., Djorgovski, S. G., et al. 2014, ApJS, 213, 9, https://doi.org/10.1088/0067-0049/213/1/9

Flannery, B. P. 1976, ApJ, 205, 217, https://doi.org/10.1086/154266

Fukugita, M., Ichikawa, T., Gunn, J. E., et al. 1996, AJ, 111, 1748, https://doi.org/10.1086/117915

Gaia Collaboration, Brown, A. G. A., Vallenari, A., et al. 2018, A&A, 616, 1, https://doi.org/10.1051/0004-6361/201833051

Girardi, L., Bressan, A., Bertelli, G., et al. 2000, A&AS, 141, 371, https://doi.org/10.1051/aas:2000126

Güzel, O. & Özdarcan, O. 2020, Contributions of the Astronomical Observatory Skalnate Pleso, 50, 535, https://doi.org/10.31577/caosp.2020.50.2.535

Hu, C.-P., Yang, T.-C., Chou, Y., et al. 2016, AJ, 151, 170, https://doi.org/10.3847/0004-6256/151/6/170

Jiang, D., Han, Z., Jiang, T., et al. 2009, MNRAS, 396, 2176, https://doi.org/10.1111/j.1365-2966.2009.14852.x

Kazarovets, E. V., Samus, N. N., Durlevich, O. V., et al. 2019, IBVS, 6261, 1, https://doi.org/10.22444/IBVS.6261
Landolt, A. U. 2009, AJ, 137, 4186, https://doi.org/10.1088/0004-6256/137/5/4186
Lapasset, E. & Claria, J. J. 1986, A&Ap, 161, 264
Latković, O., Čeki, A., & Lazarević, S. 2021, ApJS, 254, 10, https://doi.org/10.3847/1538-4365/abeb23
Leung, K.-C. & Wilson, R. E. 1977, ApJ, 211, 853, https://doi.org/10.1086/154994
Li, L., Zhang, F., Han, Z., et al. 2008, MNRAS, 387, 97, https://doi.org/10.1111/j.1365-2966.2008.12736.x
Li, K., Xia, Q.-Q., Michel, R., et al. 2019, MNRAS, 485, 4588, https://doi.org/10.1093/mnras/stz715
Liao, W.-P., Qian, S.-B., Soonthornthum, B., et al. 2017, PASP, 129, 124204, https://doi.org/10.1088/1538-3873/aa8ded
Lindgren, L., 2018, Re-normalising the astrometric chi-square in Gaia DR2 note GAIA-C3-TN-LU-LL- 124, Gaia DPAC
Liu, N.-P., Qian, S.-B., Soonthornthum, B., et al. 2014, AJ, 147, 41, https://doi.org/10.1088/0004-6256/147/2/41
Liu, N.-P., Qian, S.-B., Liao, W.-P., et al. 2023, AJ, 165, 259, https://doi.org/10.3847/1538-3881/acd04e
Lohr, M. E., Norton, A. J., Kolb, U. C., et al. 2013, A&A, 549, A86, https://doi.org/10.1051/0004-6361/201220562
Lucy, L. B. 1967,ZAp, 65, 89
Lucy, L. B. 1976, ApJ, 205, 208, https://doi.org/10.1086/154265
Lucy, L. B. & Wilson, R. E. 1979, ApJ, 231, 502, https://doi.org/10.1086/157212
Marsh, F. M., Prince, T. A., Mahabal, A. A., et al. 2017, MNRAS, 465, 4678, https://doi.org/10.1093/mnras/stw2110
Marshall, D. J., Robin, A. C., Reylé, C., et al. 2006, A&A, 453, 635, https://doi.org/10.1051/0004-6361:20053842
Michel, R., Echevarría, J., Costero, R., et al. 2003, RMxAA, 39, 291
Michel, R., Barani, C., Martignoni, M., et al. 2023, RMxAA, 59, 123, https://doi.org/10.22201/ia.01851101p.2023.59.01.09
Mullan, D. J. 1975, ApJ, 198, 563, https://doi.org/10.1086/153635
O'Connell, D. J. K. 1951, Publications of the Riverview College Observatory, 2, 85
Pecaut, M. J. & Mamajek, E. E. 2013, ApJS, 208, 9, https://doi.org/10.1088/0067-0049/208/1/9
Pollacco, D. L., Skillen, I., Collier Cameron, A., et al. 2006, PASP, 118, 1407, https://doi.org/10.1086/508556
Poro, A., Sarabi, S., Zamanpour, S., et al. 2022, MNRAS, 510, 5315, https://doi.org/10.1093/mnras/stab3775
Poro, A., Tanriver, M., Michel, R., et al. 2024, PASP, 136, 024201, https://doi.org/10.1088/1538-3873/ad1ed3
Qian, S.-B., Zhu, L.-Y., Liu, L., et al. 2020, RAA, 20, 163, https://doi.org/10.1088/1674-4527/20/10/163
Ren, A., Fu, J., De Cat, P., et al. 2016, ApJS, 225, 28, https://doi.org/10.3847/0067-0049/225/2/28
Robertson, J. A. & Eggleton, P. P. 1977, MNRAS, 179, 359, https://doi.org/10.1093/mnras/179.3.359
Ruciński, S. M. 1973, Acta Astron., 23, 79
Rucinski, S. M. 1992, AJ, 103, 960, https://doi.org/10.1086/116118
Rucinski, S. M. 2007, MNRAS, 382, 393, https://doi.org/10.1111/j.1365-2966.2007.12377.x
Samec, R. G., Clark, J., Maloney, D., et al. 2016, JAAVSO, 44, 101
Schlafly, E. F. & Finkbeiner, D. P. 2011, ApJ, 737, 103, https://doi.org/10.1088/0004-637X/737/2/103
Schlegel, D. J., Finkbeiner, D. P., & Davis, M. 1998, ApJ, 500, 525, https://doi.org/10.1086/305772
Stępień, K. 2006, Acta Astron., 56, 347, https://doi.org/10.48550/arXiv.astro-ph/0701529
Stępień, K. 2011, Acta Astron., 61, 139, https://doi.org/10.48550/arXiv.1105.2645
Struve, O. 1948, AnAp, 11, 117
Sun, W., Chen, X., Deng, L., et al. 2020, ApJS, 247, 50, https://doi.org/10.3847/1538-4365/ab7894
Tylenda, R., Hajduk, M., Kamiński, T., et al. 2011, A&A, 528, A114, https://doi.org/10.1051/0004-6361/201016221
van Hamme, W. 1982, A&Ap,, 105, 389
Wang, J.-M. 1994, ApJ, 434, 277, https://doi.org/10.1086/174725
Wilson, R. E. & Devinney, E. J. 1971, ApJ, 166, 605, https://doi.org/10.1086/150986
Wilson, R. E. 1990, ApJ, 356, 613, https://doi.org/10.1086/168867
Wilson, R. E. 1994, PASP, 106, 921, https://doi.org/10.1086/133464
Wilson, R. E. & van Hamme, W., 2016, Computing Binary Stars Observables. ftp.astro.u.edu, directory pub/wilson/lcdc2015
Yakut, K. & Eggleton, P. P. 2005, ApJ, 629, 1055, https://doi.org/10.1086/431300
Yang, Y. & Liu, Q. 2001, AJ, 122, 425, https://doi.org/10.1086/321110
Zhao, G., Zhao, Y.-H., Chu, Y.-Q., et al. 2012, RAA, 12, 723, https://doi.org/10.1088/1674-4527/12/7/002
Zhang, X.-D. & Qian, S.-B. 2020, MNRAS, 497, 3493, https://doi.org/10.1093/mnras/staa2166
Zhu, L., Qian, S.-B., Mikulášek, Z., et al. 2010, AJ, 140, 215, https://doi.org/10.1088/0004-6256/140/1/215
Zhu, L. Y., Qian, S. B., Soonthornthum, B., et al. 2014, AJ, 147, 42, https://doi.org/10.1088/0004-6256/147/2/42

Zhu, L.-Y., Qian, S.-B., Jiang, L.-Q., et al. 2015, ASPC 496, Living Together: Planets, Host Stars and Binaries, ed. S. M. Rucinski, G. Torres, and M. Zejda, (San Francisco, CA: ASPC), 200
Zhu, L.-Y., Zhao, E.-G., & Zhou, X. 2016, RAA, 16, 68, https://doi.org/10.1088/1674-4527/16/4/068

F. Acerbi: Via Zoncada 51, Codogno, LO, 26845, Italy (acerbifr@tin.it).
H. Aceves: Instituto de Astronomía, UNAM. A.P. 877, 22800 Ensenada, BC, México (aceves@astro.unam.mx).
L. Altamirano-Dévora: Facultad de Ingeniería, Arquitectura y Diseño, UABC, Ctra. Tij-Ens 3917, 22860 Ensenada, BC, México (lili@astro.unam.mx).
C. Barani: Via Verdi 25, Codogno, LO, 26845, Italy (carlobarani.cb@gmail.com).
M. Martignoni: Via Don G. Minzoni 26/D, Magnago, MI, 20020, Italy (massimiliano.martignoni@outlook.it).
R. Michel: Instituto de Astronomía, UNAM. A.P. 877, 22800 Ensenada, BC, México (rmm@astro.unam.mx).

Revista Mexicana de Astronomía y Astrofísica, **61**, 65–86 (2025)

https://doi.org/10.22201/ia.01851101p.2025.61.01.05

DENSE MOLECULAR GAS AND DUSTY TORUS IN NGC 4303

Ángel A. Soní[1], Irene Cruz-González[1], Martín Herrera-Endoqui[1,2], Erika Benítez[1], Yair Krongold[1], and Arturo I. Gómez-Ruiz[3]

Received December 12 2023; accepted October 15 2024

ABSTRACT

Spectrum analysis at 3 mm of the central region ($r \approx 800$ pc) of NGC 4303 showed molecular gas lines of both dense gas tracers (HCN, HNC, HCO^+, and C_2H) and diffuse gases (^{13}CO and $C^{18}O$). Molecular gas parameters: H_2 mass $M_{H_2}=(1.75\pm0.32)\times10^8\,M_\odot$; radial velocity $V_{dense}=178\pm60\,km\,s^{-1}$, and $V_{CO}=151\pm29$ km s^{-1}; HCN luminosity $L_{HCN}=(7.38\pm1.40)\times10^6$ K km s^{-1} pc^2; dense gas mass $M_{dense}=(4.7\pm0.3)\times10^7\,M_\odot$, indicating a significant contribution of dense to total molecular gas mass. To explore the AGN nature and central dusty torus of the galaxy, CIGALE was used to fit the integrated spectral energy distribution. Large torus properties are estimated: luminosity $L_{TORUS}=(7.1\pm2.8)\times10^{43}\,erg\,s^{-1}$ and line of sight inclination of $67\pm16°$, which is consistent with a Type 2 AGN; total infrared luminosity $L_{IR}=(3.51\pm0.30)\times10^{44}\,erg\,s^{-1}$; star formation rate $SFR=6.0\pm0.3\,M_\odot\,yr^{-1}$. A marginal AGN contribution of $\approx$20% was found.

RESUMEN

El análisis del espectro a 3 mm de la región central ($r \approx 800$ pc) de NGC 4303, mostró líneas de trazadores de gas molecular denso HCN, HNC, HCO^+ y C_2H, y difuso ^{13}CO y $C^{18}O$. Se obtuvo: masa del H_2 $M_{H_2}=(1.75\pm0.32)\times10^8$ $M_\odot$; velocidad radial de gas denso $V_{dense}=178\pm60$ km s^{-1}, y gas difuso $V_{CO}=151\pm29\,km\,s^{-1}$ luminosidad de HCN $L_{HCN}=(7.38\pm1.40)\times10^6\,K\,km\,s^{-1}\,pc^2$, masa de gas denso $M_{dense}=(4.7\pm0.3)\times10^7\,M_\odot$, i. e., contribuye significativamente a la masa total del gas molecular; y abundancias de trazadores de gas denso. Se utilizó CIGALE para ajustar la distribución espectral de energía integrada y explorar la actividad y el toro de polvo central. Para el toro se obtuvo: luminosidad $L_{TORUS}=(7.1\pm2.8)\times10^{43}\,erg\,s^{-1}$ y ángulo de visión $67\pm16°$, i. e., AGN tipo 2; luminosidad total infrarroja $L_{IR}=(3.5\pm0.3)\times10^{44}\,erg\,s^{-1}$; tasa de formación estelar $SFR=6.0\pm0.3\,M_\odot\,yr^{-1}$. Se halló que la contribución del AGN es marginal, $\approx$20%.

Key Words: galaxies: active — galaxies: individual: NGC 4303 — galaxies: ISM — galaxies: molecular gas

1. INTRODUCTION

Molecular gas characterization of the few central kiloparsecs region of galaxies is important to understand how the gas is accreted into the supermassive black hole (SMBH), and the role of it in the host galaxy evolution (e.g. Costagliola et al. 2011; Jiménez-Donaire et al. 2019). The activity in the nuclei of galaxies (AGN) can be dominated by SMBH accretion or starburst (SB) processes, which have different physical and chemical properties that affect their interstellar medium (ISM).

In some AGN the obscuration of the nuclear region by dust and gas is parametrized by the neutral hydrogen column density N_H. Infrared and submillimeter observations are less susceptible to dust, especially in the 3 mm window, where the brightest emission lines such as HCN or HCO^+ trace dense molecular gas, whereas the ^{12}CO line traces diffuse gas. These lines have proven useful to understand the central ISM in nearby galaxies (for example,

[1]Instituto de Astronomía, Circuito Exterior, C. U., Universidad Nacional Autónoma de México, 04510 CdMx, México.
[2]Estancia Posdoctoral por México, CONAHCYT, Coordinación de Apoyos a Becarios e Investigadores.
[3]CONAHCYT-Instituto Nacional de Astrofísica Óptica y Electrónica, Luis E. Erro 1, 72840 Tonantzintla, Puebla, México.

Costagliola et al. 2011; Aladro et al. 2015). On the other hand, in the infrared the dust emission can be observed and studied using broad-band photometry.

Simultaneous observations of ^{12}CO isotopic varieties ^{13}CO and C^{18}O in galaxies are valuable for understanding the relationship between the bulk of molecular gas and its environment influenced by the SMBH accretion (e.g., García-Burillo 2016). In addition, these lines are crucial for deriving the gas mass that will be converted into stars.

Furthermore, observations of molecular dense gas tracers such as HCN, HNC, HCO$^+$, CS, and N$_2$H are valuable because their critical densities are of the same order as the molecular cloud cores, which are the star formation sites. Such studies base their analysis on the emission line ratios; for example, HCN/HCO$^+$ has been used as a discriminator between AGNs, segregating them into non-Seyfert galaxies (nuclear SB) or pure Seyfert (Sy) galaxies (Kohno 2003). Additionally, HCN/HCO$^+$ has been used as an indicator of the presence of AGNs, although this has been challenged several times without conclusive evidence (e.g., Costagliola et al. 2011; Privon et al. 2020). HCN/HNC has been used to characterize photon-dominated regions (PDRs) and X-ray dominated regions (XDRs) (e.g., Meijerink et al. 2007). In addition, both ratios show variations between different galaxy locations such as the center, disk, spiral arms and interarm regions in different studies (e.g., Bigiel et al. 2016; Jiménez-Donaire et al. 2019; Sorai et al. 2019; Morokuma-Matsui et al. 2020). Finally, the dense to diffuse gas ratio HCN/^{12}CO associated to star-forming regions is used as a proxy for the dense gas fraction, f_{dense}, as in Neumann et al. (2023).

In the study of dense gas tracers the HCN luminosity (L_{HCN}) can be converted to dense gas mass (M_{dense}), which has been linked by a tight correlation with the far-infrared luminosity, which is closely correlated to the star formation rate (SFR): $L_{HCN} \propto M_{dense} \propto L_{FIR} \propto SFR$ (see for example, Gao & Solomon 2004a; Jiménez-Donaire et al. 2019; Neumann et al. 2023). This relationship has been observed in individual molecular clouds in the Milky Way and in nearby galaxies (Wu et al. 2005; Graciá-Carpio et al. 2006; Bigiel et al. 2008; Wu et al. 2010; Usero et al. 2015; Bigiel et al. 2016; Jiménez-Donaire et al. 2019), and also in a few distant galaxies ($z \geq 1$). Before the work of Rybak et al. (2022) only two SF galaxies and three quasar hosts exhibited HCN emissions. These authors showed the difficulties of detecting HCN at z=2.5-3.3, but concluded that the HCN/FIR ratios found were consistent with normal starburst galaxies, but not with ultraluminous ones (c.f., their Figure 5).

Additional information about the properties of the gas in the central kiloparsecs of galaxies can be obtained studying other emission mechanisms that occur inside those spatial scales, such as AGNs. According to the Unified AGN model (see Antonucci 1993; Urry & Padovani 1995), the key to distinguish between Seyfert 1 and 2 galaxies is the existence of a dust structure surrounding the central engine that obscures the inner parts of the AGN on the line of sight (LOS). Based on its geometric shape this structure is called a dusty torus; however, different distributions have been proposed for dust, such as those in Fritz et al. (e.g., 2006); Nenkova et al. (e.g., 2008); Hönig & Kishimoto (e.g., 2017). The contribution of the dusty torus luminosity to the integrated spectral energy distribution (SED) could be estimated by an SED fitting analysis (e.g., Ciesla et al. 2015; Miyaji et al. 2019) which yields the dusty torus properties together with the galaxy continuum and line-emitting components, as well as the contribution of the AGN. As part of a study of nearby galaxies with obscured AGN, we analyzed the molecular gas spectra in the 3 mm band of the central region (1.6 kpc in diameter), of the galaxy NGC 4303 (M 61). NGC 4303 is a barred spiral in the Virgo supercluster at z =0.00522 (D_L = 16.99 Mpc; 1″=81 pc (Wright 2006)), with an inclination of 25° (Frei et al. 1996), classified as SAB(rs)bc (de Vaucouleurs et al. 1991). Its nuclear activity has been debated, as Huchra et al. (1982) classified it as a LINER, whereas Filippenko & Sargent (1985) as a Seyfert 2, which was confirmed by Veron-Cetty & Veron (1986) based on an equivalent width (EW) of [NII] of 400 km s^{-1}. Jiménez-Bailón et al. (2003) used Chandra images with a central radius of 3 pc and showed that in this X-ray region, both a core source (either an AGN or ultraluminous x-ray source) with a hydrogen column density $N_H \approx 1\times10^{20}$ cm^{-2}, and an annular starburst region of radius 3″, which is more obscured with $N_H \approx 5\times10^{21}$ cm^{-2}, coexist. The AGN characterization of NGC 4303 was confirmed using an infrared color-color diagram (Colina et al. 2015) and BPT diagrams (Malkan et al. 2017). Furthermore, Esparza-Arredondo et al. (2020) suggested that the nucleus is a candidate for the AGN fading phase.

The AGN contribution in NGC 4303 will be studied by analyzing the continuum emission from UV to far-infrared wavelengths. The dusty torus properties provide important parameters that complement the molecular gas characterization of the central 1.6 kpc region studied in this paper. Our aim is to obtain parameters of the interstellar medium in NGC 4303, such as the molecular gas mass, HCN gas luminosity, far-infrared luminosity and star formation rate.

The remainder of this paper is organized as follows: § 2 describes the observational details of the 3 mm band spectroscopy. § 3 presents the data reduction. An analysis of the molecular line emission spectra of NGC 4303 is described in § 4. The spectral energy distribution (SED) characterization to study the dusty torus and AGN contribution is presented in § 5. The discussion of results is given in § 6. A summary of the main conclusions and final remarks is presented in § 7. Throughout our work we adopt a cosmology where H_0=69.6 $\mathrm{km\,s^{-1}\,Mpc^{-1}}$, Ω_m=0.286 and Ω_λ =0.714 (Bennett et al. 2014).

2. OBSERVATIONS

Observations of NGC 4303 were obtained on June 28 and December 22, 2015, with the Redshift Search Receiver (RSR) on the Large Millimeter Telescope Alfonso Serrano (LMT), henceforth RSR/LMT, in its early science phase, which operated with a 32-m active surface. Observing conditions at the Volcán Sierra Negra site were good most of the time. During the observations the opacity at the Volcán Sierra Negra site at a frequency of 225 GHz was in the range of $\tau = 0.18$ - 0.19. The system temperature, T_{sys}, was between 85 and 110 K. Observations were centered on the coordinates of the galaxy nucleus (α_{2000}: 12^h:21^m:54^s.9, δ_{2000}: $+04^o$:$28'$:$25''$), with the OFF beam 39 arcsec apart. The pointing accuracy was better than $2''$. The total ON source integration time for NGC 4303 was 1 hr.

The RSR is an autocorrelator spectrometer with a monolithic microwave integrated circuit system that receives signals over four pixels, simultaneously covering the frequency range 73 to 111 GHz at $\Delta\nu = 31$ MHz spectral resolution, which corresponds to $\approx$100 $\mathrm{km\,s^{-1}}$ at 90 GHz (see Erickson et al. 2007). Hence, across the whole 3 mm band, the velocity resolution changes from 125 $\mathrm{km\,s^{-1}}$ to 85 $\mathrm{km\,s^{-1}}$. The RSR/LMT-32m has an angular resolution or beam full width at half-maximum (FWHM) that is also frequency dependent, ranging from 28 to 19 arc seconds, between the frequencies 73 and 111 GHz.

3. REDUCED SPECTRA

Autocorrelations, spectral co-adding, calibration, and baseline removal were performed using the *Data REduction and Analysis Methods in Python* (DREAMPY) software developed by Gopal Narayanan for the RSR. After removing integrations with unstable bandpass, the remaining spectra were averaged, weighted by the RMS noise in each individual spectrum. A simple linear baseline was removed in each spectral chassis, which covered a section of 6.5 GHz of the total RSR bandwidth after masking strong emission lines. To convert the antenna temperature (T_A) units to flux units (Jy), we used a conversion factor G, the gain of the LMT-32m, given by

$$G(\nu) = 7\left(\frac{\nu\,[GHz]}{100\,[GHz]}\right)[Jy\,K^{-1}]. \quad (1)$$

The spectral reduction last step was to obtain the main beam temperature (T_{mb}). To convert antenna temperature to T_{mb}, we divided the spectrum by the main beam efficiency (η_{mb})

$$\eta_{mb} = \left(1.2\,\exp(\nu/170)^2\right)^{-1}, \quad (2)$$

where ν denotes the sky frequency of the observed line. Equation (2), was obtained from calibration observations performed in June and December 2015. Details of the RSR/LMT data reduction can be found in several studies, for example Snell et al. (2011); Lee et al. (2014); Yun et al. (2015); Cybulski et al. (2016).

The RSR covers a frequency range of 84 - 111 GHz in the rest frame of NGC 4303. The entire RSR spectrum is shown in Figure 1, together with the identified lines. The RMS of the spectrum varies slightly across the frequency band from 0.618 mK at the low-frequency end (ν > 92 GHz) to 0.854 mK at the high-frequency end. Several molecular spectral lines are clearly detected in this spectrum. Using a 3σ detection threshold on the line integrated intensity and rest frequencies from the *Splatalogue*[4], we detected seven spectral lines: C_2H at 87.31 GHz N=1–0, which is a blend of 6 lines: J=3/2-1/2 (F=1-1, 2-1, 1-0) and J=1/2-1/2 (F=1-1, 0-1, 1-0); HCN(1-0), HCO^+(1-0), HNC(1-0), CS(2-1), $C^{18}O$(1-0), and ^{13}CO(1-0) at 88.63, 89.18, 90.66, 109.78 and 110.20GHz, respectively, and the possible detection of three additional lines: N_2H^+ at 93.17 GHz, NH_2CN at 99.75 GHz and ^{13}CN at 108.65 GHz.

We note that the OFF beam position of the RSR/LMT observations falls within the main body of the galaxy; however, after careful inspection of the reduced data, we found that the ^{13}CO(1-0) spectra do not exhibit an absorption feature, which would appear if the 39 arcsec OFF beam were affected by the OFF galaxy emission. Contamination from the galaxy in the OFF position would be produced

[4] `https://splatalogue.online/#/home`.

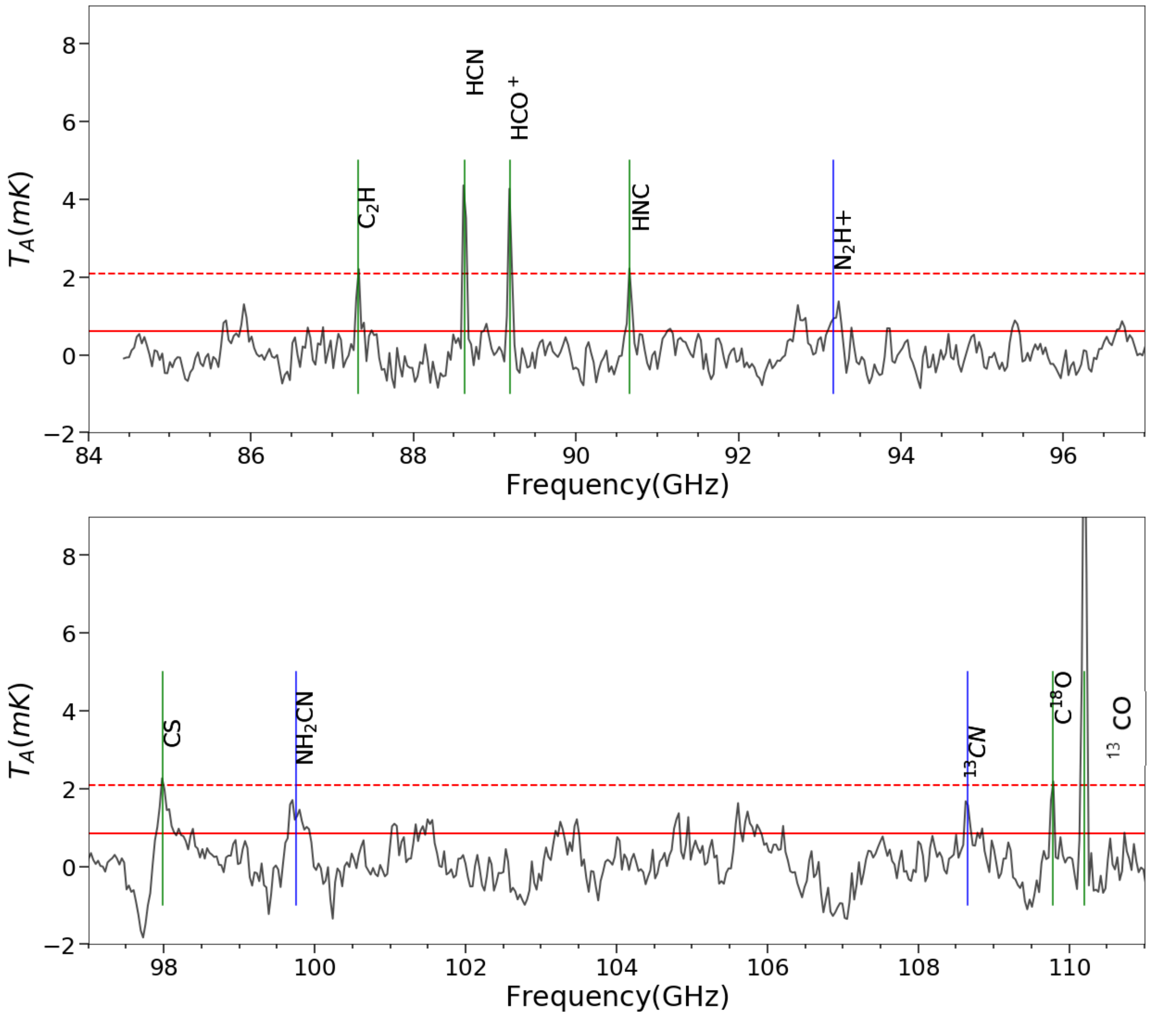

Fig. 1. NGC 4303 rest-frame spectra from 84 to 111 GHz obtained with the Redshift Search Receiver (RSR/LMT). The vertical color lines indicate the likely frequencies of some molecular transitions. The red solid line indicates the root mean square (RMS) value in each panel. The red dashed line represents the value of 3σ. Note that the detected transitions, vertical green lines, are detections of C_2H, HCN, HCO^+, HNC, CS(2-1), $C^{18}O$, and ^{13}CO, whereas the possible detections, vertical blue lines, are N_2H^+, NH_2CN and ^{13}CN (see Table 1). The color figure can be viewed online.

by faint CO emission in the spiral arms or interarm regions, c.f., PHANGS-ALMA CO(2-1) image of NGC 4303 in Leroy et al. (2021) and would affect all lines, dense and diffuse. This is not found in any of the lines detected, so contamination, if present, is small.

4. ANALYSIS

4.1. *Molecular Gas*

Seven molecular lines were measured to have integrated line intensity with $S/N > 3$, but CS(2-1) which shows a drop at the low-frequency end, was considered a marginal detection, and so is not included in the line analysis. For each line, a single Gaussian fit was performed to obtain the integrated intensity, calculated in a range of -250 to $+250\,\mathrm{km\,s^{-1}}$, centered on their rest frequencies. The error was computed using the covariance matrix of the fit. The FWHM and peak intensities were obtained using fitting parameters. Individual plots of the detected lines are shown in Figure 2 and the derived parameters are listed in Table 1.

The most intense line is $^{13}CO(1\text{-}0)$ followed by HCN, HCO^+ and HNC. In a previous study on molecular gas in NGC 4303, Yajima et al. (2019) detected integrated intensities similar to those re-

TABLE 1

MOLECULAR LINE TRANSITIONS DETECTED IN NGC 4303

Molecule	Frequency[b] (GHz)	Integrated Flux (K km s^{-1})	Δv[c] (km s^{-1})	Peak Intensity[d] (mK)
(1)	(2)	(3)	(4)	(5)
C_2H(1-0)	87.31	0.77±0.03	192±38	3.47±0.96
HCN(1-0)	88.63	1.55±0.11	138±59	9.28±0.97
HCO^+(1-0)	89.18	1.41±0.09	171±73	6.98±0.97
HNC(1-0)	90.66	0.90±0.04	225±48	3.47±0.98
CS(2-1)[a]	97.98	<2.03±0.68[e]	–	–
$C^{18}O$(1-0)	109.78	0.77±0.04	146±28	4.37±1.54
^{13}CO(1-0)	110.20	4.53±0.26	155±29	24.45±1.55

Notes:

[a]Possible detection.

[b]Rest frequencies, obtained from the Splatalogue database at https://splatalogue.online/#/home.

[c]FWHM in velocity units.

[d]Peak intensity of main beam temperature (T_{MB}).

[e]Upper limit; because line has a blue absorption feature the integrated flux and error are large (see Figure 1).

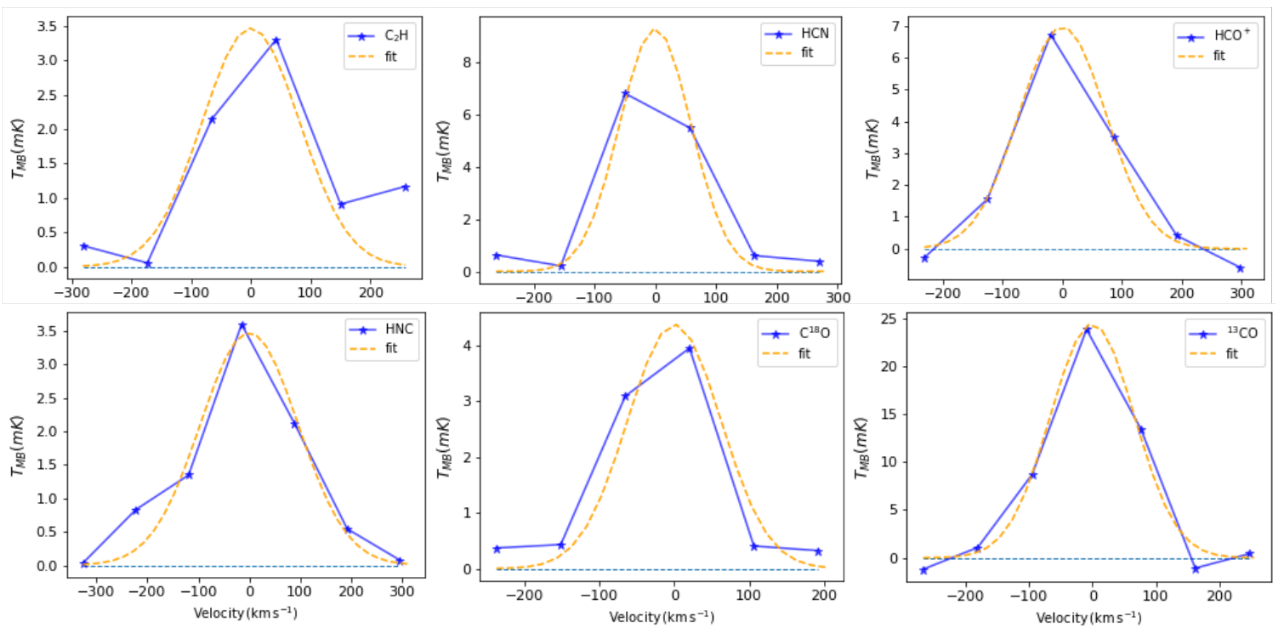

Fig. 2. Observed (blue) molecular lines with $S/N > 3$ of NGC 4303 and their Gaussian fits (orange dashed lines). We detected dense gas tracers as well as ^{12}CO isotopic varieties. From left to right the molecular lines are as follows: (top row) C^2H, HCN, HCO^+; (bottom row) HNC, $C^{18}O$ and ^{13}CO. The color figure can be viewed online.

ported here for ^{12}CO(1-0) and ^{13}CO(1-0) using the Nobeyama 45 m radio telescope, but they were not able to detect $C^{18}O$(1-0). Also, Li et al. (2021) detected the same dense gas tracer lines (HCN, HCO^+, HNC) with the IRAM 30 m and reported integrated measurements similar to those of this work.

In the following steps, we calculate the mass of the dense molecular gas in the central 1.6 kpc. First, with a combination of optically thin and thick lines, optical depth can be derived. Then, we calculate the column density to finally use it in the calculation of the molecular gas mass. Following Jiménez-

Donaire et al. (2017), and assuming local thermodynamic equilibrium (LTE), solar abundances and a given excitation temperature in a cloud, the optical depth (τ_{13}) for ^{13}CO can be calculated from the integrated intensities of ^{12}CO and ^{13}CO, I_{12} and I_{13}, respectively. Assuming the beam-filling factor of each line to be the same in the equation of radiative transfer, the optical depth is:

$$\tau_{13} = -\ln\left[1 - \frac{I_{13}}{I_{12}}\right]. \tag{3}$$

Because ^{12}CO in NGC 4303 cannot be detected in the frequency range of our observations, we used the value $I_{12} = 55.2 \pm 5.5$ K km s^{-1} obtained with the EMIR spectrograph at the IRAM 30m telescope (FWHM beam size 22″) reported by Israel (2020) and I_{13} derived from our spectra[5]. Using the values in equation (3) yields $\tau_{13} = 0.09 \pm 0.01$, that is, an optically thin line. For ^{12}CO, the optical depth is calculated by multiplying τ_{13} by the relative solar abundance[6] [^{12}CO/^{13}CO] = 89 (Wilson & Rood 1994), which yields $\tau_{12} = 7.12 \pm 0.89$; that is, the ^{12}CO line is optically thick.

Now, we used the integrated intensity I_{13} and τ_{13} to obtain the column density N_{13}. Equation (4) is the result of using the radiative transfer equation to calculate the number of molecules of ^{13}CO over a path length (see equation 1.7 in Jiménez-Donaire 2017):

$$\left[\frac{N_{13}}{cm^{-2}}\right] = 3 \times 10^{14} \left[\frac{I_{13}}{K\,km\,s^{-1}}\right] \left[\frac{1}{1-e^{-\tau_{13}}}\right] \frac{\tau_{13}}{1-e^{-5.29/T_{ex}}}. \tag{4}$$

Three excitation temperature (T_{ex}) values commonly found in dense molecular clouds, 10, 20 and 30 K, are assumed in equation (4) for the subsequent calculations.

To obtain the mass of H_2, it was necessary to convert N_{13} to $N(H_2)$ using the following equation:

$$\left[\frac{N(H_2)}{cm^{-2}}\right] = \left[\frac{H_2}{^{13}CO}\right] \left[\frac{N_{13}}{cm^{-2}}\right], \tag{5}$$

where the relative abundance was [H_2/^{13}CO] = 588,235 (Dickman 1978). Finally, the H_2 mass was obtained from equation (6) assuming a spherical cloud with a diameter calculated for

[5] The difference in beam size of 3″ between the two telescopes is small, and might not strongly affect the LMT value of I_{13} used, also it is unlikely that $\tau_{13} > 1$.

[6] This is the value that most studies assume, but it can vary by a factor of 4.5 between galaxy centers, the local ISM or the solar system.

TABLE 2

COLUMN DENSITIES OF ^{13}CO AND H_2 AND $M(H_2)$

T_{ex} [K]	N_{13} [$\times 10^{15}$cm^{-2}]	$N(H_2)$ [$\times 10^{21}$cm^{-2}]	$M(H_2)^*$ [$\times 10^7 M_\odot$]
10	3.44 ± 0.63	2.02 ± 0.37	6.88 ± 1.26
20	6.08 ± 1.11	3.58 ± 0.65	12.17 ± 2.23
30	8.74 ± 1.60	5.14 ± 0.94	17.50 ± 3.20

Note: $^*M(H_2)$ was calculated from equation (6).

the telescope main beam, which for the ^{13}CO line is 20″, which at the distance of NGC 4303 corresponds to a diameter d = 1.647 kpc; m_{H_2} is the molecular mass of H_2,

$$M(H_2) = \frac{\pi d^2}{4} N(H_2)\, m_{H_2}. \tag{6}$$

The derived parameters for NGC 4303 are presented in Table 2, which includes the column densities N_{13}, $N(H_2)$ and mass $M(H_2)$ for the three values of T_{ex}.

To obtain the total molecular gas mass (M_{mol}), the contribution of molecular helium to molecular hydrogen must be included in the relationship $M_{mol} \approx 1.36\ M(H_2)$ from Teng et al. (2022). Therefore, for T_{ex} = 30 K we obtain $M_{mol} = (2.38 \pm 0.43) \times 10^8$ M$_\odot$. To derive the amount of gas in the observed region, we calculated the surface density of the molecular gas (Σ_{mol}), which is the mass of H_2 per square parsecs area. Taking M_{mol} and the equivalent area of a circle of 1647 pc in diameter, the total surface density of molecular gas is $\Sigma_{mol} = 112 \pm 20$ M$_\odot$ pc^{-2}.

Using the same procedure as described above, we obtained the total molecular gas mass and surface density of the molecular gas for T_{ex} = 10 K, that is, $M_{mol} = (9.35 \pm 1.71) \times 10^7$ M$_\odot$ and $\Sigma_{mol} = 46.5 \pm 8.5$ M$_\odot$ pc^{-2}. Within this range of possible values of T_{ex}, Σ_{mol} varies by a factor of 2.

Usero et al. (2015) calculated the surface density of molecular gas from the intensity of ^{12}CO using the following equation:

$$\Sigma_{mol}[M_\odot\, pc^{-2}] = \alpha_{CO}\, I_{12} \cos(i), \tag{7}$$

where i is the inclination of the galaxy, and α_{CO} is the conversion factor of ^{12}CO to molecular gas mass with an adopted value of 4.4 M$_\odot$pc^{-2}(K km s^{-1})$^{-1}$ (including the 1.36 factor for helium), with a ±30% uncertainty given by Bolatto et al. (2013). Using I_{12} from literature, we obtain $\Sigma_{mol} = 220 \pm 79$ M$_\odot$ pc^{-2}.

Analogously, we calculated the surface density of the dense molecular gas traced by the HCN line using the equation:

$$\Sigma_{dense}[M_\odot\, pc^{-2}] = \alpha_{HCN}\, I_{HCN} \cos(i), \quad (8)$$

where $\alpha_{HCN} = 10$ $M_\odot$ pc^{-2} (K km $s^{-1})^{-1}$, proposed by Gao & Solomon (2004b) is a typical upper limit for spiral galaxies[7]. The result is Σ_{dense}=14±1 $M_\odot$ pc^{-2}.

We calculate the dense gas mass as traced by HCN, M_{dense}, by multiplying Σ_{dense} by the area of the telescope's main beam, with a diameter of 25″ for the HCN line. The result is: $M_{dense} = (4.7 \pm 0.3) \times 10^7$ $M_\odot$.

Finally, with Σ_{dense} and Σ_{mol} for $T_{ex} = 30$ K, we can calculate the dense molecular fraction (f_{dense}) in the observed region as:

$$f_{dense} = \frac{\Sigma_{dense}}{\Sigma_{mol}} = 0.13 \pm 0.06\,. \quad (9)$$

4.2. *Luminosities*

Gao & Solomon (2004b) calculated the luminosity of an extended source with a size larger than the main beam of the telescope. Because the galaxy is not mapped along the major axis, it is considered a source with a size equal to or smaller than the telescope's main beam. The calculation is given by:

$$L'_{HCN}\,[K\, km\, s^{-1}\, pc^2] \approx \Omega_{mb}\, I_{HCN}\, D_L^2\, (1+z)^{-3}, \quad (10)$$

where Ω_{mb} is the solid angle of the main beam, D_L(pc) is the luminosity distance, I_{HCN} is the integrated HCN line intensity and z is the redshift. We can rewrite Ω_{mb} in terms of the antenna parameters, that is, the FWHM of the main beam $\theta_{\rm FHWM}$ (in radians) and obtain the HCN luminosity as

$$L'_{HCN}\,[K\, km\, s^{-1}\, pc^2] \approx \frac{\pi}{4\, ln(2)} \theta^2_{\rm FHWM}\, I_{HCN}\, D_L^2\, (1+z)^{-3}. \quad (11)$$

We then calculate the luminosity of the dense gas tracers substituting the integrated intensities of this work, e.g., HCN by HCO^+ and the corresponding values of $\theta_{\rm FHWM}$ at the observing frequency, ≈25″ for the dense gas tracers and 20″ for ^{13}CO (see Table 3).

[7]Leroy et al. (2017) reported an extensive analysis of the use of millimeter-wave emission line ratios to trace molecular gas density. In the dense gas conversion factors, they considered a range of densities for the models as well as the distribution of widths and temperatures.

TABLE 3

LUMINOSITIES FOR DIFFUSE AND DENSE GAS EMISSION LINES IN NGC 4303

Line	L_{gas} $\times 10^6$ [K km s^{-1} pc^2]	$\log(L_{gas})$ [K km s^{-1} pc^2]
^{13}CO	9.60 ± 3.90	6.98 ± 0.09
C_2H	3.78 ± 0.68	6.58 ± 0.07
HCN	7.38 ± 1.40	6.87 ± 0.08
HCO^+	6.63 ± 1.24	6.82 ± 0.08
HNC	4.09 ± 0.75	6.61 ± 0.08
Total dense	21.88 ± 4.07	7.34 ± 0.08

If we use the mass-luminosity conversion factor defined as $\alpha_{^{13}CO}$ with units $M_\odot$ pc^{-2} (K km $s^{-1})^{-1}$, we can rewrite the Solomon relation (Solomon et al. 1997) as $M(H_2) = \alpha_{^{13}CO}\, L'_{13}$ or

$$\alpha_{^{13}CO} = \frac{\Sigma_{H_2}}{I_{13}}. \quad (12)$$

Using the previously calculated data for $M(H_2)$, Σ_{H_2} $=82 \pm 15$ $M_\odot$ pc^{-2} and equation (12), we calculated both the factor $\alpha_{^{13}CO}$ and the ^{13}CO luminosity, obtaining $\alpha_{^{13}CO} = (18.2 \pm 4.4)\, M_\odot\, pc^{-2}\, (K\, km\, s^{-1})^{-1}$ and $L'_{13} = (9.6 \pm 3.9) \times 10^6\, K\, km\, s^{-1}\, pc^2$. The ^{12}CO luminosity was calculated with equation (7) and the FWHM of 22″ of the observed line, which results in $L'_{12} = 1.29 \times 10^8\, K\, km\, s^{-1}\, pc^2$.

To estimate the abundance of molecular gas in the nuclear obscured region, we used the integrated intensity of the different emission lines of dense gas tracers (C_2H, HCN, HNC and HCO^+), diffuse gas tracers (^{13}CO, $C^{18}O$) and ^{12}CO integrated intensity $I_{12} = 55.2 \pm 5.5$ K km s^{-1} (Israel 2020) to calculate their line ratios (Table 4).

4.3. *Dusty Torus, SFR and AGN Contribution to the SED*

As mentioned in § 1, previous multiwavelength studies confirmed that the nuclear activity of NGC 4303 is influenced by an accreting SMBH (Filippenko & Sargent 1985; Veron-Cetty & Veron 1986; Malkan et al. 2017; Colina et al. 2015), classifying it as Sy 2 (Véron-Cetty & Véron 2006). In this work we are also interested in the physical properties of NGC 4303, mainly the star formation rate (SFR), in order to compare the values derived here with those from the literature. A good tool to achieve this task is integrated spectral energy distribution (SED) fitting analysis, which includes an AGN component. Interestingly, this complementary analysis allows us

DOI: https://doi.org/10.22201/ia.01851101p.2025.61.01.05

TABLE 4

ABUNDANCES OF DENSE GAS RELATIVE TO DIFFUSE AND DENSE GAS TRACERS

Ratio*	Value
C_2H / $C^{18}O$	1.01 ± 0.07
HCN/ $C^{18}O$	2.01 ± 0.18
HCO^+/ $C^{18}O$	1.83 ± 0.15
HNC / $C^{18}O$	1.17 ± 0.08
CS / $C^{18}O$	2.67 ± 0.19
^{13}CO/ $C^{18}O$	5.88 ± 0.46
HCN / ^{12}CO	0.028 ± 0.002
HCO^+ / ^{12}CO	0.025 ± 0.003
HNC / ^{12}CO	0.016 ± 0.003
^{13}CO / ^{12}CO	0.082 ± 0.010
$C^{18}O$ / ^{12}CO	0.013 ± 0.002
HNC/ HCN	0.58 ± 0.04
HCO^+ / HCN	0.91 ± 0.08
C_2H / HCN	0.38 ± 0.04

Note: * For ^{12}CO we used $I_{12} = 55.2 \pm 5.5$ K km s^{-1} (Israel 2020).

to obtain not only the galactic properties but also the AGN properties, including dusty torus characteristics. All these properties are useful for follow-up studies.

For this purpose, we used the Code Investigating GALaxy Evolution , called CIGALE, developed by Boquien et al. (2019), which allows fitting the SED of galaxies using different models for the relevant physical components. For instance, it is possible to select from different star-forming history models, stellar populations, initial mass functions, attenuation laws, dust emissions and AGN models. The different components are fitted to preserve the energy balance principle, which means that the energy absorbed at UV and optical wavelengths is re-emitted at infrared wavelengths. To select the best fit, CIGALE performs a minimization of the χ^2 statistics and a Bayesian analysis to determine the probability distribution of the physical parameters obtained from the fits.

We searched for photometric data of NGC 4303 in the literature, using the VizieR photometry tool[8], which allows visualization of photometric points extracted from catalogues in ViZieR around a sky position. We used a default search radius of 5″ centered on NGC 4303, which is small enough to consider data truly corresponding to the emission of the galaxy; we found multi-wavelength observations at UV, optical, infrared and sub-millimeter wavelengths (see Table 5). According to de Vaucouleurs et al. (1991), the isophotal dimensions (R_{25}) of NGC 4303 are 6.′46±0.′15 and 5.′75±0.′27, for the major and minor axes, respectively. This means that all the observations retrieved form the literature include the total emission of the galaxy.

The UV data consist of Galaxy Evolution Explorer (GALEX; Martin et al. 2005) observations in the far-ultraviolet (FUV; $\lambda_{\rm eff} = 0.153$ μm) and near-ultraviolet (NUV; $\lambda_{\rm eff} = 0.231$ μm) bands with an angular resolution of 5.″3 and a 1.°2 field of view (FOV), taken from Cortese et al. (2012). The optical data consist of observations from the Sloan Digital Sky Survey Data Release 7 (SDSS-DR7; Abazajian et al. 2009) in the five bands *u, g, r, i* and *z*, taken from Kim et al. (2014). These data have an angular resolution of ≤ 1.″5, and a 3° FOV. In the IR regime we compiled data from different sources: the Two Micron All Sky Survey (2MASS; Skrutskie et al. 2006), the Spitzer Space Telescope (Werner et al. 2004), the Infrared Astronomical Satellite (IRAS; Neugebauer et al. 1984), the Wide-field Infrared Survey Explorer (WISE; Wright et al. 2010), and the Herschel Space Telescope (Pilbratt et al. 2010). In the case of 2MASS data, we used photometry in the J (1.2 μm), H (1.6 μm) and K (2.2 μm) bands from Bai et al. (2015), Dalya et al. (2016) and Stassun (2019), respectively, all of them with an angular resolution of 2″ and a 8.°5 FOV. In the case of Spitzer data, we considered observations obtained with the InfraRed Array Camera (IRAC; Fazio et al. 2004) in the IRAC1 (3.6 μm), and IRAC2 (4.5 μm) bands from Sheth et al. (2010), and IRAC4 (8 μm) band from Ciesla et al. (2014). These data have resolutions of 1.″7, 1.″6, 1.″9, respectively, with a 5′ FOV for IRAC1 and IRAC2 bands, and 5.′2×5.′2 for IRAC4. In the case of IRAS data, we used the photometry in the 12 μm band from Moustakas & Kennicutt (2006), in the 25 and 60 μm bands from Rahman et al. (2006), and in the 100 μm band from Yun et al. (2001), with a resolution of 0.′5, 0.′5, 1.′0 and 2.′0, respectively, and a common 63.′6 FOV. We also considered data in the MIPS 24 and 160 μm bands from Bendo et al. (2012), whose angular resolution is 6″ with a 5.′4 × 5.′4 FOV. From WISE, we used observations in the W1 (3.4 μm) and W2 (4.6 μm) bands from Stassun (2019), the W3 (12 μm) band from Ciesla et al. (2014), and the W4 (22 μm) band from Boselli et al. (2014). These data have angular resolution of 6.″1, 6.″4, 6.″5, 12.″0, respectively,

[8] `http://vizier.cds.unistra.fr/vizier/sed/doc/`.

DOI: https://doi.org/10.22201/ia.01851101p.2025.61.01.05

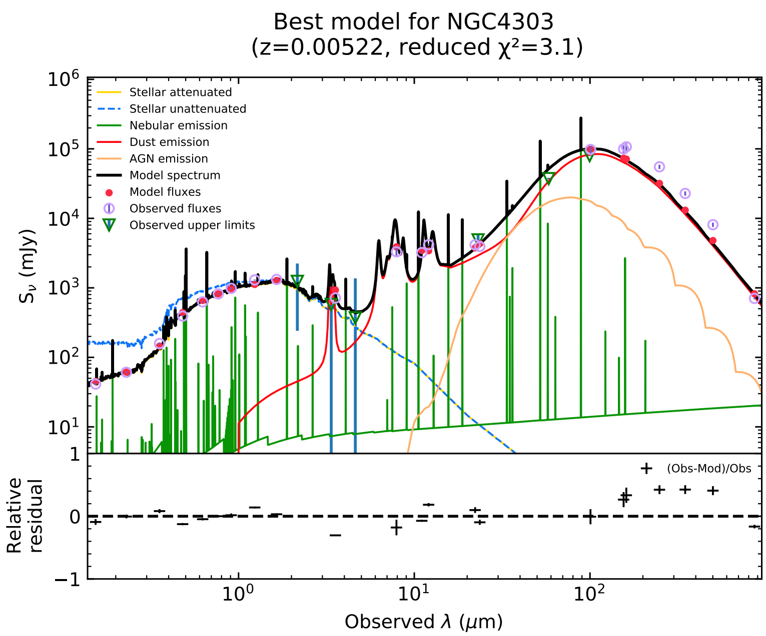

Fig. 3. The best SED model fit for NGC 4303 using CIGALE. Shown are the observed fluxes (purple circles), model fluxes (red dots), total model (black line), unattenuated stellar emission (blue line), attenuated stellar contribution (yellow line), nebular emission (green line), dust emission (red line) and AGN emission (orange line). The bottom panel shows the residuals of the observed to the model fluxes. The color figure can be viewed online.

and a common 47′ FOV. In the case of Herschel data, we used observations obtained with the Photodetector Array Camera and Spectrometer (PACS; Poglitsch et al. 2010), in the 100 μm (PACSgreen) and 160 μm (PACSred) bands with angular resolution of 8″ and 13″, respectively, and a 3′.5×1′.75 FOV, as well as the Spectral and Photometric Imaging Receiver (SPIRE; Griffin et al. 2010), in the 250 μm (PSW), 350 μm (PMW) and 500 μm (PLW) bands with angular resolutions of 18″, 25″ and 36″, and a 8′.0×4′.0 FOV. PACS data were collected from Auld et al. (2013), whereas the SPIRE data were collected from Chen et al. (2018). Finally, we used observations taken with the Submillimeter Common-User Bolometer Array (SCUBA; Holland et al. 1999) instrument on the James Clerk Maxwell Telescope (JCMT). These observations in the 850 μm band were taken from Di Francesco et al. (2008) having an angular resolution of 22″.9 and a 2′.3 FOV.

We fitted the SED of NGC 4303 using typical choices of the components to fit galaxies harbouring an AGN (e.g. Wang et al. 2020; Santos et al. 2021), a delayed star formation history with an optional exponential burst, and stellar populations model by Bruzual & Charlot (2003) using the `sfhdelayed` module with a Chabrier (2003) initial mass function (`bc03`). We considered nebular emission to account for any Lyman continuum emission (`nebular`). The attenuation law (`dustatt_modified_starburst`) is that of Calzetti et al. (2000), whereas the dust emission was modeled using Jones et al. (2017) models (`themis`). For the AGN component we used the CLUMPY[9] models through the `nenkova2008` module, which considers the emission from a clumpy torus (Nenkova et al. 2008a,b). This latter module has recently been used successfully in other SED fitting studies of AGNs given its flexibility regarding the geometrical parameters of the torus (Miyaji et al. 2019; Yamada et al. 2023). Each of the aforementioned modules, corresponding to the physical components, has its own parameters that can take several values to form the grid of models to be fitted to the SED. The physical components, corresponding modules, parameters, and values adopted in this analysis are listed in Table 6.

In Figure 3 we present the best fit for the NGC 4303 SED. The observed fluxes (purple circles), model fluxes (red circles), and total model (black line) are shown. The different physical components used were as follows: the stellar component before (yellow line) and after attenuation (blue dashed line), dust emission (red line), nebular emission (green lines), and AGN component (ap apri-

[9]`https://clumpy.org/`.

cot line). The flux residuals in each band are shown in the bottom panel and are calculated as $(S_{\nu,\rm obs} - S_{\nu,\rm model})/S_{\nu,\rm obs}$. The reduced χ^2 of the fit was 3.1.

Regarding the geometrical parameters of the clumpy dusty torus obtained with the best fit and the Bayesian analysis values (in parenthesis), we obtained a thick torus given its aperture above the equatorial plane `op_angle` = 60° (56°±9°), a large optical depth `tau_V`=200 (184±38), a large number of clouds along the equatorial plane `N_0`=15 (14±2), and an inner to outer radius ratio of `Y_ratio`=100 (97±12). The power of the radial distribution of clouds ($\propto r^{-q}$) is q=0.0 (0.12±0.29) and the viewing angle is `incl`=80° (67°±16°). Considering the classical unified AGN model (Antonucci 1993; Urry & Padovani 1995) this viewing angle is in agreement with the Sy 2 classification of Véron-Cetty & Véron (2006).

The total AGN and torus luminosities of the best fit and the Bayesian analysis values (in parenthesis) are $L_{\rm AGN} = 1.5\times10^{44}$ erg s^{-1} [$(1.5 \pm 0.6)\times10^{44}$ erg s^{-1}], $L_{\rm TORUS} = 6.975\times10^{43}$ erg s^{-1} [$(7.1 \pm 2.8)\times10^{43}$ erg s^{-1}], while the galaxy dust luminosity is $L_{\rm DUST} = 2.8\times10^{44}$ erg s^{-1} [$(2.8 \pm 0.1)\times10^{44}$ erg s^{-1}], and the total IR luminosity is 3.5×10^{44} erg s^{-1} $(3.51 \pm 0.30)\times10^{44}$ erg s^{-1}. Another important quantity derived from CIGALE is the star formation rate, which in this case is $SFR = 6.014$ M$_\odot$ yr^{-1} (5.969± 0.298 M$_\odot$ yr^{-1}). The parameters derived from CIGALE are presented in Table 7.

5. DISCUSSION

5.1. *Dense and Diffuse Gas Masses and Kinematics*

The molecular hydrogen mass obtained for the telescope's main beam center in the ^{13}CO line can be compared with that found by Schinnerer et al. (2002) in a high spatial resolution study (≈ 150 pc) of gas traced by the ^{12}CO (J=1-0) line made with the *Owens Valley Radio Observatory* (OVRO). As can be seen in Figure 4, the molecular gas emission is found in two lanes: the western gas lane (LW) and the eastern gas lane (LE), both curving towards the nucleus (N). It was found that the central 8″ (≈ 630 pc) concentrates a mass $M(H_2) \approx 7\times10^7$ M$_\odot$. Their estimation used the conversion factor α_{CO}= 4.36 M$_\odot$ pc^{-2}(K km s^{-1})$^{-1}$ from Strong et al. (1988), with a ±30% uncertainty. In addition, the southern component of LW and the north component of LE that extend to an area of ≈22″×22″, concentrate almost twice the value of the nuclear disk or central 8″ mass, see Table 3 in Schinnerer et al. (2002). Consequently this yields a total central molecular mass $M(H_2) \approx 1.81\times10^8$ M$_\odot$.

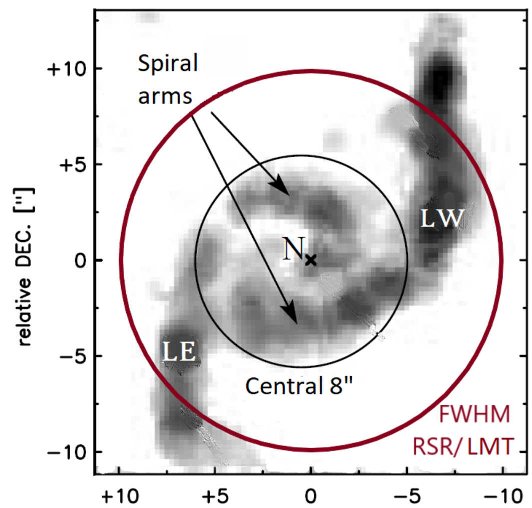

Fig. 4. A high spatial resolution (≈150 pc) map of the center of NGC 4303 observed with OVRO in the ^{12}CO (1-0) line obtained by Schinnerer et al. (2002) covering 22″×22″. The center (black circle) has a diameter of 8″, and the red circle is an RSR/LMT region of 20″which represents the LMT main beam for the ^{13}CO frequency. The bulk of molecular gas in this region obtained by Schinnerer et al. (2002) was compared with that obtained in our study using the ^{13}CO line. The color figure can be viewed online.

If we use instead the integrated intensity of the ^{12}CO (J=1-0) line obtained from the literature (Israel 2020), the molecular mass associated with this line derived from Σ_{mol} = 220 ± 79 M$_\odot$ pc^{-2} (see §4.1), for an area with a diameter of 22″ (≈1.8 kpc) is (5.7 ± 2.0) × 10^8 M$_\odot$. Using the same conversion factor α_{CO} in both calculations, the factor of 3 difference in both masses could be due to the spatial resolution with which the observations were made, a beam of ≈150 pc vs. ≈1.8 kpc. In the second case, assuming a constant beam filling factor overestimates the amount of emission within the observed area.

In this study, the calculated molecular H_2 mass was $M(H_2)$=(1.75±0.32)×10^8 M$_\odot$, which is in good agreement with the value reported by Schinnerer et al. (2002). We note that although the RSR/LMT observed region (the circle of 20″≈1.6 kpc of diameter) does not completely cover the arms as shown in Figure 4, most of the molecular gas is concentrated in the central region, which explains the similar values. Schinnerer's work covers a slightly larger area than the one presented here, so to properly compare $M(H_2)$, we consider the value from Schinnerer et al. (2002) presented above as an upper limit.

TABLE 5

PHOTOMETRY USED IN THE SED FITTING WITH CIGALE

Band	$\lambda_{\rm eff}$ (μm)	Flux† (mJy)	Telescope/Instrument or Survey	Res. †† ($''$)	FOV ($'$)	Ref.
FUV	0.153	41.3±1.9	GALEX	5.3	72.0	1
NUV	0.231	61.0±1.7	GALEX	5.3	72.0	1
u	0.352	158.0±5.0	SDSS	≤ 1.5	180.0	2
g	0.482	392.0±7.0	SDSS	≤ 1.5	180.0	2
r	0.625	628.0±12.0	SDSS	≤ 1.5	180.0	2
i	0.763	819.0±15.0	SDSS	≤ 1.5	180.0	2
z	0.902	982.0±28.0	SDSS	≤ 1.5	180.0	2
J	1.2	1300.0±20.0	2MASS	2.0	8.5	3
H	1.6	1320.0±20.0	2MASS	2.0	8.5	4
Ks	2.2	1240.0±-999.0	2MASS	2.0	8.5	5
W1	3.35	578.0±-999.0	WISE	6.1	47.0	5
IRAC1	3.6	714.0±1.0	Spitzer/IRAC	1.7	5.0	6
IRAC2	4.5	479.0±1.0	Spitzer/IRAC	1.6	5.0	6
W2	4.60	370.0±-999.0	WISE	6.4	47.0	5
IRAC4	8.0	3300.0±410.0	Spitzer/IRAC	1.9	5.2×5.2	7
W3	12	4180.0±110.0	WISE	6.5	47.0	7
IRAS1	12	3210.0±50.0	IRAS	30.0	63.6	8
W4	22	4160.0±190.0	WISE	12.0	47.0	9
MIPS24	24	3940.0±160.0	Spitzer/MIPS	6.0	5.4×5.4	10
IRAS2	25	4900.0±-999.0	IRAS	30.0	63.6	11
IRAS3	60	37300.0±-999.0	IRAS	60.0	63.6	11
PACSgreen	100	97900.0±11800.0	Herschel/PACS	8.0	3.5×1.75	12
IRAS4	100	79700.0±-999.0	IRAS	120.0	63.6	13
MIPS160	160	99800.0±12000.0	Spitzer/MIPS	38.0	2.1×5.3	10
PACSred	160	107000.0±13000.0	Herschel/PACS	13.0	3.5×1.75	12
PWS	250	55200.0±3900.0	Herschel/SPIRE	18.0	8.0×4.0	14
PWM	350	22800.0±1600.0	Herschel/SPIRE	25.0	8.0×4.0	14
PWL	500	8100.0±580.0	Herschel/SPIRE	36.0	8.0×4.0	14
SCUBA2	850	705.0±20.0	JCMT/SCUBA	22.9	2.3	15

REFERENCES: (1) Cortese et al. (2012); (2) Kim et al. (2014); (3) Bai et al. (2015); (4) Dalya et al. (2016); (5) Stassun (2019): (6) Sheth et al. (2010); (7) Ciesla et al. (2014); (8) Moustakas & Kennicutt (2006); (9) Boselli et al. (2014); (10) Bendo et al. (2012); (11) Rahman et al. (2006); (12) Auld et al. (2013); (13) Yun et al. (2001); (14) Chen et al. (2018); (15) Di Francesco et al. (2008).

†The flux data without error estimates (-999.0) are taken as upper limits in the SED fitting analysis (green upside down triangles in Figure 3).

††Telescope resolution.

As we saw in the previous section, the $M(H_2)$ value obtained with ^{12}CO and equation (7) is three times the value obtained with ^{13}CO. This difference may be due to the conversion factor α_{CO}, although in many studies it is assumed to be a constant value across various scales, and environments, recent studies have found variations of 1-2 orders of magnitude that depend on the physical properties of the medium. Teng et al. (2023) observed the central ≈2 kpc region of two barred spiral galaxies at ≈100 pc resolution with ^{12}CO and found a correlation between α_{CO} and the optical depth, an anticorrelation with kinetic temperature of the gas and low values of α_{CO} by factors of 4-15 in the central regions of these galaxies. As we can see, this variation has a significant impact on the calculation of molecular

TABLE 6

PARAMETERS USED IN THE SED FITTING WITH CIGALE

Component	Module	Parameter	Values
SFH	`sfhdelayed`	`tau_main`	1000, 2000, 4000, 6000 (Myr)
		`age_main`	1500, 4000, 8000 (Myr)
		`tau_burst`	10, 25 (Myr)
		`age_burst`	10, 20 (Myr)
		`f_burst`	0.0, 0.01
Stellar emission	`bc03`	`imf`	Chabrier (2003)
		`metallicity`	0.0001, 0.0004, 0.004, 0.008, 0.02, 0.05
		`separation_age`	10 (Myr)
Nebular emission	`nebular`	`logU`	-2.0
		`f_esc`	0.0
		`f_dust`	0.0
		`lines_width`	300.0
Attenuation	`dustatt_modified`	`E_BV_lines`	0.0, 0.3, 0.6, 0.9, 1.2, 1.5, 1.8, 2.1, 2.4
law	`_starburst`	`E_BV_factor`	0.44
		`uv_bump_wavelength`	217.5
		`uv_bump_width`	35.0
		`uv_bump_amplitude`	0, 1.5, 3
		`powerlaw_slope`	-0.2, 0
		`Ext_law_emission_lines`	1 (MW)
		`Rv`	3.1
Dust emission	`themis`	`qhac`	0.06, 0.17, 0.36
		`umin`	0.1, 1.0, 10.0, 50.0
		`alpha`	1.0, 2.0, 3.0
		`gamma`	0.1, 0.25
AGN	`nenkova2008`	`Y_ratio`	5, 10, 30, 60, 100
		`op_angle`	20, 40, 60
		`tau_V`	20, 60, 80, 120, 200
		`N_0`	3, 5, 10, 15
		`incl`	10, 30, 60, 80
		`q`	0.0, 0.5, 1.0, 2.0, 3.0
		`fracAGN`	0.0, 0.1, 0.2, 0.3, 0.4, 0.5, 0.6, 0.7, 0.8, 0.9

masses and the quantities derived from it, so care must be taken in choosing the value of α_{CO} according to the scale and characteristics of the ISM. In this paper, we consider the value of $M(H_2)$ obtained with ^{13}CO to be the most accurate.

The surface density of dense molecular gas (Σ_{dense}) obtained using equation (8) is integrated in a region where the molecular gas is not homogeneously distributed and thus Σ_{dense} may be underestimated (see Figure 4). An important result is the calculation of the amount of dense gas traced by the HCN in the same region $M_{dense} = (4.7 \pm 0.3) \times 10^7\,\mathrm{M}_\odot$. This value resulted $\approx$4 times smaller than the total mass of molecular hydrogen. This dense star-forming gas provides the conditions for the 200–250 pc diameter circumnuclear ring studied by Riffel et al. (2016), through observations in the UV-optical-IR; they reveal intense bursts of star formation. The relationship between dense and molecular mass is M_{dense}=0.21 $M(H_2)$ which is comparable to f_{dense}= 0.13±0.06, within the uncertainties.

TABLE 7

AGN AND DUSTY TORUS PROPERTIES AFTER SED FITTING WITH CIGALE

Parameter	Best Fit Result	Bayessian Analysis
`Y_ratio`	100	97 ± 12
`op_angle`(°)	60	56 ± 9
`tau_V`	200	184 ± 38
`N_0`	15	14 ± 2
`incl`(°)	80	67 ± 16
`q`	0.0	0.12 ± 0.29
`fracAGN`	0.2	0.20 ± 0.07
SFR ($M_\odot$ yr^{-1})	6.0	6.0 ± 0.3
$L_{\rm AGN}$ (erg s^{-1})	1.5×10^{44}	(1.5 ± 0.6)×10^{44}
$L_{\rm TORUS}$ (erg s^{-1})	7.0×10^{43}	(7.1 ± 2.8)×10^{43}
$L_{\rm DUST}$ (erg s^{-1})	2.8×10^{44}	(2.8 ± 0.1)×10^{44}
L_{IR} = (erg s^{-1})	3.5×10^{44}	(3.51 ± 0.30)×10^{44}

Regarding gas kinematics, we analyzed the velocity of the molecular emission lines and compared them with those of previous studies. The rotational curve of the galaxy traced by molecular gas ^{12}CO J=(2-1) with a resolution of ≈150 pc from ALMA observations (Figure D3, Lang et al. 2020) shows the fitting of the observational data, resulting in an asymptotic rotation velocity $V_0 = 178.2^{+75.1}_{-43.0}\,\mathrm{km\,s^{-1}}$. Meanwhile, the curves obtained by simulations of a central bar formation made by Iles et al. (2022), show that, for an $r \leq 2$ kpc radius, the rotational velocity V_{rot} from the simulations (IsoB IC, blue curves in Figure A1 in that paper) is in the range of 150 to 175 km s^{-1}.

In this study, the velocities for the diffuse gas, i.e., ^{13}CO and C^{18}O, gave us a mean velocity of $V_{CO} = 151 \pm 29\,\mathrm{km\,s^{-1}}$ that matches with the rotational velocity in the $r \leq 2$ kpc radii obtained by Iles et al. (2022), i.e., which covers partially the bar radius $r_{bar} = 2.50 \pm 0.63$ kpc (e.g., Zurita et al. 2021); this is important because in this region the bar dominates the gas kinematics. Meanwhile, the mean value of the velocity for dense gas tracers HCN, HNC, and HCO$^+$ is $V_{dense} = 178 \pm 60$ km s^{-1}, which is consistent with the results obtained by Lang et al. (2020). The dense gas velocity is comparable to the diffuse gas, even having different FOVs. This is maybe due to the dominance of the structural component of the bar.

5.2. *Emission Line Ratios*

The molecular emission line ratio method helps to quantify the molecular gas in specific regions of the galaxy, as in the case of AGN, and can provide information to characterize the star formation or SMBH accretion processes. In this work, we are trying to determine if the presence of the AGN is hinted at by the line ratios and to characterize the ISM from this central 1.6 kpc region.

Previous studies have attempted to classify the activity of galaxies using molecular emission line diagrams such as HNC/HCN, or highest values of HCN/HCO$^+$ (Kohno et al. 2001; Costagliola et al. 2011; Jiang et al. 2011).

Another example is the use of the HNC/HCN ratio as an indicator of shock and non-standard heating, or the CS/HCN ratio, which should be greater than one at large column densities for both XDRs and PDRs, suggesting a correlation with column density (Baan et al. 2008).

Jiménez-Donaire et al. (2019) studied dense gas in nine nearby galaxies at ≈1-2 kpc resolution and showed that the main emission line ratios had a maximum value at the center (with radius ≈ 0.8 kpc) and decreased radially towards the outermost parts of the disk or spiral arms. Using values from Jiménez-Donaire et al. (2019) and our study, we present in Figure 5 the diagnostic diagram of HNC, HCN, HCO$^+$ relative to ^{12}CO. We observe an increasing relationship that clearly separate the galaxy regions, with the galactic centers being the most intense. The ratios HCN/^{12}CO, HCO$^+$/^{12}CO and HNC/^{12}CO presented in Table 4 for the center of NGC 4303 are located in the diagnostic diagram as mentioned previously. As shown, our values are located in the region where the galactic central regions are also located. It should be noted that the center of the galaxy closest to our point is the barred spiral galaxy NGC 6946, which is also classified as a Sy 2.

The ratio between ^{12}CO and ^{13}CO is denoted by $R_{12/13}$ and has been studied for a large sample of galaxies because these lines are generally more intense and easier to detect (e.g., Aladro et al. 2015; Israel 2020). The value $R_{12/13}$ for the nucleus of the galaxy NGC 4303 is 12.1 ± 1.4, consistent with the mean value $R_{12/13} = 13 \pm 6$ of nearby starburst galaxies found by Aalto et al. (1995). This ratio provides information on the variation in optical depth in each galaxy, as well as on the relative abundances of ^{12}C and ^{13}C. In the case of ^{12}C, this can be produced by supernovas of massive stars, whereas ^{13}C can be produced in low-mass stars or ion exchange ^{13}C$^+$ in regions with temperatures ≈ 10 K (see, for example, Keene et al. 1998; Davis 2014).

The HNC/HCN $= 0.58 \pm 0.04$ ratio shows that the HNC abundance is lower than that of HCN. Hirota et al. (1998) observed 19 nearby dark cloud

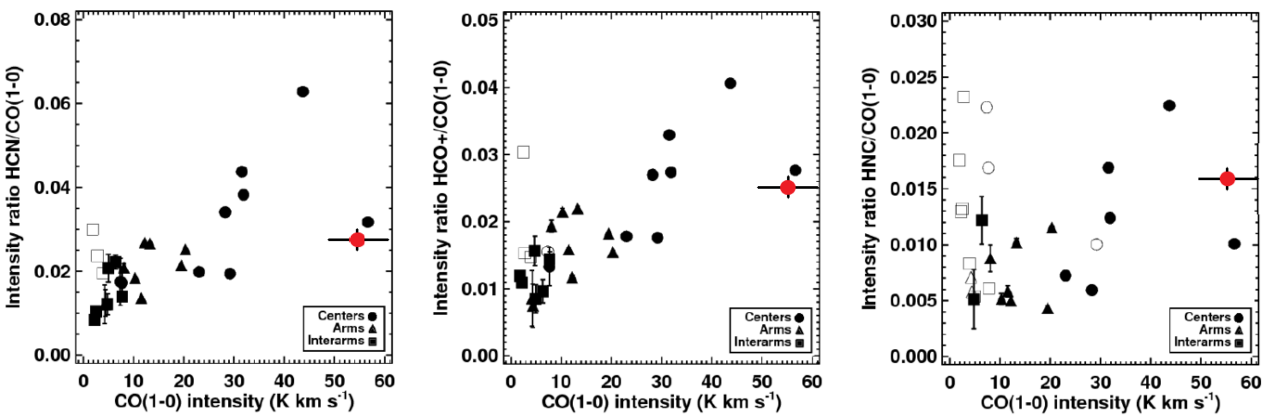

Fig. 5. Diagnostic diagrams left-to-right HCN/^{12}CO, HCO$^+$/^{12}CO and HNC/^{12}CO for a sample of nine nearby galaxies from Jiménez-Donaire et al. (2019). Squares are the values in the interarm regions, triangles are the values in the arms and circles are the values in the centers of these galaxies. Open symbols represent upper limits. The red circles represent the values for the central region of NGC 4303 obtained in this study, which is consistent with the location of the centers of other spiral galaxies on the diagram. The color figure can be viewed online.

cores with Nobeyama 45 m. According to them, the HNC/HCN value is a consequence of the temperature of the central molecular region, $T_{ex} > 24$ K, where neutral-neutral reactions occur. In this manner, the HNC molecule is destroyed to form its isomer, HCN. This supports the use of $T_{ex} = 30$ K to derive surface densities with the corresponding value of $M(H_2)$.

HCN/HCO$^+$ is the ratio most sensitive to density changes, because the critical density of HCO$^+$ is one order of magnitude smaller than that of HCN. Therefore, HCO$^+$ tends to recombine faster than HCN when the medium is dense, owing to free electrons. However, both molecules have similar abundances, indicating that at high densities there is a possible mechanism that enhances the abundance of HCO$^+$. Studies of molecular abundance by Meijerink & Spaans (2005) suggest that, in PDRs, this molecule abundance enhancement occurs at densities $n > 10^5$ cm^{-3}. As mentioned previously, HCN/HCO$^+$ has also been used to determine the nature of the nuclear emitting source. In particular, values of HCN/HCO$^+$ greater than one were found in XDRs, caused by AGN with low density $n > 10^4$ cm^{-3} and $N(H_2) < 10^{22}$ cm^{-2} (for example, Loenen et al. 2008), which agrees with the values of HCN/HCO$^+ = 1.10$ and $N(H_2)$ found in our study (see Table 2). Recently, Nishimura et al. (2024) found in a sample of 23 local ULIRGs that this ratio (J=3-2 lines) shows no trend with AGN luminosity and no implication in the SFR, but the presence of outflows or inflows has the most crucial influence. The HCN/HCO$^+$ ratio indicates a very similar abundance between the two molecules. Thus, HCO$^+$ can form in the dense region, that is, when $n_{critic} > 10^5$ cm^{-3}, ionization must occur in the medium through shock waves or PDRs produced by young stars. The stellar populations of the circumnuclear region described by Dametto et al. (2019) are young ($t < 2$ Gyr) and add a high density to the medium, reinforcing the idea that the gas in the region has high ionization probabilities for radical formation.

Recently, Neumann et al. (2023) presented the results of the ALMOND (ACA Large-sample Mapping Of Nearby galaxies in Dense gas) survey, where they traced the molecular gas density using resolved measurements of HCN(1-0) across 25 nearby spiral galaxies, one of which was NGC 4303. The HCN beam in that work (20″ ≈1.6 kpc) is similar to ours, and therefore the results can be compared. The HCN integrated intensity in the 2 kpc galactocentric radius has a peak temperature of 9.4 mK, similar to our value (see Table 1). In the upper left panel of Figure 6 of Neumann et al. (2023), the relationship between HCN(1-0)/^{12}CO(2-1) and (Σ_{mol}) is presented; our logarithmic values are −1.55 and 2.05, respectively, which lie on their linear relation. This data point is within the range of values for log HCN/^{12}CO reported for NGC 4303 (see their Figure I4). Our Σ_{mol} is in the lower end of the range reported in Neumann et al. (2023), but we note that their value was calculated as a cloud-scale property at 150 pc resolution using α_{CO}, whose uncertainty can be attributed to variations in the galactocentric radius (e.g., Sandstrom et al. 2013).

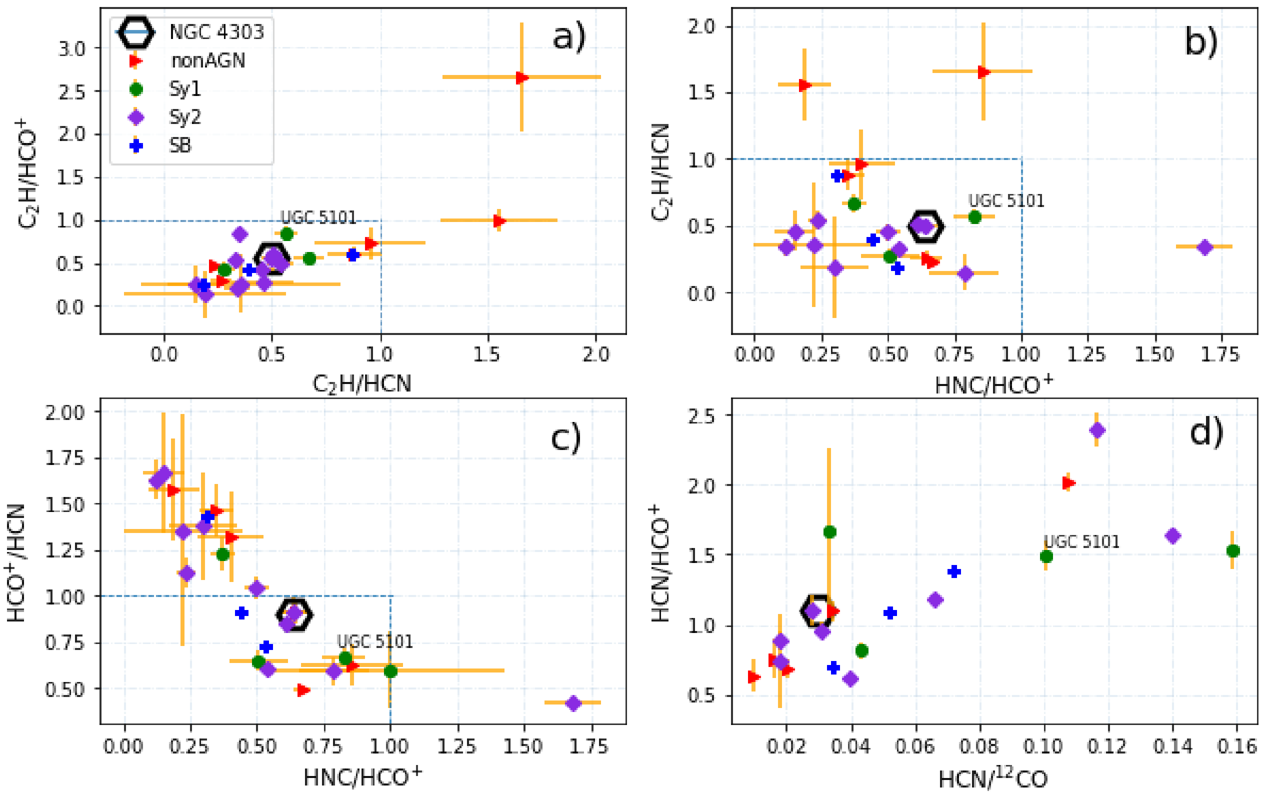

Fig. 6. Line ratio diagrams for a set of 22 galaxies in the literature plus the central 1.6 kpc of NGC 4303. Left to right: a) C_2H/HCN vs. C_2H/HCO^+, b) HNC/HCO^+ vs. C_2H/HCN, c) HNC/HCO^+ vs. HCO^+/HCN, d) HCN/^{12}CO vs. HCN/HCO^+. The line ratio values from the literature are integrated values, the open black hexagons are the values for the central 1.6 kpc of NGC 4303. In addition, the values for UGC 5101 obtained by Cruz-González et al. (2020) in a similar study are labeled in each diagram. The dashed blue line encloses the region where the ratio is less than one. The color figure can be viewed online.

Diagnostic diagrams were constructed to determine possible relationships between type of galaxy activity and emission lines. In Table 8 we present a sample of 23 normal main sequence, starburst (SB), AGN Sy 1 and AGN Sy 2 galaxies with integrated intensities of HCN, HNC, C_2H, HCO^+, ^{12}CO and ^{13}CO reported in the literature. The sample is displayed in Figure 6, and includes the values for the central region of NGC 4303 as a black circle. In these diagrams no relationship between the line intensity ratios and galaxy activity is observed, the SB types and AGNs are mixed, and NGC 4303 lies between the groups. Linearity trends can be observed between the ratios: C_2H/HCN vs. C_2H/HCO^+, HNC/HCO^+ vs. HCO^+/HCN and HCN/^{12}CO vs. HCN/HCO^+.

In the first relation, (a) in Figure 6, we can see a linear relation between these ratios; also, the majority of the galaxies lie in the region where the ratios are less than one, with the special cases of NGC 3556 and IC 180. The diagram (d) HCN/^{12}CO vs. HCN/HCO^+ shows an increasing relation too, where, for values of HCN/HCO^+ less than one, most of the galaxies have a low fraction of dense gas ($\lesssim 0.05$) and for values greater than one the amount of dense gas, with respect to diffuse gas, grows by a factor of 5-8. This last point may indicate a strong relationship between HCO^+ and CO. Additionally, having a dense gas fraction greater than 5% may be linked to the recombination of HCO^+ and increase the abundance of HCN molecules.

The presence of C_2H in the central region may be associated with reactions produced by PDRs in massive, hot star formation regions (for example, Martín, S. et al. 2015). This molecule, like other simple hydrocarbons (^{13}CN, CH, c-C_3-H_2) is the product of keeping a large amount of carbon ionized with warm gas associated with ultraviolet radiation, therefore, the intensity of the field is proportional to its abundance (Meier & Turner 2005; Meier et al. 2015). It

TABLE 8

MOLECULAR LINE TRANSITIONS DETECTED IN NGC 4303 AND OTHER GALAXIES

Galaxy	$\frac{C_2H}{HCO^+}$	$\frac{C_2H}{HCN}$	$\frac{HCN}{HCO^+}$	$\frac{HNC}{HCO^+}$	$\frac{HCN}{^{12}CO}$	Activity*	Reference**
NGC 4303	0.55	0.50	1.10	0.64	0.03	Sy2	*a*
UGC 5101	0.84	0.56	1.50	0.83	0.10	Sy1.5	*b*
IC 180	2.65	1.66	1.60	0.86	-	-	*c*
NGC 1614	0.26	0.54	0.74	0.22	0.02	Sy2	*c*
NGC 3079	0.48	0.54	0.89	0.24	0.02	Sy2	*c*
NGC 4194	0.73	0.96	0.76	0.40	0.02	-	*c*
NGC 4388	0.14	0.19	0.73	0.30	-	Sy2	*c*
NGC 4418	0.25	0.15	1.69	0.79	-	Sy2	*c*
NGC 6090	0.27	0.46	0.60	0.15	-	Sy2	*c*
NGC 6240	0.21	0.34	0.61	0.12	0.04	Sy2	*c*
NGC 7771	0.29	0.26	1.10	0.65	0.03	-	*c*
NGC 660	0.43	0.45	0.96	0.50	0.03	Sy2	*c*
NGC 3556	0.99	1.56	0.64	0.19	0.01	-	*d*
NGC 2273	-	-	1.67	1.00	0.03	Sy1-2	*d*
NGC 5236	0.43	0.39	1.09	0.44	0.05	SB	*e*
NGC 253	0.60	0.51	1.18	0.61	0.07	Sy2	*e*
M82	0.61	0.87	0.70	0.31	0.03	SB	*e*
M51	0.47	0.23	2.02	0.67	0.11	-	*e*
NGC 1068	0.54	0.33	1.64	0.54	0.14	Sy2	*e*
NGC 7469	0.55	0.67	0.82	0.37	0.04	Sy1.2	*e*
ARP 220	0.83	0.35	2.39	1.68	0.12	Sy2	*e*
MRK 231	0.43	0.28	1.54	0.51	0.16	Sy1	*e*
IC 342	0.25	0.18	1.38	0.54	0.07	SB	*f*

Notes: *Activity type from NASA/IPAC Extragalactic Database (NED).
**Dense gas emission line ratios from: [a]This work, [b]Cruz-González et al. (2020), [c]Jiang et al. (2011), [d]Costagliola et al. (2011), [e]Aladro et al. (2015), [f]Nakajima et al. (2018).

is worth noting that we have possible detections of some hydrocarbons that reinforce the idea of the presence of these PDRs.

In Figure 7 we show $R_{12/13}$ vs. HCO^+/HCN. We can observe another increasing relation, where the galaxies with values of HCO^+/HCN less than one have values of $R_{12/13} < 15$, that is, close to the mean value for nearby starburst galaxies found by Aalto et al. (1995). Note that this ratio is an indicator of the optical depth of the gas, that is, when $R_{12/13}$ increases, the medium becomes optically thicker. Therefore, HCO^+/HCN could be a possible indicator of highly obscured galaxies.

As described above, the integrated molecular gas diagrams cannot offer a diagnosis of the presence or absence of obscured AGNs, as the Sy 1 and Sy 2 galaxies show no differences. However, they can tell us more about the abundance of the molecular gas in terms of the change in density and temperature conditions in the regions near the galactic centers. This can lead to a characterization of the conditions of active star formation or its suppression in the regions surrounding an SMBH.

Separating the contribution of the central AGN from the rest of the galaxy is a problem. Observationally, the telescope's main beam is usually larger than the galaxy diameter; hence, the intensity of the lines usually includes contribution of arms (disk) and the bar (if any). In addition to this spatial resolution problem, it is important to detect high transitions of dense gas tracers with the disadvantage that they are even weaker in intensity than those of the rotational transition J=(1-0), when they are optically thin. An example of such a study is reported in Imanishi et al. (2023), a study with ALMA $\lesssim$0.5 kpc resolution, where they detected the J=2-1, J=3-2 and J=4-3 high transition of several emission lines in 11 ULIRGs and showed the spatial variations of physical and chemical properties of molecular gas within the $\lesssim$2 kpc nuclear regions.

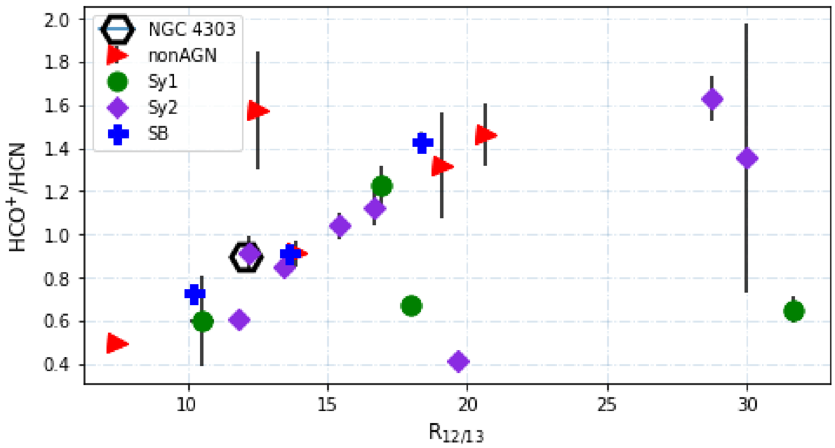

Fig. 7. $R_{12/13}$ vs. HCO^+/HCN for a sample of 12 nearby galaxies. The open black hexagon is the value for the center of NGC 4303. Although a clear linear dependence can be seen between the lines, there is no dependence on galactic activity. The color figure can be viewed online.

5.3. L_{HCN} *vs.* L_{IR} *Relation*

One of the outcomes of the SED fitting analysis is the total infrared luminosity L_{IR}, which is estimated as the sum of the torus luminosity L_{TORUS}, and the dust luminosity, L_{DUST}. From the Bayesian analysis values we obtained $\log(L_{IR}) = 10.96{\pm}0.04\,L_{\odot}$ (see Table 7). Sanders et al. (2003) reported a similar value $\log(L_{IR})=$ 10.51 $L_{\odot}$ for NGC 4303, determined using the fluxes in all four IRAS bands. Both L_{IR} values were larger than those of Li et al. (2020), who reported $\log(L_{IR})=$ $9.6{\pm}0.03\,L_{\odot}$. However, Li et al. (2020) processed calibrated IR image data from Spitzer MIPS and Herschel PACS instruments and corrected to the IRAM telescope main beam (which is close in size to the main beam of the LMT), to estimate L_{IR}. For that reason, we use the value of $\log(L_{IR})$ from Li et al. (2020), together with our derived value for $\log(L_{HCN}) = 6.87{\pm}0.08$ K km s^{-1} pc^2 (Table 3) to place NGC 4303 in Figure 2 of Bigiel et al. (2016) and Figure 5 of Neumann et al. (2023). In both cases, NGC 4303 lies close to the star formation sequence of a sample of nearby galaxies and individual molecular cloud cores, in the group of active star-forming disk galaxies. As we can see, the L_{HCN} vs. L_{IR} relation presented by Neumann et al. (2023) is independent of disc, arm or interarm regions in spatially resolved galaxies.

From a similar analysis for the galaxy UGC 5101 presented by Cruz-González et al. (2020), which was observed in the same season with the RSR/LTM, we obtain $\log(L_{HCN}) = 8.87 \pm 0.02$ K km s^{-1} pc^2 and taking $\log(L_{IR}) = 11.81 \pm 0.08$ $L_{\odot}$ from Soifer et al. (1989), this object falls among the luminous infrared galaxies (LIRGs) in the correlation from Bigiel et al. (2016).

5.4. *AGN Component and SFR in NGC 4303 from SED Fitting*

According to the results of the SED fitting (see Table 7), the AGN component in NGC 4303 is rather low, with an AGN fraction value (`fracAGN`) of 0.2. Indeed, other studies that use CIGALE to fit AGN components to SEDs of galaxies have analyzed its reliability in determining the AGN contribution compared with optical classification and color-color diagrams (for example, Wang et al. 2020) and found a minimum value of `fracAGN` = 0.2 as a reliable lower limit for classifying AGNs using this method. Thus, the value of `fracAGN` that we find allows us to classify NGC 4303 at least as a marginally AGN, and could be in agreement with the difficulties to classify this galaxy as centrally dominated by star formation or a SMBH, and perhaps is speaking in favor of the fading phase AGN scenario (Esparza-Arredondo et al. 2020).

To asses the goodness of the fit and to validate the properties derived from it, we look at the value of the reduced χ^2, which in our case is 3.1. We consider that this value corresponds to a fairly good fit and confirm this by visual inspection (see Figure 3). We notice, however, that the residuals at far-infrared wavelengths are higher than those at both, shorter and longer (sub mm) wavelengths, but the model fluxes (red dots) still describe the shape of the observations. This could be caused by the fact that the observation at 100μm, just before the region of the higher residuals, is very well described by the model (residual ≈ 0), hence pinning the model at that point and preventing it from describing the far-infrared observations in a better manner.

Regarding the SFR in NGC 4303, previous works have reported its estimated value using UV and infrared maps. Utomo et al. (2018) estimated the SFR from the combined GALEX FUV map, corrected for galactic extinction, and the WISE W4 infrared map. The maps were convolved to have an angular resolution of 15″ and background subtracted. After this, they applied the prescriptions described in Kennicutt & Evans (2012) and Jarrett et al. (2013), obtaining a SFR=5.24 $M_\odot$ yr^{-1}. A similar analysis was done by Chevance et al. (2020) in a FOV of roughly the size of the galaxy (see their Figure 1), obtaining a SFR=4.37 ± 0.87 $M_\odot$ yr^{-1}. Leroy et al. (2019) calibrated the above mentioned prescriptions to match the results from Salim et al. (2016, 2018) who combined GALEX, WISE and SDSS data to estimate the integrated SFR for low-redshift galaxies using CIGALE. The value they found is SFR=5.49±1.58 $M_\odot$ yr^{-1}. More recently, Leroy et al. (2021) adopted the prescription of Leroy et al. (2019) using a linear combination of FUV and W4 light, converting the luminosity of each band to SFR using the respective conversion factors and adding the UV and infrared terms to obtain the value SFR=5.37 $M_\odot$ yr^{-1}.

In summary, previous values of the SFR are similar to our CIGALE value, SFR=6.0±0.3, but most authors quote somewhat smaller values. We note that our analysis has the advantage that it incorporates UV to mm wavelength photometry, and the clumpy torus component. Assuming that the values of SFR from the literature are the true values, our similar result validates the good quality of our CIGALE fit and the derived properties. Furthermore, using SFR and $M_\star$ from (Leroy et al. 2021) we note that NGC 4303 lies along the star-formation main sequence (see for example, Cano-Díaz et al. 2019, for MaNGA SDSS-IV), for nearby galaxies.

6. CONCLUSIONS

With the aim of studying the molecular gas in the obscured core of the galaxy NGC 4303, in this work we analyze the emission line spectrum obtained with the *Redshift Search Receiver* at the Large Millimeter Telescope (in its initial phase of 32 m) in the band of 3 mm (73 - 110 GHz), which correspond to 1.6 kpc centered on the ^{13}CO (110.20 GHz) line.

We detected six molecular lines with S/N>3 in the J=(1-0) rotational transition: C_2H (87.31 GHz), HCN (88.63 GHz), HCO^+ (89.18 GHz), HNC (90.66 GHz), $C^{18}O$ (109.78 GHz) and ^{13}CO (110.20 GHz). The first four lines are gas with critical densities $n_{critic} > 10^4$ cm^{-3} which makes them ideal for the study of dense gas that is directly responsible for star formation in the galaxy. The average velocities obtained from the Gaussian fit were 151 ± 29 km s^{-1} for the diffuse gas, and 178 ± 60 km s^{-1} for the dense gas. The result for the diffuse gas velocity is in agreement with the result of Iles et al. (2022), as well with that in the observed ^{12}CO J=(2-1) rotation curve of Lang et al. (2020).

The isotopic varieties of carbon monoxide $C^{18}O$ and ^{13}CO trace the diffuse molecular gas with $n_{critic} \approx 10^3\,\mathrm{cm}^{-3}$ and taking advantage of the fact that the ^{13}CO line is optically thin, that is, $\tau_{13} = 0.09 \pm 0.01$, the column densities relative to ^{12}CO and H_2 for three excitation temperatures (10, 20 and 30 K) were calculated. The results obtained with $T_{ex} = 30$ K are $N(H_2) = (5.14 \pm 0.94) \times 10^{21}\,\mathrm{cm}^{-2}$ and $M(H_2) = (1.75 \pm 0.32) \times 10^8\,M_\odot$, in good agreement with the expected theory and with results obtained by other methods. For example, the last result for the mass of molecular hydrogen is of the same order of magnitude as that found for a central region of 22″×22″using a ^{12}CO(1-0) high resolution map obtained by Schinnerer et al. (2002). Using the HCN integrated intensity it was possible to calculate the amount of dense gas in the observed area. The value $M_{dense} = (4.7 \pm 0.3) \times 10^7\ M_\odot$ is only 4 times smaller than the amount of gas in H_2.

The intensities of the emission lines of the dense and diffuse molecular gas tracers clearly show that the abundance with which these species enrich the chemistry of the medium is due to certain star formation activity in the circumnuclear region. PDRs are a consequence of the interaction of young stars or regions of star formation and are responsible for generating this abundance of radicals in a very dense region that would cause them to recombine quickly. The accretion mechanisms of this gas towards the center responsible for such density must be linked to both the spiral arms and the bar that reach the circumnuclear region, which may be influenced by the gravitational potential of the SMBH. Meanwhile, when comparing the line ratios obtained here with those of a sample of galaxies in the literature, no clear trend is observed to distinguish nuclear activity (SF or AGN) from normal galaxies.

Our spectral energy distribution analysis using the CIGALE code shows that NGC 4303 has a large clumpy dusty torus, with the following parameters obtained based on the Bayesian analysis: aperture above the equatorial plane sigma = 56°±9°, dust optical depth tau_V=184±38, number of dust clouds along the equatorial plane N_0=14±2, an inner to outer radius ratio of Y_ratio=97±12, and a viewing angle of incl≈70°. By considering the classical unified AGN model (Antonucci 1993; Urry & Padovani 1995); this viewing angle is in agreement with the Sy 2 classification previously given by Véron-Cetty & Véron (2006).

Furthermore, for NGC 4303 CIGALE yields the total AGN and torus luminosities of $L_{\rm AGN} = (1.5 \pm 0.6) \times 10^{44}$ erg s^{-1}, $L_{\rm TORUS} = (7.1 \pm 2.8) \times 10^{43}$ erg s^{-1}; while the galaxy dust luminosity is $L_{\rm DUST} = (2.8 \pm 0.1) \times 10^{44}$ erg s^{-1}, which yield a total infrared luminosity $L_{\rm IR} = (3.51 \pm 0.30) \times 10^{44}$ erg s^{-1}. Finally, the star formation rate obtained is SFR=6.0 ± 0.3 M$_\odot$/yr, which, together with the total stellar mass, places this galaxy along the star-formation main-sequence for normal nearby galaxies.

From the molecular gas and dusty torus analysis, we conclude that the central 1.6 kpc emission from NGC 4303 is a mixture of an AGN with a marginal contribution of $\leq$20%, most probably a Type 2, with a large clumpy dusty torus and a starburst host galaxy, as evidenced by intense dense molecular gas lines (C_2H, HCN, HCO^+, and HNC). We found that dense gas contributed significantly to the total molecular gas mass.

The authors thank the referee for a detailed and thorough review of the manuscript and for her/his valuable comments, which have enriched our work and are greatly appreciated. AS acknowledges support from a graduate studies scholarship from CONAHCYT and CONAHCYT/SNI research assistant fellowship. ICG, EB, MHE and AS acknowledge financial support from DGAPA-UNAM grant IN-119123 and CONAHCYT grant CF-2023-G-100. MHE acknowledges financial support from CONAHCYT program *Estancias Posdoctorales por México*. We acknowledge support from CONAHCYT-Mexico, during the construction and Early Science Phase of the Large Millimeter Telescope Alfonso Serrano (LMT/GTM), as well as support from the US National Science Foundation via the University Radio Observatory program, the Instituto Nacional de Astrofísica, Óptica y Electrónica (INAOE), and the University of Massachusetts (UMASS). We also thank LMT/GTM Observatory technical staff for their assistance during the observations and data processing periods. This research made use of the SIMBAD database, operated at CDS, Strasbourg, France, and the NASA/IPAC Extragalactic Database (NED), which is operated by the Jet Propulsion Laboratory, California Institute of Technology, under contract with the National Aeronautics and Space Administration.

REFERENCES

Aalto, S., Booth, R. S., Black, J. H., & Johansson, L. E. B. 1995, A&A, 300, 369

Abazajian, K. N., Adelman-McCarthy, J. K., Agüeros, M. A., & et al. 2009, ApJS, 182, 543, https://doi.org/10.1088/0067-0049/182/2/543

Aladro, R., Martín, S., Riquelme, D., & et al. 2015, A&A, 579, 101, https://doi.org/10.1051/0004-6361/201424918

Antonucci, R. 1993, ARA&A, 31, 473, https://doi.org/10.1146/annurev.aa.31.090193.002353

Auld, R., Bianchi, S., Smith, & et al. 2013, MNRAS, 428, 1880, https://doi.org/10.1093/mnras/sts125

Baan, W. A., Henkel, C., Loenen, A. F., Baudry, A., & Wiklind, T. 2008, A&A, 477, 747, https://doi.org/10.1051/0004-6361:20077203

Bai, Y., Zou, H., Liu, J., & Wang, S. 2015, ApJS, 220, 6, https://doi.org/10.1088/0067-0049/220/1/6

Bendo, G. J., Galliano, F., & Madden, S. C. 2012, MNRAS, 423, 197, https://doi.org/10.1111/j.1365-2966.2012.20784.x

Bennett, C. L., Larson, D., Weiland, J. L., & Hinshaw, G. 2014, ApJ, 794, 135, https://doi.org/10.1088/0004-637X/794/2/135

Bigiel, F., Leroy, A., Walter, F., et al. 2008, AJ, 136, 2846, https://doi.org/10.1088/0004-6256/136/6/2846

Bigiel, F., Leroy, A. K., Jiménez-Donaire, M. J., & et al. 2016, 2016, ApJ, 822, 26, https://doi.org/10.3847/2041-8205/822/2/L26

Bolatto, A. D., Wolfire, M., & Leroy, A. K. 2013, ARA&A, 51, 207, https://doi.org/10.1146/annurev-astro-082812-140944

Boquien, M., Burgarella, D., Roehlly, Y., et al. 2019, A&A, 622, 103, https://doi.org/10.1051/0004-6361/201834156

Boselli, A., Voyer, E., Boissier, S., & et al. 2014, A&A, 570, 69, https://doi.org/10.1051/0004-6361/201424419

Bruzual, G. & Charlot, S. 2003, MNRAS, 344, 1000, https://doi.org/10.1046/j.1365-8711.2003.06897.x

Calzetti, D., Armus, L., Bohlin, R. C., & et al. 2000, ApJ, 533, 682, https://doi.org/10.1086/308692

Cano-Díaz, M., Ávila-Reese, V., Sánchez, S. F., & et al. 2019, MNRAS, 488, 3929, https://doi.org/10.1093/mnras/stz1894

Chabrier, G. 2003, PASP, 115, 763, https://doi.org/10.1086/376392

Chen, P. S., Yang, X. H., Liu, J. Y., & Shan, H. G. 2018, AJ, 155, 17, https://doi.org/10.3847/1538-3881/aa988c

Chevance, M., Kruijssen, J. M. D., Hygate, & et al. 2020, MNRAS, 493, 2872, https://doi.org/10.1093/mnras/stz3525

Ciesla, L., Boquien, M., Boselli, A., & et al. 2014, A&A, 565 128, https://doi.org/10.1051/0004-6361/201323248

Ciesla, L., Charmandaris, V., Georgakakis, A., & et al. 2015, A&A, 576, 10, https://doi.org/10.1051/0004-6361/201425252

Colina, L., Piqueras López, J., Arribas, S., Riffel, R., Riffel, R. A., & et al. 2015, A&A, 578, 48, https://doi.org/10.1051/0004-6361/201425567

Cortese, L., Boissier, S., Boselli, A., & et al. 2012, A&A, 544, 101, https://doi.org/10.1051/0004-6361/201219312

Costagliola, F., Aalto, S., Rodriguez, M. I., & et al. 2011, A&A, 528, 30, https://doi.org/10.1051/0004-6361/201015628

Cruz-González, I., Gómez-Ruiz, A. I., Caldú-Primo, A., et al. 2020, MNRAS, 499, 2042, https://doi.org/10.1093/mnras/staa2949

Cybulski, R., Yun, M. S., Erickson, N., & et al. 2016, MNRAS, 459, 3287, https://doi.org/10.1093/mnras/stw798

Dalya, G., Frei, Z., Galgoczi, G., Raffai, P., & de Souza, R. S. 2016, VizieR Online Data Catalog, VII/275

Dametto, N. Z., Riffel, R., Colina, L., Riffel, R. A., Piqueras López, J., & et al. 2019, MNRAS, 482, 4437, https://doi.org/10.1093/mnras/sty2996

Davis, T. A. 2014, MNRAS, 445, 2378, https://doi.org/10.1093/mnras/stu1850

de Vaucouleurs, G., de Vaucouleurs, A., Corwin, Herold G., J., & et al. 1991, Third Reference Catalogue of Bright Galaxies

Di Francesco, J., Johnstone, D., Kirk, H., MacKenzie, T., & Ledwosinska, E. 2008, ApJS, 175, 277, https://doi.org/10.1086/523645

Dickman, R. L. 1978, ApJS, 37, 407, https://doi.org/10.1086/190535

Erickson, N., Narayanan, G., Goeller, R., & Grosslein, R. A. J. 2007, in ASPC 375, From Z-Machines to ALMA: (Sub)Millimeter Spectroscopy of Galaxies, ed. R. A. J. Baker, J. Glenn, A. I. Harris, J. G. Mangum, & M. S. Yun (ASPC) 71

Esparza-Arredondo, D., Osorio-Clavijo, N., González-Martín, O., & et al. 2020, ApJ, 905, 29, https://doi.org/10.3847/1538-4357/abc425

Fazio, G. G., Hora, J. L., Allen, L. E., & et al. 2004, ApJS, 154, 10, https://doi.org/10.1086/422843

Filippenko, A. V. & Sargent, W. L. W. 1985, ApJS, 57, 503, https://doi.org/10.1086/191012

Frei, Z., Guhathakurta, P., Gunn, J. E., & Tyson, J. A. 1996, AJ, 111, 174, https://doi.org/10.1086/117771

Fritz, J., Franceschini, A., & Hatziminaoglou, E. 2006, MNRAS, 366, 767, https://doi.org/10.1111/j.1365-2966.2006.09866.x

Gao, Y. & Solomon, P. M. 2004a, ApJS, 152, 63, https://doi.org/10.1086/383003

__________. 2004b, ApJ, 606, 271, https://doi.org/10.1086/382999

García-Burillo, S. IAUS15, From Interstellar Clouds to Star-Forming Galaxies: Universal Processes?, ed. P. Jablonka, P. André, & F. van der Tak, 207, https://doi.org/10.1017/S1743921316007213

Graciá-Carpio, J., García-Burillo, S., Planesas, P., & Colina, L. 2006, ApJ, 640, 135, https://doi.org/10.1086/503361

Griffin, M. J., Abergel, A., Abreu, A., & et al. 2010, A&A, 518, 3, https://doi.org/10.1051/0004-6361/201014519

Hirota, T., Yamamoto, S., Mikami, H., & Ohishi, M. 1998, ApJ, 503, 717, https://doi.org/10.1086/306032

Holland, W. S., Robson, E. I., Gear, W. K., & et al. 1999, MNRAS, 303, 659, https://doi.org/10.1046/j.1365-8711.1999.02111.x

Hönig, S. F. & Kishimoto, M. 2017, ApJ, 838, 20, https://doi.org/10.3847/2041-8213/aa6838

Huchra, J. P., Wyatt, W. F., & Davis, M. 1982, AJ, 87, 1628, https://doi.org/10.1086/113254

Iles, E. J., Pettitt, A. R., & Okamoto, T. 2022, MNRAS, 510, 3899, https://doi.org/10.1093/mnras/stab3330

Imanishi, M., Baba, S., Nakanishi, K., & Izumi, T. 2023, ApJ, 954, 148, https://doi.org/10.3847/1538-4357/ace90d

Israel, F. P. 2020, A&A, 635, 131, https://doi.org/10.1051/0004/6361/201834198

Jarrett, T. H., Masci, F., Tsai, C. W., & et al. 2013, AJ, 145, 6, https://doi.org/10.1088/0004-6256/145/1/6

Jiang, X., Wang, J., & Gu, Q. 2011, MNRAS, 418, 1753, https://doi.org/10.1111/j.1365-2966.2011.19596.x

Jiménez-Bailón, E., Santos-Lleó, M., Mas-Hesse, J. M., et al. 2003, ApJ, 593, 127, https://doi.org/10.1086/376554

Jiménez-Donaire, M. J. 2017, PhD thesis, Dense Gads and Interstellar Medium in nearby Galaxies, Ruprecht-Karls University of Heidelberg, Germany

Jiménez-Donaire, M. J., Bigiel, F., Leroy, A. K., et al. 2017, MNRAS, 466, 49, https://doi.org/10.1093/mnras/stw2996

__________. 2019, ApJ, 880, 127, https://doi.org/10.3847/1538-4357/ab2b95

Jones, A. P., Köhler, M., Ysard, N., Bocchio, M., & Verstraete, L. 2017, A&A, 602, 46, https://doi.org/10.1051/0004-6361/201630225

Keene, J., Schilke, P., Kooi, J., Lis, D. C., Mehringer, D. M., & Phillips, T. G. 1998, ApJ, 494, 107, https://doi.org/10.1086/311164

Kennicutt, R. C. & Evans, N. J. 2012, ARA&A, 50, 531, https://doi.org/10.1046/annurev-astro-081811-125610

Kim, S., Rey, S.-C., Jerjen, H., et al. 2014, ApJS, 215, 22, https://doi.org/10.1088/0067-0049/215/2/22

Kohno, K. 2003, ASPC 289, The Proceedings of the IAU 8th Asian-Pacific Regional Meeting, Volume I, ed. S. Ikeuchi, J. Hearnshaw, & T. Hanawa (San Francisco, CA: ASP) 349

Kohno, K., Matsushita, S., Vila-Vilaró, B., Okumura, S. K., & Shibatsuka, T. 2001, ASPC 249, Proceedings, The Central Kiloparsec of Starbursts and AGNS: The La Palma Connection, ed. J. H. Knapen, J. E. Beckman, I. Shlosman, & T. J. Mahoney, (San Francisco CA: ASP), 672

Lang, P., Meidt, S. E., Rosolowsky, E., et al. 2020, ApJ, 897, 122, https://doi.org/10.3847/1538-4357/ab9953

Lee, C., Chung, A., Yun, M. S., et al. 2014, MNRAS, 441, 1363, https://doi.org/10.1093/mnras/stu670

Leroy, A. K., Sandstrom, K. M., Lang, D., et al. 2019, ApJS, 244, 24, https://doi.org/10.3847/1538-4365/ab3925

Leroy, A. K., Schinnerer, E., Hughes, A., et al. 2021, ApJS, 257, 43, https://doi.org/10.3847/1538-4365/ac17f3

Leroy, A. K., Usero, A., Schruba, A., et al. 2017, ApJ, 835, 217, https://doi.org/10.3847/1538-4357/835/2/217

Li, F., Wang, J., Fang, M., et al. 2020, PASJ, 72, 41, https://doi.org/10.1093/pasj/psaa025

Li, F., Wang, J., Gao, F., et al. 2021, MNRAS, 503, 4508, https://doi.org/10.1093/mnras/stab745

Loenen, A. F., Spaans, M., Baan, W. A., & Meijerink, R. 2008, A&A, 488, 5, https://doi.org/10.1051/0004-6361:200810327

Malkan, M. A., Jensen, L. D., Rodriguez, D. R., Spinoglio, L., & Rush, B. 2017, ApJ, 846, 102, https://doi.org/10.3847/1538-4357/aa8302

Martin, D. C., Fanson, J., Schiminovich, D., et al. 2005, ApJ, 619, 1, https://doi.org/10.1086/426387

Martín, S., Kohno, K., Izumi, T., et al. 2015, A&A, 573, 116, https://doi.org/10.1051/004-6361/201425105

Meier, D. S. & Turner, J. L. 2005, ApJ, 618, 259, https://doi.org/10.1086/426499

Meier, D. S., Walter, F., Bolatto, A. D., et al. 2015, ApJ, 801, 63, https://doi.org/10.1088/0004-637X/801/1/63

Meijerink, R. & Spaans, M. 2005, A&A, 436, 397, https://doi.org/10.1051/0004-6361:20042398

Meijerink, R., Spaans, M., & Israel, F. P. 2007, A&A, 461, 793, https://doi.org/10.1051/0004-6361:20066130

Miyaji, T., Herrera-Endoqui, M., Krumpe, M., et al. 2019, ApJ, 884, 10, https://doi.org/10.3847/2041-8213/ab46bc

Morokuma-Matsui, K., Sorai, K., Sato, Y., et al. 2020, PASJ, 72, 90, https://doi.org/10.1093/pasj/psaa084

Moustakas, J. & Kennicutt, Jr., R. C. 2006, ApJS, 164, 81, https://doi.org/10.1086/500971

Nakajima, T., Takano, S., Kohno, K., Harada, N., & Herbst, E. 2018, PASJ, 70, 7, https://doi.org/10.1093/pasj/psx153

Nenkova, M., Sirocky, M., Ivezic, Z., & Elitzur, M. 2008, ApJ, 685, 160, https://doi.org/10.1086/590483

Nenkova, M., Sirocky, M. M., Ivezić, Ž., & Elitzur, M. 2008a, ApJ, 685, 147, https://doi.org/10.1086/590482

Nenkova, M., Sirocky, M. M., Nikutta, R., Ivezić, Ž., & Elitzur, M. 2008b, ApJ, 685, 160, https://doi.org/10.1086/590483

Neugebauer, G., Habing, H. J., van Duinen, R., & et al. 1984, ApJ, 278, 1, https://doi.org/10.1086/184209

Neumann, L., Gallagher, M. J., Bigiel, F., & et al. 2023, MNRAS, 521, 3348, https://doi.org/10.1093/mnras/stad424

Nishimura, Y., Aalto, S., Gorski, M. D., et al. 2024, arXiv:2402.15436, https://doi.org/10.48550/arXiv.2402.15436

Pilbratt, G. L., Riedinger, J. R., Passvogel, T., et al. 2010, A&A, 518, 1, https://doi.org/10.1051/0004-6361/201014759

Poglitsch, A., Waelkens, C., Geis, N., et al. 2010, A&A, 518, 2, https://doi.org/10.1051/0004-6361/201014535

Privon, G. C., Ricci, C., Aalto, S., et al. 2020, ApJ, 893, 149, https://doi.org/10.3847/1538-4357/ab8015

Rahman, N., Helou, G., & Mazzarella, J. M. 2006, ApJ, 652, 1068, https://doi.org/10.1086/508566

Riffel, R. A., Colina, L., Storchi-Bergmann, T., & et al. 2016, MNRAS, 461, 4192, https://doi.org/10.1093/mnras/stw1609

Rybak, M., Hodge, J. A., Greve, T. R., & et al. 2022, A&A, 667, 70, https://doi.org/10.1051/0004-6361/202243894

Salim, S., Boquien, M., & Lee, J. C. 2018, ApJ, 859, 11, https://doi.org/10.3847/1538-4357/aabf3c

Salim, S., Lee, J. C., Janowiecki, S., et al. 2016, ApJS, 227, 2, https://doi.org/10.3847/0067-0049/227/1/2

Sanders, D. B., Mazzarella, J. M., Kim, D.-C., Surace, J. A., & Soifer, B. T. 2003, AJ, 126, 1607, https://doi.org/10.1086/376841

Sandstrom, K. M., Leroy, A. K., Walter, F., et al. 2013, ApJ, 777, 5, https://doi.org/10.1088/0004-637X/777/1/5

Santos, D. J. D., Goto, T., Kim, S. J., et al. 2021, MNRAS, 507, 3070, https://doi.org/10.1093/mnras/stab2352

Schinnerer, E., Maciejewski, W., Scoville, N., & Moustakas, L. A. 2002, ApJ, 575, 826, https://doi.org/10.1086/341348

Sheth, K., Regan, M., Hinz, J. L., et al. 2010, PASP, 122, 1397, https://doi.org/10.1086/657638

Skrutskie, M. F., Cutri, R. M., Stiening, R., & et al. 2006, AJ, 131, 1163, https://doi.org/10.1086/498708
Snell, R. L., Narayanan, G., Yun, M. S., et al. 2011, AJ, 141, 38, https://doi.org/10.1088/0004-6256/141/2/38
Soifer, B. T., Boehmer, L., Neugebauer, G., & Sanders, D. B. 1989, AJ, 98, 766, https://doi.org/10.1086/115178
Solomon, P. M., Downes, D., Radford, S. J. E., & Barrett, J. W. 1997, ApJ, 478, 144, https://doi.org/10.1086/303765
Sorai, K., Kuno, N., & et al. 2019, PASJ, 71, 14, https://doi.org/10.1093/pasj/psz115
Stassun, K. G. 2019, VizieR Online Data Catalog, IV/38
Strong, A. W., Bloemen, J. B. G. M., Dame, T. M., et al. 1988, A&A, 207, 1
Teng, Y.-H., Sandstrom, K. M., Sun, J., et al. 2023, ApJ, 925, 72, https://doi.org/10.3847/1538-4357/ac382f
Teng, Y.-H., Sandstrom, K. M., Sun, J., & et al. 2023, ApJ, 950, 119, https://doi.org/10.3847/1538-4357/accb86
Urry, C. M. & Padovani, P. 1995, PASP, 107, 803, https://doi.org/10.1086/133630
Usero, A., Leroy, A. K., Walter, F., et al. 2015, AJ, 150, 115, https://doi.org/10.1088/0004-6256/150/4/115
Utomo, D., Sun, J., Leroy, A. K., et al. 2018, ApJ, 861, 18, https://doi.org/10.3847/2041-8213/aacf8f
Veron-Cetty, M. P. & Veron, P. 1986, A&AS, 66, 335
Véron-Cetty, M.-P. & Véron, P. 2006, A&A, 455, 773, https://doi.org/10.1051/0004-6361:20065177
Wang, T.-W., Goto, T., Kim, S. J., et al. 2020, MNRAS, 499, 4068, https://doi.org/10.1093/mnras/staa2988
Werner, M. W., Roellig, T. L., Low, F. J., et al. 2004, ApJS, 154, 1, https://doi.org/10.1086/422992
Wilson, T. L. & Rood, R. 1994, ARA&A, 32, 191, https://doi.org/10.1146/annurev.aa.32.090194.001203
Wright, E. L. 2006, PASP, 118, 1711, https://doi.org/10.1086/510102
Wright, E. L., Eisenhardt, P. R. M., Mainzer, A. K., et al. 2010, AJ, 140, 1868, https://doi.org/10.1088/0004-6256/140/6/1868
Wu, J., Evans II, Neal J., Gao, Y., et al. 2005, ApJ, 635, 173, https://doi.org/10.1086/499623
Wu, J., Evans II, Neal J., Shirley, Y. L., & Knez, C. 2010, ApJS, 188, 313, https://doi.org/10.1088/0067-0049/188/2/313
Yajima, Y., Sorai, K., Kuno, N., et al. 2019, PASJ, 71, 13, https://doi.org/10.1093/pasj/psz022
Yamada, S., Ueda, Y., Herrera-Endoqui, M., et al. 2023, ApJS, 265, 37, https://doi.org/10.3847/1538-4365/acb349
Yun, M. S., Aretxaga, I., Gurwell, M. A., et al. 2015, MNRAS, 454, 3485, https://doi.org/10.1093/mnras/stv1963
Yun, M. S., Reddy, N. A., & Condon, J. J. 2001, ApJ, 554, 803, https://doi.org/10.1086/323145
Zurita, A., Florido, E., Bresolin, F., Pérez-Montero, E., & Pérez, I. 2021, MNRAS, 500, 2359, https://doi.org/10.1093/mnras/staa2246

Erika Benítez, I. Cruz-González, Martín Herrera-Endoqui, Yair Krongold, and Ángel A. Soní: Instituto de Astronomía, Universidad Nacional Autónoma de México, Apdo. Postal 70-264, Cd. de México (irene@astro.unam.mx).

Arturo I. Gómez-Ruiz: CONAHCYT-Instituto Nacional de Astrofísica Óptica y Electrónica, Luis E. Erro 1, 72840 Tonantzintla, Puebla, México.

Martín Herrera-Endoqui: Estancia Posdoctoral por México, CONAHCYT, Coordinación de Apoyos a Becarios e Investigadores.

Revista Mexicana de Astronomía y Astrofísica, **61**, 87–97 (2025)

https://doi.org/10.22201/ia.01851101p.2025.61.01.06

THE EFFECT OF OPACITY ON NEUTRON STAR TYPE I X-RAY BURST QUENCHING

Martín Nava-Callejas[1], Yuri Cavecchi[2], and Dany Page[1]

Received September 17 2024; accepted November 4 2024

ABSTRACT

One long standing tension between theory and observations of Type I X-ray bursts is the accretion rate at which the bursts disappear due to stabilization of the nuclear burning that powers them. This is observed to happen at roughly one third of the theoretical expectations. Various solutions have been proposed, the most notable of which is the addition of a yet unknown source of heat in the upper layers of the crust, below the burning envelope. In this paper we ran several simulations using the 1D code `MESA` to explore the impact of opacity on the threshold mass accretion rate after which the bursts disappear, finding that a higher than expected opacity in the less dense layers near the surface has a stabilizing effect.

RESUMEN

Una tensión largamente persistente entre teoría y observaciones de estallidos de rayos-X Tipo I es la tasa de acreción a la cual los estallidos desaparecen debido a la estabilización del quemado nuclear que los origina. Se ha observado que esto ocurre aproximadamente a un tercio de las expectativas teóricas. Varias soluciones se han propuesto; la más notable ha sido la adición de una fuente de calor de origen desconocido en las capas más altas de la corteza, debajo de la envolvente en quemado. En este artículo corrimos varias simulaciones empleando el código 1D `MESA` para explorar el impacto de la opacidad en la tasa de acreción límite arriba de la cual los estallidos desaparecen; encontramos que una opacidad más alta de lo esperado en las zonas menos densas cerca de la superficie tiene un efecto estabilizador.

Key Words: accretion, accretion discs — stars: neutron — X-rays: binaries — X-rays: bursts

1. INTRODUCTION

In binary systems hosting a neutron star and a small mass star, when the companion expands to fill its Roche lobe mass can be transferred to the compact object via an accretion disk. Under the right conditions, especially mass accretion rate, the accreted fuel on the neutron star surface will burn unstably, producing X-ray flashes known as the Type I bursts (see e.g. Strohmayer & Bildsten 2010). The fluid begins burning in the upper layers, but the cooling processes are able to compensate the heating due to the nuclear reactions. As the fluid sinks deeper under the push of newer accreted layers, the burning rate increases, especially due to the increase of temperature. When the cooling cannot compensate the reaction rate anymore, the burning turns explosive and initiates the burst (e.g. Fujimoto et al. 1981; Bildsten 1998). Depending on the accretion rate, the first unstable ignition could be due to hydrogen or helium, and the burst can have a larger or smaller amount of hydrogen left to burn at its later stages (Fujimoto et al. 1981; Bildsten 1998). Above a certain accretion rate bursts are suppressed because the fluid never reaches unstable burning conditions.

To date, one of the persistent discrepancies between theory and observations of Type I X-ray bursts is the critical accretion rate $\dot{M}_{\rm crit}$ above which bursts are suppressed. While observations indicate $\dot{M}_{\rm crit} \approx 0.3\dot{M}_{\rm Edd}$ (Cornelisse et al. 2003; Watts & Maurer 2007; Galloway et al. 2008; Galloway & Keek 2021), numerical simulations employing different codes indicate $\dot{M}_{\rm crit} \approx 1$ to $3\dot{M}_{\rm Edd}$ (Bildsten

[1]Instituto de Astronomía, UNAM, Mexico.
[2]Universitat Politècnica de Catalunya, Spain.

1998; Heger et al. 2007; Fisker et al. 2007), where $\dot{M}_{\rm Edd}$ is the Eddington accretion rate. One proposed mechanism to keep the burning layer stable is the presence of a heating source injecting up to a few MeV per baryon at densities of 10^7 g cm^{-3} or above, the so called *shallow heating* (Brown & Cumming 2009; Wijnands et al. 2017), which is currently of unknown origin. Several explanations or alternatives have been proposed over the years, as for instance modification to the CNO break out $^{15}{\rm O}(\alpha,\gamma)^{19}{\rm Ne}$ (Cooper & Narayan 2006; Davids et al. 2011), diffusion of ^{4}He or rotation effects (Piro & Bildsten 2007; Keek, L. et al. 2009; Inogamov & Sunyaev 2010; Cavecchi et al. 2020).

In this note we show that it is possible to suppress the bursts in numerical simulations at the observed mass accretion rate by modifying the opacity. Our results indicate that this is achievable if the opacity in the layers between the surface and the ignition depth is $\gtrsim 8$ times the electron scattering opacity expected to dominate at these depth.

2. METHODOLOGY

We simulated the evolution of accreted neutron star envelopes employing the public code `MESA` v.15140 (Paxton et al. 2011, 2015). The initial profiles were constructed with an envelope code which solves the time-independent equations of stellar structure and temperature up to an inner boundary density of $\rho_b = 10^{9.5}$ g cm^{-3} (Nava-Callejas et al. 2024).

As an inner boundary conditions for `MESA` at ρ_b one needs to fix the inner luminosity, L_b, coming from the stellar interior. Initially, to focus on the effect of opacity, we employed two different values for the base luminosity: a very low one of $L_b = 2.5\times10^{-5}L_\odot$ and a high one of $L_b = 2.5\times10^{-1}L_\odot$. Later, we explored the impact of changing this value by selecting a range of values up to $2.5\times10^3 L_\odot$. It is usually assumed that this inner luminosity is controlled by the accretion rate coming from an energy release deeper in the crust with an expression of the type $L_b = Q_b \times \dot{M}/m_u$ (m_u being the atomic mass unit). For the sake of comparison, our choices of L_b would correspond, when $\dot{M} \simeq 0.3\dot{M}_{\rm Edd}$, to values $Q_b = 10^{-7} - 30$ MeV baryon^{-1}. Following Schatz et al. (1999) we adopt $\dot{M}_{\rm Edd} = 1.1\times10^{18}$ g s^{-1} as the Eddington accretion rate.

The amount of cells of the spatial grid, as well as the time-step, are factors which might have some impact on the simulation results. In `MESA`, the `mesh_delta_coeff` parameter controls the mesh refinement during a simulation: above 1.0, the number of grid cells tends to be smaller, while below 1.0 the number might reach up to 3000 cells. Unless explicitly stated, we adopt 5.0 for this coefficient. Besides the size of the mesh, `MESA` allows to have some control over the chosen time step. With `time_delta_coeff` (hereafter `tdc`), the user can ask for overall large steps in time, while `min_timestep_factor` (hereafter `mtf`) controls the minimum ratio between the new and the previous time step. By default, their respective values are 1.0 and 0.8. By trial and error, for some simulations we have found suitable to replace these defaults by a customized configuration of 5.0 and 1.2, which we employ unless another combination is explicitly stated. In Appendix A we show that these values are a good choice and that our conclusions do not depend on it.

For the majority of the simulations we employed a customized network containing 140 species and capable of simulating an rp-process exhausting H at around 10^6 g cm^{-3}. Dubbed `approx140`, this network ranges from $A = 1$ to $A = 80$ and covers H burning via CNO and rp-process, He burning via 3α and α-captures, C-O fusion and electroweak decays of heavy nuclides at $A > 56$ as a result of the production of ashes. The list of nuclides used in `approx140` can be found in Table 1 and more details about it can be found in Appendix B. As a refractory layer at the base, we use ^{80}Kr.

For the chemical composition of the accreted material we employed a Solar-like scheme with 70% ^{1}H, 29% ^{4}He and the remaining 1% automatically distributed, among the remaining nuclides in the network, by `MESA`, throughout the command `accretion_zfracs` = 3, corresponding to the distribution of metals from Grevesse & Sauval (1998). A little exploration on the sensitivity of our results to choosing this automatized distribution or a simple mixture of ^{1}H, ^{4}He and ^{12}C is explored in the Appendix.

We override the opacity using a custom routine, based on the one provided by Bill Wolf's website, `my_other_kap_get`[3]. The total opacity is given by $\kappa = [\kappa_{\rm rad}^{-1} + \kappa_{\rm cond}^{-1}]^{-1}$, receiving contributions from radiation, $\kappa_{\rm rad}$, and conduction, $\kappa_{\rm cond}$. For the latter, in all the simulations the routine uses the tables provided by `MESA`. For $\kappa_{\rm rad}$, we considered and compared the results using values from the tables provided with the `MESA` source code and from the extra subroutines by Wolf. These subroutines are based on the additive combination of free-free opacity from Schatz et al. (1999), electron scattering from

[3] `https://billwolf.space/projects/leiden_2019/`.

TABLE 1

LIST OF NUCLIDES IN THE NETWORK
`APPROX140`

Z	A	Z	A	Z	A
n	1	S	28-32	Cu	56-60
H	1	Cl	32-34	Zn	58-62,64
He	4	Ar	33-36	Ga	61-65
C	12	K	36-38	Ge	62-66,68
N	13-15	Ca	37-40	As	66-69
O	14-18	Sc	40-42	Se	68-70,72
F	17-19	Ti	41-44	Br	70-73
Ne	18-20	V	44-46	Kr	72-74,76,80
Na	20-21	Cr	45-48	Rb	74-77,80
Mg	21,22,24	Mn	48-50	Sr	76-78,80
Al	23-25	Fe	49-52,54	Y	78-80
Si	24-26,28	Co	52-56	Zr	80
P	27-30	Ni	53-58,60		

Paczynski (1983b), and the correction factor from Potekhin & Yakovlev (2001). We will call this opacity the fiducial opacity. For some models we replaced Paczynski's fit with the one of Poutanen (2017), as indicated in the text.

To make sure that our conclusions are not affected by our choices for the mesh, the time step or the network, we conducted extensive tests which we report in Appendix A. In what follows we focus on the results based on changing the opacity.

3. RESULTS

3.1. *Increased/Decreased Opacity at Fixed Accretion Rate*

We first analyze the impact of applying an overall opacity factor. We consider a fixed mass accretion rate, $5.26 \times 10^{-9}\ M_\odot\ \mathrm{yr}^{-1}$ (roughly corresponding to $0.3\dot{M}_{\mathrm{Edd}}$) and show the results in Figure 1. One sees from panel (a) that the base model, with the fiducial opacity, exhibits a typical bursting behavior, with a recurrence time of the order of 2.5 hours, after an initial heating phase. With κ reduced by a factor of 10 it takes much longer for the first burst to appear while with the 10 times larger opacity the bursting behavior is much accelerated, similar to millihertz oscillations (Paczynski 1983a; Revnivtsev et al. 2001; Heger et al. 2007).

Panel (b), showing the temperature profiles just before explosion, explains this difference in behaviors. Increased opacity keeps the burning layer warmer, allowing it to explode at lower density. In contradistinction, the lowered opacity implies a very effective dissipation of the released nuclear energy,

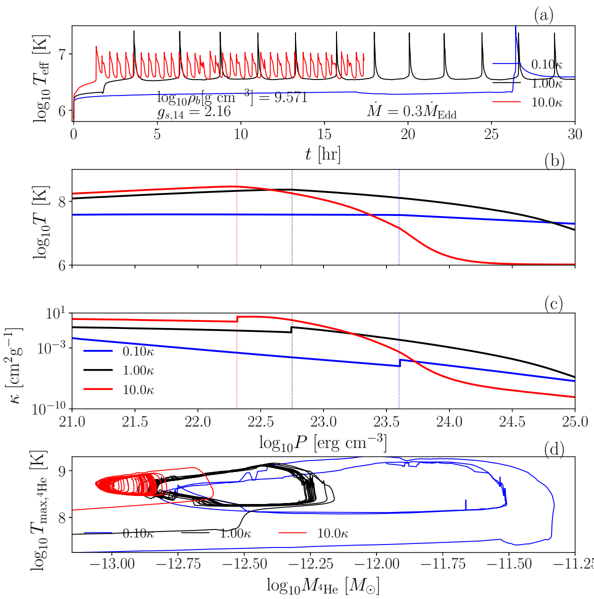

Fig. 1. Effects of a change in opacity κ at a fixed mass accretion rate of $\dot{M} = 5.26 \times 10^{-9} M_\odot\ \mathrm{yr}^{-1} = 0.3\,\dot{M}_{\mathrm{Edd}}$. We consider three models with κ unaltered, or multiplied or divided by a factor of 10. Panel (a): time evolution of T_{eff}. Panel (b): temperature profiles just before the first explosion. Panel (c): opacity profiles at the same time. Panel (d): temperature vs total mass evolution of the helium layer. In panels (b) and (c) the three dotted vertical lines indicate the depth at with the explosion is occurring. The luminosity at the base for the three models is $L_b = 2.5 \times 10^{-5} L_\odot$, corresponding to $Q_b = 3 \times 10^{-7}$ MeV baryon^{-1}. The color figure can be viewed online.

resulting in much lower temperatures, with little density dependence, thus forcing the accreted matter to reach higher densities before it can explode at a much delayed time.

In panel (c) dramatic changes in opacity are visible. As expected from our arbitrary 10 - 1/10 altering factor, we observe a global increase/decrease of opacity with respect to the fiducial one, although the effect is more pronounced in the 1/10 reduction scenario than in the 10-times amplified one. This is a consequence of the induced differences in nuclear burning: the colder 1/10 decreased opacity produces less heavy elements through the rp-process, and thus sees its opacity further reduced by having more abundant low Z nuclei. The sharp transition in opacity observed in the three models, nevertheless, still marks the transition from a low-Z to a high-Z region between accreted and compressed matter.

Finally, in panel (d) we display the time evolution of the total mass of accreted helium, $M_{^4\mathrm{He}}$, and the temperature at its maximum density, $T_{\mathrm{max},^4\mathrm{He}}$

clearly exhibiting a cyclic behavior. In the fiducial model, explosions are triggered when $M_{^4\mathrm{He}}$ reaches $\approx 10^{-12.25} M_\odot$ at temperatures $T \approx 10^{8.3}$ K and the exploding layer heats up reaching $\approx 10^{9.1}$ K: subsequently $M_{^4\mathrm{He}}$ rapidly decreases, helium being consumed, T decreases as well and the cycle resumes (compare to Heger et al. 2007). In the increased opacity case, one clearly sees that the higher temperatures trigger the explosion at lower densities; the maximum temperature reached is, however, lower. In the lowered opacity case the contrary is happening: the cycles are pushed to much higher densities and higher temperatures are reached during the bursts.

3.2. *Accretion Rate for Stabilization at 10 Times the Reference Opacity*

Usually, in numerical simulations, the recurrence time between bursts decreases with increasing accretion rate, until the critical rate for stabilization is reached (see e.g. Heger et al. 2007). Considering the behavior of the $0.3\dot{M}_{\mathrm{Edd}}$ envelope model at 10κ, we kept this higher opacity fixed and varied the accretion rate. As shown in the upper panel of Figure 2, the bursting behavior actually ceases between 5.26 and 6.26 $\times 10^{-9}$ $M_\odot\,\mathrm{yr}^{-1}$, corresponding to 0.3 and $0.35 \times \dot{M}_{\mathrm{Edd}}$ respectively. Considering the $0.35 \times \dot{M}_{\mathrm{Edd}}$ case, after a first burst, which should be regarded as an artifact of the simulations, the luminosity shows damped oscillations and in less than 1 hr reaches an equilibrium value. As intuitively expected, this equilibrium value depends on $\dot{M}$.

We ran more simulations between 0.5 and 1.0 $\dot{M}_{\mathrm{Edd}}$ displayed in the upper panel of Figure 2 as well, and found that indeed all show stable burning. We also tested the effect of increasing the base luminosity to $L_b = 2.5 \times 10^{-1} L_\odot$. The resulting luminosities as function of time are displayed in the lower panel of Figure 2. Despite the small differences - at fixed accretion rate, among the models of upper and lower panels - in both scenarios the burning stabilizes between 0.3 and 0.35 $\dot{M}_{\mathrm{Edd}}$, as found in observations.

3.3. *The Role of the Different Contributions to the Opacity*

All models in the former sections have a common factor applied to the whole opacity function at all depths. However, the opacity contains several components, from electrons and from photons, and for the latter contributions from electron scattering and free-free. In Figure 3 we exhibit a typical profile of κ and the contributions of its various components.

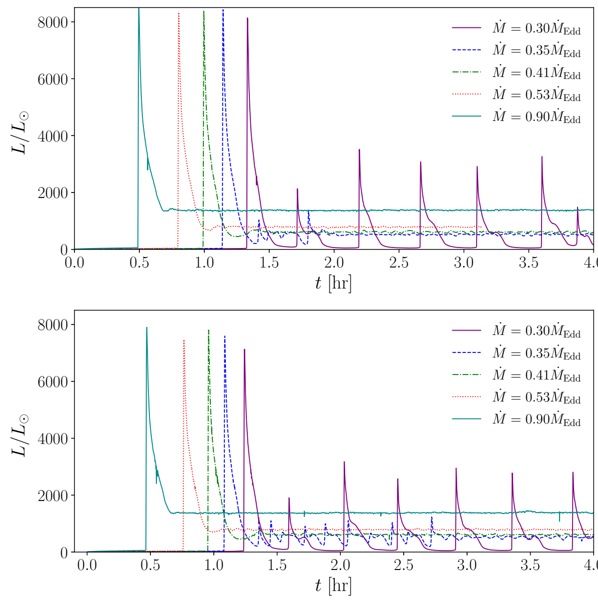

Fig. 2. Luminosity (in units of $L_\odot$) as a function of time for different values of mass accretion rate. The luminosity at the base is $L_b = 2.5 \times 10^{-5} L_\odot$ in the upper panel and $L_b = 2.5 \times 10^{-1} L_\odot$ in the lower one (equivalent Q_b ranges, corresponding to the $\dot{M}$ range explored, are $1 - 3 \times 10^{-7}$ and $1 - 3 \times 10^{-3}$ MeV per baryon in the upper and lower panels, respectively). In all cases the opacity is globally increased by a factor of 10. The color figure can be viewed online.

Here, we will explore the impact of each component as well as the various options for the components of the radiative part. We will designate by $\kappa_{\mathrm{Analytic}}$ the opacity where the radiative part is from the analytical fits described in Section 2 and by $\kappa_{\mathtt{MESA}}$ the one where we employ the `MESA` supplied radiative opacity. Similarly we have, in our analytical fits, two options for the electron scattering contribution which we denote as κ_{es} (Paczynski) and κ_{es} (Poutanen).

As a first step we compare the effect of employing the two schemes for the radiative opacity, multiplying the whole opacity by a factor of ten. These are the models $10\kappa_{\mathrm{Analytic}}$ and $10\kappa_{\mathtt{MESA}}$ shown in Figure 4 where one sees that the differences are minimal.

As a second step we multiply by 10 only the radiative part, leaving untouched the conductive part: this is the model $10\kappa_{\mathrm{rad}}$ (in which we used the analytical scheme of radiative opacity). This one also exhibits quenching of bursts with the only difference, compared to the previous models, that its initial explosion previous to quenching is delayed. The lower panel shows how the accreted layer has to reach higher densities for the first explosion to occur: this is due to the fact that in this region the opacity is

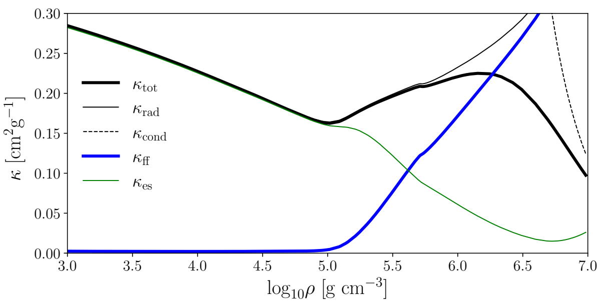

Fig. 3. Opacity profile for a typical stationary accreted envelope at $\dot{M}_{\rm Edd}$. The color figure can be viewed online.

dominated by the electron opacity, which we do not alter in this case, and this allows a strong leakage of heat towards the interior, keeping these deeper layers colder than in the previous cases. However, after this first burst, the model converges toward the same state as the previous $10\kappa_{\rm Analytic}$ and $10\kappa_{\texttt{MESA}}$ runs. This result proves that electron conduction has little effect on the bursting behavior and its possible quenching.

As a final step we determine which component of the radiative opacity is responsible for the quenching. For this we consider the three models $10\kappa_{\rm ff}$, $10\kappa_{\rm es}$ (Paczynski), and $10\kappa_{\rm es}$ (Poutanen) in which either the free-free opacity (first model) or the electron scattering one (second and third models) is increased by a factor 10. The last two are also exploring whether small changes in $\kappa_{\rm es}$ may have an effect (changing from the old fit of Paczynski (1983b) to the recent one of Poutanen (2017)). Figure 4 shows that the model $10\kappa_{\rm ff}$ does not result in stable burning, while the other two do. This definitively proves that the mechanism for the quenching of bursting behavior is the increase in the opacity at low densities, the region where $\kappa_{\rm es}$ dominates (see Figure 3).

3.4. *Exploring the Interplay Between Opacity, Base Luminosity, and Mass Accretion Rate*

Having found that a strong increase in the opacity, essentially the electron scattering part, is able to quench the bursts at the right $\dot{M}$, we here explore in more detail the sensitivity of this proposed mechanism to the two other basic parameters of the simulations: the base luminosity L_b or, equivalently, Q_b, and the mass accretion rate $\dot{M}$. We consider cases with the whole opacity multiplied by 2, 4, 6, and 8, and a wide range of values of L_b, listed in Table 2. For each of these we apply three values of $\dot{M}$ covering the estimated range in which the quenching of burst is occurring: $0.2\dot{M}_{\rm Edd}$, $0.3\dot{M}_{\rm Edd}$, and $0.4\dot{M}_{\rm Edd}$.

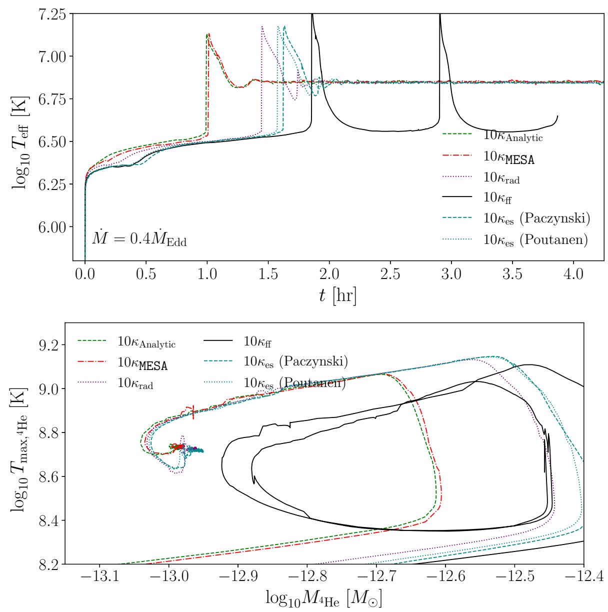

Fig. 4. Upper panel: effective temperature as a function of time for different opacities. Lower panel: maximum temperature of helium matter in the envelope versus the total mass of ^{4}He for the same models. The base luminosity is $2.5 \times 10^{-5} L_\odot$. The color figure can be viewed online.

Results of these many combinations are displayed in Figure 5. At the highest level of L_b no burst ever appears because the envelope is way too hot. At the second highest (model 4 in Table 2), we see that with an opacity factor of 2, panel (a), the frequency of bursts sharply increases with $\dot{M}$, and millihertz oscillations are clearly displayed at $0.4\dot{M}_{\rm Edd}$: these have been identified as a signal of the transition from unstable to stable burning (Heger et al. 2007). When pushing the opacity factor to 4 we effectively find that burst have been completely quenched.

Concerning the three lowest cases of L_b, one sees that Models 1 and 2 are very similar to each other at every panel regardless of $\dot{M}$ and `opacity_factor`. Model 3, on the other hand, exhibits variations in the number of bursts according to the accretion rate and opacity factor. However, once the `opacity_factor` is equal to 8, all three lowest levels reach a state of stable burning at $0.4\dot{M}_{\rm Edd}$.

4. DISCUSSION AND CONCLUSIONS

In this short letter we have explored the possibility of bursting suppression, between 0.3 and 0.4 $\dot{M}_{\rm Edd}$, as a consequence of changing the opacity of the envelope. We first used a global `opacity_factor` to change the opacity across the whole envelope profile, finding that increasing the

TABLE 2

BASE LUMINOSITY LEVELS FOR THE FIVE MODELS IN FIGURE 5, EXPRESSED IN DIFFERENT UNITS

			Q_b [MeV baryon^{-1}]		
Model #	$\log_{10} T_{\mathrm{eff},b}$ [K]	L_b [$L_\odot$]	$0.2\dot{M}_{\mathrm{Edd}}$	$0.3\dot{M}_{\mathrm{Edd}}$	$0.4\dot{M}_{\mathrm{Edd}}$
1	5.00	2.5×10^{-5}	4.5×10^{-7}	3.0×10^{-7}	2.2×10^{-7}
2	6.00	2.5×10^{-1}	4.5×10^{-3}	3.0×10^{-3}	2.2×10^{-3}
3	6.50	2.5×10^{1}	0.450	0.300	0.220
4	6.75	2.5×10^{2}	4.5	3.0	2.2
5	7.00	2.5×10^{3}	45	30	22

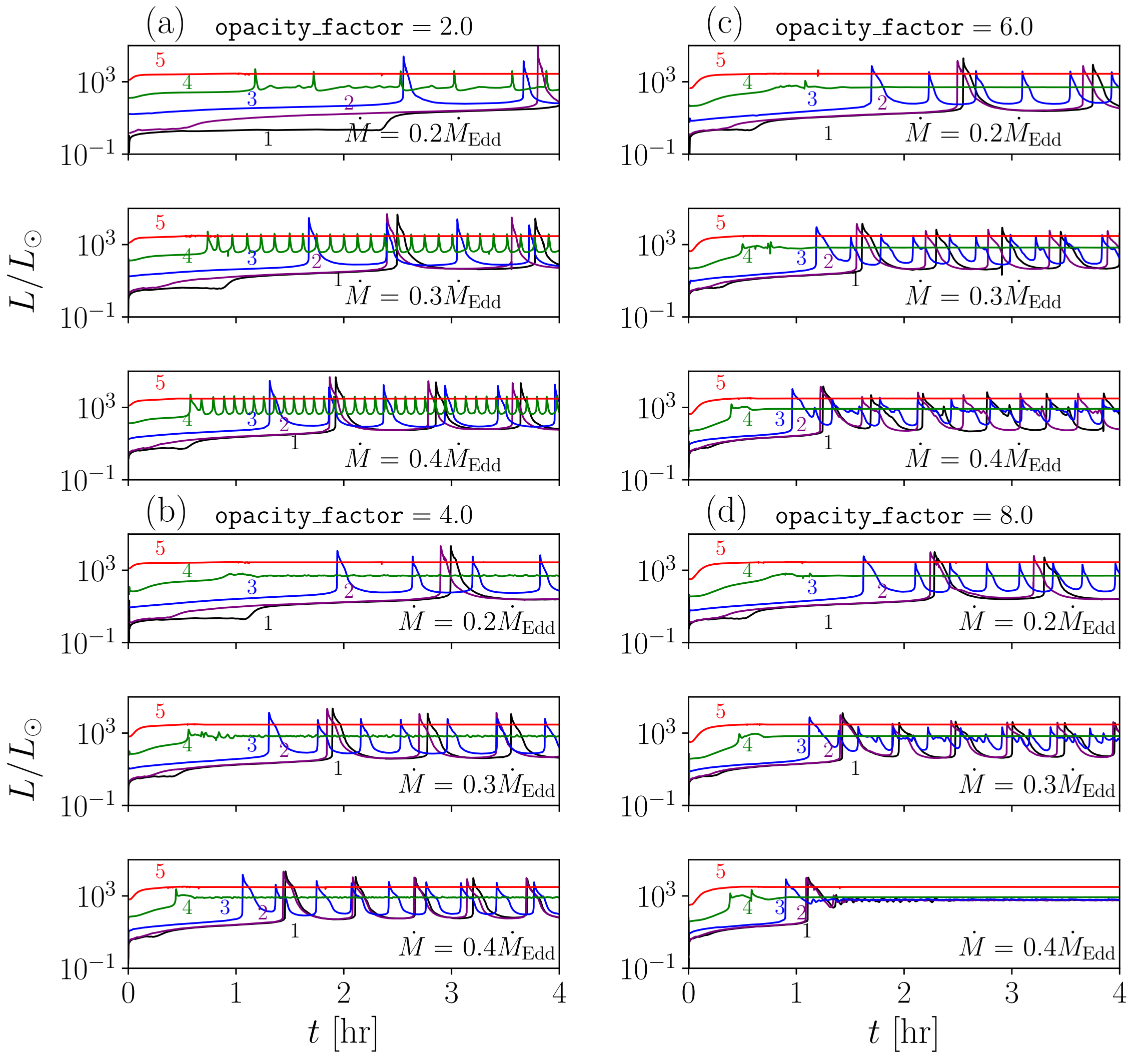

Fig. 5. Bursting and quenching sensitivity to opacity at various mass accretion rates and base heat flows L_b. The whole opacity is scaled by a factor 2 in Panel (a), 4 in Panel (b), 6 in Panel (c) and 8 in Panel (d). The three frames in each panel correspond to different mass accretion rates as indicated. Curves labeled 1 to 5 correspond to different values of L_b as listed in Table 2. The color figure can be viewed online.

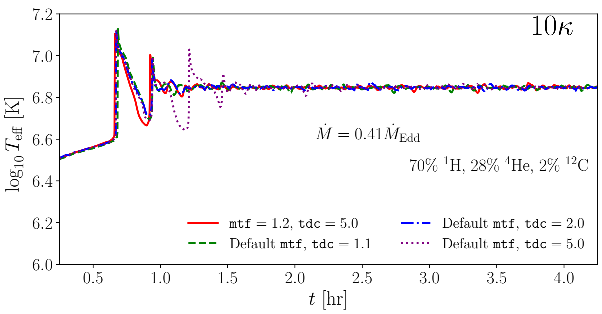

Fig. 6. Effective temperature as a function of time, at fixed opacity factor and accretion rate, for different setups of timestep. Here we use $\log_{10} \rho_b = 9.57$, $g_{s,14} = 2.16$, `mesh` $= 5.0$, ^{80}Kr at the base, `approx140` and the composition of the accreted matter is indicated in the plot. The color figure can be viewed online.

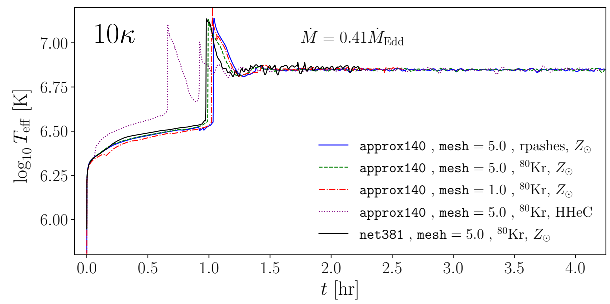

Fig. 7. Effective temperature as a function of time, at fixed opacity factor and accretion rate, for different combinations of parameters. For each model the network, `mesh` parameter, composition at the base and of accreted material is indicated in the labels, HHeC corresponding to the same distribution of H, He and C as in Figure 6. Common to all models are: $g_{s,14} = 2.16$, $\log_{10} \rho_b = 9.57$. The color figure can be viewed online.

opacity by a factor of 10 does stabilize the nuclear burning above 0.35 $\dot{M}_{\rm Edd}$.

We then explored which of the main three components (free-free and scattering contribution to the radiative opacity or the conductive opacity) was responsible for the bursting suppression. We found that it is essentially the electron scattering part that is able to quench the bursts, while an increase in the free-free component or the conductive part did not induce a noticeable suppression.

Burst suppression is also controlled by the assumed base luminosity $L_b = Q_b \cdot \dot{M}/m_u$ (see Table 2) flowing into the envelope from the stellar interior. Extremely high values of L_b/Q_b, as in Model 5, totally suppress bursts independently of the applied changes in the opacity. (Such high Q_b are, though, in the range of shallow heating inferred in the case of the system MAXI J0556-332, Deibel et al. 2015; Parikh et al. 2017; Page et al. 2022, even if most of this heat actually flows toward the interior and not into the envelope.) In the other extreme cases of vanishingly small values of L_b/Q_b, as Models 1 and 2, an enhancement in opacity of 8 is needed to induce burst suppression above 0.4 $\dot{M}_{\rm Edd}$ and intermediate cases are shown in Figure 5.

Although our numerical simulations need an increased opacity for suppressing the bursts, it is unlikely that electron scattering by itself could be increased by such a large factor. However, this could be seen only as a proxy replacement for an actual physical process enhancing the opacity of the envelope. This process should be acting at densities below $\approx 10^5$ g cm^{-3}, because we found that changing the electron scattering part of the opacity is sufficient, and this is the density range where that is the dominant process (see Figure 3).

On the other hand, a positive aspect of our results, considering that the rp-process produces nuclei with charge much higher than the values calculated in the Los Alamos tables (Colgan et al. 2016), is that even large uncertainties on the free-free contribution to the opacity at the high densities where it dominates have only very little effect on the predictions of bursting behavior.

APPENDICES

A. IMPACT OF SEVERAL PARAMETERS

One concern could be that the bursting suppression is also a consequence of our other choices for the parameters, not only of the change in opacity. For example, setting `mtf` $= 1.2$ leads to progressively longer time steps, which may influence the evolution of the column by skipping important variations in the burning. To test whether this is the case, we ran a few simulations, keeping the accretion rate fixed at $7.26 \times 10^{-9}\ M_\odot\,{\rm yr}^{-1}$ ($\approx 0.4\dot{M}_{\rm Edd}$) as well as an increased opacity of 10κ, but changing other parameters. In particular, we focus on the following, and the resulting light curves can be found in Figures 6 and 7:

- **Limits to the time step in the mesh.** We modified both `time_delta_coeff` and `min_timestep_factor` to favor longer or shorter time steps.

- **Number of cells in the mesh.** This is partially controlled by the user via the `mesh_delta_coeff` parameter. In our simulations, a value around and above 5 restricts the amount of cells below 500, while with a value

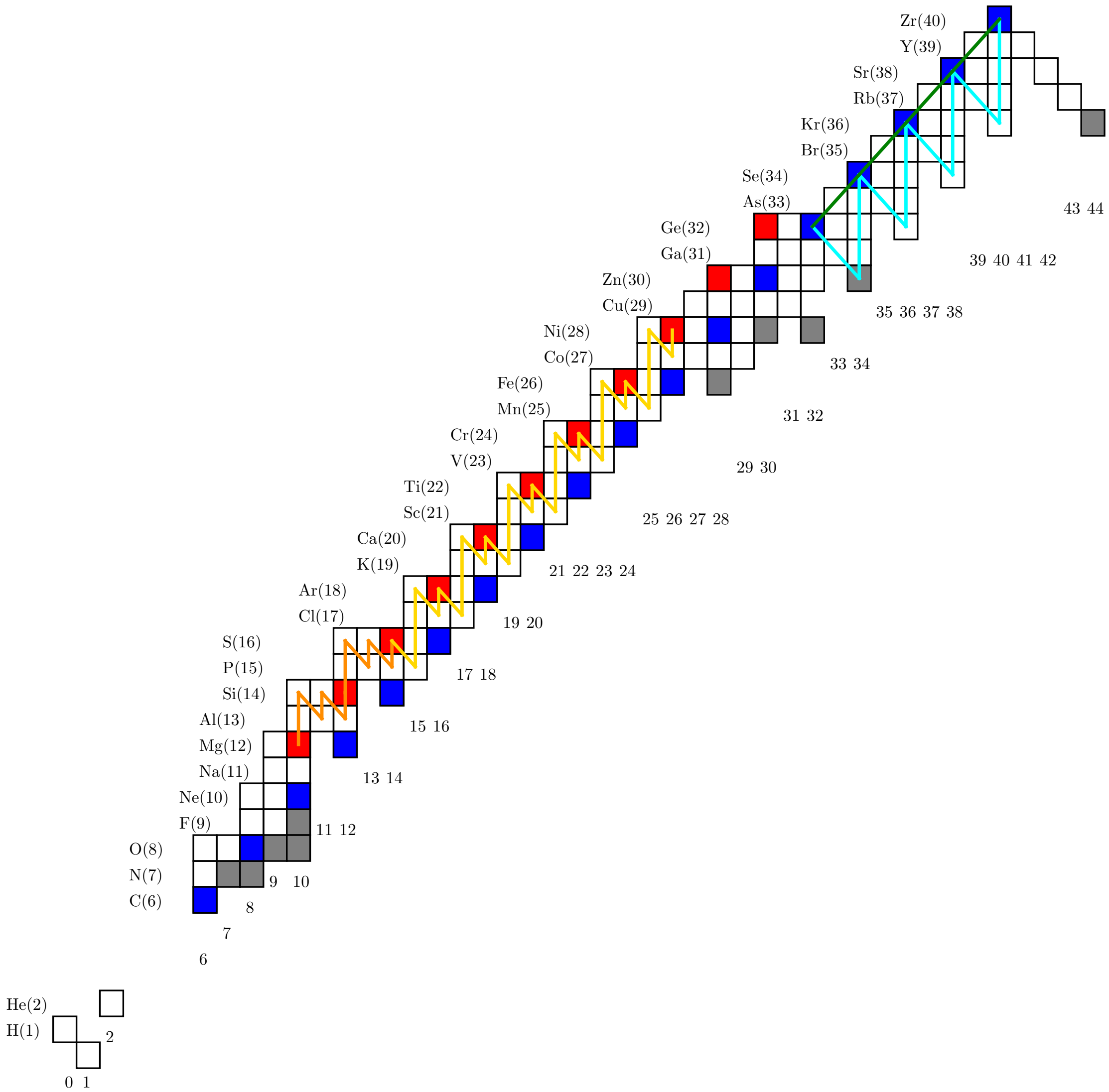

Fig. 8. Nuclide chart of the `approx140` network. Numbers in parenthesis after element symbols are the charges Z, while numbers below the chart are the neutron numbers $N = A - Z$ of the various isotopes. Red squares: $T_z = -1$ nuclides. Blue squares: α nuclides. Dark-gray squares: nuclides in the valley of stability. The orange and yellow lines correspond to the main flow of the rp-process below $A = 56$, while the green and cyan lines correspond to the main flow above $A = 64$. See the main text for further details. The color figure can be viewed online.

around 1 the cells can be as many as 2000 to 3000.

- **Number of species in the network.** To rule out the possibility of the electroweak reactions from the omitted nuclides in the `approx140` network altering the bursting behavior, we used the network of 380 species described in Nava-Callejas et al. (2024), adding neutrons for a fair comparison with the `approx140`, and thus resulting in 381 species. We refer to this larger network as `net381`.

- **Composition of the base.** We chose two compositions: either the rp-ashes mixture, or a single-species with a heavy nucleus, ^{80}Kr, common to both networks we considered.

- **Composition of accreted material.** We explored two compositions: the first is the Solar-like distribution, detailed in Section 2, while the second composition is a simpler mixture of 70%

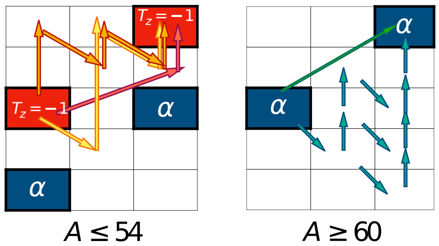

Fig. 9. Left panel: box scheme of the rp-process occurring for nuclides with $A \leq 54$. Here we observe three paths of reactions, illustrated with arrows: $(a,p)-(p,\gamma)$ in red, sawtooth in orange and β-3p-β-p in yellow. Right panel: triangle-like structure of the rp-process for $A \geq 60$ nuclides. The green arrow illustrates the (α,γ) capture while the cyan arrows illustrate the paths of proton captures and β^+ decays. The color figure can be viewed online.

^{1}H, 28% ^{4}He and 2% ^{12}C, key species in the actual synthesis of heavier elements via the rp-process. ^{12}C is necessary for a fair comparison between `net381` and `approx140` due to the absence of Li, Be and B isotopes directly connecting ^{4}He with C, N and O in the latter network.

To test the impact of time-step controls on stabilization, we performed simulations altering both `mtf` and `tdc`, employing the `approx140` network, ^{80}Kr as the composition of the base and the simpler accretion mixture. The models discussed in the main text have `mtf` $= 1.2$ and `tdc` $= 5.0$ (this is the red curve in the Figures of this Appendix), while we test combinations with `MESA`'s default value of `mtf` $= 0.8$ and `tdc` $= 1.1, 2, 5$. The overall similarity of all results with respect to our fiducial one strongly suggest that our previous results are solely due the the change in opacity and not an artifact of the numerical integration. Some discrepancies can still be seen, though they don't change the conclusions. For instance, employing the default value for `mtf` in combination with a large `tdc` induces an additional burst and delays the stabilization for 0.5 hr. The equilibrium temperature, however, is similar to that of the rest of the models. The second difference is the time span of the decay phase after the burst peak, which is slightly shorter in the `mtf` $= 1.2$ case than in the rest of the simulations.

The other important numerical parameter is resolution. The difference in mesh size does not produce appreciable deviations, neither in the first "numerical" burst nor in the equilibrium temperature, suggesting that our fiducial parameters for the resolution are high enough (Figure 7).

We now turn to more physical parameters (Figure 7). Regarding the size of the network, although the decay after the peak of the first burst using `net381` is faster than for the `approx140` model, the overall behavior is the same: only one burst occurs, followed by a damping process finally converging to a stable state. The oscillations from the `net381` network around the equilibrium value are slightly more visible than those generated by the `approx140` network, but this difference is minor.

With respect to the base composition we observe little difference in the stabilization properties when using either of the ashes mixtures or pure ^{80}Kr , although some differences in the rise and decay phases of the first burst are visible. The overall simulation reaches stabilization nonetheless, and there is little difference in the equilibrium temperature with respect to the rest of the models. When considering a different accreted composition, we notice that the absence of $Z > 6$ species in the fuel material delays the stabilization process after a secondary less-energetic burst has occurred. However, no major changes are noticeable when the burning turns stable.

B. MOTIVATION OF THE `APPROX140` NETWORK

The nuclides included in this network were listed in Table 1 and the resulting flow is pictured in Figure 8.

As a first step, pp chains were omitted since the energy production occurs just at the very surface, where compression is actually more energetic than nuclear reactions. Li, Be and B nuclides are thus ignored. All C, N and O isotopes for the hot CNO cycle are included. For $A \leq 54$, β^+ decays take less than 1 hour to occur (a remarkable exception is ^{26}Al). This implies that once a proton-rich A isotope has been synthesized during the rp-process, it might decay towards the valley of stability in just a few minutes. Due to the local maxima at α-nuclides in the distribution of ashes, we make the approximation of allowing the whole chain of β^+ decays towards the valley of stability only to isotopes leading to α-nuclides. Considering that the integrated flow of the rp-process, either in stable or explosive burning, proceeds between isospin $T_z \equiv (2Z-A)/2 = -1$ nuclides and α-nuclides, such approximation should not affect the evolution of ashes well below 10^8 g cm^{-3}. A secondary consequence of the necessity of keeping α-nuclides in the network is to adequately simulate ^{4}He burning. Between ^{22}Mg and ^{54}Ni we have a "box scheme" (Rembges et al. 1997), where a competition between the three chains of reactions pointed out by Fisker et al. (2006), occurring between $T_z = -1$ isotopes, takes place (see Figure 9, left). To decide which chain is more relevant, we considered the results of Schatz et al. (1999, 2001) as well as our own simulations (with updated reaction rates from Cyburt et al. 2010 and JINA Reaclib Database 2022): from ^{22}Mg to ^{26}Si and to ^{30}S, the saw-tooth path is the most prominent one and thus the associated isotopes are included in the network. On the other hand, from ^{30}S to ^{54}Ni, the β-3p-β-p path is the dominant one.

Between the $T_z = -1$ nuclides ^{54}Ni and ^{62}Ge, as well as the α nuclide ^{60}Zn, the fictitious axis of the main flow moves from $T_z = -1$ to α nuclides and those at two β^+ decays of separation from them, as for instance ^{60}Ni and ^{64}Zn.

At $A = 64$, specifically at ^{64}Ge synthesized during the peak of the bursts, the main flow now follows a triangular-like structure (a cascade of proton captures and β^+ decays connecting α-nuclides, Figure 9 right), while heavy isotopes such as ^{64}Zn, ^{68}Ge and ^{72}Se are synthesized and do not further decay due to their long lifetimes.

To reduce as many species in the network as possible, we simulate an endpoint to the rp process following two basic criteria: (i) H is fully exhausted at around 10^6 g cm^{-3}, and (ii) the heaviest nuclide must have a large (above 6 days) lifetime against β^+ decay. We find ^{80}Kr, and specifically the $A = 80$ family, as a suitable artificial endpoint for the process.

REFERENCES

Bildsten, L. 1998, ASIC 515, The Many Faces of Neutron Stars, ed. R. Buccheri, J. Van Paradijis, and M. A. Alpar (Boston, MA: Kluwer Academic Publishers), 419

Brown, E. F. & Cumming, A. 2009, ApJ, 698, 1020, https://doi.org/10.1088/0004-637X/698/2/1020

Cavecchi, Y., Galloway, D. K., Goodwin, A. J., Johnston, Z., & Heger, A. 2020, MNRAS, 499, 2148, https://doi.org/10.1093/mnras/staa2858

Colgan, J., Kilcrease, D. P., Magee, N. H., et al. 2016, ApJ, 817, 116, https://doi.org/10.3847/0004-637X/817/2/116

Cooper, R. L. & Narayan, R. 2006, ApJ, 648, 123, https://doi.org/10.1086/508167

Cornelisse, R., in't Zand, J. J. M., Verbunt, F., et al. 2003, A&A, 405, 1033, https://doi.org/10.1051/0004-6361:20030629

Cyburt, R. H., Amthor, A. M., Ferguson, R., et al. 2010, ApJS, 189, 240, https://doi.org/10.1088/0067-0049/189/1/240

Davids, B., Cyburt, R. H., José, J., & Mythili, S. 2011, ApJ, 735, 40, https://doi.org/10.1088/0004-637X/735/1/40

Deibel, A., Cumming, A., Brown, E. F., & Page, D. 2015, ApJ, 809, 31, https://doi.org/10.1088/2041-8205/809/2/L31

Fisker, J. L., Görres, J., Wiescher, M., & Davids, B. 2006, ApJ, 650, 332, https://doi.org/10.1086/507083

Fisker, J. L., Tan, W., Görres, J., Wiescher, M., & Cooper, R. L. 2007, ApJ, 665, 637, https://doi.org/10.1086/519517

Fujimoto, M. Y., Hanawa, T., & Miyaji, S. 1981, ApJ, 247, 267, https://doi.org/10.1086/159034

Galloway, D. K. & Keek, L. 2021, ASSL 461, Timing neutron Stars: Oscillations and Explosions, ed. T. M. Belloni, M. Méndez, and Chengmin, Z. (Berlin, Heidelberg: Springer), 209, https://doi.org/10.1007/978-3-662-62110-3_5

Galloway, D. K., Muno, M. P., Hartman, J. M., Psaltis, D., & Chakrabarty, D. 2008, ApJS, 179, 360, https://doi.org/10.1086/592044

Grevesse, N. & Sauval, A. J. 1998, SSC, 85, 161, https://doi.org/10.1023/A:1005161325181

Heger, A., Cumming, A., & Woosley, S. E. 2007, ApJ, 665, 1311, https://doi.org/10.1086/517491

Inogamov, N. A. & Sunyaev, R. A. 2010, AstL, 36, 848, https://doi.org/10.1134/S1063773710120029

JINA Reaclib Database. 2022, JINA Reaclib Database, https://reaclib.jinaweb.org

Keek, L., Langer, N., & in 't Zand, J. J. M. 2009, A&A, 502, 871, https://doi.org/10.1051/0004-6361/200911619

Nava-Callejas, M., Cavecchi, Y., & Page, D. 2024, arXiv e-prints, arXiv:2403.13994, https://doi.org/10.48550/arXiv.2403.13994

Paczynski, B. 1983a, ApJ, 264, 282, https://doi.org/10.1086/160596

_________. 1983b, ApJ, 267, 315, https://doi.org/10.1086/160870

Page, D., Homan, J., Nava-Callejas, M., et al. 2022, ApJ, 933, 216, https://doi.org/10.3847/1538-4357/ac72a8

Parikh, A. S., Homan, J., Wijnands, R., et al. 2017, ApJ, 851, 28, https://doi.org/10.3847/2041-8213/aa9e03

Paxton, B., Bildsten, L., Dotter, A., et al. 2011, ApJS, 192, 3, https://doi.org/10.1088/0067-0049/182/1/3

Paxton, B., Marchant, P., Schwab, J., et al. 2015, ApJS, 220, 15, https://doi.org/10.1088/0067-0049/220/1/15

Piro, A. L. & Bildsten, L. 2007, ApJ, 663, 1252, https://doi.org/10.1086/518687

Potekhin, A. Y. & Yakovlev, D. G. 2001, A&A, 374, 213, https://doi.org/10.1051/0004-6361:20010698

Poutanen, J. 2017, ApJ, 835, 119, https://doi.org/10.3847/1538-4357/835/2/119

Rembges, F., Freiburghaus, C., Rauscher, T., et al. 1997, ApJ, 484, 412, https://doi.org/10.1086/304300
Revnivtsev, M., Churazov, E., Gilfanov, M., & Sunyaev, R. 2001, A&A, 372, 138, https://doi.org/10.1051/0004-6361:20010434
Schatz, H., Bildsten, L., Cumming, A., & Wiescher, M. 1999, ApJ, 524, 1014, https://doi.org/10.1086/307837
Schatz, H., Aprahamian, A., Barnard, V., et al. 2001, PhRvL, 86, 3471, https://doi.org/10.1103/PhysRevLett.86.3471
Strohmayer, T. & Bildsten, L. 2010, in Compact Stellar X-ray Sources, ed. W. Lewin & M. van der Klis, CUP, 113
Watts, A. L. & Maurer, I. 2007, A&A, 467, 33, https://doi.org/10.1051/0004-6361:20077326
Wijnands, R., Degenaar, N., & Page, D. 2017, JApA, 38, 49, https://doi.org/10.1007/s12036-017-9466-5

DOI: https://doi.org/10.22201/ia.01851101p.2025.61.01.06

Yuri Cavecchi: Departament de Fisíca, EEBE, Universitat Politècnica de Catalunya, Av. Eduard Maristany 16, 08019 Barcelona, Spain (yuri.cavecchi@upc.edu).
Martín Nava-Callejas and Dany Page: Instituto de Astronomía, Universidad Nacional Autónoma de México, Apartado Postal 70-264, 04510 México, CDMX, México (mnava, page@astro.unam.mx).

Revista Mexicana de Astronomía y Astrofísica, **61**, 99–110 (2025)

https://doi.org/10.22201/ia.01851101p.2025.61.01.07

FERRERS BAR RESPONSE MODELS: A GRID CALCULATION FOR GALACTIC MODELS

A. Silva-Castro[1] and I. Puerari[1]

Received October 21 2024; accepted January 29 2025

ABSTRACT

This study numerically investigates the dynamics of barred spiral galaxies using 3D Ferrers bar response models. A total of 708 models were analyzed, incorporating variations in the axisymmetric potential (nucleus, bulge, disk, halo), bar length, mass, angular velocity, and disk stellar velocity dispersion. Model evaluation employed the Spearman correlation (to assess input-output relationships) and permutation feature importance in a Random Forest Regressor (to measure input variable impacts). Orbital configurations of test particles reveal the critical role of bar dynamics in shaping galaxies' morphological and kinematic properties. Key findings emphasize how the bar potential influences major orbital families, affecting barred galaxies' long-term structure. These results provide deeper insights into galactic component interactions and a robust framework for understanding bar properties.

RESUMEN

Este estudio investiga numéricamente la dinámica de galaxias espirales barradas mediante modelos de respuesta de barras de Ferrers en 3D. Se analizaron 708 modelos, variando el potencial axisimétrico (núcleo, bulbo, disco, halo), la longitud, masa y velocidad angular de la barra, y la dispersión estelar del disco. La evaluación incluyó la correlación de Spearman y el "*permutation feature importance*" en un "*Random Forest Regressor*". Las configuraciones orbitales revelan el papel crítico de la barra en la formación de propiedades morfológicas y cinemáticas. Los resultados destacan cómo su potencial influye en las principales familias orbitales y afecta la estructura galáctica a largo plazo. Estos hallazgos permiten una comprensión más profunda de las interacciones galácticas y un marco sólido para estudiar las barras.

Key Words: galaxies: evolution — galaxies: fundamental parameters — galaxies: kinematics and dynamics — galaxies: statistics — galaxies: structure

1. INTRODUCTION

Barred spiral galaxies are one of the most intriguing kind of objects in the universe. In these galaxies, a large bisymmetrical structure grows in the center of the disk component, modifying drastically the kinematics and the dynamics of the barions contained in the central part of the galaxy. Dark matter is also influenced by the formation of the bar structure (Valenzuela & Klypin 2003).

For decades, barred galaxies have been the subject of several observational, theoretical and numerical studies. It is now well established that bars significantly influence their host galaxies in various ways. As the bar grows over time, it transfers angular momentum from the inner disk to the outer disk and the dark matter halo, as discussed by several authors (Lynden-Bell & Kalnajs 1972; Sellwood 1981; Athanassoula 2003; Athanassoula et al. 2013). The growing bar will also direct gas to the center of the galaxy along the narrow lanes that represent loci of shocks within the bar region (Sorensen et al. 1976; Athanassoula 1992; Davoust & Contini 2004; Villa-Vargas et al. 2010; Spinoso et al. 2017; George et al. 2019) triggering the nuclear activity. The influence of the bar on gas dynamics has been the subject of extensive research over the years, with a wide range of studies dedicated to this topic (e.g. van Albada &

[1]INAOE, México.

Roberts 1981; Schwarz 1985; Piner et al. 1995; Maciejewski et al. 2002; Kim & Stone 2012; Pastras et al. 2022; Romeo et al. 2023; Sormani et al. 2024 and references therein).

There are also studies proving the kinematics of bars to be significant. In numerical simulations, the bar pattern speed (Ω_B), or angular velocity of the bar, is closely linked to the evolution of both the bar and its host galaxy. As the bar grows and transfers angular momentum to its surroundings, it generally slows down, resulting in a decrease in the pattern speed (Debattista & Sellwood 2000; Athanassoula 2003; Martinez-Valpuesta et al. 2006; Okamoto et al. 2015; Wu et al. 2018). The bar evolution is also influenced by its surrounding environment. Recent studies have demonstrated that the angular momentum of the dark matter halo plays a crucial role in shaping the evolution of both the bar and the disk, impacting the bar pattern speed, instability timescales, and other dynamics (Saha & Naab 2013; Petersen et al. 2016; Collier et al. 2018; Collier & Madigan 2021).

Observational studies have shown that barred galaxies exhibit increased star formation in their central regions (Matsuda & Nelson 1977; Hawarden et al. 1986; Garcia-Barreto et al. 1991; Kenney et al. 1992; Alonso-Herrero & Knapen 2001; Hunt et al. 2008; Coelho & Gadotti 2011; Ellison et al. 2011; Lin et al. 2020; Géron et al. 2024) as well as in the bar-end regions (Reynaud & Downes 1998; Verley et al. 2007; Díaz-García et al. 2020; Fraser-McKelvie et al. 2020; Maeda et al. 2020; Géron et al. 2024). Conversely, star formation is suppressed along the arms of the bar (Reynaud & Downes 1998; Zurita et al. 2004; Watanabe et al. 2011; Haywood et al. 2016; Géron et al. 2024). These observational and numerical studies highlight the significant role that bars play in the evolution of their host galaxies.

In this paper, we present a new numerical investigation by studying a large number of three-dimensional response models. The axisymmetric part of the models is generated to fit the Galactic circular rotation curve proposed by Sofue (2020). We tested a number of parameters such as disk particles velocity dispersion, and mass, size and angular pattern speed of the imposed bar. In § 2 we present our models, parameters, initial conditions and orbit integrations, and in § 3 we discuss the resulting bar structure observed in the particle distributions. The resulting values are discussed in § 4 and, finally, in § 5 we present a general discussion and our conclusions.

DOI: https://doi.org/10.22201/ia.01851101p.2025.61.01.07

2. SIMULATIONS

2.1. *Galactic Models*

The selected gravitational potentials are composed by a sum of the axisymmetric and bar components. The axisymmetric component itself is a superposition of several elements: a core and a bulge, both modeled by a Plummer potential (Plummer 1911), a disk represented by a Miyamoto-Nagai model (Miyamoto & Nagai 1975), and a halo described by a logarithmic potential (Richstone 1980). The full axisymmetric potential is then

$$\Phi_{ax} = -\frac{GM_{c1}}{r^2+r_{c1}^2} - \frac{GM_{c2}}{r^2+r_{c2}^2} - \frac{GM_D}{\sqrt{R^2+(a+\sqrt{z^2+b^2})^2}} + \frac{v_H^2}{2}\ln(r^2+r_H^2), \tag{1}$$

where $r^2 = x^2 + y^2 + z^2$, while $R^2 = x^2 + y^2$. M_{c1} and M_{c2} are the masses of the bulge and the core, respectively, and r_{c1} and r_{c2} are their radial scale lengths. M_D is the disk mass and a and b its structural parameters. For the halo, v_H is the asymptotic velocity and r_H its radial scale length. By comparing the circular velocity profiles obtained from different parameter sets with the observed velocities in the Milky Way within the first 40 kpc, as reported by Sofue (2020), and by employing the gradient descent method, we identified three parameter sets with nearly identical χ^2 values. This indicates that the potentials corresponding to these parameters are degenerate. However, these potentials exhibit distinct characteristics from one another. Figure 1 displays the circular velocities derived from the three models, which we will henceforth refer to as Model 1 (left panel), Model 2 (middle panel), and Model 3 (right panel), based on the influence of their respective disks. The parameter values corresponding to each model are provided in Table 1.

2.2. *Bar Models*

For the bar component, we employed the ellipsoidal Ferrers potential. The mass density associated with this potential is defined as:

$$\rho_B(m) = \begin{cases} \rho_{B_c}(1-m^2)^n & \text{for } m \le 1 \\ 0 & \text{for } m > 1, \end{cases} \tag{2}$$

where $\rho_{B_c} = \frac{105}{32\pi}\frac{M_B}{a_B b_B c_B}$ is the central density and $m = (x/a_B)^2 + (y/b_B)^2 + (z/c_B)^2$, while a_B, b_B and c_B are the semi-axes of the ellipsoid. The index n

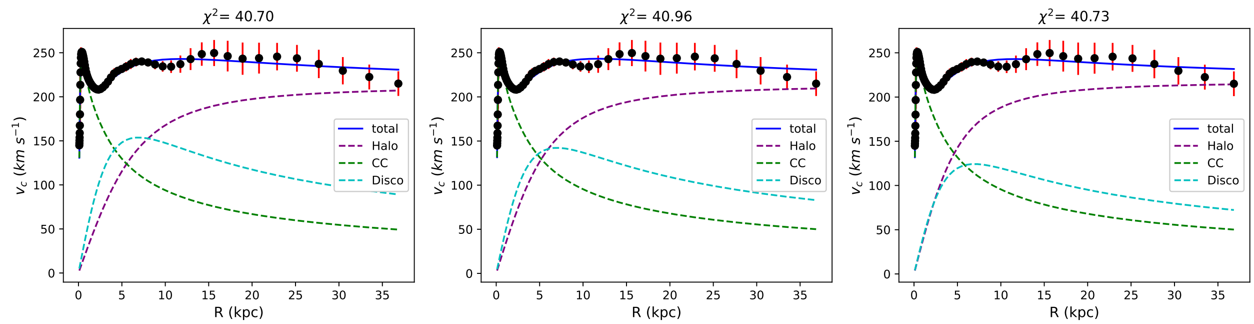

Fig. 1. The circular velocity curves corresponding to the axisymmetric potential for three different sets of parameter values. CC means Central Component (bulge+core). These curves are compared with the circular velocity of the Milky Way (Sofue 2020) within the first 40 kpc, along with their associated χ^2. The color figure can be viewed online.

TABLE 1

PARAMETERS FOR THE AXISYMMETRIC MODELS

Model	$\mathbf{r_{c1}}$ **(kpc)**	$\mathbf{M_{c1}}$ **($\mathbf{M_\odot}$)**	$\mathbf{r_{c2}}$ **(kpc)**	$\mathbf{M_{c2}}$ **($\mathbf{M_\odot}$)**	**a (kpc)**	**b (kpc)**	$\mathbf{M_D}$ **($\mathbf{M_\odot}$)**	$\mathbf{r_H}$ **(kpc)**	$\mathbf{v_H}$ **(km/s)**
1	1.46	1.07×10^{10}	0.278	1.01×10^{10}	4.66	0.233	6.99×10^{10}	7.68	212
2	1.46	1.15×10^{10}	0.275	1.00×10^{10}	4.72	0.236	6.06×10^{10}	6.78	213
3	1.45	1.16×10^{10}	0.274	9.96×10^{9}	4.69	0.235	4.60×10^{10}	5.73	217

is chosen to be $n = 2$. The forces generated by this potential are described in Pfenniger (1984).

To simplify the models, we fixed the ratios between the semi-axes, setting $b_B = a_B/3$ and $c_B = a_B/6$. However, the major semi-axis a_B was varied, considering three distinct values: 6, 4.5, and 3 kpc. We introduced the bar component as a smooth time-dependent function by gradually transferring mass from the disk to the bar in the following way:

$$M_B(t) = \begin{cases} \dfrac{M_{B_f}}{2}\left(1 - \cos\left(\dfrac{\pi}{T_{max}} t\right)\right) & \text{for } 0 \leq t \leq T_{\max} \\ M_{B_f} & \text{for } t > T_{\max}. \end{cases} \tag{3}$$

Here, M_{B_f} represents the final mass of the bar after its growth is completed at $T_{\max}$ which is set to 1 Gyr out of a total simulation time of 11.25 Gyr. Then, our models have a transient phase of 1 Gyr and are time independent after that. The evolution of the disk mass is then expressed as $M_D(t) = M_{D_i} - M_B(t)$. Rather than directly referring to M_{B_f}, we will use $\mu_B = \frac{M_{B_f}}{M_{D_i}}$, which denotes the final fraction of mass transferred from the disk to the bar.

The parameter $\mathcal{R} = \frac{R_{CR}}{a_B}$ (R_{CR} is the corotation radius, i.e., the radius at which the stars have the same angular speed as the pattern speed of the bar) is used to characterize the bar rotation rate. Bars are kinematically classified as 'slow' if $\mathcal{R} > 1.4$, 'fast' if $1.0 < \mathcal{R} < 1.4$ or 'ultrafast' if $\mathcal{R} < 1.0$ (see Debattista & Sellwood (2000); Rautiainen et al. (2008); Aguerri et al. (2015); Lee et al. (2022)). Concerning the $\mathcal{R}$ found for our barred models, we must note that each of the models has different axisymmetric backgrounds (Model 1, 2 or 3), different bar semi major axis a_b, different $\mu_B = \frac{M_{B_f}}{M_{D_i}}$ and different Ω_B. However, after the bar growth phase, with all parameters set, $\mathcal{R}$ depends solely on R_{CR} (determined by Ω_B) and a_B.

We are now able to analyze the bar rotation rate in a two-dimensional parameter space for $\mathcal{R}$ corresponding to each axisymmetric model, alongside the three selected values for the bar length, as illustrated in Figure 2 for Model 1. This methodology allows for the identification of models featuring either fast or slow bars, with varying values of μ_B and Ω_B. Therefore, we focused on models with $\mu_B = 0.1, 0.2, 0.3, 0.4, 0.5$ and $\Omega_B = 20, 25, 30, 35, 40, 50, 60$ km/s. Furthermore, only models with $1 \leq \mathcal{R} \leq 3$ were analyzed (indicated by red dots in Figure 2), corresponding to bars classified as fast and slow by Aguerri et al. (2015).

2.3. *Initial Conditions and Orbit Integrations*

Given our focus on stars within the disk, we selected the initial positions of the test particles following the axisymmetric distribution of the Kuzmin

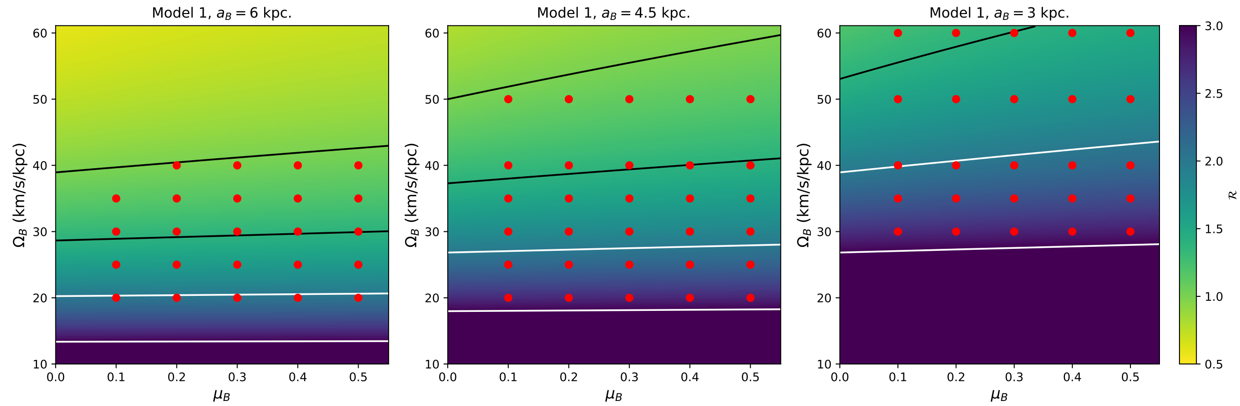

Fig. 2. Parameter space for $\mathcal{R}$ with respect to the parameters μ_B and Ω_B for model 1 and three values of bar length. The red dots are the models we studied in this article. Here we show the values only for Model 1, because there is no significant change of $\mathcal{R}$ when considering the three axisymmetric models (Model 1, Model 2 and Model 3), once they are time independent (see text). From bottom to top, the straight lines in each plot denote equal $\mathcal{R}$: 3 and 2 (white solid lines) and 1.4 and 1 (black solid lines). The color figure can be viewed online.

model whose surface density is (Binney & Tremaine 2008):

$$\Sigma_K(R) = \frac{aM_D}{2\pi(R^2 + a^2)^{3/2}}. \tag{4}$$

We have chosen to use KT models to create the initial particle distribution since our Miyamoto-Nagai models have a scale length ratio (a/b) of 20, i.e. the disks are very thin. Furthermore, all the particles are initially in the galactic plane ($z(t = 0) = 0$). Considering the relationship between surface density and the number of stars, we observe that at a given radius, the number of stars can be expressed as $N_K(R) = 2\pi\Sigma_K(R)$. By employing the Monte Carlo method, we can achieve a well-distributed arrangement of stars within the galactic plane. The maximum radius selected was given by $R_{max} = 1.5R_{CR}$. Although all particles are initially positioned within the galactic plane, the three-dimensional aspect of the simulations is established through the introduction of an initial velocity component along the z-axis.

For the velocity initial conditions, we decided to make $\bar{v}_\theta = v_c = \sqrt{R\frac{d\Phi_{ax}}{dR}}$, while $\bar{v}_R = \bar{v}_z = 0$, since all the stars in an axisymmetric galaxy (as in our models for $t = 0$) have near-circular orbits. On the other hand, the velocity dispersion for each coordinate decreases exponentially with radius as noted by Lewis & Freeman (1989):

$$\begin{aligned} \sigma_R(R) =& \sigma_R(0)\exp\left(-\frac{R}{2h_R}\right), \\ \sigma_T(R) =& \sigma_T(0)\exp\left(-\frac{R}{2h_T}\right), \\ \sigma_z(R) =& \sigma_z(0)\exp\left(-\frac{R}{2h_z}\right), \end{aligned} \tag{5}$$

where σ_R, σ_T and σ_z are the radial, tangential and vertical velocity dispersions, $\sigma_R(0)$, $\sigma_T(0)$ $\sigma_z(0)$ are their central values, and h_R, h_T and h_z are the scale lengths. In their work, Lewis & Freeman (1989) computed the specific values of h_R and h_T for the Milky Way, which were found to be 4.37 kpc and 3.36 kpc, respectively. In the same work, Lewis and Freeman also assumed that the ratio of radial velocity dispersion σ_R to vertical velocity dispersion σ_z remains constant. Consequently, we have chosen $h_z = h_R$.

For our research, we have chosen to equate the three central velocity dispersions ($\sigma_R(0) = \sigma_T(0) = \sigma_z(0) = \sigma_D$). Additionally, we explore three distinct values for this new parameter: 100, 80 and 50 km/s.

Hence, in total, we have 5 different galactic parameters: three different axisymmetric models, five distinct bar/disk mass ratios, seven angular velocities, three sets of bar lengths and three disk central velocity dispersion. This resulted in 945 different models. However, as mentioned before, only models with $1 \leq \mathcal{R} \leq 3$ were studied, and then our final set of simulations discussed here included 708 simulations. Each simulation comprised a total of 30,000 test particles, yielding a total of 21,240,000

TABLE 2

MODELS PARAMETER SPACE

Parameter	**Value**
Model	1, 2, 3
σ_D (km/s)	50, 80, 100
a_B (kpc) [a]	3, 4.5, 6
μ_B	0.1, 0.2, 0.3, 0.4, 0.5
Ω_B (km/s/kpc)	20, 25, 30, 35, 40, 50, 60

[a]The axis ratios are $b_B = a_B/3$ and $c_B = a_B/6$.

calculated orbits. A concise summary of the model parameter space is presented in Table 2.

The integration was carried out using a fourth-order Runge-Kutta integrator, employing Fortran subroutines. To assess stability, we monitored the Jacobi energy of test particles following bar growth. Typically, ΔE_J is better than 10^{-10} for $t > T_{max}$, since only then the models become time independent. The total simulation time was 11.25 Gyr, during which 1225 snapshots were captured at equidistant intervals. The bar mass growth ceases at $T_{max} = 1$ Gyr to ensure 1024 snapshots after the bar mass evolution. This number of points (2^{10}) was chosen to simplify the Fast Fourier Transform analysis.

3. ESTIMATING PROPERTIES OF THE BAR

3.1. *Detecting the Periodic Orbits x_1 and x_2*

As highlighted by several authors (e.g., Contopoulos (1970), Athanassoula et al. (1983), Sellwood & Wilkinson (1993), Skokos et al. (2002a) and Patsis & Athanassoula (2019), periodic orbits play a crucial role in shaping the structure of barred galaxies. These periodic orbits are categorized into four primary families, namely the x_1, x_2, x_3 and x_4 family orbits, following the classification by Contopoulos & Papayannopoulos (1980), with the most significant being the x_1 and x_2 families. Identifying these periodic orbits is essential for understanding the dynamics of barred galaxies.

To detect these orbits in our simulations, we applied a Fourier transform on the particle coordinates projected onto the equatorial plane: $x(t)$, $y(t)$, and $R'(t) = R(t) - \bar{R}$, where $\bar{R}$ is the mean radius of the particle orbit. This allowed us to extract the dominant frequencies, i.e., those with the highest amplitudes, in each coordinate. These frequencies are denoted as ω_x, ω_y, and ω_R, respectively. Additionally, the corresponding amplitudes were determined and labeled as A_x, A_y, and A_R.

It is crucial to emphasize that this analysis was conducted after the bar has reached its final mass, i.e., for $t > T_{max}$, as in our approach the stellar orbits stabilize and maintain a consistent pattern after the bar growth. In addition, prior to performing the Fourier transform, we applied a Hanning window function to the orbit positions. The purpose of this window function was to mitigate signal 'leakage' in the Fourier spectra.

We can now identify sticky orbits around the x_1 and x_2 families of periodic orbits (Contopoulos & Harsoula 2008; Katsanikas et al. 2013), but for simplicity, we will refer to them as members of the x_1 or x_2 families. An orbit is classified as part of the x_1 family if it satisfies the condition $1.9 \leq \omega_R/\omega_x \leq 2.1$ and $A_x/A_y \geq 2$. On the other hand, orbits that meet the criteria $1.9 \leq \omega_R/\omega_x \leq 2.1$ and $A_x/A_y \leq 0.5$ are associated with either the x_2 or x_3 family. However, it is important to note that the x_3 family is significantly less stable than the x_2 family (Skokos et al. 2002b), and as such, the presence of sticky-chaotic orbits around x_3 is expected to be minimal, making them insignificant for classification purposes.

Having identified the orbits belonging to the x_1 and x_2 families, we can now quantify the number of orbits in each family, denoted as N_{x_1} and N_{x_2}, respectively. Alternatively, we can calculate the proportion of x_1 and x_2 orbits relative to the total number of elliptical orbits, i.e., orbits that satisfy $1.9 \leq \omega_R/\omega_x \leq 2.1$. These proportions are denoted as P_{x_1} and P_{x_2}, respectively.

3.2. *Bar Strength*

We also performed a Fourier analysis on the stars positions to calculate the bar strength. For this, we computed the $m = 2$ mode Fourier coefficients (a_2 and b_2) based on the particle positions located within an annulus of width ΔR at a radius R. Hence, as highlighted by Chantavat et al. (2024), the amplitude of the bar is:

$$\tilde{A}_2^2(R) = a_2^2 + b_2^2, \tag{6}$$

where the bar strength corresponds to the maximum value $\tilde{A}_2$ within R_{CR}, expressed as:

$$A_2 \equiv \max_{R<R_{cor}} \tilde{A}_2(R). \tag{7}$$

We applied this method to each snapshot, making A_2 a time-dependent parameter $A_2(t)$. This time evolution of $A_2(t)$ was then used to analyze the properties and dynamics of the orbits in our galaxy models. In Figure 3, we observe the temporal evolution

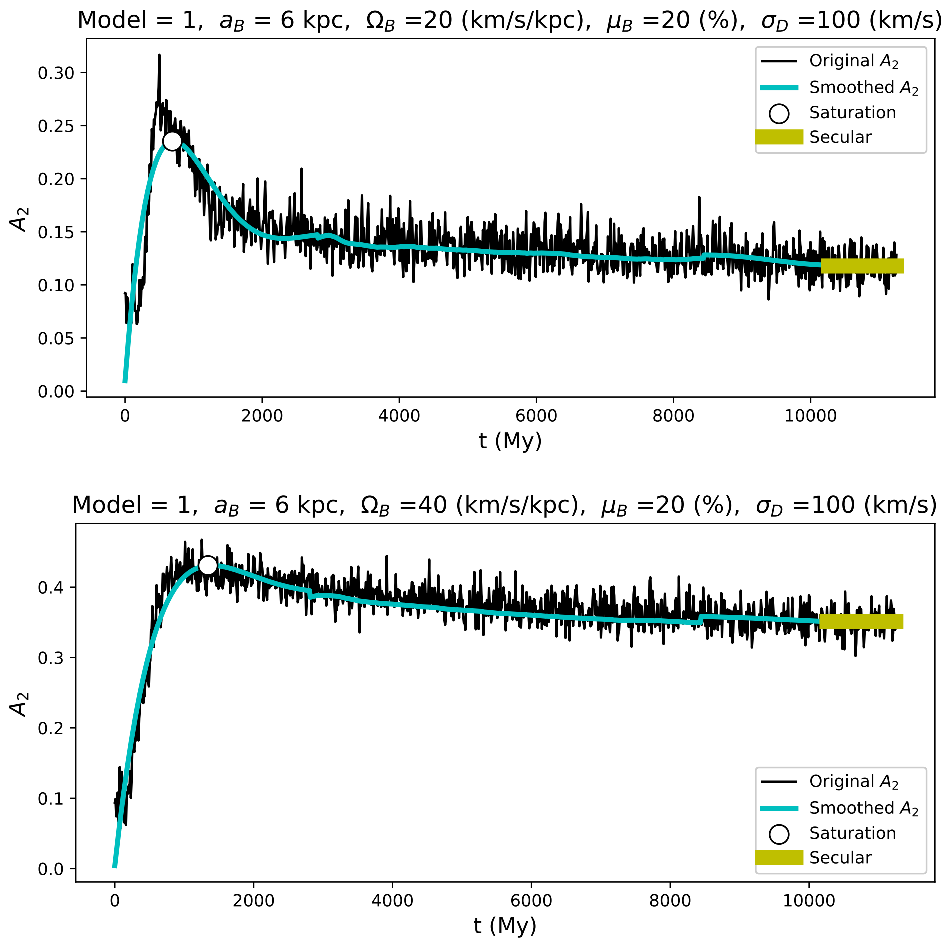

Fig. 3. Evolution of the bar strength $A_2(t)$ over time (black line) for two different models. The cyan line corresponds to the smoothed versions. Additionally, the white/black dot indicates the point of saturation in $A_2(t)$, while the horizontal yellow line represents the secular value associated. Notice the different behavior of $A_2(t)$; in one simulation, $A_2(t)$ decreases after the time of saturation, while in the other model, $A_2(t)$ remains more or less constant. The color figure can be viewed online.

of $A_2(t)$ for two given simulations. In the same figure, a smoothed version of this quantity is shown (the smoothing process employed a Savitzky-Golay filter with a sixth-order polynomial).

Even with the smoothed curves of $A_2(t)$, analyzing each curve individually is impractical since we have a very large number of galaxy models; therefore, we seek for characteristic values that help us to evaluate the model.

One such value is the saturation point in $A_2(t)$. As observed in Figure 3, the $A_2(t)$ curves initially experience a rapid growth, followed by a decline. Notably, several curves exhibit this decline after a specific time. We designate the values at this inflection point as A_{sat} and t_{sat}.

Another characteristic value becomes evident toward the end of the simulations for $A_2(t)$. At this point, the curves exhibit minimal changes over time. This behavior is expected since the structure of rotating Ferrers bars is primarily supported by the stable portion of the x_1 family. In a response model, any changes in A_2 after a couple of bar revolutions beyond $T_{\max}$ can therefore be attributed to the influence of chaotic or escaping orbits. To quantify this stability in the A_2 values, we calculated the average values over the last 1 Gyr. Specifically, we denote these values as $< A_{sec} >$.

An additional observation is the difference between A_{sat} and $< A_{sec} >$. Consequently, we designate this difference as another characteristic value, denoted by $\Delta A = A_{sat} - < A_{sec} >$.

4. FEATURE PARAMETERS VS RESULT VALUES

Having obtained several parameters that characterize the orbital behavior in each galaxy model, namely: N_{x_1}, N_{x_2}, P_{x_1}, P_{x_2}, A_{sat}, t_{sat}, $< A_{sec} >$, and ΔA, collectively referred to as the 'result values', we can now proceed to compare these values with the parameters that describe the galaxy, hereafter called the 'feature parameters'. These feature parameters include: Model, a_B, Ω_B, μ_B, and σ_D. Additionally, we will incorporate the parameter $\mathcal{R}$ previously introduced, along with the quadrupole moment of the bar as calculated by Garma-Oehmichen et al. (2021) for $n = 2$ (equation 8) and the bar angular momentum for $n = 2$ (equation 9),

$$Q_B = \frac{M_B}{9}\left(a_B^2 - b_B^2\right), \tag{8}$$

$$L_B = \frac{M_B \Omega_B}{9}(a_B^2 + b_B^2). \tag{9}$$

We employed two methods to compare the result values and the feature parameters. The first method involves calculating Spearman correlation coefficients (Spearman 1904), which measure the strength and direction of a monotonic relationship between two ranked variables. This approach allows us to observe how the feature parameters affect the result values. The coefficients, along with their corresponding p-values (which represent the probability of obtaining test results at least as extreme as the result actually observed (Spearman 1904)) are presented in Figure 4.

The second method, derived from machine learning, uses the permutation feature importance within a Random Forest Regressor (RFR). An RFR (Breiman 2001) is an ensemble learning method that combines multiple decision trees to improve predictive performance and reduce overfitting.

Initially applied in this field by Garma-Oehmichen et al. (2021), this approach evaluates the contribution of each feature to a given result value by randomly shuffling the values of a specific feature and measuring the resulting change in the so called R^2 score. The R^2 score quantifies how well the model explains the variance in the result value, ranging from 1 (perfect fit) to $-\infty$ (arbitrarily poor fit) (Pedregosa et al. 2011). The difference between the R^2 score for the original data (R^2_{baseline}) and the permuted data (R^2_{permuted}) reveals the feature's contribution to the model's performance (Garma-Oehmichen et al. 2021; Breiman 2001). This method helps to identify the most influential features, facilitating effective feature selection.

We trained the RFRs using 80% of the data, reserving the remaining 20% for testing, to find the optimal number of features for each result value. We set the number of trees in the model to 1,000 and determined the optimal model by selecting the one with the highest R^2. After identifying the best parameters for each result value, we retrained the models using the entire data set, following the method proposed by Garma-Oehmichen et al. (2021).

Finally, we estimated the permutation feature importance after 1,000 permutations for all result values, with the outcomes illustrated in Figures 5 and 6, along with the feature parameter distributions. It is crucial to emphasize that the importance values, represented by $R^2_{baseline} - R^2_{permuted}$, are not absolute. Consequently, these values should not be compared across different result values, but rather among feature parameters within the same result value.

As previously noted, we are now able to assess the relative importance of each feature parameter for a given result value through the use of feature importance, as illustrated in Figures 5 and 6. Additionally, the Spearman correlation coefficients presented in Figure 4 provide insights into the nature and direction of the relationships between feature parameters and result values. By combining these two methods, we have uncovered notable findings, which will be explored in detail in the following section.

5. DISCUSSION AND CONCLUSIONS

From the results presented in Figures 4, 5 and 6 we can derive numerous insights for each result value (N_{x_1}, N_{x_2}, ... $< A_{sec} >$, and ΔA, see § 4). However, we will limit our discussion to what we consider the three most significant findings in the following subsections:

5.1. *Evolution of x_1 and x_2 Orbits and Double Barred Galaxies*

It is essential to note that the methods introduced in § 4 are directly applied to the response model, allowing for the tracking of changes introduced whenever the parameter combinations depicted in Figure 4 occur. This approach provides significant practical value in the analysis of fully self-consistent N-body models, enabling a comprehensive assessment of the evolution of key orbital structures, particularly the x_1 and x_2 families.

In Figure 5, it is evident that the $\mathcal{R}$ parameter is the second most influential feature for determining N_{x_1}. Notably, the correlation coefficient between these two parameters in Figure 4 is strongly negative.

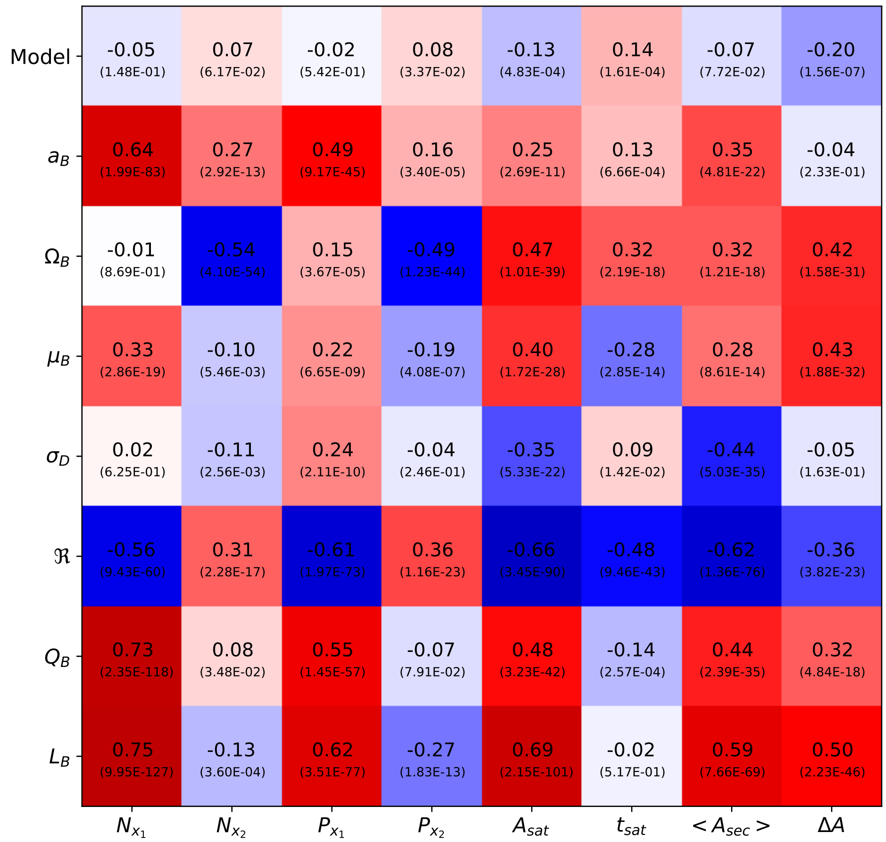

Fig. 4. Spearman correlation coefficients between the result values and the feature parameters for all of our models (708 models). The associated p-values are provided in parentheses. Bright red colors represent high correlations, while bright blue ones represent high anti-correlations. The lighter the color, the weaker the correlation of a given feature parameter with the result value.

Conversely, the most significant feature for N_{x_2} is Ω_B, which also exhibits a negative correlation.

Previous studies using N-body simulations (e.g., Athanassoula 2003; Manos & Machado 2014) have demonstrated that in barred galaxies, Ω_B tends to decrease over time, consequently $\mathcal{R}$ increases. When combined with our findings, this suggests that barred galaxies may initially feature a fast bar, characterized by a high number of x_1 orbits, and gradually lose some of these orbits as the system evolves. Simultaneously, as Ω_B decreases, the bar could be acquiring a larger number of x_2 orbits.

Moreover, the presence of a significant concentration of x_2 orbits could offer an explanation for the existence of a secondary bar in certain galaxies (Friedli et al. 1996; Maciejewski et al. 2002; Erwin 2004; Wozniak 2015; Erwin 2024). This indicates that double-barred galaxies may be dynamically more evolved systems.

5.2. *Characterizing Bar Strength Evolution Through* ΔA

Figure 3 presents two distinct bar strength curves over time, $A_2(t)$. The first curve exhibits rapid growth until it reaches a saturation point. After saturation, the bar rapidly weakens until it reaches an equilibrium (as expected for response models) with $< A_{sec} >$. In contrast, in the second curve the bar also weakens beyond the saturation point, although at a much slower rate. Looking at the other $A(t)$ curves we can note that there are intermediate cases.

The parameter ΔA plays a crucial role in understanding this behavior. A large positive value of ΔA indicates that A_{sat} is larger than $< A_{sec} >$, aligning with the behavior observed in the first case in Figure 3. Conversely, a small ΔA corresponds to a behavior more related to the second case shown in the same figure.

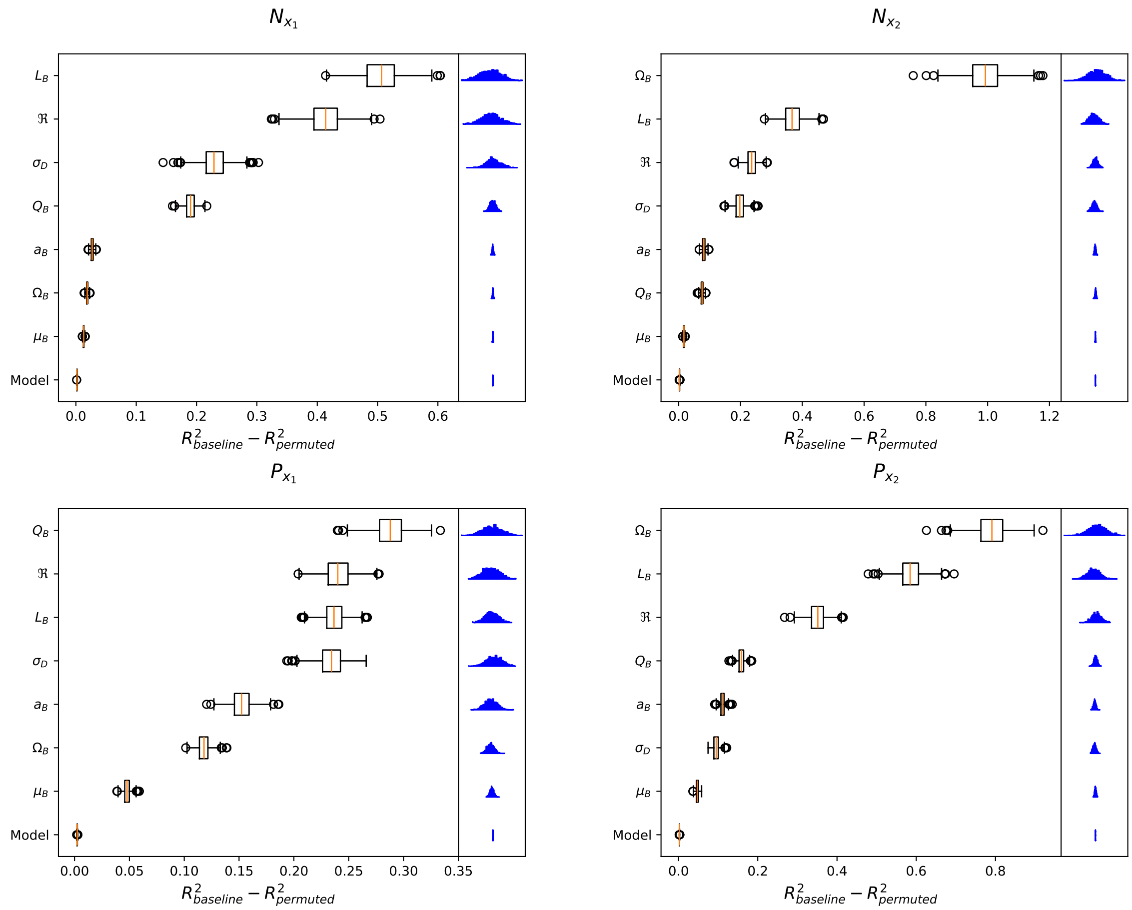

Fig. 5. The permutation feature importance calculated using RFRs, trained to predict each specific result value related to the x_1 and x_2 families, is depicted. Each feature was permuted 1000 times, generating a distribution of $R^2_{baseline} - R^2_{permuted}$ scores. The orange line represents the median value of the distribution. The box limits indicate the 25th and 75th percentiles, while the whiskers extend to the minimum and maximum values. Outliers in the distribution are shown as open circles. The distribution itself is illustrated on the right side for each feature parameter. The color figure can be viewed online.

As previously discussed, the x_1 family of orbits forms the backbone of rotating Ferrers bars, remaining stable in the region that supports the bar. In a response model, the decreasing of ΔA could be attributed to the presence of chaotic or escape orbits within the system. To verify this last statement, a study using an index to quantify the chaotic behavior of the orbits as GALI2 (Skokos et al. 2007; Chaves-Velasquez et al. 2017; Caritá et al. 2019) could be performed. However, this is beyond the scope of the present paper.

The permutation feature importance analysis for ΔA (Figure 6) shows that the primary feature parameter, with a significantly larger importance compared to other feature parameters, is $\mathcal{R}$. Furthermore, the Spearman correlation between ΔA and $\mathcal{R}$ (as shown in Figure 4) is negative. From this, we can infer the following:

- **Slow Bars:** In cases of slow bars, the models lose x_1 particles at a very slow rate after reaching the saturation point (as in the second case mentioned earlier in Figure 3).
- **Fast Bars:** Conversely, fast bars experience fast particle loss beyond the saturation point (similar to the first case mentioned previously in Figure 3).

5.3. *Impact of Disk-to-Halo Ratio on Bar Formation*

In § 2.1, we constructed three distinct axisymmetric models. These models exhibit the circular velocity closest to that of the Milky Way within the

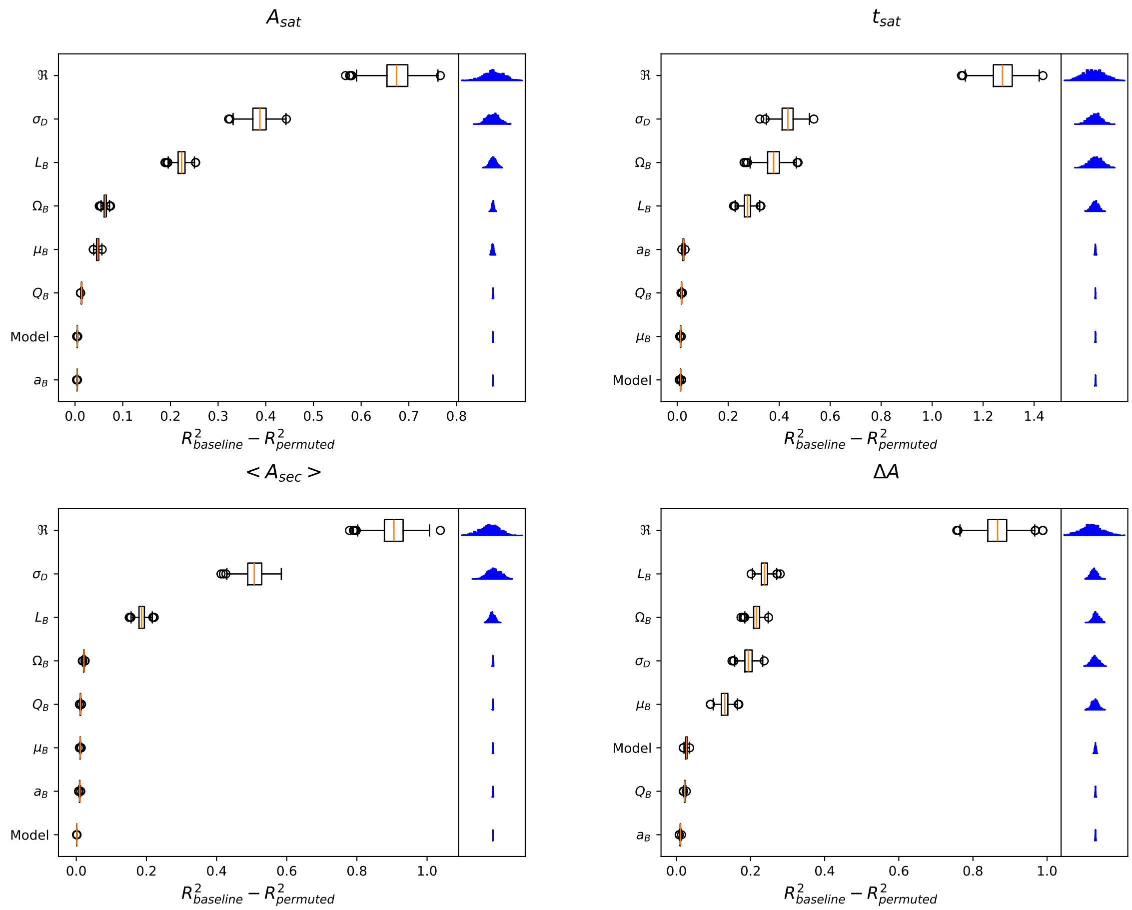

Fig. 6. As in Figure 5 but for the result values related to the bar strength.

first 40 kpc, as shown in Figure 1. Despite exhibiting degeneracy in terms of circular velocity, discernible differences exist among them, primarily in the disk-to-halo ratio. Model 1 shows a strong disk influence compared to the halo for $R < 8$ kpc, whereas Model 3 shows a stronger halo influence compared to the disk from $R > 3$ kpc. Model 2 represents an intermediate case.

Since earlier works by Athanassoula & Sellwood (1986), it is known that galaxies with a stronger disk influence, as seen in Model 1, tend to form bars more rapidly than those in which the halo is predominant, like in Model 3 (see also Valencia-Enríquez et al. 2023). However, the permutation importance for all eight result values shown in Figures 5 and 6 indicate that the variations among the axisymmetric models have a negligible impact on the result values. This finding is corroborated by the Spearman correlation coefficients presented in Figure 4, where it is evident that most of the coefficients related to the axisymmetric model are nearly zero. The most significant correlation is for ΔA with a coefficient of -0.20, which is insufficient to establish a strong anticorrelation.

The apparent contradiction presented here arises from the context of this work, which belongs to rigid potential models. It is noteworthy that when one performs a N-body fully self-consistent models, the structural parameters of the galactic components exhibit temporal evolution, and there is a transfer of angular momentum among the components. In our research, we are imposing the same bar model characterized by parameters μ_B, a_B, and Ω_B across all three axisymmetric models.

Consequently, we can conclude that for degenerate models, using rigid potentials, the variation in disk-to-halo does not significantly affect the the formation of x_1 and x_2 orbits.

Finally, it is crucial to highlight that combining the Spearman correlation coefficients with the feature importance derived from a Random Forest Regressor significantly enhances the analysis of the effects of different input parameters on output results. The Spearman correlation provides insight into the monotonic relationships between values, while the feature importance in a Random Forest Regressor evaluates the overall significance of each parameter. Using both methods allows for a comprehensive understanding of the importance and behavior of various parameters.

In conclusion, our work provides a detailed investigation into the dynamics of barred galaxies, offering insights into the interplay between various galactic parameters and the formation and evolution of galactic structures. The methodologies employed and the findings derived from this study contribute to the broader understanding of galactic dynamics and serve as a foundation for future research in this field.

We sincerely thank the referee for his/her comments which have greatly improved and clarified the presentation of our study.

REFERENCES

Aguerri, J. A. L., Méndez-Abreu, J., Falcón-Barroso, J., et al. 2015, A&A, 576, A102, https://doi.org/10.1051/0004-6361/201423383

Alonso-Herrero, A. & Knapen, J. H. 2001, AJ, 122, 1350, https://doi.org/10.1086/322130

Athanassoula, E., Bienayme, O., Martinet, L., et al. 1983, A&A, 127, 349

Athanassoula, E. & Sellwood, J. A. 1986, MNRAS, 221, 213, https://doi.org/10.1093/mnras/221.2.213

Athanassoula, E. 1992, MNRAS, 259, 345, https://doi.org/10.1093/mnras/259.2.345

Athanassoula, E. 2003, MNRAS, 341, 1179, https://doi.org/10.1046/j.1365-8711.2003.06473.x

Athanassoula, E., Machado, R. E. G., & Rodionov, S. A. 2013, MNRAS, 429, 1949, https://doi.org/10.1093/mnras/sts452

Binney, J. & Tremaine, S. 2008, Galactic Dynamics (2nd ed.; Princeton, NJ: PUP)

Breiman, L. 2001, Machine Learning, 45, 5, https://doi.org/10.1023/A:1010933404324

Caritá, L. A., Rodrigues, I., Puerari, I., et al. 2019, RMxAA, 55, 321, https://doi.org/10.22201/ia.01851101p.2019.55.02.17

Chantavat, T., Yuma, S., Malelohit, P., & Worrakitpoonpon, T. 2024, ApJ, 965, 77, https://doi.org/10.3847/1538-4357/ad3218

Chaves-Velasquez, L., Patsis, P. A., Puerari, I., Skokos, Ch., & Manos, T. 2017, ApJ, 850, 145, https://doi.org/10.3847/1538-4357/aa961a

Coelho, P. & Gadotti, D. A. 2011, ApJ, 743, 13, https://doi.org/10.1088/2041-8205/743/1/L13

Collier, A., Shlosman, I., & Heller, C. 2018, MNRAS, 476, 1331, https://doi.org/10.1093/mnras/sty270

Collier, A. & Madigan, A.-M. 2021, ApJ, 915, 23, https://doi.org/10.3847/1538-4357/ac004d

Contopoulos, G. 1970, AJ, 75, 96, https://doi.org/10.1086/110948

Contopoulos, G. & Harsoula, M. 2008, IJBC, 18, 2929, https://doi.org/10.1142S0218127408022172

Contopoulos, G. & Papayannopoulos, T. 1980, A&A, 92, 33

Davoust, E. & Contini, T. 2004, A&A, 416, 515, https://doi.org/10.1051/0004-6361:2003172

Debattista, V. P. & Sellwood, J. A. 2000, ApJ, 543, 704, https://doi.org/10.1086/317148

Díaz-García, S., Moyano, F. D., Comerón, S., et al. 2020, A&A, 644, 38, https://doi.org/10.1051/0004-6361/202039162

Ellison, S. L., Nair, P., Patton, D. R., et al. 2011, MNRAS, 416, 2182, https://doi.org/10.1111/j.1365-2966.2011.19195.x

Erwin, P. 2004, A&A, 415, 941, https://doi.org/10.1051/0004-6361:20034408

Erwin, P. 2024, MNRAS, 528, 3613, https://doi.org/10.1093/mnras/stad3944

Fraser-McKelvie, A., Aragón-Salamanca, A., Merrifield, M., et al. 2020, MNRAS, 495, 4158, https://doi.org/10.1093/mnras/staa1416

Friedli, D., Wozniak, H., Rieke, M., Martinet, L., & Bratschi, P. 1996, A&AS, 118, 461, https://doi.org/10.48550/arXiv.astro-ph/9603067

Garcia-Barreto, J. A., Dettmar, R.-J., Combes, F., Gerin, M., & Koribalski, B. 1991, RMxAA, 22, 197

Garma-Oehmichen, L., Martinez-Medina, L., Hernández-Toledo, H., & Puerari, I. 2021, MNRAS, 502, 4708, https://doi.org/10.1093/mnras/stab333

George, K., Joseph, P., Mondal, C., et al. 2019, A&A, 621, 4, https://doi.org/10.1051/0004-6361/201834500

Géron, T., Smethurst, R. J., Lintott, C., et al. 2024, ApJ, 973, 129, https://doi.org/10.3847/1538-4357/ad66b7

Hawarden, T. G., Mountain, C. M., Leggett, S. K., & Puxley, P. J. 1986, MNRAS, 221, 41, https://doi.org/10.1093/mnras/221.1.41P

Haywood, M., Lehnert, M. D., Di Matteo, P., et al. 2016, A&A, 589, 66, https://doi.org/10.1051/0004-6361/201527567

Hunt, L. K., Combes, F., García-Burillo, S., et al. 2008, A&A, 482, 133, https://doi.org/10.1051/0004-6361:20078874

Katsanikas, M., Patsis, P. A., & Contopoulos, G. 2013, IJBC, 23, 1330005, https://doi.org/10.1142/S021812741330005X

Kenney, J. D. P., Wilson, C. D., Scoville, N. Z., Devereux, N. A., & Young, J. S. 1992, ApJ, 395, 79, https://doi.org/10.1086/186492

Kim, W.-T. & Stone, J. M. 2012, ApJ, 751, 124, https://doi.org/10.1088/0004-637X/751/2/124

Lee, Y. H., Park, M.-G., Hwang, H. S., et al. 2022, ApJ, 926, 58, https://doi.org/10.3847/1538-4357/ac3bc1

Lewis, J. R. & Freeman, K. C. 1989, AJ, 97, 139, https://doi.org/10.1086/114963
Lin, L., Li, C., Du, C., et al. 2020, MNRAS, 499, 1406, https://doi.org/10.1093/mnras/staa2913
Lynden-Bell, D. & Kalnajs, A. J. 1972, MNRAS, 157, 1, https://doi.org/10.1093/mnras/157.1.1
Maciejewski, W., Teuben, P. J., Sparke, L. S., & Stome, J. M. 2002, MNRAS, 329, 502, https://doi.org/10.1046/j.1365-8711.2002.04957.x
Maeda, F., Ohta, K., Fujimoto, Y., Asao, H., & Kaito, U. 2020, MNRAS, 495, 3840, https://doi.org/10.1093/mnras/staa1296
Manos, T. & Machado, R. E. G. 2014, MNRAS, 438, 2201, https://doi.org/10.1093/mnras/stt2355
Martinez-Valpuesta, I., Shlosman, I., & Heller, C. 2006, ApJ, 637, 214, https://doi.org/10.1086/498338
Matsuda, T. & Nelson, A. H. 1977, Natur, 266, 607, https://doi.org/10.1038/266607a0
Miyamoto, M. & Nagai, R. 1975, PASJ, 27, 533
Okamoto, T., Isoe, M., & Habe, A. 2015, PASJ, 67, 63, https://doi.org/10.1093/pasj/psv037
Pastras, S., Patsis, P. A., & Athanassoula, E. 2022, Univ, 8, 290, https://doi.org/10.1093/pasj/psv037
Patsis, P. A. & Athanassoula, E. 2019, MNRAS, 490, 2740, https://doi.org/10.1093/mnras/stz2588
Pedregosa, F., Varoquaux, G., Gramfort, A., et al. 2011, JMLR, 12, 2825, https://doi.org/10.48550/arXiv.1201.0490
Petersen, M. S., Weinberg, M. D., & Katz, N. 2016, MNRAS, 463, 1952, https://doi.org/10.1093/mnras/stw2141
Pfenniger, D. 1984, A&A, 134, 373
Piner, B. G., Stone, J. M., & Teuben, P. J. 1995, ApJ, 449, 508, https://doi.org/10.1086/176075
Plummer, H. C. 1911, MNRAS, 71, 460, https://doi.org/10.1093/mnras/71.5.460
Rautiainen, P., Salo, H., & Laurikainen, E. 2008, MNRAS, 388, 1803, https://doi.org/10.1111/j.1365-2966.2008.13522.x
Reynaud, D. & Downes, D. 1998, A&A, 337, 671
Richstone, D. O. 1980, ApJ, 238, 103, https://doi.org/10.1086/157963
Romeo, A. B., Agertz, O., & Renaud, F. 2023, MNRAS, 518, 1002, https://doi.org/10.1093/mnras/stac3074
Saha, K. & Naab, T. 2013, MNRAS, 434, 1287, https://doi.org/10.1093/mnras/stt1088
Schwarz, M. P. 1985, MNRAS, 212, 677, https://doi.org/10.1093/mnras/212.3.677
Sellwood, J. A. 1981, A&A, 99, 362
Sellwood, J. A. & Wilkinson, A. 1993, RPPh, 56, 173, https://doi.org/10.1088/0034-4885/56/2/001
Skokos, C., Patsis, P. A., & Athanassoula, E. 2002a, MNRAS, 333, 847, https://doi.org/10.1046/j.1365-8711.2002.05468.x
Skokos, C., Patsis, P. A., & Athanassoula, E. 2002b, MNRAS, 333, 861, https://doi.org/10.1046/j.1365-8711.2002.05469.x
Skokos, C., Bountis, T. C., & Antonopoulos, C. 2007, PhD, 231, 30, https://doi.org/10.1016/j.physd.2007.04.004
Sofue, Y. 2020, Galaxies, 8, 37, https://doi.org/10.3390/galaxies8020037
Sormani, M. C., Sobacchi, E., & Sanders, J. L. 2024, MNRAS, 528, 5742, https://doi.org/10.1093/mnras/stae082
Sorensen, S.-A., Matsuda, T., & Fujimoto, M. 1976, Ap&SS, 43, 491, https://doi.org/10.1007/BF00640025
Spearman, C. 1904, The American Journal of Psychology, 15, 72, https://doi.org/10.2307/1412159
Spinoso, D., Bonoli, S., Dotti, M., et al. 2017, MNRAS, 465, 3729, https://doi.org/10.1093/mnras/stw2934
Valencia-Enríquez, D., Puerari, I., & Chaves-Velasquez, L. 2023, MNRAS, 525, 3162, https://doi.org/10.1093/mnras/stad2437
Valenzuela, O. & Klypin, A. 2003, MNRAS, 345, 406, https://doi.org/10.1046/j.1365-8711.2003.06947.x
van Albada, G. D. & Roberts, W. W. 1981, ApJ, 246, 740, https://doi.org/10.1086/158969
Verley, S., Combes, F., Verdes-Montenegro, L., et al. 2007, A&A, 474, 43, https://doi.org/10.1051/0004-6361:20077650
Villa-Vargas, J., Shlosman, I., & Heller, C. 2010, ApJ, 719, 1470, https://doi.org/10.1088/0004-637X/719/2/1470
Watanabe, Y., Sorai, K., Kuno, N., & Habe, A. 2011, MNRAS, 411, 1409, https://doi.org/10.1111/j.1365-2966.2010.17746.x
Wozniak, H. 2015, A&A, 575, A7, https://doi.org/10.1051/0004-6361/201425005
Wu, Y.-T., Pfenniger, D., & Taam, R. E. 2018, ApJ, 860, 152, https://doi.org/10.3847/1538-4357/aac5e8
Zurita, A., Relaño, M., Beckman, J. E., & Knapen, H. 2004, A&A, 413, 73, https://doi.org/10.1051/0004-6361:20031049

Ivânio Puerari & Alan Silva-Castro: Instituto Nacional de Astrofísica, Óptica y Electrónica, Calle Luis Enrique Erro, No. 1, 72840, Santa María Tonantzintla, Puebla, México (puerari, alan.silva@inaoep.mx).

Revista Mexicana de Astronomía y Astrofísica, **61**, 111–116 (2025)

https://doi.org/10.22201/ia.01851101p.2025.61.01.08

TAXONOMIC CLASSIFICATION OF 2018 CB DURING ITS CLOSE APPROACH TO EARTH

J. R. Valdés[1], J. Guichard[1,2], R. Mújica[1], S. Camacho[1,2], A. V. Ojeda[1,3], E. Buendía[1], S. Noriega[4], and J. Martínez[4]

Received November 15 2023; accepted February 12 2025

ABSTRACT

We present the results of a low resolution optical spectroscopic observation of Near-Earth Asteroid (NEA) 2018 CB during its close approach to Earth, conducted with the 2.1 m telescope of the Guillermo Haro Astrophysical Observatory (OAGH), located in Cananea, Sonora, Mexico, using a Boller & Chivens Spectrograph, with a grating of 50 l/mm that covers the interval between 4000Å and 9500Å. The taxonomic classification was performed using the values of the “spectral distance” (D_x), calculated with respect to the mean spectra of the 24 taxonomic classes of DeMeo et al. (2009), and also with respect to individual asteroid spectra from the Phase II of the Small Main-Belt Asteroid Spectroscopy Survey (SMASSII). We determined that 2018 CB is an Xk-class NEA.

RESUMEN

Presentamos los resultados de las observaciones espectroscópicas de baja resolución del Asteroide Cercano a la Tierra (NEA) 2018 CB durante su aproximación a la Tierra, realizadas con el telescopio de 2.1m del Observatorio Astrofísico Guillermo Haro (OAGH), ubicado en Cananea, Sonora, México, utilizando el espectrógrafo Boller & Chivens, con una rejilla de difracción de 50 l/mm que cubre el intervalo de longitudes de onda entre 4000Å y 9500Å. La clasificación taxonómica se estableció usando los valores de la “distancia espectral” (D_x), calculados con respecto a los espectros promedio de las 24 clases espectrales de DeMeo et al. (2009), así como con respecto a los espectros individuales de la Fase II del Small Main-Belt Asteroid Spectroscopy Survey (SMASSII). Determinamos que el asteroide 2018 CB es un NEA de clase taxonómica Xk.

Key Words: minor planets, asteroids: individual: 2018 CB — techniques: spectroscopic

1. INTRODUCTION

Today, the threat that some NEAs, especially potentially hazardous asteroids (PHAs), pose to terrestrial civilization in case of a collision with our planet, is widely recognized (Chapman 1994; Morrison et al. 2002). On the other hand, NEAs with low relative velocities with respect to Earth may become targets for future robotic sample-return and manned space missions (Reddy et al. 2012). In both cases, the determination of the physical properties of these objects is of crucial importance, in particular, its taxonomic classification and, eventually, when near-infrared observations become available, the analysis of their possible mineralogical composition.

Near-Earth Asteroid 2018 CB made a close approach to Earth on February 9, 2018 (22:29 UT), at a distance of 0.000466 AU (69,700 km or 0.18 lunar distances), with a relative velocity of V_{rel}=7.2710 km/s. It was first observed by the Catalina Sky Survey on February 4, 2018 (MPEC 2018-C12), using the 0.68 m Schmidt telescope. Despite its rapid sky motion (1459.5 arcsec/min at the closest approach) that caused a drastic change of its coordinates, from

[1]Instituto Nacional de Astrofísica, Óptica y Electrónica (INAOE), Luis E. Erro No.1, Santa María Tonantzintla, Puebla, México.

[2]Centro Regional de Enseñanza de Ciencia y Tecnología del Espacio para América Latina y el Caribe (CRECTEALC). Luis E. Erro No.1, Santa María Tonantzintla, Puebla, México.

[3]Centro de Investigación y Desarrollo de Tecnología Digital, Instituto Politécnico Nacional. Av. Instituto Politécnico Nacional No. 1310, Tijuana, B. C., México.

[4]Observatorio Astrofísico Guillermo Haro (OAGH). Av. Sinaloa 25, Cananea 84620, Sonora, México.

TABLE 1

OBSERVATIONAL CIRCUMSTANCES OF 2018 CB (2018 FEBRUARY 09.34 UT, JD=2458158.68103)

Object	Coordinates (J2000.0)	exp.time (s)	V (mag)	Δ (AU)	r (AU)	Ph	L_{PAB}	B_{PAB}
2018 CB	07:27:45.3 +51:18:35	4×900	14.9	0.003	0.989	43.9	188.6	−2.4

RA=08h 01m and DEC=+48 d 54 m, on Feb 8 (00:00 UT) to RA=23 h 15 m, and DEC=−14 d 15 m, on February 10 (00:00 UT), we were able to observe this NEA during the night of February 8, 2018, a day before its closest approach. Asteroid 2018 CB is a super-fast rotator (P=0.089241 ± 0.000027 h, (Birtwhistle 2021)) Apollo object.

Close approaches offer a unique opportunity to better observe asteroids in order to determine their physical properties; in particular, small asteroids such as 2018 CB, because of their size (H=25.9), are generally faint and inaccessible to a 2m diameter telescope such as the one at the Observatorio Astrofísico Guillermo Haro (OAGH) observatory.

The observations we report here for 2018 CB are part of an ambitious program to establish the taxonomic classification of NEAs and other asteroids belonging to different families of the Main Belt. In this program, asteroids at close approaches are included as high-priority objects. At the time of observation, 2018 CB reached a magnitude of 14.9 in the V-band, representing an excellent opportunity to observe it at the OAGH.

With these goals in mind, we have begun a large program of optical spectroscopic observations of NEAs and main-belt asteroids of different families. Up to now we have observed more than 900 asteroids from different families. The results of the taxonomic classification of NEAs and asteroids of the Flora family will be presented in forthcoming papers.

In this paper, given the importance of 2018 CB as an asteroid that passed very close to the Earth, we present the results of its taxonomic classification. In § 2 we describe the observations and data reduction procedure; in § 3 we present the results, including the proposed taxonomic classification; and in § 4 we discuss about the size and the possible mineralogical composition of 2018 CB.

2. OBSERVATION AND DATA REDUCTION

Optical spectra of 2018 CB were obtained with the 2.1 m telescope of the Guillermo Haro Astrophysical Observatory, located in Cananea, Sonora, Mexico, using a Boller & Chivens spectrograph with an E2V42-40 2048 × 2048 pixels CCD. A low-resolution diffraction grating of 50 l/mm, which provides a dispersion of 5.2 Å/pix and a spectral coverage between 4200 Å and 9500 Å was used. In order to minimize the effects of the atmospheric differential refraction, and to reduce the loss of light, a slit width of 400 microns was selected. With an image scale of 8.18 arcsec/mm in the focal plane of the telescope, the slit width corresponds to 3.2 arcsec in the sky. The slit remained fixed in E-W orientation.

The new control system installed in the OAGH allows for moving the telescope, in both coordinates, at non sidereal rates, performing the tracking based on the instantaneous position of the observed asteroids, instead of guiding the telescope with a position in the sky.

Using the orbital elements of asteroids, referred to the equinox J2000.0, and the rectangular geocentric equatorial coordinates X, Y, and Z of the Sun referred to the same equinox, the control system is capable of calculating the geocentric positions (equatorial coordinates) of these objects for a given epoch.

The orbital elements of 2018 CB were taken from the file MPCORD.dat, provided by the Minor Planet Center (https://minorplanetcenter.net/data). The equatorial coordinates of the objects were calculated at one hundred millisecond intervals, and the control system instructed the telescope to follow this series of coordinates, guaranteeing that 2018 CB was always in the same position of the slit. In addition, every time that the control system calculated the position of an observed asteroid, it also calculated the corrections for precession, nutation, and atmospheric refraction, as well as the parallax correction to the equatorial coordinates.

The use of this new control system, with non-sidereal tracking, has been one of the most important factors in the success of our asteroid spectroscopic observations program.

The observations were carried out on February 8, 2018, a day before the closest approach. The observational circumstances of 2018 CB are listed in Table 1. The coordinates, the V-band magnitude, the distance from the observer (Δ) and from the sun to the object (r), the phase angle (Ph), and the phase angle bisector longitude (L_{PAB}) and latitude (B_{PAB}) refer to the time of observation, and were

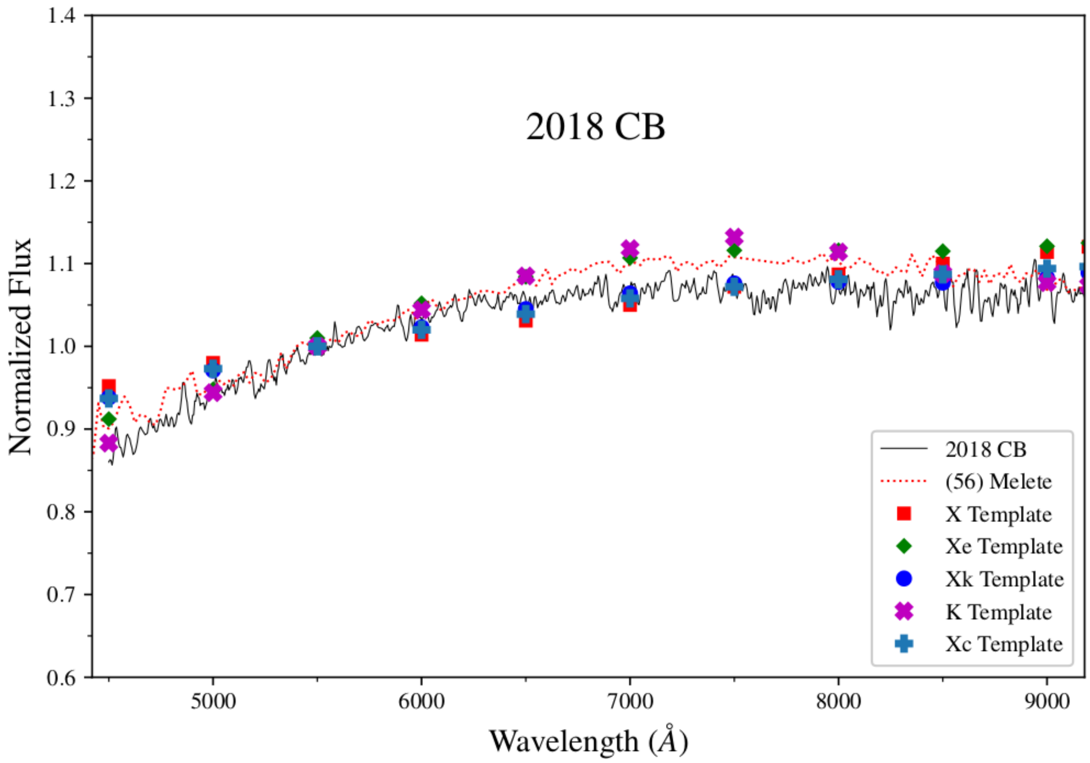

Fig. 1. Comparison of the 2018 CB spectrum (solid line) with the lowest calculated D_x values templates from DeMeo et al. (2009). Additionally, the spectrum of (56) Melete (dotted line), the prototype of the Xk class proposed by DeMeo et al. (2009), is plotted.

taken from the Minor Planet & Comet Ephemeris Service of the Minor Planet Center.

To remove the contribution of sunlight from the 2018 CB spectra, and to obtain the asteroid relative reflectance spectrum, the solar analog HD047309 (López-Valdivia et al. 2014) was observed at an airmass of $X = 1.072$, closely matched to the NEA airmass ($X = 1.096$).

The image reduction was performed using the standard Image Reduction and Analysis Facility (IRAF) packages to reduce long-slit spectra. The extinction corrected spectra of 2018 CB and the solar analog HD047309 were normalized to 5500 Å. The relative reflectance spectrum of 2018 CB was obtained by dividing the object spectrum by the solar analog spectrum. Upon extraction, the spectrum of 2018 CB was rebinned to a uniform dispersion of 25 Å per pixel. The normalized optical spectrum of 2018 CB, obtained by this procedure, is shown in Figure 1.

3. DETERMINING THE TAXONOMIC CLASS OF 2018 CB

A direct way to determine the taxonomic class to which an asteroid belongs is to calculate the "spectral distance" (Yang et al. 2003) between the asteroid spectrum and known spectral templates, defined by:

$$D_x = [\sum_{n=1}^{k}(X_n - Y_n)^2]^{1/2}, \tag{1}$$

where D_x is the spectral distance between the unclassified spectrum X and a classified spectrum Y (spectral template), n represents each of the individual selected points in the spectra to find the best fit between X and Y, and k is the total number of points used in the fitting procedure.

We have calculated the spectral distance between the reflectance spectra of 2018 CB and the mean spectra of the 24 taxonomic classes of DeMeo et al. (2009). The best fits obtained are for the following taxonomic classes: Xk-class ($D_x = 0.0830$), Xc-class ($D_x = 0.0872$), K-class ($D_x = 0.0916$), Xe-class ($D_x = 0.1076$), X-class ($D_x = 0.1132$), and S-class ($D_x = 0.1499$).

A similar result arose when the spectral distance was calculated with respect to individual asteroid spectra from the Phase II of the Small Main-Belt Asteroid Spectroscopy Survey (SMASSII) database (Binzel et al. 2001; Bus & Binzel 2002). By checking the resulting fifteen lowest values (7 Xk, 4 K, 2 Xe & 2 X) of spectral distances with the corresponding taxonomic class of the SMASSII database, a trend indicating that this asteroid can belong to the X-complex was observed.

It should be noted that while DeMeo et al. (2009) and Bus & Binzel (2002) implemented similar but not identical taxonomic schemes, our analysis is not in conflict with their results. The taxonomic classes in our discussion (Xk, Xe, and Xc) are directly linked, with no significant changes, between these schemes.

Extending the results of the fitting procedure to the one hundred lowest values of spectral distances, we have 31 objects with spectral templates belonging to the Xk-class, 26 objects to the K-class, 18 objects to the S-class, 12 objects to the Xe-class, 9 objects to the X-class, and 4 objects to the Sk-class, with 21 Xk-class objects among the 50 lowest values of D_x (42%). There is no available information about the albedo of this asteroid, so we based the analysis of the 2018 CB taxonomic classification only on its spectral properties.

We found some S-type asteroids among the one hundred smallest values of spectral distance D_x. S-type asteroids are considered to be the most likely progenitors of ordinary chondrites. Spectrally, they are redder than ordinary chondrites and tend to show weaker absorption bands in the visible and near-infrared regions of the spectrum. It is clear, from the spectrum of 2018 CB that we obtained (Figure 1), that its reflectance increases with wavelength, at least up to 9500 Å. The continuum slope between 0.45 μm and 0.75 μm, in units of μm^{-1}, calculated as the change in normalized reflectance with respect to wavelength, is 0.864, but it does not show any absorption band, indicating that 2018 CB does not belong to the S-complex. Thus, we discarded the Sk- and S-class as taxonomic classification possibilities for 2018 CB.

Due to a similar spectral analysis, we have also eliminated the Xe-class from the list of likely candidates for the taxonomic classification of this NEA. Within the DeMeo et al. (2009) classification system, an absorption band feature short-ward of 0.55 μm distinguishes the Xe-class, which is evidently absent in our spectrum of 2018 CB. This leaves us with only those taxonomic classes that belong to the K-complex (K- and Xk-class), and the X-class.

Taking into account the high frequency (42%) of the Xk-class among the fifty lowest values of spectral distance, and the 47% among the fifteen lowest values of D_x, calculated from the spectra of the SMASSII database, we suggest that 2018 CB is an Xk-class NEA, an intermediate class between the X- and K-class. In the taxonomic classification proposed by Bus & Binzel (2002), the Xk objects are a combination of T, C, X, M, P, and E objects from the Tholen (1984) classification.

As discussed in DeMeo et al. (2009) and Bus & Binzel (2002), the Xk taxonomic class exhibits a subtle feature between 0.8 and 1.0 microns. However, this feature is not consistently observed in 100 % of the spectra in the SMASSII database, and even in the prototype of this class suggested by DeMeo et al. (2009), (56) Melete, this feature is not evident, as seen in Figure 1. While we have high confidence in the proposed taxonomic classification, we acknowledge that the distinction between the classes included in the type-X may fall within our uncertainty. Therefore, we assign, conservatively, a type-X for 2018 CB.

4. SOME WORDS ABOUT THE SIZE AND THE POSSIBLE COMPOSITION OF 2018 CB

As is known, there is a relationship between the absolute magnitude H, the albedo value, and the diameter of an asteroid, as well as a relationship between the albedo value and the taxonomic class of these objects. We used both relationships to estimate the size of 2018 CB. The absolute magnitude $H = 25.9$ was taken from the JPL HORIZONS online solar system data service. In § 3 we proposed that 2018 CB was an asteroid of the taxonomic complex X. As its albedo is not known, to estimate its size we use the average albedo values for different taxonomic classes reported by DeMeo and Carry (2013). Taking into account the EMP degeneracy, the extreme values of albedos for a X-type asteroid are 0.053+-0.012 and 0.536+-0.246 for P- and E-class asteroids, respectively. Using, in addition, equation (2) from Pravec & Harris (2007), we estimate that the size of 2018 CB is between 11.9 and 38.1 meters.

Having proposed a taxonomic classification for 2018 CB and taking into account that it has a featureless visible spectrum and a clear positive slope towards the red wavelengths, we discuss the possible mineralogical composition of this NEA. We have to remember that some important asteroid minerals do not exhibit characteristic absorption features. In particular, iron meteorites have featureless spectra, with red spectral slopes (Cloutis et al. 1990). On the other hand, enstatite chondrites, because of the absence of Fe^{2+} in their silicates, also show relatively featureless VNIR spectra (from 0.3 to 2.5μm),

DOI: https://doi.org/10.22201/ia.01851101p.2025.61.01.08

with red spectral slopes, for example, EH4 Abee and EL6 Hvittis (Gaffey 1976). However, because of the limitations of a classification scheme based only on spectral features, the mineralogy represented in the X-complex is much more diverse that in the C- and S-complexes. Several types of meteorite analogs have been proposed to match the VNIR spectra of X-complex asteroids: the anhydrous CV/CO carbonaceous chondrites (Barucci et al. 2012; Clark et al. 2009; Burbine et al. 2002; Burbine & Binzel 2002), enstatite chondrites (Vernazza et al. 2011; Ockert-Bell et al. 2010), stony-iron (Ockert-Bell et al. 2010), and iron meteorites (Fornasier et al. 2011).

Given the limited available information about the physical properties of 2018 CB, we are not able to make a definitive assertion on its mineralogical composition. Albedo, density, and degree of porosity determinations and radar observations during future oppositions of 2018 CB, as well as efforts in the shape and size modeling of this NEA, will be necessary and very useful to clarify its composition.

5. CONCLUSIONS

Based on observations made during the close approach to Earth of Near-Earth asteroid 2018 CB in 2018, we obtained the reflectance spectrum of this NEA in the range between 4000Å and 9500Å . We then calculated the spectral distance (D_x) with respect to the mean spectra of the 24 taxonomic classes of DeMeo et al. (2009), and to individual asteroid spectra from the Phase II of the Small Main-Belt. From this analysis, we classify 2018 CB as an Xk-class NEA, and being more conservative, as an X-type. As we have mentioned, several authors have proposed different types of meteorite analogs to match the VNIR spectra of X-complex asteroids. However, because the insufficient information on the physical properties of 2018 CB and the limitations of a classification scheme based only on spectral features, we were not able to make a definitive assertion on its mineralogical composition. More optical, NIR, and radar observations during future apparitions of 2018 CB are needed to provide its physical properties (albedo, density, and degree of porosity) in order to distinguish between iron, stony-iron, and enstatite meteorites that have been proposed by many authors, as the most probable meteorite analogues that could explain the VNIR spectral characteristics of Xk-class asteroids.

The authors want to express their sincere gratefulness to the night technicians J. Miramon† and G. Miramon for their valuable assistance during the observation of 2018 CB, as well as to the whole staff of the OAGH for the successful implementation of the new telescope control system that allowed us to obtain high signal-to-noise spectra of this asteroid.

This article is dedicated to the memory of our great friend and colleague Javier Miramon.

REFERENCES

Barucci, M. A., Belskaya, I. N., Fornasier, S., et al. 2012, Planet. Space Sci., 66, 23, https://doi.org/10.1016/j.pss.2011.11.009

Binzel, R. P., Harris, A. W., Bus, S. J., and Burbine 2001, Icar, 151, 139, https://doi.org/10.1006/icar.2001.6613

Birtwhistle, P. 2021, MPBu, 48, 26

Burbine, T. H., McCoy, T. J., Meibom, A., Gladman, B., & Keil, K. 2002, Asteroids III, ed. W. F. Bottke Jr., A. Cellino, P. Paolicchi, and R. P. Biznel, UAP

Burbine, T. H. & Binzel, R. P. 2002, Icar, 159, 468, https://doi.org/10.1006/icar.2002.6902

Bus, S. J. & Binzel, R. P. 2002, Icar, 158, 146, https://doi.org/10.1006/icar.2002.6856

Chapman, C. R. 1994, Natur, 367, 33, https://doi.org/10.1038/367033a0

Clark, B. E., Ockert-Bell, M. E., Cloutis, E. A., et al. 2009, Icarus, 202, 119, https://doi.org/10.1016/j.icarus.2009.02.027

Cloutis, E. A., Gaffey, M. J., Smith, D. G. W., & Lambert, R. St. J. 1990, JGR, 95, 281, https://doi.org/10.1029/JB095iB01p00281

DeMeo, F. E., Binzel, R. P., Slivan, S. M., & Bus, S. J. 2009, Icar, 202, 160, https://doi.org/10.1016/j.icarus.2009.02.005

DeMeo, F. E. & Carry, B. 2013, Icar, 226, 723, https://doi.org/10.106/j.icarus.2013.06.027

Fornasier, S., Clark, B. E., & Dotto, E. 2011, Icar, 214, 131, https://doi.org/10.1016/j.icarus.2011.04.022

Gaffey, M. J. 1976, J. Geophys. Res., 81, 905, https://doi.org/10.1029/JB081i005p00905

López-Valdivia, R., Bertone, E., Chávez, M., et al. 2014, MNRAS, 444, 2251, https://doi.org/10.1093/mnras/stu1555

Morrison, D., Harris, A. W., Sommer, G., Chapman, C. R., & Carusi, A. 2002, Asteroids III, ed. W. F. Bottke Jr., A. Cellino, P. Paolicchi, & R. P. Biznel, UAP

Ockert-Bell, M. E., Clark, B. E., Shepard, M. K., et al. 2010, Icar, 210, 674, https://doi.org/10.1016/j.icarus.2010.08.002

Pravec, P. & Harris, A. W., 2007, Icar, 190, 250, https://doi.org/10.1016/j.icarus.2007.02.023

Reddy, V., Le Corre, L., Hicks, M., et al. 2012, Icar, 221, 678, https://doi.org/10.1016/j.icarus.2012.08.035

Tholen, D. J. 1984, Asteroid Taxonomy from Cluster Analysis of Photometry, Ph. D. Thesis, The University of Arizona

Vernazza, P., Lamy, P., Groussin, O., et al. 2011, Icar, 216, 650, https://doi.org/10.1016/j.icarus.2011.09.032

Viateau, B. 2000, A&A, 354, 725

Yang, B., Zhu, J., Gao, J., et al. 2003, AJ, 126, 1086, https://doi.org/10.1086/376839

E. Buendía, S. Camacho, J. Guichard, R. Mújica, A. V. Ojeda, and J. R. Valdés: Instituto Nacional de Astrofísica, Óptica y Electrónica (INAOE). Luis Enrique Erro # 1, Tonantzintla, Puebla, México C.P. 72840 (buendia, sergio.camacho, jguich, rmujica@inaoep.mx, aojeda@citedi.mx, jvaldes@inaoep.mx).

S. Camacho and J. Guichard: Centro Regional de Enseñanza de Ciencia y Tecnología del Espacio para América Latina y el Caribe (CRECTEALC) (sergio.camacho, jguich@inaoep.mx).

J. Martínez and S. Noriega: Observatorio Astrofísico Guillermo Haro (OAGH). Av. Sinaloa 25, Cananea 84620, Sonora, México (jmartínez, snoriega@inaoep.mx).

A. V. Ojeda: Centro de Investigación y Desarrollo de Tecnología Digital, Instituto Politécnico Nacional. Av. Instituto Politécnico Nacional No. 1310, Tijuana, B.C., México (aojeda@citedi.mx).

Revista Mexicana de Astronomía y Astrofísica, **61**, 117–122 (2025)

https://doi.org/10.22201/ia.01851101p.2025.61.01.09

LONG-TERM VARIABILITY OF WATER MASER EMISSION IN S128

E. E. Lekht[1], J. E. Mendoza-Torres[2], N. T. Ashimbaeva[1], V. V. Krasnov[3], and V. R. Shoutenkov[4]

Received September 13 2024; accepted February 14 2025

ABSTRACT

The evolution of the H_2O maser emission at the S128 source during 1981-2024 is analyzed, based on long-term regular observations. The emission from -73 to -70 km/s corresponds mainly to source B, while that of velocities < -76 km/s to source A. It was identified that in the time interval 2004-2006, the maser activity gradually shifted from source B to source A. The active phases of masers B and A lasted approximately 23 and 16 years, respectively. It is assumed that the common cause of the variability of the maser emission at both sources (A and B) can be shock waves that occur near the ionization front. When clouds collide, a disturbance propagates along the resulting ionization front, which leads to the appearance of shock waves. It is shown that the disturbance is spreading in the south-north direction. The star formation process occurs in the same direction.

RESUMEN

Se analiza la evolución de la emisión maser de H_2O en la fuente S128 durante 1981-2024, con base en su monitoreo regular. La emisión de -73 a -70 km/s proviene principalmente de la fuente B, mientras que la de < -76 km/s de la fuente A. Se identificó que en el intervalo de tiempo 2004−2006, la actividad maser cambió gradualmente de la fuente B a la fuente A. Las fases activas de los maseres B y A duraron aproximadamente 23 y 16 años, respectivamente. Se supone que la causa común de la variabilidad de la emisión maser en ambas fuentes (A y B) puede ser ondas de choque, que ocurren cerca del frente de ionización. Cuando las nubes chocan, la perturbación se propaga a lo largo del frente de ionización resultante, que conduce a la aparición de ondas de choque. Se observa que la perturbación se está extendiendo en dirección sur−norte. El proceso de formación estelar ocurre en la misma dirección.

Key Words: clouds — masers — stars formation

1. INTRODUCTION

Maser emission sources have been found to be associated with a variety of distributions of active star formation regions. In addition to the frequent appearance of OH masers at hyper-compact H II regions, masers can be located at the front of shock waves. Such configurations can occur, for example, during the movement of the H II region in the molecular core of the interstellar medium. At high velocities, the H II region acquires a comet-like shape and a shock wave front appears at the boundary between the leading region and the interstellar medium. Favorable conditions for maser radiation arise near this front. An example of such a configuration is the star formation region W44C (G 34.3+0.15), shown in Figure 1. This hyper-compact H II region is embedded in a compact molecular core with a temperature of about 225 K and a hydrogen density of $10^7 \mathrm{cm}^{-3}$ (Wood & Churchwell 1989)

Another possible scenario could be that of two interacting (colliding) molecular CO clouds. Favorable conditions for maser emission arise at the boundary between them. An example of such a structure is the active star formation region S128. A schematic rep-

[1]Lomonosov Moscow State University, Sternberg Astronomical Institute, Moscow, 119991 Russia.

[2]Instituto Nacional de Astrofísica, Óptica y Electrónica, Puebla, México.

[3]Lebedev Physical Institute, Astro Space Center, Russian Academy of Sciences, Moscow, 117997 Russia.

[4]Pushchino Radio Astronomy Observatory, Astro Space Center, Lebedev Physical Institute, Russian Academy of Sciences, Pushchino, 142290 Russia.

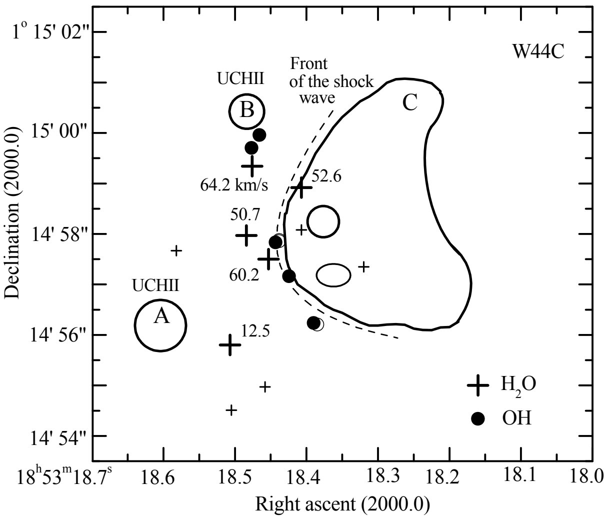

Fig. 1. The structure of the W44C star formation region. Crosses indicate the positions of clusters of H_2O maser spots. Bold crosses correspond to the main clusters, the labels near them refer to the radial velocities of the main features. The circles represent the positions of the main OH emission areas.

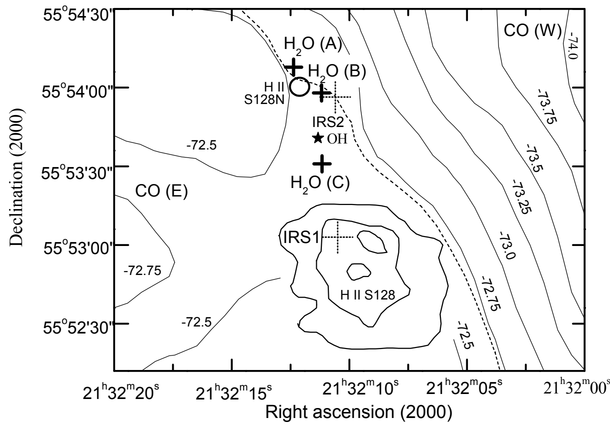

Fig. 2. The structure of the S128 star formation region. Crosses denote the locations of the H_2O maser spots, the bold ones indicate the main H_2O spot clusters, (see text).

resentation of the S128 source is shown in Figure 2. The basic data for constructing this figure were taken from Haschick & Ho (1985) and from Ashimbaeva et al. (2023).

The distance to S128 is assumed to be the kinematic one, which is equal to 7.5 kps. The CO(E) cloud of Figure 2 has a small radial velocity gradient. The CO(W) cloud has a radial velocity of -74 km/s with no velocity gradient in it. Between the clouds, the medium is highly compressed and has a large radial velocity gradient. In addition, an ionization front appears along the boundary of the cloud interaction.

It is assumed that a more distant CO cloud is pushing the collision area towards us. According to Richards et al. (2005) the disturbance spreads from south to north.

A hyper-compact region, whose size is $\approx 3''$, is located near the ionization front of the S128N H II region (Ho et al. 1981), at a distance of $60''$, on the south of the hyper-compact H II region. It is S128, an extended H II region (Ho et al. 1981). Near each H II region there is an IR source: IRS1 near the extended region, and IRS2 near the hyper-compact region H II (Mampaso et al. 1984). It is believed that the star formation process in S128 takes place along the boundary that separates the colliding clouds CO(E) and CO(W).

Along the ionization front, at the North and at the South of the H II S128N hyper-compact region, two sources of H_2O maser emission, denoted respectively, as A and B, and separated by a distance of $13''$, have been detected (Ho et al. 1981; Haschick & Ho 1985; Migenes et al. 1999). A third maser source of water vapor is located $30''$ south of S128N (Richards et al. 2005). However, unlike A and B, maser C is quite far away from the ionization front. The masers are associated with the ionization front, not with a specific young stellar object (YSO). Some clusters of maser condensations are elongated by hundreds of astronomical units.

The study of the variability of maser emission H_2O is described in the works of Berulis et al. (1995), Lekht et al. (2002) and Ashimbaeva et al. (2018).

The hydroxyl maser is also located far from the ionization front. The emission of this maser was discovered in 1986 (Wouterloot et al. 1988). It is located south of the super-compact H II region S128N. The OH maser emission is quite weak. The study of the variability of OH emission in the 18 cm line was described in the works of Ashimbaeva et al. (2018, 2023).

In this work we focus on the study of the long-term variability of H_2O maser emission in S128, during the entire period of our monitoring, which extends for more than forty years (from 1981 to 2024).

2. OBSERVATIONS AND CONSTRUCTION OF 3D IMAGES

Regular long-term observations of the H_2O maser emission in the direction of S128 ($\alpha_{2000} = 21^h32^m13^s, \delta_{2000} = 55°54'39''$) were performed at the 22-m radio telescope in Pushchino Radio Astronomy Observatory (PRAO), in Russia, from 1981 to 2024. The FWHM of the beam antenna of the radio telescope, at a wavelength of 1.35 cm, is $2.6'$. The

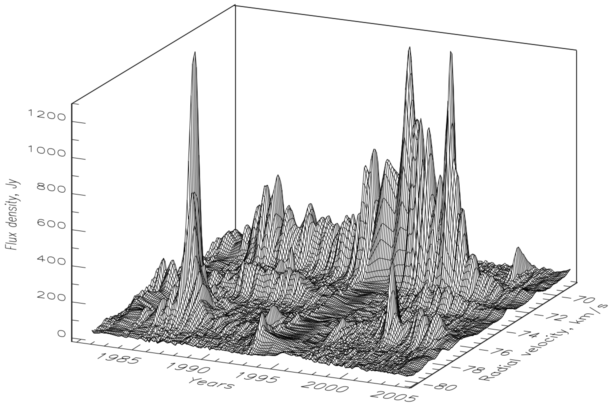

Fig. 3. 3D representation of H_2O maser emission spectra in S128 in the period 1981–2005. (see text).

noise temperature of the system was in the range of 150–300 K, depending on the observational conditions. The sensitivity of the telescope was 25 Jy/K.

From 1981 to 2005 a 128-channel filter-type analyzer with a resolution of 0.101 km/s was used. To obtain a sufficiently wide band (about 25 km/s) for a proper analysis of the emission features from the source under study, the observations were carried out in two stages, by adjusting the frequency of the first heterodyne of the receiver. Since 2005, a 2048-channel autocorrelation receiver with a resolution of 0.0822 km/s in radial velocity has been used. For S128 the range of overlapping in radial velocity was from −156 to 12 km/s.

To construct and analyze the figures we used only the central parts of the spectra where maser emission was observed (from −90 to −60 km/s). The uncertainty in the determination of the radial velocity was within 20-25 m/s. The intervals between two consecutive observations were of about one month. In 1993, 1994 and 2007, there were interruptions in the observations due to technical reasons. All spectra were adjusted for signal absorption in the Earth's atmosphere.

Whenever possible, the different S128 observations were carried out at positional angles close to each other. This made it possible to avoid noticeable changes in the angle between the polarization planes of the antenna feed and the source emission in the presence of linear polarization of the source maser emission.

In the program to compute the radial velocities, until March 2018, the velocity of the Sun's movement towards the apex was assumed to be 19.5 km/s. Since March 2018, we adopted a velocity value of 20 km/s. For this reason, the radial velocities of all spectra, as well as previously published observational

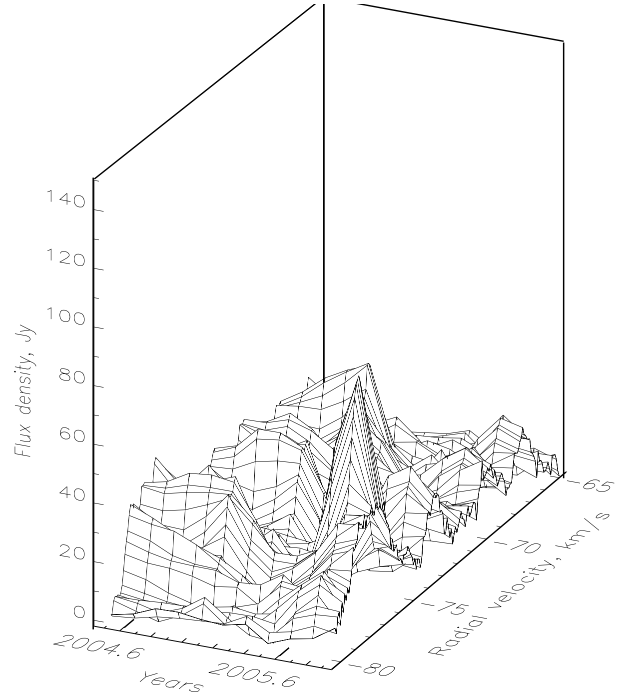

Fig. 4. 3D representation of H_2O spectra in S128 during the period 2004.5–2006 (see text).

results used in this paper, were corrected. The correction value for S128 was 0.36 km/s. Therefore, the total duration of the monitoring of the H_2O maser in S128 extends by more than 40 years. When constructing a 3D image, this observation period was divided into three intervals according to the following criteria: 1 – long duration of the entire monitoring; 2 – the different resolutions of the spectra in terms of radial velocity; 3 – the different structure of the spectra. Taking this into account, the following time intervals were chosen: 1981–2005, 2004.5–2006.0 and late 2005–early 2024. The time intervals overlap slightly in observation time.

Figures 3–5 show a three-dimensional (3D) representation of the evolution of H_2O maser emission in the S128 direction for all three observation intervals of our monitoring (1981-2024). Time in years, radial velocity in km/s and flux density in Jy are respectively represented in the x, y and z axes. This method requires a uniform series of data along the x and y axes. This condition was eventually but rarely not fulfilled on the time scale. In these time intervals, the spectra used in the 3D plots were obtained by triangulation of the fluxes of the original spectra, according to the times of the observations and of the regular times for the 3D plot. The obtained spectra were used to build the 3D plots.

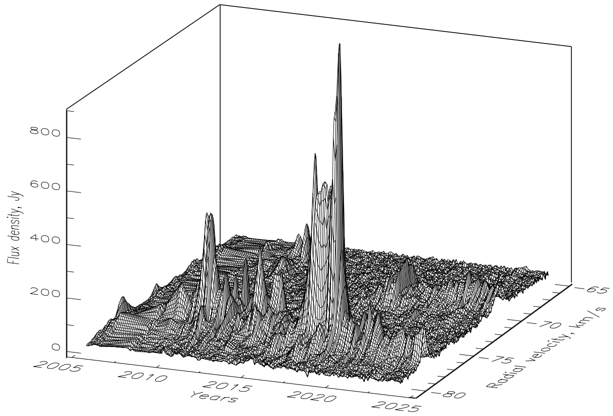

Fig. 5. 3D representation of H_2O spectra in S128 during the period 2005–2024 (see text).

For Figures 3 and 4, the observations have been made with a spectrum analyzer consisting of a bank of filters, and for Figure 5 with an autocorrelator. To construct a 3D image, the central part of the spectra was selected: from −80.0 to −68.5 km/s for Figure 3 and from −80.0 to −65.0 km/s for Figures 4 and 5, where maser emission H_2O was detected.

3. PROPERTIES OF H_2O MASERS A AND B

As we noted in the introduction, the H_2O maser emission in S128 was detected by Ho et al. (1981). They conducted observations of this maser in 1979 and 1980 at four epochs. The emission is concentrated mainly in the range of velocity from −88 to −65 km/s. In addition, two isolated features were observed at −89 and −57 km/s. According to Haschick & Ho (1985) and Migenes et al. (1999) the H_2O emission in S128 from −73 to −70 km/s belongs mainly to maser B, and the lower-velocity emission (< -76 km/s) comes mainly from source A.

As may be seen from Figures 3 to 5, during the entire time interval, the maser emission from both sources showed a flaring character. The flares were usually short-lived, which distinguishes the maser in S128 from masers in other sources, for example, from G43.8-0.1 (Colom et al. 2019). According to our long-term observations, in the time interval 2004-2006, the emission activity gradually shifted from maser B to maser A.

Two cycles of maser activity are identified. The first of them, from 1982 to 2004, is associated with maser B, and the second one, from 2006 to 2022, is associated with maser A. It should be noted that after 2022, the intensity of both masers dropped significantly.

It is important to note that prolonged, strong and rather variable maser emission was observed at radial velocities of −72 and −78 km/s for masers B and A, respectively. The nature of the emission of individual flares is more or less the same. The strongest flare with a flux density of 1700 Jy took place at −78.8 km/s in October 1985. The flare was short-lived and there was no significant increase in the emission intensity of the remaining features in the spectrum.

The second largest flare occurred 33 years later (in October 2018) at a similar velocity (−76.9 km/s) with a maximum flux density of 1320 Jy. It has been shown that this kind of flares can occur when at least two maser spots (Elitzur 1992), with close radial velocities, are randomly superimposed along the line of sight. In this case, an increase in the optical thickness of the ambient medium occurs and, consequently, a significant increase in the emission flux (see, for example, Lekht et al. (1983); Ashimbaeva et al. (2020)).

There are differences in the two activity cycles: the velocities of long-lived features vary significantly and the emission from source A is weaker than that from source B.

During the transition period between flare activity at sources B and A, which took place in 2004–2006, the shape of the H_2O spectrum clearly changed. The intensity of emission from both sources, during this period was approximately the same, as may be seen from Figure 4. It is possible to identify only one small flare at −75 km/s. Most likely, this detail belongs to the B source. It is known that the S128 source is at a distance from the Sun of 7.5 kpc; then, the linear distance between masers A and B is about $1.5 \cdot 10^{13}$ km. One may assume that the time interval between the end of the maser activity in A and the beginning of maser activity in B is of the order of 2 years. If the activity of the H_2O masers is associated with a disturbance propagating along the ionization front, then its velocity should be of the order of $2 \cdot 10^5$ km/s. Such a high value of the velocity is possible for the propagation not of the material itself, but of a perturbation of the ambient gas (its state, i.e. phase or areas of cloud contact). This may confirm the predominant role of cloud collisions in the generation of the H_2O maser emission.

The common cause of the variability of the maser emission of both masers may be shock waves occurring near the ionization front in the cloud contact region. The monitoring results suggest that such a region (disturbance) over time moves along the ionization front from south to north. At the same time, shock waves arise in such an area near the ionization

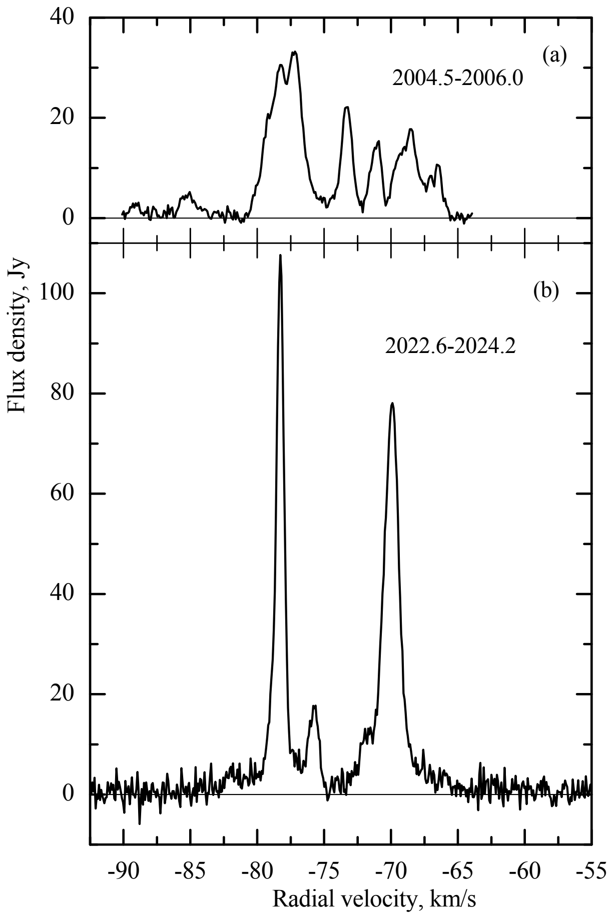

Fig. 6. The average spectra H_2O of two periods of minimal maser activity.

front, which stimulate the activity of maser condensations of sources B and A. This assumption confirms the results of Bohigas & Tapia (2003),that the star formation process in S128 proceeds in the south-north direction.

The activity of both masers (A and B) decreased significantly since the end of 2022. After that, there was a period of stable weak emission. Only the flux of two features, at -78.3 and -69.9 km/s, reached 140 and 100 Jy, respectively. The rest of the features were even weaker than the features during the transition period of 2003.5–2005.5. In addition, the emission disappeared at -89 km/s.

Figure 6 shows the average spectra of two periods of minimal maser activity. The stability of the emission during these periods allowed us to identify spectral features with a minimum flux density of up to 3 Jy. The radial velocities of the features in these two periods of low activity with a time difference of 20 years do not coincide, except for the detail at -78.3 km/s. The reason for the discrepancy could be the observed emission drift along the radial velocity (see, for example, Lekht et al. (2002); Ashimbaeva et al. (2018), which is a consequence of the impact of shock waves on maser condensations.

4. CONCLUSIONS

The main results of long-term observations of the H_2O maser emission in the direction of the S128 source, performed at the 22-m radio telescope in PRAO (Russia) in the period 1981–2024, are presented.

– The existence of a long-term evolution of the spectra, represented in a three-dimensional 3D image, is shown.

– It was found that in the time interval 2004–2006.0, the emission activity of H_2O gradually shifted from maser B to maser A.

– The duration of the active phase of the emission of masers B and A is about 23 and 16 years, respectively, i.e. quite close to each other.

– It was found that there are two periods of minimum activity of masers A and B in S128: 2004–2006 and after 2022.

– It is assumed that the common cause of the variability of maser emission from both sources (A and B) may be shock waves.They occur near the ionization front in the cloud contact region. Over time, this region (disturbance) shifts along the ionization front. According to the results of our monitoring, the disturbance is spreading in the south-north direction. This confirms the results of observations reported by Bohigas & Tapia (2003), that the star formation process occurs in the same direction.

It is assumed that the common cause of the variability of maser emission from both sources (A and B) may be shock waves occurring near the ionization front. At the same time, a disturbance propagates along such a front, which stimulates maser emission. According to the results of our monitoring, the disturbance is spreading in the south-north direction.

The authors are grateful to the staff of the Pushchino Radio Astronomy Observatory (Russia) for their substantial help in carrying out observations under the long-term monitoring program. The present study was conducted under the state assignment of Lomonosov Moscow State University.

REFERENCES

Ashimbaeva, N. T., Colom, P., Lekht, E. E., et al. 2018, ARep, 62, 609, https://doi.org/10.1134/S1063772918090019

Ashimbaeva, N. T., Krasnov, V. V., Lekht, E. E., et al. 2020, ARep, 64, 15, https://doi.org/10.1134/S1063772920010011

Ashimbaeva, N. T., Lekht, E. E., Krasnov, V. V., & Tolmachev, A. M. 2023, ARep, 67, 697, https://doi.org/10.1134/S1063772923070028

Berulis, I. I., Lekht, E. E., & Mendoza-Torres, J. E. 1995, ARep, 39, 411

Bohigas, J. & Tapia, M. 2003, AJ, 126, 1861, https://doi.org/10.1086/378054

Colom, P., Ashimbaeva, N. T., Lekht, E. E., et al. 2019, ARep., 63, 814, https://doi.org/10.1134/S0004629919100049

Elitzur, M. 1992, Astronomical masers, ASSL, 170, (Dorderecht, Kluwer), https://doi.org/10.1007/978-94-011-2394-5

Haschick, A. D. & Ho, P. T. P. 1985, ApJ, 292, 200, https://doi.org/10.1086/163147

Ho, P. T. P., Haschick, A. D., & Israel, F. P. 1981, ApJ, 243, 526, https://doi.org/10.1086/158617

Lekht, E. E., Likhachev, S. F., Sorochenko, R. L., & Strel'nitskii, V. S. 1983, ARep, 37, 367

Lekht, E. E., Mendoza-Torres, J. E., & Berulis, I. I. 2002, ARep, 46, 57, https://doi.org/10.1134/1.1436205

Mampaso, A., Gomez, P., Sanchez-Magro, C., & Selby, M. J. 1984, MNRAS, 207, 465, https://doi.org/10.1093/mnras/207.3.465

Migenes, V., Horiuchi, S., Slysh, V. I., et al. 1999, ApJ, 123, 487, https://doi.org/10.1086/313238

Richards, A. M. S., Cohen, R. J., Crocker, M., et al. 2005, ApSS, 295, 19, https://doi.org/10.1007/s10509-005-3652-7

Wood, D. O. S. & Churchwell, E. 1989, ApSC, 69, 831, https://doi.org/10.1086/191329

Wouterloot, J. G. A., Brand, J., & Henkel, C. 1988, AA, 191, 323

N. T. Ashimbaeva and V. V. Krasnov: Lebedev Physical Institute, Astro Space Center, Russian Academy of Sciences, Moscow, 117997 Russia.

E. E. Lekht: Lomonosov Moscow State University, Sternberg Astronomical Institute, Moscow, 119991 Russia (lekht@sai.msu.ru).

J. E. Mendoza-Torres: Instituto Nacional de Astrofísica, Óptica y Electrónica, Calle Luis enrique Erro No.1, Sta. María Tonantzintla, Puebla, CP 72840, México (mend@inaoep.mx).

V. R. Shoutenkov: Pushchino Radio Astronomy Observatory, Astro Space Center, Lebedev Physical Institute, Russian Academy of Sciences, Pushchino, 142290 Russia.

Revista Mexicana de Astronomía y Astrofísica, **61**, 123–153 (2025)

https://doi.org/10.22201/ia.01851101p.2025.61.01.10

A FIRST QUANTITATIVE CHARACTERIZATION OF COLOMBIAN NIGHT SKY THROUGH ALL-SKY PHOTOMETRY

J. P. Uchima-Tamayo[1], R. Angeloni[2], M. Jaque Arancibia [1,3], C. Goez Theran[4], and J. F. Rúa Restrepo[5]

Received October 1 2024; accepted February 20 2025

ABSTRACT

Light pollution, a rapidly escalating anthropogenic phenomenon driven by the excessive and often inefficient use of artificial lighting, has profound implications for astronomy, ecology, and human health. This study presents the first comprehensive characterization of night sky quality in Colombia, focusing on sites of astronomical and ecological significance. The selected locations include the Astronomical Observatory of UTP, the Tatacoa Desert, the Bogotá Botanical Garden, and Cerro Guadalupe. Utilizing the Sky Quality Camera, we collected all-sky data to measure surface brightness and correlated color temperature of the night sky. Our findings reveal a significant loss of natural sky visibility in urban areas and demonstrate the detrimental effects of artificial lighting on critical astronomical sites such as La Tatacoa. This study provides a crucial foundation for future research and informs on the development of public policies aimed at preserving the night sky.

RESUMEN

La contaminación lumínica, un fenómeno antropogénico en rápido crecimiento, es impulsada por el uso excesivo de tecnologías de iluminación. Este mal uso afecta a la astronomía, a la ecología y a la salud humana. En este estudio, caracterizamos por primera vez la calidad del cielo nocturno en Colombia desde sitios de interés astronómico y ecológico. Los lugares analizados incluyen el Observatorio Astronómico de la UTP, el desierto de La Tatacoa, el Jardín Botánico de Bogotá y el Cerro Guadalupe. Utilizando la Sky Quality Camera, obtuvimos datos *all-sky* sobre el brillo superficial del cielo nocturno y la temperatura de color correlacionada. Los resultados evidencian la pérdida de las fuentes naturales del cielo en áreas urbanas y cómo la luz artificial afecta sitios astronómicos clave, como La Tatacoa. Este estudio sienta las bases para futuras investigaciones y políticas públicas destinadas a preservar el cielo nocturno.

Key Words: instrumentation: detectors — light pollution — methods: observational — software: data analysis — techniques: photometric

1. INTRODUCTION

Light pollution, defined as the inappropriate or excessive use of artificial light, was first described by Walker (1970) and Riegel (1973) as a loss of night sky darkness, causing the loss of the ability to observe celestial objects (Cinzano et al. 2000; Falchi et al. 2011). Later, Verheijen (1985) proposed the term “photo-pollution” to refer to artificial light that adversely affects wildlife. This phenomenon can disrupt the behavioral, feeding, breeding, and migration patterns of various species (Longcore & Rich 2004; Gaston et al. 2013; Davies et al. 2014; Hölker et al. 2021). Also, light pollution is a complex disruptor of the nocturnal environment, impacting everything from molecular processes to ecosystems. Its effects can be observed from the immediate vicinity of light sources to hundreds of kilometers away. The impacts of light pollution occur over a wide range of time scales, from seconds or less to decades, all within a

[1]Departamento de Astronomía, Universidad de La Serena, La Serena, Chile (corresponding author: juan.uchima@userena.cl).

[2]Gemini Observatory, NSF’s NOIRLab, La Serena, Chile.

[3]Instituto Multidisciplinario de Investigación y Postgrado, Universidad de La Serena, La Serena, Chile.

[4]Oficina de Olimpiadas Colombianas, Universidad Antonio Nariño, Bogotá, Colombia.

[5]Observatorio Astrosur, Villavieja, Colombia.

general trend of interannual increase (Bará & Falchi 2023).

For nearly two decades, there has been a significant increase in studies examining the effects of artificial light on astronomy and ecology. Hölker et al. (2010) introduced the term Artificial Light At Night (ALAN) to describe techniques for illuminating future landscapes and contributing to environmental protection. ALAN has rapidly evolved into an interdisciplinary field, influencing various aspects including human health (Cho et al. 2015; Svechkina et al. 2020; Deprato et al. 2024), economy (Gallaway et al. 2010; Mitchell & Gallaway 2019), philosophy (Henderson 2010), urban planning (Zielinska-Dabkowska 2019), and tourism (C-Sánchez et al. 2019; Varela Perez 2023). Despite the progress made in understanding and addressing light pollution, significant challenges persist in mitigating its effects, especially in densely populated urban environments (Aubé et al. 2016; Kyba et al. 2017).

ALAN corresponds to the artificial contribution to the Night Sky Brightness (NSB). However, for a complete characterization of the sky, it is also necessary to consider the natural contributions, which come from sources not influenced by human activity. They fall into two categories: sources originating in or near the Earth's atmosphere (such as airglow, auroras) and those coming from space beyond the Earth's atmosphere (such as integrated starlight, zodiacal light, galactic light). All these contributions have been described in various studies (Hänel et al. 2018; Alarcon et al. 2021; Barentine 2022). Understanding both artificial and natural contributions is thus essential to accurately assess the impact of light pollution and to develop effective strategies for preserving the night sky (Zielinska-Dabkowska et al. 2020).

Research conducted by Kyba et al. (2017, 2023) indicates that, over the past decade, the night sky has undergone significant changes due to an increase in the amount of light emitted and the continuous expansion of artificially illuminated areas, contributing to the rise in global sky glow. This has intensified the effects of light pollution, resulting in a much brighter night environment and diminishing the natural darkness of the sky. This shift is primarily driven by the increasing use of more efficient and lower-cost lighting technologies (Tsao et al. 2010). A key technology driving this change is light-emitting diodes (LEDs). Although LEDs are more efficient and durable than traditional lighting technologies, such as high-pressure sodium lamps, they have fundamentally changed the nature of ALAN, despite their advantages in efficiency and durability (Chang et al. 2012; Nair & Dhoble 2015; Cho et al. 2017). They have also altered the spectral power distribution (SPD) of ALAN, that is, shifting from displaying only a few emission lines to dozens, and even hundreds, of lines (Hung et al. 2021).

A key factor in assessing the impact of lighting changes is the correlated color temperature (CCT), which quantifies the color of emitted light by comparing it to the light produced by a blackbody at a given temperature, measured in Kelvin (K). The shift in the SPD introduced by LED technology affects not just the intensity, but also the color characteristics of artificial light. This, in turn, influences both the nocturnal environment and biological processes (Durmus 2022). Consequently, the transition from traditional lighting to LEDs not only exacerbates light pollution but also alters how we experience and interact with artificial light during nighttime. For example, during the day, the sky typically shows CCT values between 5500 K and 6500 K. At night, these values are largely influenced by artificial lighting, such as city lights. Sodium lamps, for instance, produce lower CCT values, ranging from 2000 K to 3000 K, while white LED lights can generate higher CCT levels, between 4000 K and 6500 K. Also, atmospheric conditions and natural light sources can introduce significant variations in these measurements (Jechow et al. 2019). Furthermore, CCT has become an important measure due to its considerable impact on people's health and well-being (Mills et al. 2007; Luo et al. 2023).

To understand and evaluate the impact of ALAN, various measurement techniques have been developed. Mander et al. (2023) grouped the techniques into four categories. Space borne sensors provide global data on light pollution via satellites. Airborne sensors, including aircraft, balloons and drones, make measurements, allowing for a more accurate assessment of the effects of ALAN on the environment and communities. Ground-based monochromatic sensors, such as the Sky Quality Meter[6] (SQM) described by Cinzano (2005) and the Telescope Encoder and Sky Sensor[7] (TESS) developed by (Zamorano et al. 2016; Bará et al. 2019), are popular for measuring NSB due to their one-dimensional output, and are typically deployed in regions or countries for detailed estimates of the evolution of ALAN (Posh et al. 2018; Bertolo et al. 2019). Additionally, ground-based photometric sensors provide information on the spatial distribu-

[6] http://www.unihedron.com/projects/darksky/.

[7] https://tess.stars4all.eu/.

tion of sky brightness using pseudo-color maps and, when oriented to zenith, typically use a CCD or a CMOS sensor combined with a fast objective lens (Kolláth 2010; Aceituno et al. 2011). One of the most widely used instruments is the Sky Quality Camera (SQC), designed, developed and sold by Euromix Ltd, Slovenia. It is essentially a calibrated DSLR camera able to provide spatially-resolved NSB (in units of [mcd/m^2] or [V mag/arcsec^2]) and CCT (in units of Kelvin [K]) observations. When pointed towards the zenith, this equipment is able to capture a hemispherical view that includes both the sky and the local horizon. Thanks to is large dynamical range, it has been used for very different skies, from virtually pristine ones down to urban centers heavily light polluted (Angeloni et al. 2024). As reported in recent reviews (e.g., Mander et al. 2023), the SQC has today become the reference tool for all-sky photometric studies of light pollution because of the optimal balance between cost, ease of use, and richness of information it is able to provide (Hänel et al. 2018). It is the instrument also used in this study (§ 2.2).

In Latin America, studies on light pollution have primarily focused on regions with astronomical infrastructures, such as Chile (Krisciunas et al. 2007; Müller et al. 2011; Falchi et al. 2023; Angeloni et al. 2024), Mexico (Tovmassian et al. 2016; Plauchu-Frayn et al. 2017), and Argentina (Aubé et al. 2014; Iglesias et al. 2023). In Colombia, however, measurements have been more centered on ecological places, using SQM in locations such as Bogotá (Aguilera Camargo 2012), the Bogotá Botanical Garden (hereafter BBG - Urrego Guevara 2016), and the Tatacoa Desert (hereafter TD - Góez Therán & Vargas Domínguez 2021). Rueda-Espinosa et al. (2023) have presented the most recent study on ALAN in Colombia, examining the expansion of NSB in major cities including Bogotá, Medellín, Cali, Bucaramanga, Barranquilla, and Cartagena, using Visible Infrared Imaging Radiometer Suite[8] (VIIRS) data from 2012 to 2022. Additionally, satellite data have been employed to identify areas with low light pollution and to identify suitable sites for astronomical observation, both in the optical spectrum (Arbeláez-Cardona et al. 2020) and in the radio spectrum (Chaparro Molano et al. 2017).

Colombia is renowned for its megadiverse ecosystems, ranking fourth in plant species richness, fifth in mammals, first in birds, third in reptiles, and second in amphibians, freshwater fish, and butterflies (Andrade-C 2011). Despite this notable biodiversity and considering the important impacts of light pollution on ecosystems, there is currently no specific legislation in Colombia to protect fauna from this type of pollution. This lack of regulation is worrying, since recent studies, such as those carried out by Marín Gómez (2022) and Sánchez-González et al. (2020), have shown alterations in the songs of several species of birds due to light pollution in Armenia, a city located within the Humid Forest Biome of the central Andes. These studies highlight the urgent need to implement protection measures to preserve Colombian biodiversity. Additionally, Colombia is recognized as one of the cloudiest regions in the world, largely due to the complex interaction between its geography and atmospheric conditions (Poveda et al. 2011). The frequent cloud cover can intensify the effects of light pollution, as artificial light is scattered by the clouds, amplifying its impact. This further disrupts local wildlife and interferes with their natural cycles (Kyba et al. 2011).

In contrast to countries such as Spain[9], Mexico[10], and Chile[11], which have implemented regulations to control light pollution, Colombia lacks specific legislation aimed at protecting dark skies or properly regulating light pollution. While the country does have technical regulations governing public and general lighting systems, these standards have been criticized as overly lenient and insufficient for preserving the night sky, as noted by Benítez García (2016) in a study conducted between 2010 and 2016. Implementing stricter measures is essential to preserve the quality of the night sky. Therefore, society must become aware of and sensitive to the harmful effects of light pollution, promoting sustainable lighting practices (Vierdayanti et al. 2024).

This study presents the first comprehensive NSB and CCT maps for the Colombian skies, derived from data collected by SQC during an observing campaign in September 2022. § 2 describes the study sites, the data acquisition process, and the data reduction method. § 3 presents the results, followed by a discussion in § 4. Finally, § 5 outlines the conclusions and final observations.

2. MATERIALS AND METHODS

2.1. *Locations of Interest*

Several sites were selected to measure NSB in Colombia based on previous SQM records. These lo-

[8] `https://www.earthdata.nasa.gov/sensors/viirs`.

[9] `https://www.boe.es/buscar/pdf/2010/BOE-A-2010-20074-consolidado.pdf`.

[10] https://www.ensenada.gob.mx/wp-content/uploads/2021/11/Reglamento-para-la-prevencion-de-la-contaminacion-luminica-en-el-Municipio-de-Ensenada-Baja-California.pdf.

[11] `https://luminica.mma.gob.cl/norma-luminica/`.

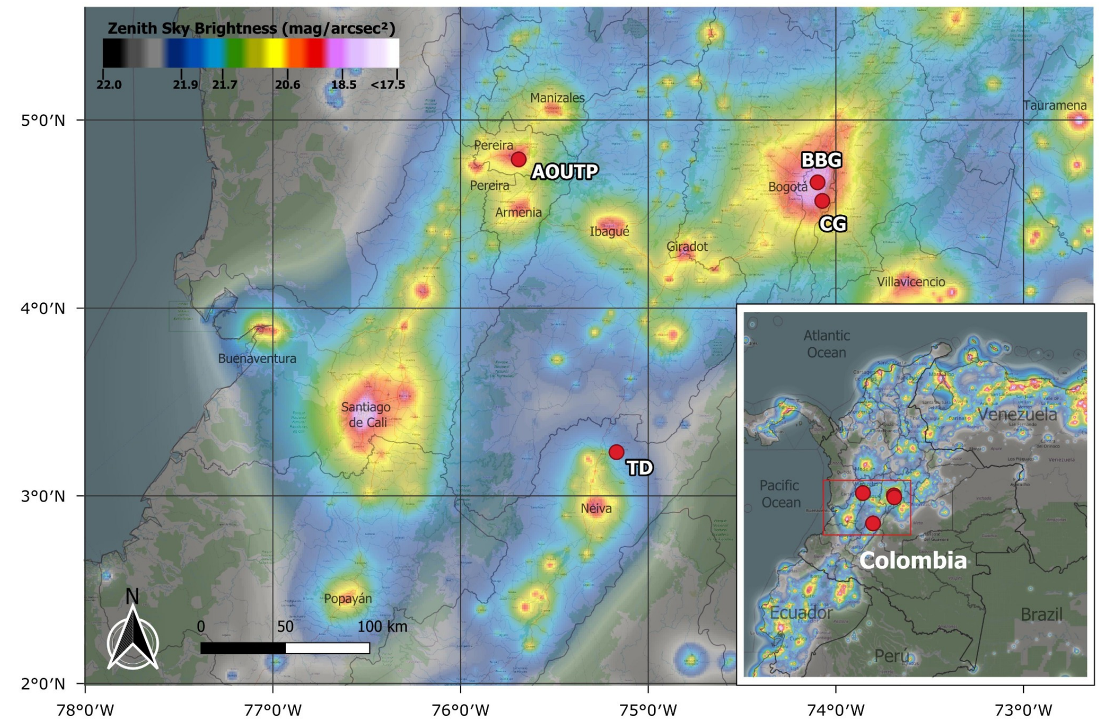

Fig. 1. The geographical distribution of the four sites analyzed in this study is represented by red points with white labels on a background color map, constructed using data from the New World Atlas of Artificial Night Sky Brightness (Falchi et al. 2016). The color figure can be viewed online.

cations include the BBG and the TD, both of which have existing SQM data (Urrego Guevara 2016 and Góez Therán & Vargas Domínguez 2021, respectively). The study also incorporates the Astronomical Observatory of the Universidad Tecnológica de Pereira (hereafter AOUTP) and Cerro Guadalupe (hereafter CG) in Bogotá. Each site has distinct characteristics in terms of topography and primary activities. AOUTP is focused on astronomical research, TD is known for astrotourism, BBG is dedicated to biodiversity conservation, and CG serves as an ecological corridor[12]. Figure 1 depicts the geographic locations of these sites overlaid on a pseudocolor map adapted from the New World Atlas of Artificial Night Sky Brightness (Falchi et al. 2016). Table 1 presents the geographic coordinates obtained and the acronyms by which each site is identified.

[12]An ecological corridor is defined by the Central American Commission on Environment and Development as “a delimited geographical space that provides connectivity between landscapes, ecosystems, and habitats, whether natural or modified, and ensures the maintenance of biological diversity as well as ecological and evolutionary processes”.

2.2. *Data Acquisition, Reduction and Analysis*

The SQC used in this study is a Canon EOS 6D Mark II featuring a 26.2-megapixel full-frame CMOS sensor and an integrated GPS. It comes equipped with a Sigma 8 mm EX DG fisheye lens able to image in a single shot a field of view of 186°. The entire setup is mounted on a Manfrotto MK055XPRO3-3W tripod. After several years of intensive use, we can confirm that the SQC maintains a photometric precision of ± 0.01 mag/arcsec^2, a CCT precision of $\pm$ 30 K, and a spatial resolution of $\pm$ 0.02°.

We took data only after astronomical twilight, i.e., when the Sun elevation was $\geq -18°$, and on those times when the Moon was $\geq 10°$ below the horizon. At each site, we identified the optimal location for the SQC installation, ensuring a 30 meter radius free of nearby luminaries and avoiding any direct illumination on the equipment. Additionally, we prioritized sites with the clearest possible view of the sky to minimize (whenever possible) obstructions from elements such as trees, mountains, and buildings. As a matter of fact, due to the natural surroundings, achieving a fully unobstructed view was not always feasible, particularly at BBG and CG.

TABLE 1

GEOGRAPHIC COORDINATES

Site	**Acronym**	**City**	**Latitude** [° ′ ″] **N**	**Longitude** [° ′ ″] **W**	**Elevation** **[masl]**
Astronomical Observatory UTP	AOUTP	Pereira	04 47 26.06	75 41 25.57	1514
Tatacoa Desert	TD	Villavieja	03 13 51.98	75 09 16.22	481
Bogotá Botanical Garden	BBG	Bogotá	04 40 03.49	74 06 02.16	2565
Cerro Guadalupe	CG	Bogotá	04 35 29.20	74 03 12.86	3273

TABLE 2

OBSERVATION LOG

Site *acronym*	**Date** *aaaa-mm-dd*	**Time** *local*	**ISO**	**Exp. Time** *[s]*	**S/N**
AOUTP	2022-09-15	19:24:07	1600	5	35
TD	2022-09-18	22:07:27	1600	150	22
BBG	2022-09-20	19:18:22	1600	3	41
CG	2022-09-20	22:45:29	1600	11	33

Subsequently, the camera was positioned to point towards the zenith, with its front aligned to geographical north using a compass. A circular bubble level was placed on the cover to ensure precise leveling. In this study, the ISO was set to 1600 at all sites, while the shutter speed was adjusted based on ambient brightness to prevent saturation and ensure a signal to noise ratio (S/N) greater than 20. All this information was recorded in the observation log, shown here as Table 2, which includes acronyms, date, time, exposure duration, and S/N values.

In order to preserve the maximum amount of information, the images were processed and analyzed in the native raw Canon .CR2 format using the commercial SQC software (v.1.9.9). After each image we also took the corresponding dark, that is automatically subtracted before the image file is written to disk. For further details about the data acquisition, reduction and analysis processes, the interested reader can refer to Angeloni et al. (2024).

3. RESULTS

This section provides a comprehensive description of each measurement location, emphasizing its unique characteristics and presenting the results of the observations. Considering that Colombia is one of the cloudiest regions in the world (Poveda et al. 2011), given its average annual cloud cover of 68.6% [13], it is essential to consider clouds as an integral part of the natural landscape when analyzing our SQC data.

Therefore, for each site, an SQC image is presented, consisting of four components (for example, Figure 2): the topocentric RGB map, the Cloud Map, the NSB map, and the CCT map. These images are arranged as follows: the RGB map is at the top left, the Cloud Map is at the bottom left, the NSB map is at the top right, and the CCT map is at the bottom right. In the RGB maps, the colored spherical triangles encapsulate the regions of interests, while in the remaining maps, the orange (yellow) line represents the galactic (ecliptic) plane, while the purple ring corresponds to the 30° elevation ring, which serves as a photometric indicator described in more detail in § 4.1. The cloud map employs a color scale to depict sky conditions: blue indicates clear skies, red signifies cloudiness, and green

[13] `https://www.extremeweatherwatch.com/countries/colombia`.

DOI: https://doi.org/10.22201/ia.01851101p.2025.61.01.10

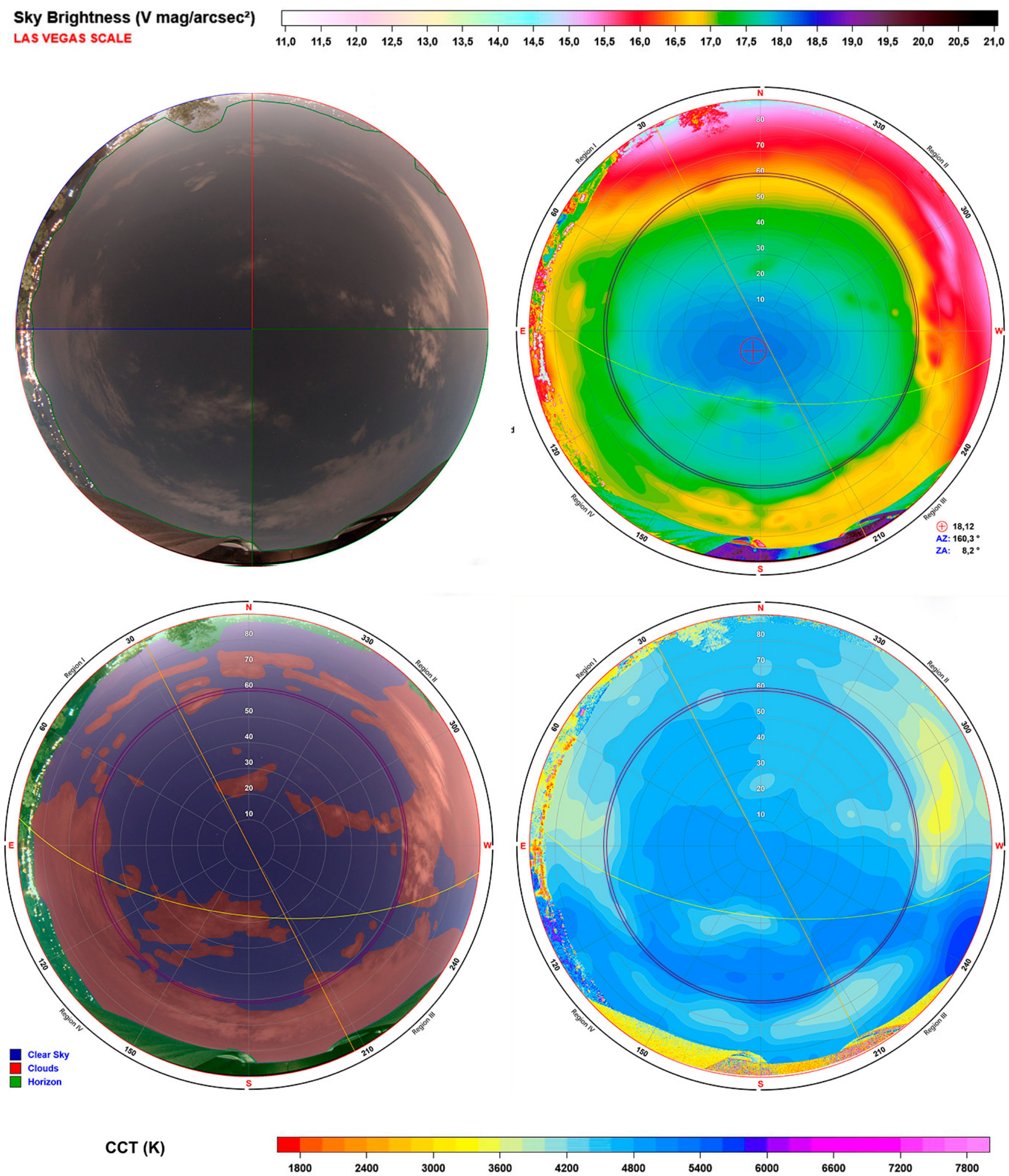

Fig. 2. SQC Images of the night sky at AOUTP captured on September 15, 2022. North is to the top and East is to the left. The upper-left panel displays the RGB image, with spherical triangles of color-coded azimuth ranges as presented in Table 3 and discussed in § 3.1. The upper-right panel shows the NSB map in V mag/arcsec^2 and includes the coordinates of the darkest point along with its corresponding NSB value ($\oplus$). The lower-left panel presents the cloud map, highlighting cloudy regions in red. The lower-right panel shows the CCT map in Kelvin. In the last three panels, the orange (yellow) line corresponds to the galactic (ecliptic) plane, while the purple ring corresponds to the 30° elevation ring (refer to § 4.1). Under very bright skies the Las Vegas scale (NSB values ranging between 11 and 21 [V mag/arcsec^2]) is displayed instead of the usual one (that goes between 14 and 24 [V mag/arcsec^2]). The color figure can be viewed online.

denotes the horizon. The NSB map includes the coordinates of the darkest point in the sky, specified in terms of azimuth (AZ) and zenith angle (ZA), along with its corresponding NSB value. The upper scale bar displays NSB values in [V mag/arcsec^2], while the lower scale bar shows CCT values in [K]. Under very bright skies the Las Vegas scale (NSB values ranging between 11 and 21 [V mag/arcsec^2]) is displayed instead of the usual one (that goes between 14 and 24 [V mag/arcsec^2]).

Subsequently, the azimuth profiles (see Figures 3, 6, 9, and 12) are presented, constructed using a 1°-wide ring. The altitude values are selected based on the horizon of each image. In the graphs, the NSB profile is displayed on the left and the CCT profile on the right, with the names of the main peaks in the NSB and CCT values labeled for reference.

On the other hand, the zenith profiles (see Figures 4, 7, 10, and 13) are constructed considering all zenith angles. However, the amplitude of these profiles varies according to the azimuthal range specified in Table 3, as each region of interest covers a different extent depending on its influence on the site. The arrangement of the zenith profiles follows the same format as the azimuth profiles, with the NSB profile on the left and the CCT profile on the right.

Table 3 details the azimuthal ranges of interest and the most significant sources of ALAN for each site, along with their corresponding distances. To identify these sources, we utilized Colombia's administrative divisions, starting with visible cities, followed by communes[14] and rural districts (vereda). In the case of Bogotá, as a capital district, the administrative divisions refer to localities. The "Region" column in the table employs a color code to represent the brightest ALAN sources at each site: blue indicates the brightest source, followed by red, green, and black. For the TD site, orange represents an ALAN-free direction, defined as an azimuthal range where no ALAN sources are detected within a distance of 150 km (Angeloni et al. 2024).

3.1. *Astronomical Observatory of the UTP (AOUTP)*

The AOUTP[15] is located in the Central West metropolitan area[16]. Specifically, the observatory is situated in the southeastern part of Pereira, on the university campus in the La Julita sector. The observatory has received several international recognitions. Notably, it has been granted the code W63 by the Minor Planet Center, identifying it as an observatory authorized to obtain astrometric data of minor bodies in the Solar System (Jiménez Villariaga et al. 2017). Additionally, the observatory holds the UTP 0383 code from the Stanford Solar Center for space weather monitoring (Galvis et al. 2019). These recognitions establish the AOUTP as one of Colombia's leading scientific centers for astronomical and space science.

In 2025, the observatory will expand its infrastructure and upgrade its astronomical equipment. A new facility will house a 70 cm diameter telescope, which, along with the existing instrumentation, will establish the observatory as the leading center for astronomical research in Colombia. These advancements will not only elevate the university's academic contributions but also strengthen its research capabilities, community outreach, and engagement in the field of astronomy.

It is worth noticing the ecological value of the UTP campus, where 58% of its surface is dedicated to forest conservation and consequently classified as Natural Wild by Botanic Gardens Conservation International[17], as plant species thrive in their natural environment without human intervention. Specifically, 13 hectares are allocated to the UTP Botanical Garden, which houses approximately 542 species of flora that are meticulously identified and protected (García Sierra & Ramírez Cardona 2011). This area serves as a valuable resource for research and environmental education, and a space for recreation and engagement with nature for students and visitors. The conservation and sustainability initiatives implemented on campus have garnered national and international recognition, establishing UTP as a model for university environmental management.

Figure 2 presents an all-sky view from the AOUTP observatory. In the RGB map, the observatory's dome is visible on the horizon to the south, while the eastern horizon reveals the surrounding mountains and the lights from nearby houses. The sky features several cloudy regions illuminated by the sky glow from the city of Pereira, as corroborated by the cloud map. The NSB map highlights a bright region extending approximately from 240° to 60° in azimuth, corresponding to the cities of Pereira and Dosquebradas. Furthermore, a zone of increased surface brightness is detected in the azimuthal range of 270° to 300°, exhibiting a lower CCT than the rest of the sky in the CCT map, indicating the presence of a cloud amplifying the city's surface brightness. The combination of these images provides valuable insights into how atmospheric conditions and urban lighting influence sky quality and, consequently, the effectiveness of astronomical observations.

[14]The National Administrative Department of Statistics (DANE, for its acronym in Spanish) defines a commune as an administrative subdivision of a city or municipality that groups several neighborhoods to facilitate local management, community participation, and the administration of public services.

[15]https://observatorioastronomico.utp.edu.co/

[16]The fifth largest in Colombia, with a population of 735,796 according to the 2018 census by DANE.

[17]https://www.bgci.org/

TABLE 3

ALAN SOURCES[a]

Site	Region	Azimuth Range [°]	ALAN *Main Sources*	Distance [*km*]
AOUTP	I	0 - 90	Universidad Commune	1.1
			Villasantana Commune	2.2
			Dosquebradas	3.7
	II	270 - 0	Centro Commune	2.7
			Cuba Commune	5.4
			Matecaña Airport	5.9
	III	180 - 270	Condina Bypass	3.0
			Altagracia Neighborhood	6.2
	IV	90 - 180	Vereda Mundo Nuevo	1.3
			El Remanso Neighborhood	2.1
TD	I	178 - 238	Ecopetrol Dina Field	23.4
			Neiva	36.8
	II	249 - 290	Villavieja	7.2
			Aipe	9.5
			3C LTDA (Agro-industrial company)	11.5
	III	11 - 45	Melgar	121
			Girardot	125
			Bogotá	193
	IV	140 - 145	ALAN-free direction (Cordillera de los Picachos National Park)	...
BBG	I	180 - 270	Kennedy Locality	6.7
			Ciudad Bolivar Locality	13
	II	90 - 180	Teusaquillo Locality	3.4
			Chapinero Locality	13
	III	270 - 360	Fontibón Locality	3.5
			Engativá Locality	5.0
	IV	0 - 90	Suba Locality	7.2
			Usaquén Locality	8.0
CG	I	180 - 270	Usme Locality	10
			Ciudad Bolivar Locality	11.5
	II	270 - 0	Bogotá	3
	III	90 - 180	Choachía	11
			Chingaza National Park	34
	IV	0-90	Usaquén Locality	13.0
			La Calera	16.7

[a]ALAN sources for each site: The numbers I, II, III, and IV correspond to the study regions, with colors coding the region with the highest contribution of artificial brightness. All sources are arranged in ascending order concerning the measurement site. For detailed information, please refer to the main text.

To identify the areas or sites that contribute most to the NSB and CCT, we constructed rings at different elevations to determine the directions of the most significant contributing sources in each study region. We refer to these segments of the sky as azimuthal profiles, abbreviated as AZ. Figure 3 presents the azimuthal profile for the AOUTP. Using the ALAN sources from Table 3, we determined the azimuth of the highest contribution to NSB and CCT for each region:

- Region I exhibits a NSB peak at $AZ \approx 21°$, corresponding to the direction of the Arboleda Mall, and a CCT minimum at $AZ \approx 83°$, corresponding to the Tokio neighborhood.

- Region II shows a maximum NSB at $AZ \approx 298°$ and a minimum CCT at $AZ \approx 280°$, corresponding to the airport direction.

- Region III displays a maximum NSB at $AZ \approx 261°$, corresponding to the Villa Verde neighborhood and two CCT maxima at $AZ \approx 192°$ and $AZ \approx 242°$, corresponding to the Altavista residential complex and the Canan Sports Complex.

- Region IV has a maximum NSB at $AZ \approx 102°$, corresponding to the sports complex of the El Remanso neighborhood, and a maximum CCT at $AZ \approx 119°$, corresponding to the parking of the Botanical Garden.

The primary contributors to the NSB for the AOUTP are the Arboleda Mall and the airport, which typically operate almost until midnight. The airport's lighting remains constant to ensure safe landings, while the mall maintains its lights for various events. In contrast, the maximum CCT values correspond to areas near the AOUTP, such as the parking of the Botanical Garden, sports complex, and residential complexes. These places typically use LED lights and, in many cases, have lighting issues such as over-illumination or improper light orientation, which disperses light both toward the ground and the sky.

To determine the altitude affected by the AOUTP, we constructed a ZA profile (see Figure 4), which revealed distinct brightness patterns across different regions as they approach the horizon. In Region I, a sharp increase in brightness is observed at ZA = 83°, attributed to the city glow. Region II exhibits a rise in brightness between ZA = 73° and ZA = 81°, likely caused by a cloud amplifying the NSB. In Region III, a slight increase is evident between ZA = 25° and ZA = 40°, associated with the presence of a cloud. Additionally, a secondary increase occurs at ZA = 83°, linked to urban glow. In Region IV, NSB increases between ZA = 26° and ZA = 43°, due to cloud covered, and again between ZA = 75° and ZA = 85°, potentially caused by urban glow. It is worth noting that some areas do not extend to the horizon, as they are physically obstructed by features like mountains or the dome.

3.2. *Tatacoa Desert (TD)*

The Tatacoa Desert is a tropical dry forest situated in the Magdalena River valley, within the department of Huila, approximately 10 km from the municipality of Villavieja[18]. It is the second driest region in Colombia, renowned for its eroded landscape, forming a labyrinth of canyons, valleys, and rock formations in striking red and gray hues. The Tatacoa Desert uniquely combines geological, climatic, and biogeographical factors, making it an ideal site for studying Neogene biodiversity in South America (Flórez et al. 2013, Montes et al. 2021) and paleogeography (Dill et al. 2020).

As one of Colombia's top tourist destinations, the TD attracts visitors with its semi-arid landscapes, outdoor activities, including stargazing (Montealegre Vega & Garavito González 2022). In September 2019, it was certified as a Starlight Destination[19], the first site in Colombia to receive this recognition. The Starlight Foundation, with support from UNESCO, the World Tourism Organization (UNWTO), and the International Astronomical Union (IAU), grant this certification to areas that protect and conserve dark skies.

Today, the Tatacoa Desert is a hub for astrotourism and a premier destination in Colombia for astronomy enthusiasts. The desert hosts several observatories and astronomical complexes. For our measurements, we were at the Astrosur Observatory[20], located approximately in the center of the desert; it provided the necessary safety conditions to conduct our research.

TD is one of the locations that presented a NSB measurement with the SQM instrument during the night of April 14-15, 2014. These measurements were made during a total lunar eclipse, and therefore with a full Moon, allowing for a record of approximately 9 hours of measurement. Each measurement was taken

[18] In 2018, the DANE census recorded a population of 7,308 inhabitants.

[19] https://fundacionstarlight.org/

[20] https://www.facebook.com/Tatacoa.Astronomia/

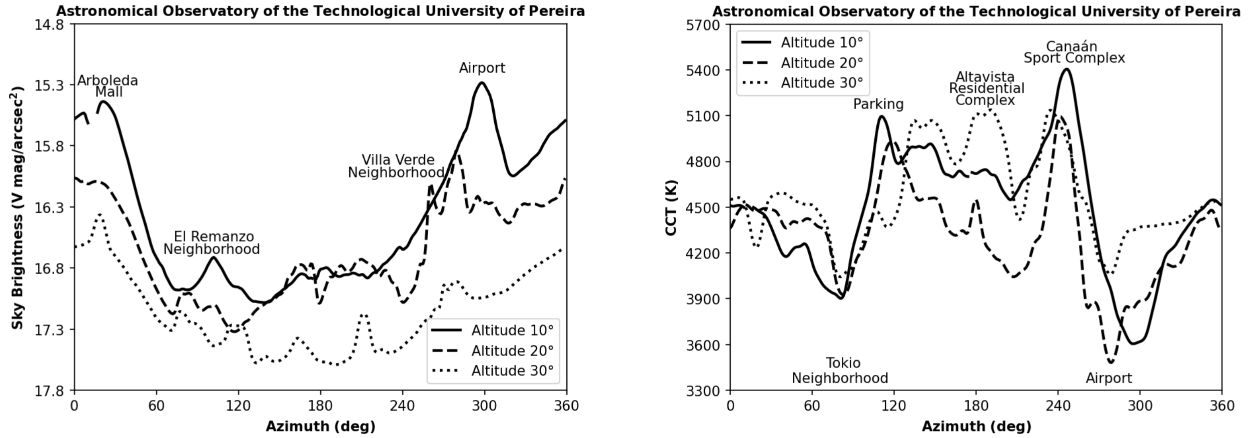

Fig. 3. Azimuthal NSB/CCT profiles (left/right panel) averaged within 1° wide rings centered at 10°, 20°, and 30° elevation at AOUTP. These profiles identify the local maxima of NSB and CCT, indicating the azimuthal directions of the ALAN sources. For more details, refer to Figure 2 and Table 3.

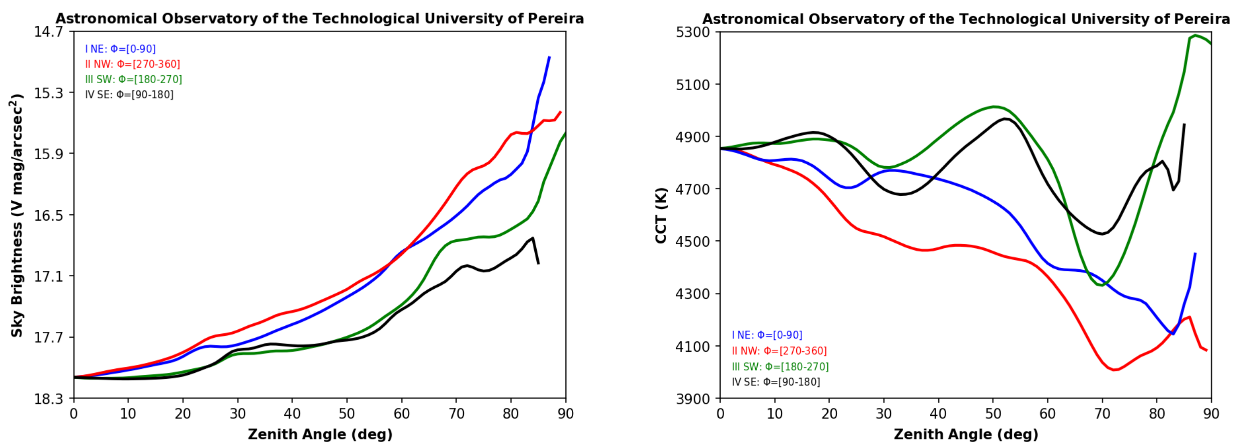

Fig. 4. Zenith profiles, NSB/CCT variance as a function of zenith angle (left panel/right panel). For details, refer to § 3.1, Figure 2, and Table 3. The color figure can be viewed online.

at 5-minute intervals; for more details, refer to Góez Therán & Vargas Domínguez (2021). As this is the only existing record of sky quality for this location, we will use the darkest measurement, which is 21.26 mag/arcsec^2, as the reference value. This reference will be fundamental for evaluating the evolution of sky quality in future studies.

The all-sky view from TD is depicted in Figure 5. The upper left image presents an RGB format, where the Milky Way can be clearly seen arcing from north to south, with Jupiter standing out as the brightest point in the sky. TD is the only location that offers an ALAN-free direction. According to the light pollution map, this direction is in the azimuthal range of 140° to 145° and corresponds to the Cordillera de los Picachos National Park. This protected area is known for its great diversity of fauna, including endemic and endangered species, and therefore experiences minimal human intervention.

On the horizon, a white glow stands out in the southern and eastern parts of the image, corresponding to the cities of Neiva, located $\sim$ 37 km away, and Villavieja-Aipe, situated roughly 7 and 10 km, respectively. To the north, another yellow/orange glow originates from the cities of Melgar (121 km), Girardot (125 km), and Bogotá (193 km). This glow is intensified by the presence of clouds, which can be identified in the cloud map. The NSB map shows the areas with the highest surface brightness, highlighting that the Milky Way is a natural contribution of light. However, the most intense contributions come from the cities, with Neiva as the main source of brightness. On the other hand, when observing the CCT maps, it can be seen how the CCT of the night

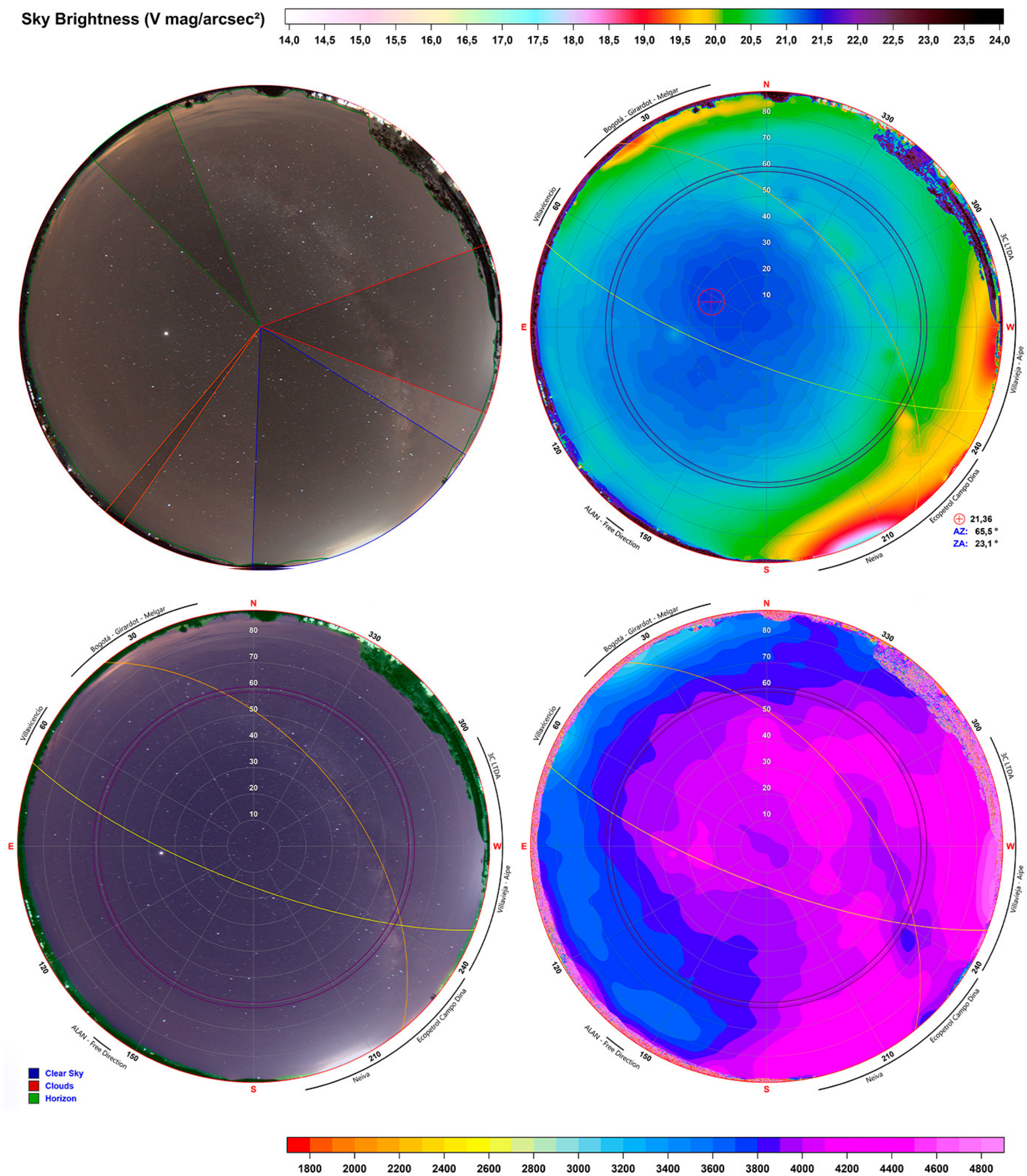

Fig. 5. Same as Figure 2, but for TD on September 18, 2022,using the standard scale bar for NSB and a CCT range of [18004800 K]. Additionally, the orange spherical triangle corresponds to the ALAN - free direction. For more details, refer to § 3.2 and Table 3. The color figure can be viewed online.

sky is confused with the CCT of the cities, with a white glow coming mainly from LED lights.

Figure 6 presents the azimuthal profile for TD. In this plot, NSB maxima can be identified for the three regions of interest at $AZ = 203°$, $AZ = 263°$, and $AZ = 35°$, respectively. Similarly, CCT maxima are observed for regions I and II at $AZ = 194°$ and $AZ = 261°$, with a minimum for region III at $AZ = 34°$. The NSB analysis highlights the need to implement controls on the type of illumination in Neiva, Villavieja, and Aipe to prevent the TD sky from losing its dark sky quality or Starlight certification.

Figure 7 presents the zenith profiles of NSB/CCT. In Region I, there is an increase in brightness at $ZA = 64°$ due to the passage of the Milky Way, with an additional increase attributed to the city of Neiva. Conversely, in the CCT, no significant variation is observed up to $ZA = 69°$, also corresponding to Neiva. In Region II, which has the second highest NSB value, an increase is observed as the horizon is approached. Within the range of ZA = 29° to ZA = 53°, the NSB is primarily influenced by the natural contribution of the Milky Way. However, beyond this ZA, the NSB rises rapidly due to the light pollution from the cities of Villavieja and Aipe. Additionally, the CCT analysis indicates that LED lights predominate in this direction, resulting in the highest CCT values observed in this region.

In Region III, the NSB contribution shows a considerable increase at $ZA = 71°$ due to the ALAN originating from the cities. It is not possible to determine the NSB of the Milky Way in this region since its passage occurs very close to the cities. The CCT shows a noticeable decrease from $ZA = 60°$, corresponding to the area affected by the city's contributions. Finally, Region IV, the ALAN-free direction is distinguished by its stable NSB profile, identifying it as the darkest area within the studied region. It is important to note, however, that stability in NSB variation does not necessarily indicate low light pollution; an area consistently illuminated by ALAN would also exhibit minimal variation, but with higher brightness levels. The NSB map remains relatively constant up to $ZA = 38°$. Beyond this angle, an increase in NSB is observed, primarily due to light scattering caused by the city of Neiva. This effect becomes more pronounced at $ZA = 48°$, where the presence of clouds significantly amplifies the sky glow. Conversely, the CCT profile exhibits a gradual decrease starting around $ZA = 14°$, reaching its minimum value near $ZA = 78°$. Beyond this zenith angle, the CCT begins to rise again. This increase is attributed to the absence of clouds over the mountainous region, allowing for clearer visibility of this portion of the sky.

3.3. *José Celestino Mutis Bogotá Botanical Garden (BBG)*

The "José Celestino Mutis" Botanical Garden in Bogotá is a research center dedicated to conserving high Andean and paramo forest ecosystems. Located in the metropolitan area of Bogotá[21], in the Engativá locality, the Garden spans approximately 20 hectares. It boasts an impressive collection of flora, featuring 55,000 individual plants representing 1,187 species distributed across 34 ecological zones. The garden also includes various botanical collections, such as ethnobiological, herbarium, carpotheque and tissue collections (Cadena-Vargas et al. 2020).

The BBG has become an environmental reference point and a must-visit destination for those interested in exploring and learning about the city's and country's rich biodiversity. In recent years, it has emerged as one of Bogotá's main tourist attractions and serves as a vital green lung in the heart of the metropolis. Additionally, it offers educational programs and interactive activities for visitors of all ages, fostering environmental awareness and respect for nature. The garden also plays a crucial role in scientific research and conservation efforts, collaborating with various institutions to preserve Colombia's unique plant species (Cadena-Vargas et al. 2021).

As previously mentioned, BBG had existing ALAN measurements recorded using an SQM. In 2014, a study was conducted using 13 measurement points distributed throughout the garden, starting near the southern part of the lake and following a circular route that ended at the main entrance. For our study, equipped with an SQC instrument, we chose a single measurement point to capture the most comprehensive information of the entire sky. To maximize sky coverage, we strategically selected a location approximately 80 meters from the Tropicarium[22] and the greenhouse circuit. This location aligns with an intermediate position between Points 4 and 5 from the study by Urrego Guevara (2016).

Furthermore, considering the differences in equipment and the SQM's limitation of providing only a single value, we used the average NSB value recorded at the 13 points in the 2014 study during September as a reference. This average value was 16.31 mag/arcsec^2.

[21]In 2018, the DANE census recorded a population of 7.181.469 inhabitants

[22]It is a building whose primary function is to protect the flora that grows below 2,400 meters above sea level.

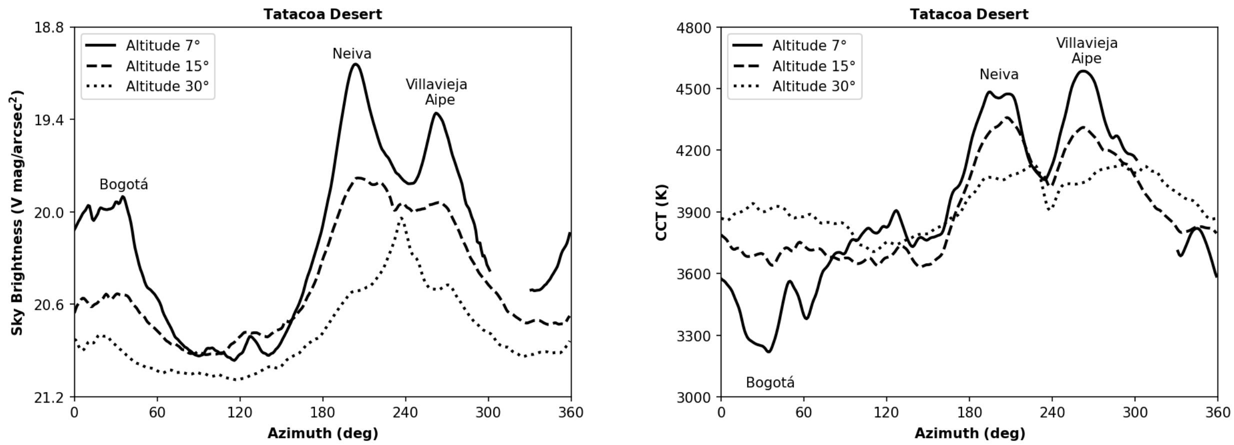

Fig. 6. Same as Figure 3, but for TD. In this case, the rings are at 7°, 15°, and 30° elevation. See Figure 5 and Table 3.

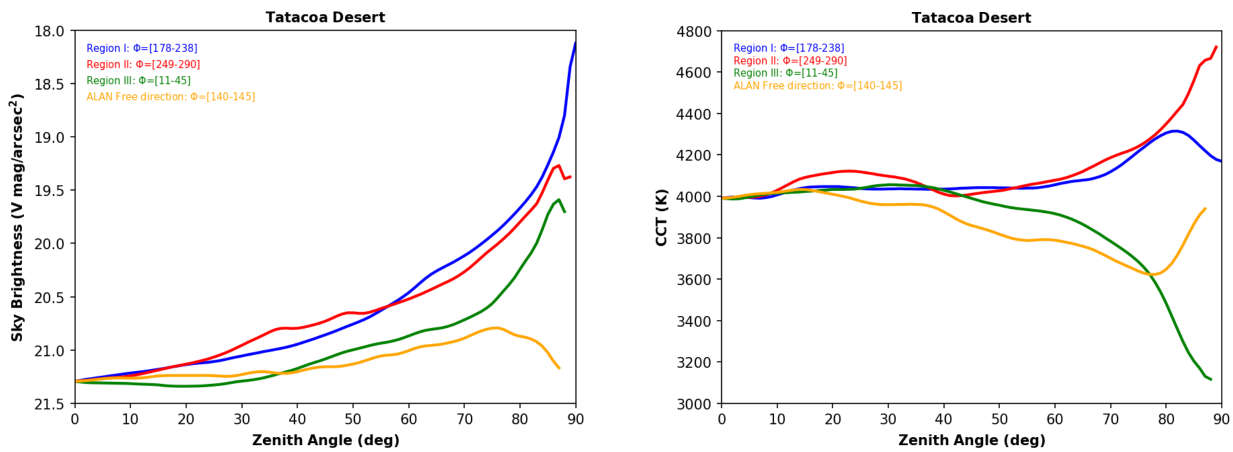

Fig. 7. Same as Figure 4, but for TD. For more details, see § 3.2, Figure 5, and Table 3. The color figure can be viewed online.

Figure 8 shows the all-sky view in RGB format from the BBG, highlighting the distribution and presence of clouds. The silhouettes of trees and part of the tropicarium structure are visible, with clouds distinctly appearing both amidst and above the treetops. Since the BBG is located in an urban area like Bogotá, where elevated levels of NSB are anticipated, the scales for the NSB and CCT maps were adjusted accordingly. The NSB map utilizes the Las Vegas scale, ranging from 11 to 21 V mag/arcsec^2, while the CCT map spans from 1600 to 7800 K. Both maps indicate an increased contribution from a $ZA = 60°$ towards the horizon.

To more accurately assess each region and identify the azimuths of significant contribution in NSB and CCT, Figure 9 illustrates the azimuthal profiles for the BBG. Selected altitudes of 30°, 40°, and 50° were chosen to mitigate interference from trees. However, Region IV is excluded from the profile due to the tropicarium and trees appearing prominently in that direction. Region I shows a peak NSB and a minimum CCT at $AZ = 188°$, corresponding to the Compensar Stadium. Region II reveals its maximum NSB at $AZ = 170°$, associated with the bowling alley and auxiliary courts of Compensar, while the minimum CCT at $AZ = 122°$ aligns with the Velodrome. Region III displays the maximum NSB and minimum CCT at $AZ = 296°$, corresponding to the Normandía fields.

The zenith profile is presented in Figure 10. Regions I and II exhibit an increase in NSB at $ZA = 48°$. Region III shows a rise in NSB from $ZA = 14°$ to $ZA = 31°$, attributable to the presence of a cloud, with a more pronounced increase from $ZA = 55°$. In Region IV, there is a gradual increase in NSB; however, data beyond $ZA = 52°$ are unavailable due to obstacles. Conversely, the zenith profile of CCT demonstrates a decrease as it approaches the horizon. In Region I, this decrease initiates at $ZA = 39°$. In Region II, the change occurs at $ZA = 45°$. Re-

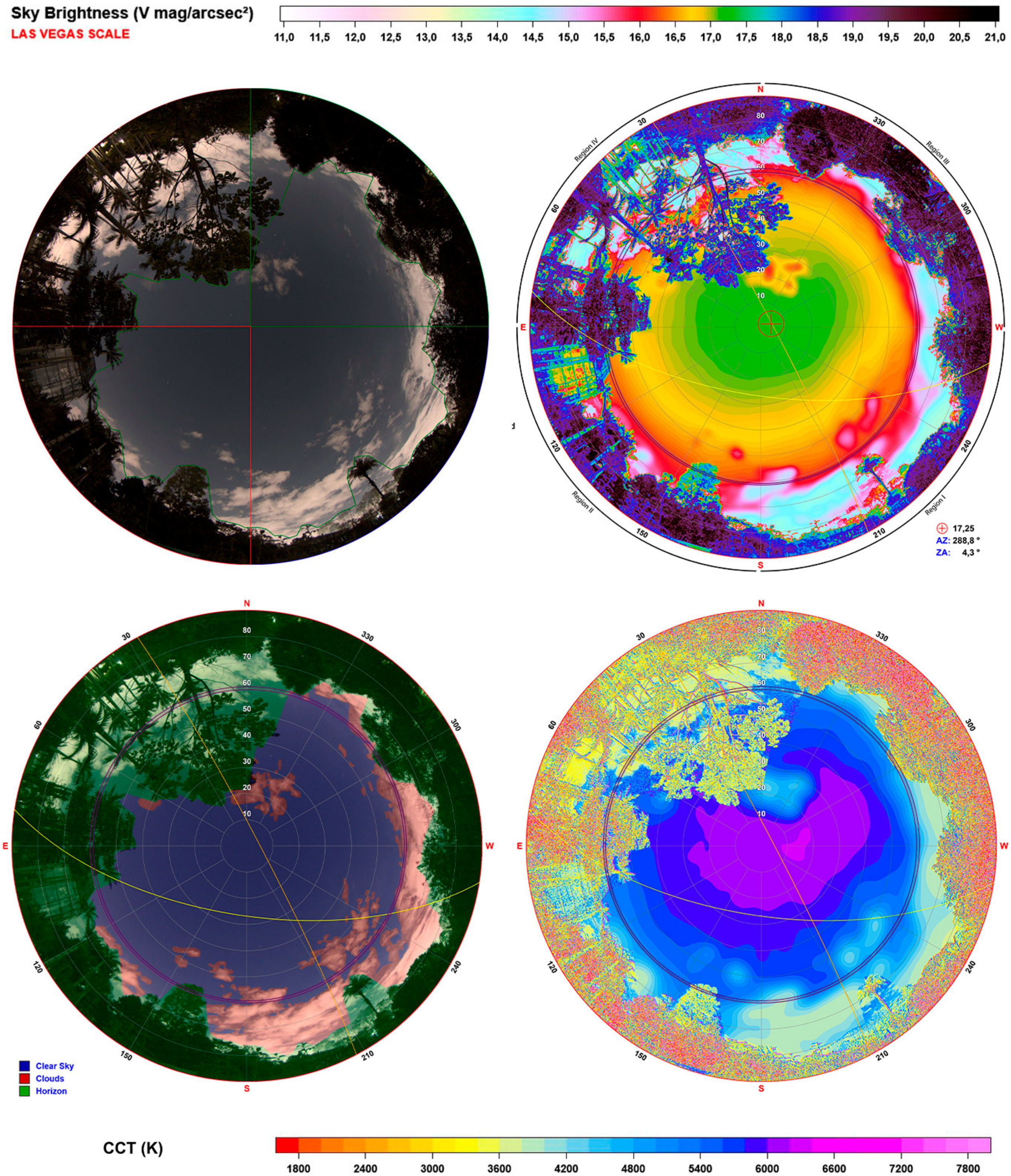

Fig. 8. Same as Figure 2, but for BBG on September 20, 2022. For more details, see § 3.3 and Table 3. It is important to note the distinct color scales used in the NSB and CCT maps, designed to accommodate the altered range of brightness and CCT levels characteristic of this heavily light-polluted urban sky. The color figure can be viewed online.

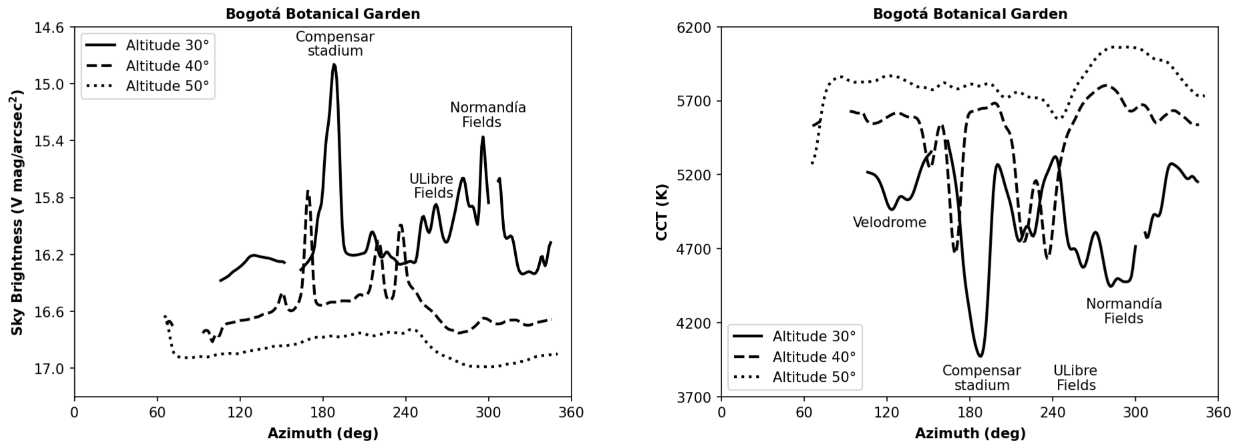

Fig. 9. Same as Figure 3, but for BBG. In this case, the rings are centered at 30°, 40°, and 50° elevation. See Figure 8 and Table 3.

gion III shows an initial decrease from $ZA = 9°$ to $ZA = 34°$, followed by a rapid decline beginning at $ZA = 40°$. Region IV exhibits a decrease from $ZA = 12°$ to $ZA = 23°$, which is attributed to the reflection of light on the clouds. This decrease continues gradually until $ZA = 52°$.

3.4. *Cerro Guadalupe (CG)*

The Cerro de Guadalupe is part of the Cerros Orientales, a group of mountains located to the east of Bogotá and the Cruz Verde pramo in the eastern mountain range. These hills are designated as a national forest reserve and their strategic location makes them a crucial ecological connector for the city, facilitating the interaction of diverse mountain ecosystems (Garzón Díaz 2014). The Cerros Orientales also play a vital role in regulating the climate and providing water for Bogotá (Bohórquez-Alfonso 2008). Additionally, they boast rich and varied biodiversity, harboring numerous species of endemic flora and fauna that contribute to the conservation of the region's natural heritage (Jiménez-Alvarado et al. 2017).

With an elevation of 3,273 meters above sea level, the Cerro de Guadalupe is the highest viewpoint accessible in Bogotá, offering a spectacular panoramic view of the Colombian capital. Since pre-Hispanic times, this site has held great significance, as rulers used it for surveillance and control over the city. Today, the hill is a subject of research in various fields such as history (Mejía 2006), environment (Rodríguez Ramos 2015), architecture (Meza 2008) and archaeoastronomy (Bonilla Romero 2011, Bonilla Romero et al. 2017). It is also a prominent site of religious pilgrimage, housing the statue of the Virgin of Guadalupe, a place of worship for many faithful. The hill features hiking trails that attract tourists and mountaineering enthusiasts, who appreciate its natural beauty and unparalleled views (Rueda Esteban 2017).

Figure 11 presents all-sky view from the parking lot of the Sanctuary of the Virgin of Guadalupe on Cerro de Guadalupe. The RGB format in the top left panel showcases numerous trees and, to the southeast, the sanctuary's advertisement sign along with clouds in the same direction. Similar to the BBG, there is a noticeable scale change in NSB map and CCT map. Although this location is not within the city limits, its elevation above the city results in contributions from the urban environment. The NSB map (top right) indicates an increase in surface brightness between $AZ = 240°$ and $AZ = 15°$, attributed to the city of Bogotá. Additionally, there is a brightness increase from $AZ = 90°$ to $AZ = 135°$, corresponding to light scattered by clouds above the advertisement sign. This is corroborated by the cloud map and the CCT map (bottom right), which show a decrease in CCT in these regions.

This decrease is more precisely detailed in the azimuthal profile. Figure 12 displays rings centered at altitudes of 20°, 30°, and 50°, accounting for the presence of trees along the horizon. The 50° altitude ring is the only one that provides full azimuthal coverage, as vegetation is unevenly distributed. In contrast, the 20° and 30° altitude rings capture variations in NSB and CCT only in specific directions, limiting the ability to detect changes in these parameters across all azimuths. The most significant NSB peak is at $AZ = 232°$, corresponding to the city of Bogotá. Additionally, there are notable increases in surface brightness at $AZ = 132°$ and $AZ = 117°$. For CCT, two peaks indicate a decrease, correspond-

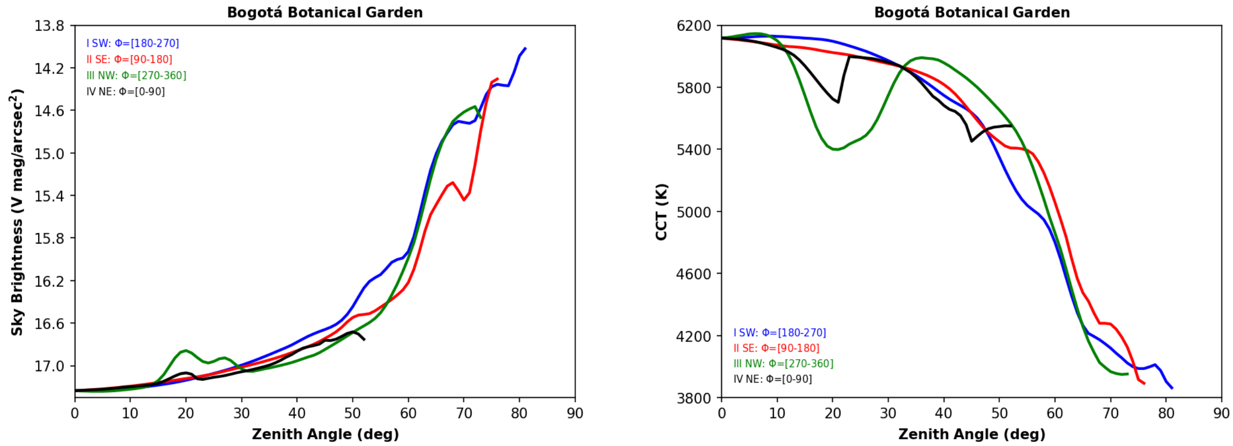

Fig. 10. Same as Figure 4, but for BBG. For more details, see § 3.3, Figure 8, and Table 3. The color figure can be viewed online.

ing to the city's glow on the cloud, with another decrease peak at $AZ = 62°$, corresponding to the direction of the church on the hill.

The zenith profile is illustrated in Figure 13. Region I shows a sharp increase in NSB at $ZA = 72°$, which decreases at $ZA = 80°$ due to light dispersion by the cloud and further decreases from $ZA = 87°$ due to the city's glow. The CCT decreases from $ZA = 58°$. Region II exhibits an increase in NSB and a decrease in CCT from the zenith to $ZA = 60°$, limited by tree coverage. Region III presents the most significant increase in NSB and decrease in CCT starting at $ZA = 57°$, corresponding to a cloud in the sector. Region IV shows a gradual increase from the zenith to $ZA = 64°$, reaching maximum brightness, then decreasing and increasing again due to clouds among the trees, with the strongest CCT decrease at $ZA = 65°$.

4. DISCUSSION

In this section, we compare our findings with those from similar sites worldwide and with available numerical models. We also explore the implications of these results for conserving and protecting the country's dark sky. The discussion includes possible measures to mitigate light pollution and preserve this unique natural resource.

4.1. *Photometric Indicators for Cross-Site Comparisons*

For comparative studies between different locations, a large number of photometric indicators of the visual quality of the night sky have been suggested in the literature (Deverchère et al. 2022; Duriscoe 2016). These indicators enable us to evaluate the impact of light pollution from various perspectives, such as astronomical (Falchi et al. 2023) and biological (Falchi et al. 2021). In Table 4, we present the alt-az coordinates and the corresponding NSB/CCT values for the darkest and brightest points of the sky, as well as for the zenith (averaged over a 5° radius circle), within a 1° wide ring centered at 30° elevation, and over the entire celestial hemisphere (i.e., all-sky) for each site.

To better understand the types of light affecting the sky at each site, Figure 14 presents a comparative histogram illustrating the percentage distribution of the sky based on CCT. The histogram for TD, shown in blue, reflects a distribution with temperatures typical of a natural sky, but it also reveals a significant percentage of LED light, with a peak around 4100 K, indicating the presence of neutral-tone LEDs.

In contrast, the histogram for AOUTP, represented in red, shows a bimodal distribution with peaks at 4500 K and 5000 K, suggesting a sky influenced by urban light sources. The 4500 K peak is associated with neutral light LEDs, commonly used in commercial areas, while the 5000 K peak corresponds to cool light LEDs, typical of large installations such as sports arenas, parking lots, or industrial facilities. Lastly, the histograms for BBG and CG reveal significant concentrations in the higher CCT ranges, between 5000 K and 6500 K. The peak near 6100 K suggests the presence of cool or high-intensity LEDs, characteristic of densely illuminated urban areas like Bogotá.

4.2. *Comparison with Other Sites*

The NSB and CCT maps of the Colombian skies presented in this study, derived from data collected by the SQC, constitute the first recorded measure-

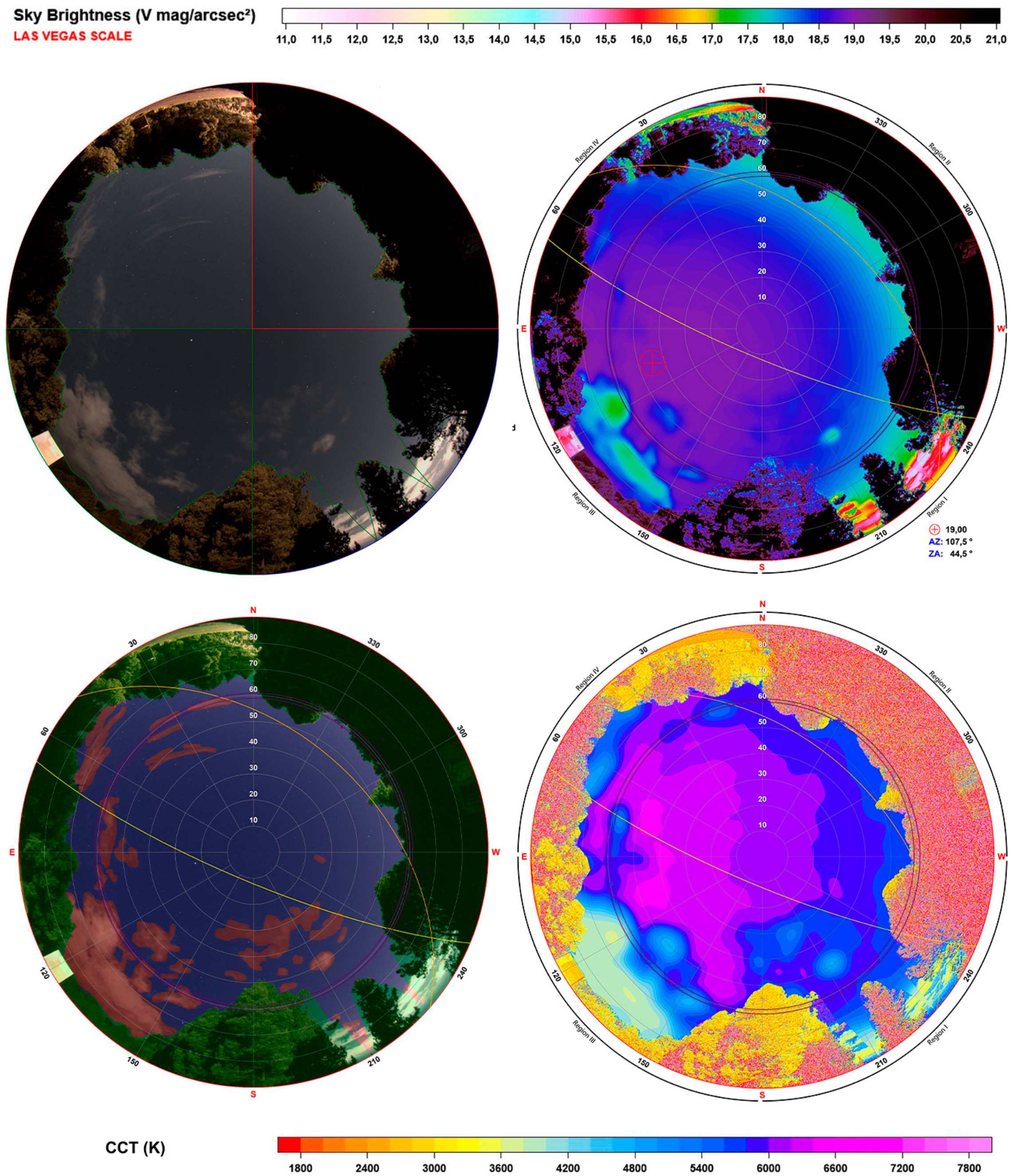

Fig. 11. Same as Figure 8, but for CG on September 20, 2022. For more details, see § 3.4 and Table 3. The color figure can be viewed online.

ments of light pollution near the equator as documented in the Light Pollution Map database. This platform compiles all files generated by the SQC instrument, allowing users to upload and share their observations, thereby ensuring public access to the data. Despite significant efforts to facilitate access to SQC data, measurements are still lacking for many cities.

For this reason, when comparing our data with those from the database, specific selection criteria were applied for each location. The AOUTP was compared with the Astronomsko-geofizikalni Obser-

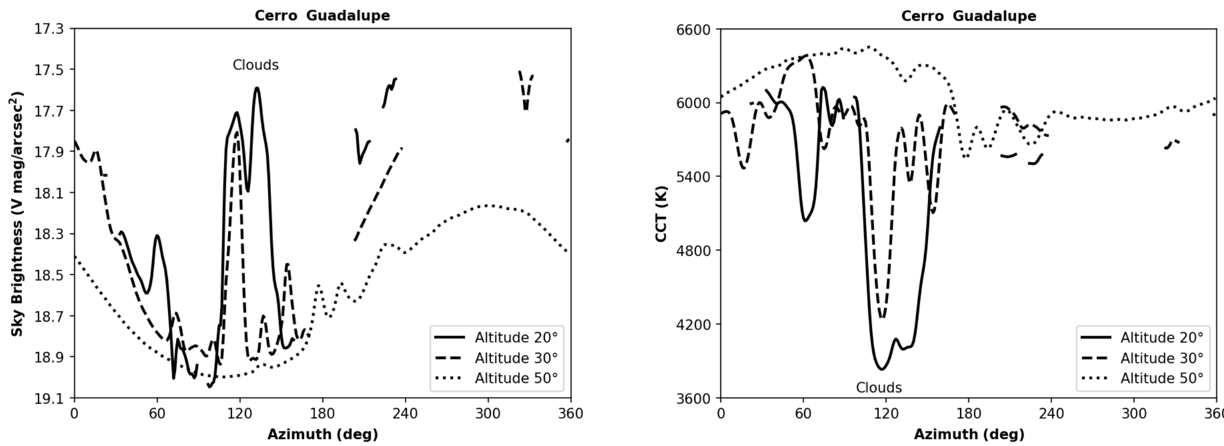

Fig. 12. Same as Figure 3, but for CG. In this case, the rings are centered at 20°, 30°, and 50° elevation. See Figure 11 and Table 3.

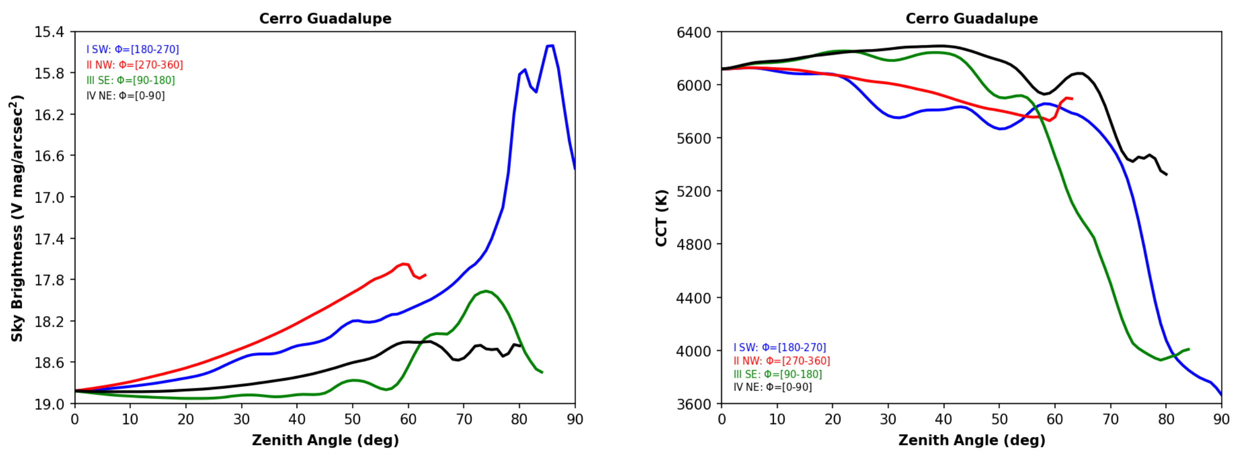

Fig. 13. Same as Figure 4, but for CG. For more details, see § 3.4, Figure 11, and Table 3. The color figure can be viewed online.

TABLE 4

PHOTOMETRIC INDICATORS[a]

Site	Brightest Point[α]				Darkest Point[α]				Zenith[β]		30°[γ]		All-Sky	
Acronym	**AZ**	**ZA**	**NSB**	**CCT**	**AZ**	**ZA**	**NSB**	**CCT**	**NSB**	**CCT**	**NSB**	**CCT**	**NSB**	**CCT**
AOUTP	290	78	15.45	3434	160	8	18.12	4884	18.09	4860	17.11	4481	16.90	4407
TD	206	90	17.41	4321	66	23	21.36	4041	21.29	4061	20.77	3995	20.59	4012
BBG	194	71	14.21	3730	289	4	17.25	6181	17.23	6100	16.01	4908	16.09	4561
CG	210	86	15.53	3503	107	44	19.00	6584	18.87	6131	18.39	5591	18.43	5502

[a]Altazimuth coordinates for the NSB (V mag/arcsec^2) and CCT (K) values of the darkest and brightest points in the sky at the time of our observations. Additionally, values for the zenith, a ring of 30° of elevation, and the entire celestial vault are included.

[α]Average value within 1 deg^2.

[β]Average value for zenith angle $ZA = 5°$.

[γ] Average value at 30° elevation with a width of 1° (i.e., for $59.5° < ZA < 60.5°$).

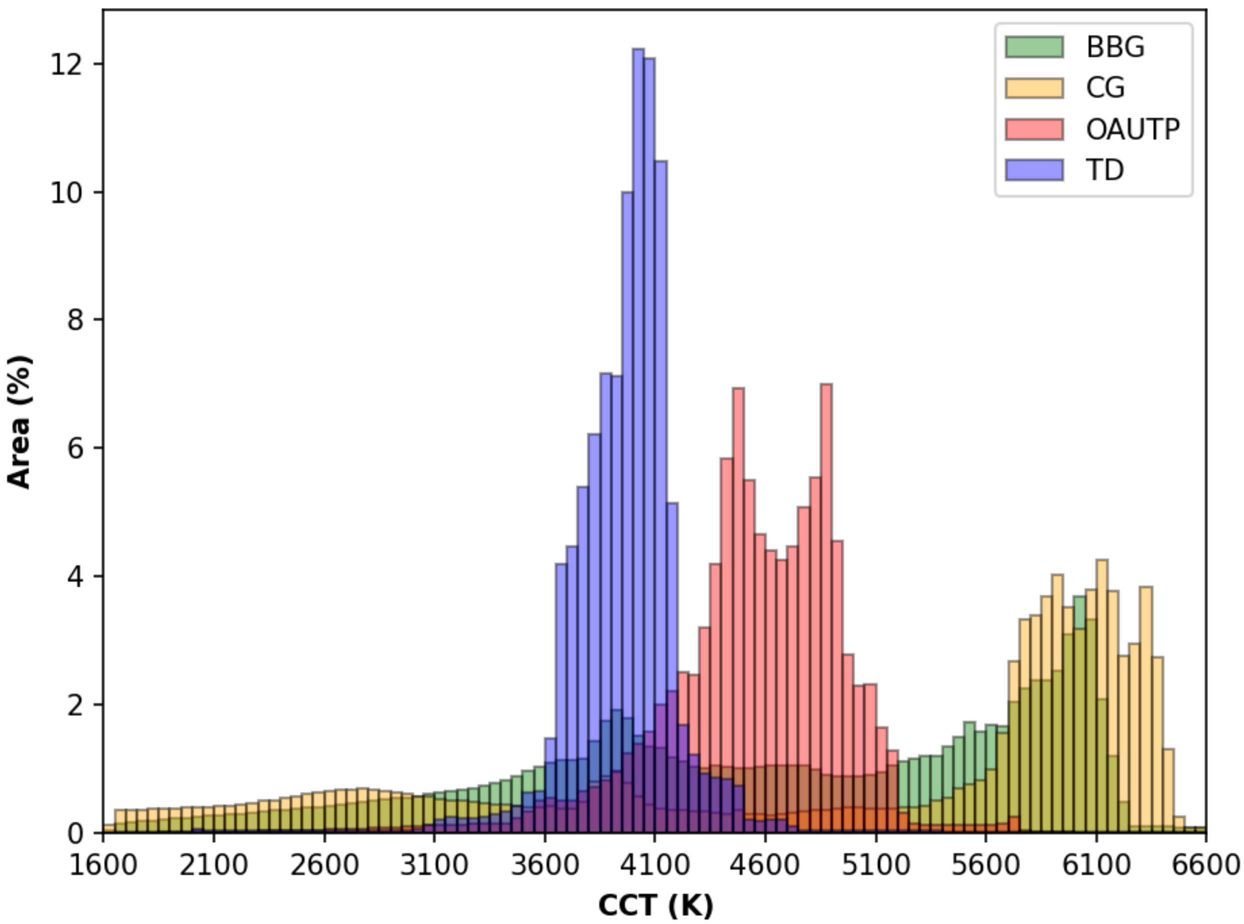

Fig. 14. The histogram represents the distribution of CCT values for four measurement sites: BBG (green), CG (yellow), AOUTP (red), and TD (blue). Each color corresponds to a different site, showing the proportion of area (%) covered by different CCT values across the range of 1600 to 6600 K. The bin width is set to 100 K. The color figure can be viewed online.

vatorij Golovec (AOG) in Slovenia, as both are observatories located less than 10 km from the center of their respective cities. For TD, the Eifel National Park[23] (ENP) was chosen, as both sites are designated for dark sky preservation. In the case of BBG and CG, a comparison was made with Mont Royal Park[24] (MRP) and the Montreal Olympic Stadium (MOS), both located in Montreal, Canada. This comparison was based on the search for a city that had two measurement points no more than 12 km apart, where one of the sites was a park or an environmentally protected area.

First, the AOUTP was compared with the AOG in Slovenia. The AOG is located in Ljubljana, a city of approximately 285,604 inhabitants (2021 data[25]), while the AOUTP is situated in Pereira, which has around 477,068 inhabitants (2018 data[26]). They exhibit significant differences in terrain and climate, which may influence light pollution measurements. Ljubljana lies in a basin surrounded by mountains, potentially trapping light pollution, whereas Pereira is located in the Andean region, with distinct atmospheric conditions. These differences highlight the importance of contextual factors when interpreting light pollution data.

Figure 15 compares the NSB maps of AOUTP and AOG. From the maps, the darkest point values are highlighted, which are 18.12 mag/arcsec^2 and 19.58 mag/arcsec^2, respectively. The photometric indicator for the 30° elevation ring shows values of 17.11 mag/arcsec^2 and 18.89 mag/arcsec^2, respec-

[23]https://www.eifel.info/
[24]https://montreal.ca/en/places/parc-du-mont-royal
[25]https://www.stat.si/
[26]https://www.dane.gov.co/

tively. This indicates that the night sky over AOG is 1.78 mag/arcsec^2 darker compared to Pereira. This difference can be attributed to several factors, including the higher population density of Pereira and the presence of an airport within its urban area, both of which contribute to increased NSB. Moreover, the frequent partial cloud cover over Pereira further elevates the recorded NSB by scattering and amplifying artificial light sources.

In the case of TD, we compared our data with ENP, located in western Germany within the state of North Rhine-Westphalia, near the Belgian border in the Eifel mountain region. The park is situated close to the towns of Schleiden and Monschau, as well as the cities of Aachen and Cologne. Covering approximately 110 km^2, ENP is home to thousands of endangered animal and plant species. In 2014, it was designated as a protected area by the International Dark Sky Association[27], becoming one of the few regions in Germany where the Milky Way is visible to the naked eye (Gabriel et al. 2017).

Figure 16 shows the NSB maps of TD and ENP. From the maps, the values of the darkest points stand out, which are 21.36 mag/arcsec^2 and 21.22 mag/arcsec^2, respectively. The photometric indicator for the 30° elevation ring shows values of 20.77 mag/arcsec^2 for TD and 20.38 mag/arcsec^2 for ENP, indicating that the night sky over TD is 0.39 mag/arcsec^2 darker than that over ENP. This difference is primarily due to the proximity of large cities near ENP, such as Cologne (Germany, 50 km away) and Liége (Belgium, 60 km away), compared to Neiva, which is 37 km away from TD. Furthermore, the populations of Cologne and Liége are 2.7 and 1.7 times larger than that of Neiva, respectively, contributing to the higher NSB observed in ENP. Despite these differences, it is important to note that both sites have implemented measures to protect their night skies, supported by their respective certifications. However, special attention should be given to the NSB levels at TD, as ENP is located in one of the most densely populated regions in Europe, making it particularly vulnerable to the effects of surrounding light pollution.

As outlined earlier, we selected two locations in each city, situated no more than 12 km apart, for analysis. The first point of interest focuses on conservation parks that blend natural and urban environments: BBG in Bogot and MRP in Montreal. These spaces are distinguished by their commitment to environmental preservation within an urban setting.

[27]https://www.darksky.org/

The second comparison point includes CG in Bogot and MOS in Montreal. Both locations are within 12 km of their respective parks and serve as prominent city viewpoints. In Bogot, CG is a religious sanctuary that, beyond its spiritual significance, provides a breathtaking panoramic view of the city. Meanwhile, MOS features the iconic inclined tower of the Montreal Olympic Stadium, the tallest of its kind in the world. Known as the Montreal Tower, it offers a stunning 360-degree vantage point, allowing visitors to admire the city and its surroundings from an unparalleled perspective.

These cities exhibit notable differences in their geography and demographics. Bogot, situated high in the Andes Mountains at 2,565 meters above sea level, is defined by its rugged, mountainous terrain. In contrast, Montreal is located on an island in the St. Lawrence River, featuring a relatively flat and gently rolling landscape. Demographically, Bogot is significantly larger, with approximately 8.034.649 inhabitants as of 2018 according to DANE, compared to Montreal's 1,762,949[28] residents in 2021. However, Montreal is notable for having multiple SQC measurements recorded in the Light Pollution Database.

Figure 17 compares the NSB maps of MRP and BBG, highlighting the darkest points, which are 17.78 mag/arcsec^2 and 17.25 mag/arcsec^2, respectively. The photometric indicator (30° elevation ring) shows values of 17.08 mag/arcsec^2 and 16.01 mag/arcsec^2, respectively. According to the photometric indicator, MRP has a sky approximately 1.07 mag/arcsec^2 darker than BBG. This disparity is likely influenced by several factors, including Bogotá's size, which is 4.4 times that of Montreal.

Figure 18 compares the NSB maps of MOS and CG, highlighting the values of the darkest points, which are 17.75 mag/arcsec^2 and 19.00 mag/arcsec^2, respectively. The photometric indicator (30° elevation ring) shows values of 17.27 mag/arcsec^2 and 18.39 mag/arcsec^2, respectively. According to this indicator, CG presents a sky approximately 1.12 mag/arcsec^2 darker than MOS. This difference could be attributed to the location of CG on the outskirts of Bogotá, in contrast to MOS, which is situated within the city's interior. Both locations provide panoramic views of the city: CG, situated at an elevation of approximately 3,273 meters above sea level, and MOS, at 167 meters. From MOS, one can observe the city's most iconic buildings and urban landscape, while CG serves as a natural look-

[28]https://www.statcan.gc.ca/

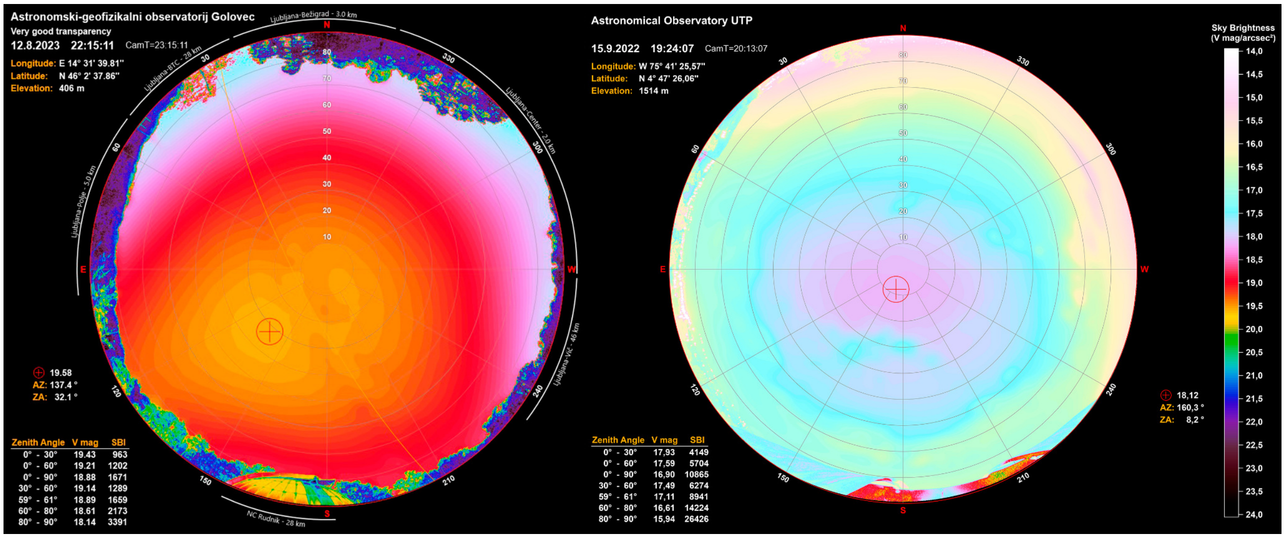

Fig. 15. Comparison of all-sky NSB images from the AOG (left) obtained from the Light Pollution database and from the AOUTP (right). The date, time, and geographic coordinates are displayed at the top left of each map, while NSB values in [V mag/arcsec^2] are represented in the color bar on the right. The dark point, along with its coordinates, is marked above the table containing the NSB data at the bottom left. The color figure can be viewed online.

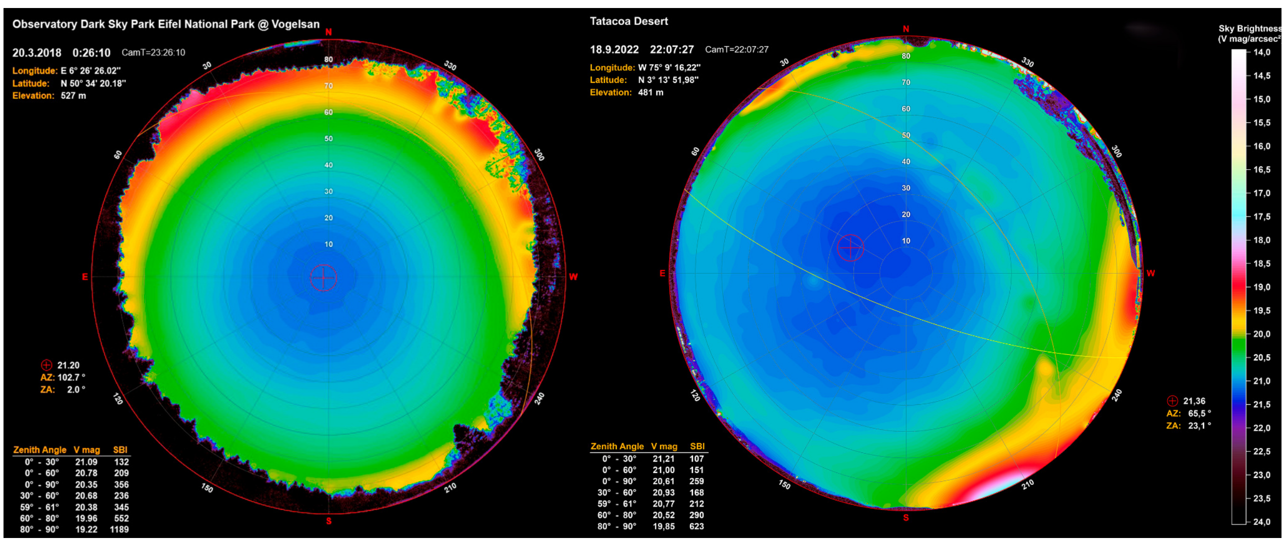

Fig. 16. Comparison of ENP and TD data, with analogous information to Figure 15. The color figure can be viewed online.

out that also offers opportunities to observe local wildlife.

4.3. *GAMBONS Model*

The night sky is not completely dark due to contributions from several natural sources, including integrated starlight, diffuse galactic light, extragalactic light, and zodiacal light. Additionally, phenomena such as airglow result from the interaction of particles in the upper atmosphere. These natural effects create a background glow that is always present in the night sky.

The GAMBONS model, as detailed in Masana et al. (2021, 2022), accounts for various factors to simulate natural NSB under conditions devoid of clouds, the Moon, and planets. A key innovation of GAMBONS is its seamless integration of the Gaia-DR3 and Hipparcos catalogs, combined with detailed modeling of diffuse galactic and extragalactic light, zodiacal light, airglow, and atmospheric attenuation

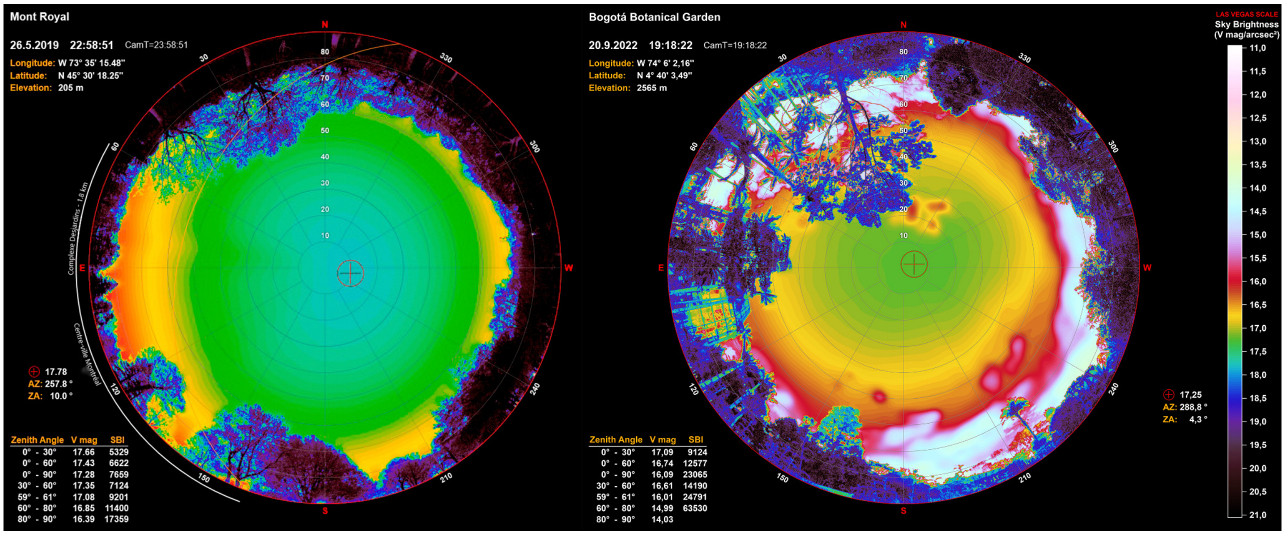

Fig. 17. Comparison of MRP and BBG data, with analogous information to Figure 15. The color figure can be viewed online.

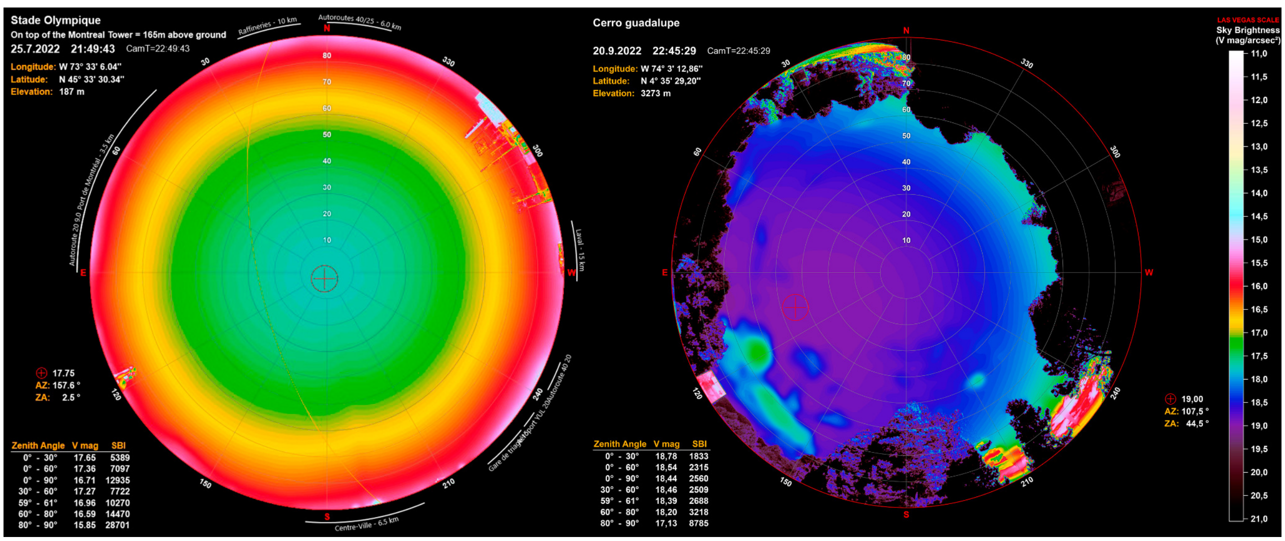

Fig. 18. Comparison of MOS and CG data, with analogous information to Figure 15. The color figure can be viewed online.

and scattering effects. The model operates with default airglow and aerosol parameters, providing a reliable initial approximation of the typical conditions at our monitoring sites.

Using these parameters, GAMBONS generates an all-sky NSB map for a specified time and location. The presence or absence of the Milky Way and the elevation of the ecliptic above the horizon are the primary factors influencing this model. Additionally, the model can estimate synthetic NSB values in different photometric pass bands, such as the SQM, TESS, or specific photometric bands. This feature is precious for theoretically assessing natural light contributions and comparing them with observed data, thereby facilitating the estimation of the percentage of ALAN at each site.

Table 5 compares values measured with the SQC at the zenith and all-sky, alongside the values obtained from the GAMBONS model (GMB). The final column indicates the estimated percentage of ALAN at each location. This estimation is derived from the model's values, with conversions following the methodology outlined in Kolláth et al. (2020). It is important to note that the GMB model tends to overestimate natural NSB near the horizon and un-

TABLE 5

COMPARISON OF NSB SQC VS GMB[a]

Site	Zenith			All-sky		
Acronym	**GMB**	**SQC**	Δm	**GMB**	**SQC**	**ALAN%**
AOUTP	21.46	18.09	3.37	21.45	16.90	98
TD	21.57	21.29	0.28	21.56	20.59	59
BBG	21.26	17.23	4.03	21.43	16.08	99
CG	21.60	18.87	2.73	21.53	18.43	94

[a]Comparison between the GAMBONS model (GMB) and the observed NSB (SQC) at zenith (V mag/arcsec^2) and all-sky. For more details, see § 4.3.

derestimate it at the zenith by up to 0.1 mag/arcsec^2 (Masana et al. 2022).

TD and BBG are the only sites for which prior ALAN data were available in the literature, all recorded using the SQM photometer (21.26 mag/arcsec^2 for TD and 16.31 mag/arcsec^2 for BBG). These historical data are utilized here for a direct comparison with our SQC measurements, providing a potential means to estimate the evolution of ALAN over the past years (Urrego Guevara 2016 (hereafter UG, 2016); Góez Therán & Vargas Domínguez 2021 (hereafter GT&VD, 2021)).

Table 6 compares the values reported in the literature (SQM LIT) with those obtained using the GMB models (SQM GMB) for the same location, date, and time. While direct measurements taken with a SQM were not available in this study, the SQC methodology enables the calculation of a synthetic SQM value based on SQC data. This synthetic value is included in the SQM LIT column. Conversely, the SQM GMB column reports the results of the GMB model simulations for the dates and times analyzed in this study.

Although a direct comparison is challenging due to variations in dates, times, measurement locations, instruments used, and meteorological conditions, the obtained values provide valuable insights into the evolution of NSB at both locations. To account for intrinsic and previously unknown variations in natural conditions, the original SQM measurements reported in the literature and our synthetic values derived from SQC were compared with the theoretical predictions generated by the GMB SQM model.

For this purpose, a column labeled Δm is included, representing the difference in NSB between the SQM GMB and SQM LIT values. Similarly, the corresponding row includes ΔM, which indicates the time difference between the SQM GMB and SQM LIT values. These metrics not only facilitate the evaluation of discrepancies and similarities between the simulated data and the literature-reported data but also enable an analysis of the temporal evolution of NSB.

Figures 19 and 20, generated using VIIRS Day/Night Band (DNB) data sourced from the Light Pollution Map platform, illustrate the temporal evolution of NSB for the years 2014 and 2022, respectively. Figure 19 covers an area of 1600 km^2 and shows a radiance of $2840.6 \cdot 10^{-9}$ W/cm$^2\cdot$ sr in 2014, decreasing to $1595.3 \cdot 10^{-9}$ W/cm$^2\cdot$ sr in 2022. This suggests a reduction in the way the desert is being illuminated, which can be visually observed as a decrease in radiance in the lower-left part of the image. However, this area corresponds to the Dina Field, one of the oil and gas production fields operated by Ecopetrol, the main oil and gas company in Colombia. This observed reduction may be attributed to the adoption of LED technology, the predominant lighting source during the measurement period. However, Table 6 reveals an increase in NSB, whereas VIIRS data suggest an apparent decrease. This discrepancy is primarily due to the limited sensitivity of the VIIRS DNB channel, which excludes wavelengths predominantly emitted by LEDs. Consequently, NSB tends to be underestimated in regions dominated by LED lighting. For a comprehensive discussion on the characteristics and limitations of VIIRS, refer to Cao & Bai (2014).

On the other hand, Figure 20 covers an area of 4 km^2 and shows an increase in radiance, from $796.0 \cdot 10^{-9}$ W/cm$^2\cdot$ sr in 2014 to $905.3 \cdot 10^{-9}$ W/cm$^2\cdot$ sr in 2022. The increase in NSB is attributed not only to the 558 lamps[29] within the BBG, but also to the contributions from all the surrounding neighborhoods.

Figures 21, 22, 23, and 24 display the all-sky images generated by the GAMBONS model, alongside the images obtained by the SQC for each site. For each GAMBONS image, spatial and temporal data were replicated, while for the SQC image the NSB value was recalculated, including the contributions of the resolved stars without applying smoothing. A detailed description of each site is provided below.

In the AOUTP case, as illustrated in Figure 21, 98% of ALAN in Pereira originates from artificial contributions to NSB. This dominance is evident in Table 5, Column 7, where the impact of artificial lighting on sky glow is clearly observed. ALAN results from a combination of natural NSB contribu-

[29]`https://datosabiertos.bogota.gov.co/dataset/luminarias_upz-bogota-d-c`

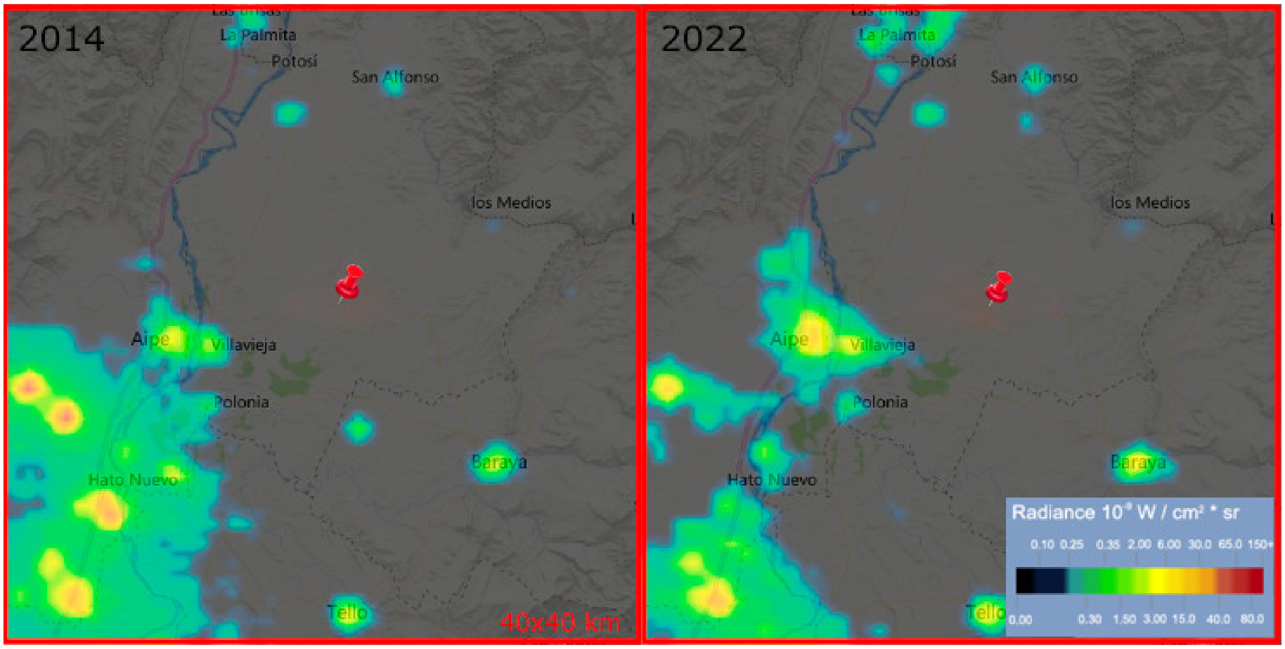

Fig. 19. Comparison of NSB using VIIRS/DNB radiance data in a 40x40 km area centered on the 2022 measurement point at TD (red pin) for the years 2014 (left) and 2022 (right). The color figure can be viewed online.

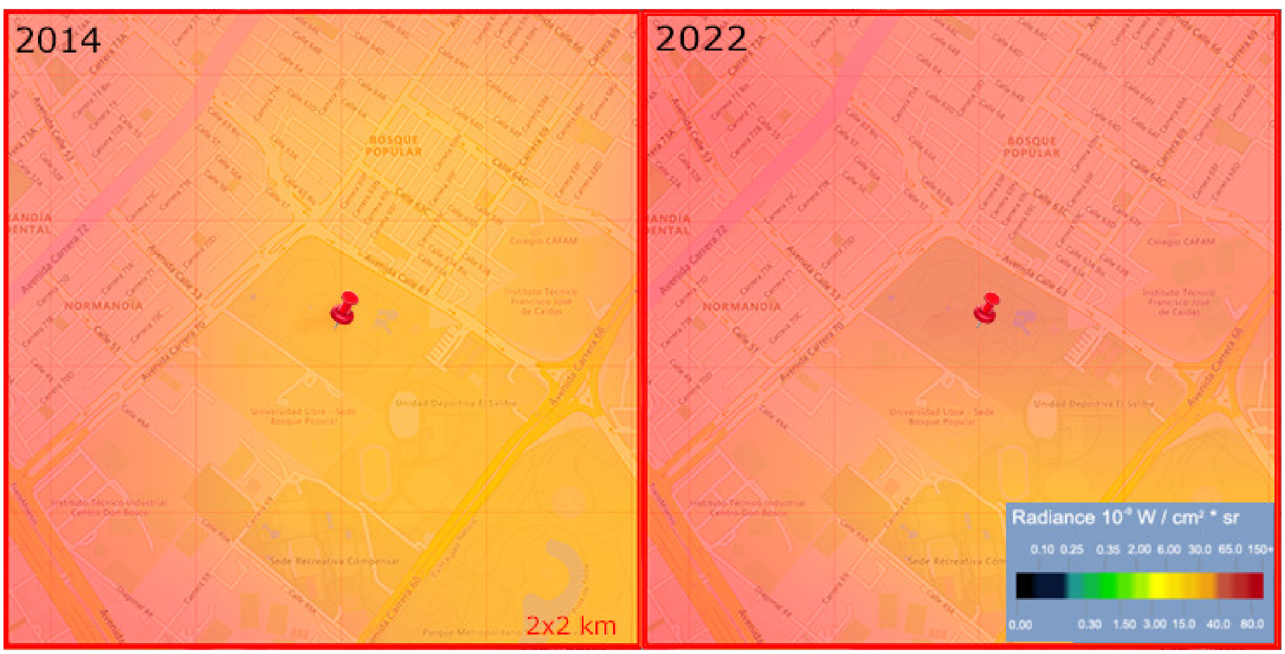

Fig. 20. Same as Figure 19, **but** focused on BBG and centered within a 2×2 km area. The color figure can be viewed online.

tions, estimated using the GAMBONS model, and artificial NSB contributions, derived from our data. The overwhelming presence of artificial light highlights the profound transformation of the night sky in urban environments like Pereira. In Figure 22, it is evident that, with the naked eye, one can still appreciate the stars and our galaxy, the Milky Way in TD. However, the NSB from the cities almost completely dominates the horizon. Table 5 indicates that approximately 59% of the sky is dominated by ALAN,

TABLE 6

COMPARISON OF SQM VALUES

Date aaaa-mm-dd	**SQM GMB**	**SQM LIT**	Δm
TD			
2014-04-15	21.87	21.26 (GT&VD, 2021)	0.61
2022-09-18	21.81	21.09 (This work)	0.72
ΔM	0.06	0.17	-
BBG			
2014-09-20	21.60	16.31 (UG, 2016)	5.29
2022-09-20	21.55	16.96 (This work)	4.59
ΔM	0.05	-0.65	-

[a]Comparison between the SQM values obtained from previous works (SQM LIT) and SQM GAMBON model (SQM GMB). For more details, see § 4.3.

which is highly concerning for a Starlight destination whose mission is to conserve and protect the night sky.

Raising awareness among people is crucial, as most inhabitants make their living from tourism, with astrotourism being the main attraction for visitors to the desert (Montealegre Vega & Garavito González 2022). Efforts should prioritize Ecopetrol, a private company, and the city of Neiva, as these are the primary sources of light pollution in the desert. This is especially important during lighting transitions, such as the shift to LED technology. While LEDs provide significant economic benefits and enhance conditions for nighttime activities, it is essential to ensure these lights are properly directed toward the ground and avoid over-illumination of space. Protecting the night sky is not only vital for environmental conservation but can also boost the local economy by attracting more tourists interested in astrotourism, thereby fostering sustainable development in the region.

Figure 23 shows that the sky at the BBG is dominated by ALAN. This result was predictable, given that BBG is located within one of the largest metropolises in Latin America. However, this does not imply that the night sky should not be protected. In this particular case, studies are recommended to evaluate how ALAN is affecting the plants in the various ecosystems present in the garden (Cadena-Vargas et al. 2020). Additionally, measures should be taken to protect those collections and plants that are highly sensitive to light changes.

Moreover, the sky over CG (see Figure 24), like that of the BBG, is dominated by ALAN due to its proximity to the city of Bogotá. However, a 5% decrease in ALAN is observed compared to BBG. This is because CG is 700 meters higher in elevation and almost 10 km away from the urban center. This difference in altitude and distance allows for better night sky quality in CG, reducing light interference. Additionally, the area's vegetation and natural relief help to mitigate light pollution. For these reasons, CG could be considered a strategic point for astronomical observation and ecological studies. In summary, the analysis of NSB using the GAMBONS model highlights the significant impact of ALAN on astronomical observations and ecological systems. Locations like the TD and BBG demonstrate varying levels of light pollution, emphasizing the need for targeted measures.

5. CONCLUSIONS

We have presented the first quantitative study of sky quality from different sites in Colombia, one of the most biodiverse countries globally. Our data update the existing values for the zenith in the BBG and TD and provide the first records for Pereira and Cerro Guadalupe. Additionally, the measurements were made with an all-sky instrument, allowing us to obtain information from the entire celestial vault to monitor and quantify the effects of light pollution.

We identified the cities that contribute most to light pollution at each site, along with the azimuths and distances from the observing site. The most polluted site was the BBG, located within Bogotá, one of the most populated cities in Latin America. AOUTP is the second most polluted site, located within the city of Pereira, the sixteenth most populated city in Colombia. CG is the third most contaminated site; although it is 700 meters above the city and partially protected by the trees on the hill, it still suffers from significant light pollution. The TD is the least polluted, with an ALAN contribution of 59%. Measures must be taken to reduce light pollution in these critical areas. The implementation of more efficient and less intrusive lighting technologies can help mitigate this problem.

The Starlight or Dark Sky certification not only ensures that a location offers exceptional conditions for astronomical observation but also serves as a vital tool for protecting and conserving the night sky amidst the growing threat of light pollution. Preserving and renewing these certifications is crucial for safeguarding both the natural environment and

DOI: https://doi.org/10.22201/ia.01851101p.2025.61.01.10

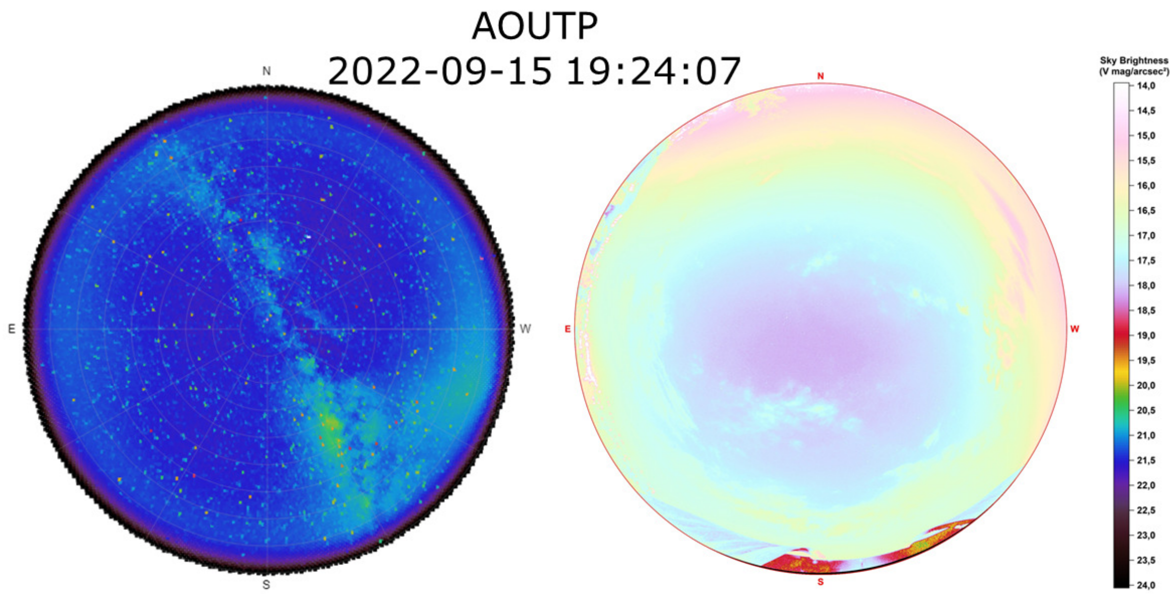

Fig. 21. Comparison of the NSB all-sky images generated by the GAMBONS model (left) and the SQC (right) from AOUTP. For more details, see § 4.3 and Table 5. The color figure can be viewed online.

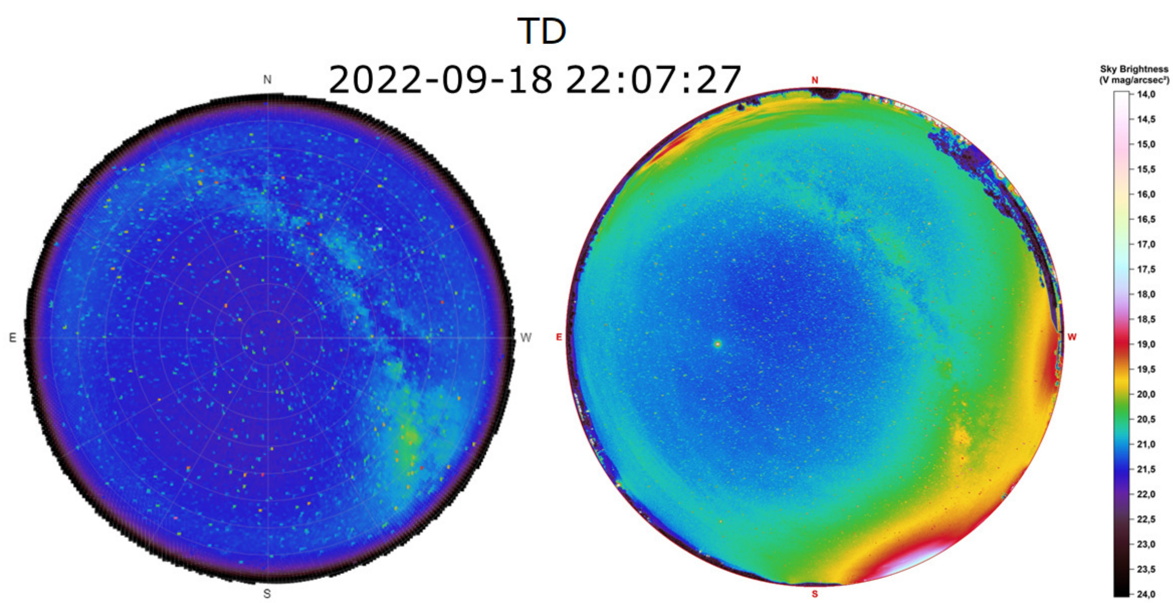

Fig. 22. As in Figure 21, but for TD. For more details, see § 4.3 and Table 5. The color figure can be viewed online.

the biodiversity that depends on the cycles of light and darkness, as well as for supporting scientific research. Moreover, such certifications stimulate astrotourism, an increasingly important source of income in many regions, promoting sustainable tourism centered on education and the appreciation of nature. To protect the future of these destinations, local administrations need to implement effective measures to conserve dark skies, regularly renew certifications, and foster awareness among tour operators and communities about the significance of environmental protection and sustainability.

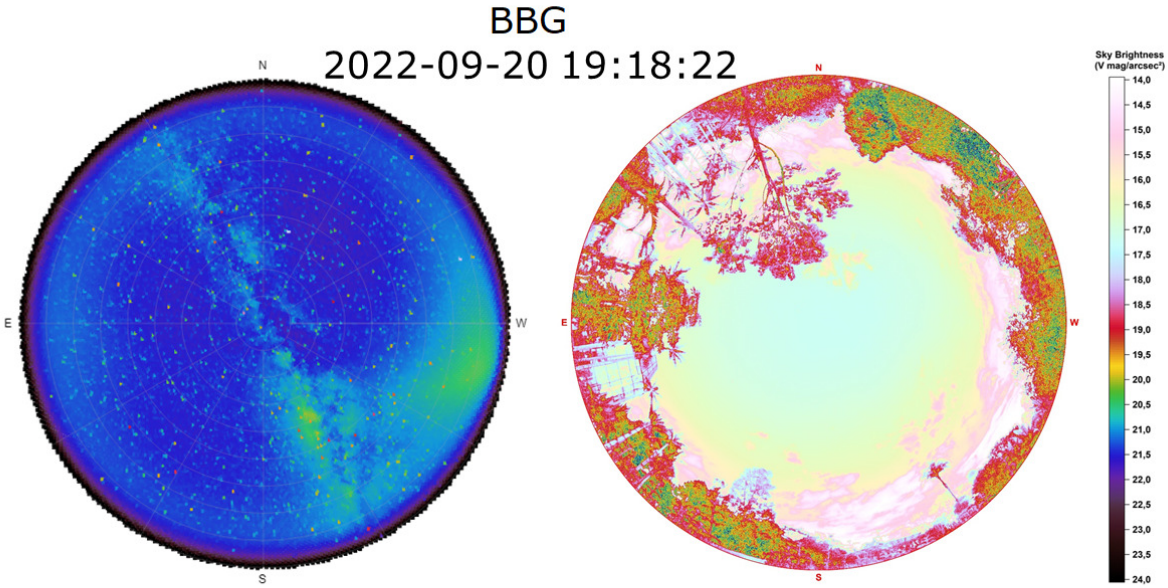

Fig. 23. As in Figure 21, but for BBG. For more details, see § 4.3 and Table 5. The color figure can be viewed online.

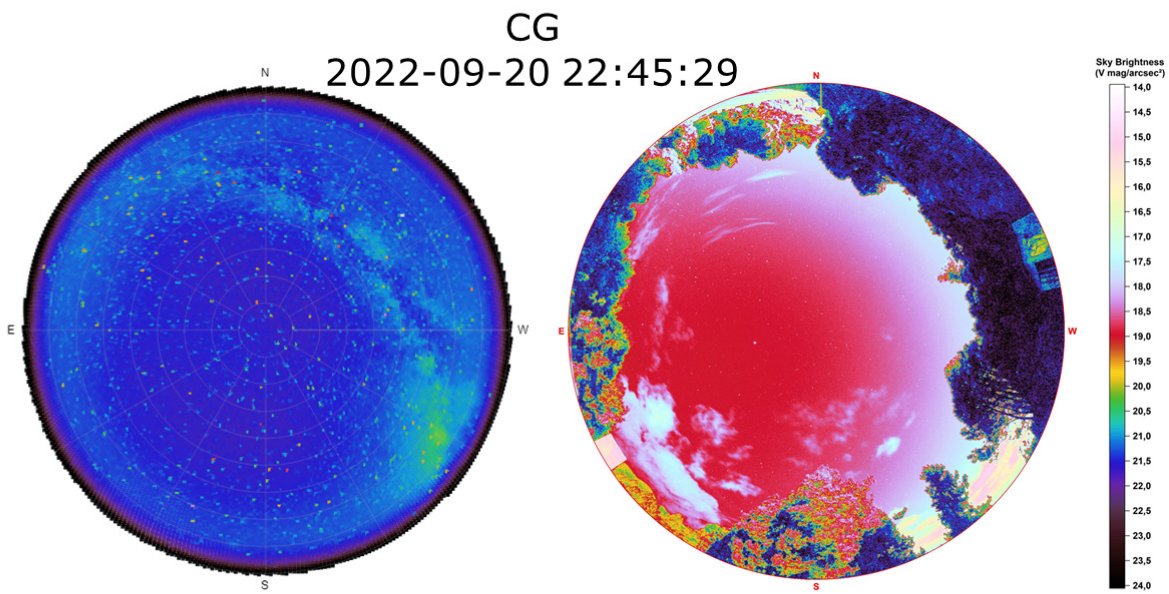

Fig. 24. As in Figure 21, but for CG. For more details, see § 4.3 and Table 5. The color figure can be viewed online.

In this context, the TD has emerged as Colombia's premier sky observation destination, even before receiving its Starlight certification. This has enabled many local residents to benefit from astrotourism as a valuable source of income. However, local administrations have yet to establish concrete strategies for the conservation and protection of this crucial asset. A study by Montealegre Vega & Garavito González (2022) underscores the challenges faced by the Villavieja administration regarding the desert. During our data collection, we were struck by the prevalence of lights directed toward the sky by local businesses and the lack of environmental awareness among tour operators. We hope that our findings can contribute to the development of strategies by both the municipality and government to preserve this unique Starlight destination in Colombia.

On the other hand, astrotourism has become a vital component of sustainable tourism by generating economic benefits for local communities while encouraging environmental conservation. However, this activity must be accompanied by education and awareness initiatives aimed at protecting the natural environment, especially the night sky. Regions like the Tatacoa Desert can capitalize on their dark skies to attract visitors interested in both astronomy and natural beauty. Preserving the night sky is essential to maintaining the desert's irreplaceable heritage. Educating and raising awareness among the local population about the importance of protecting this natural resource is imperative to ensuring that future generations can continue to marvel at the splendor of the starry night sky (Vierdayanti et al. 2024).

LED lights represent the new generation of lighting, and it is crucial to pay attention to this transformation in our society. This change in the spectral distribution of the sky will have impacts on fauna, flora, and humans. LED lights were found at all sites analyzed, but their presence is especially notable at TD. In Figure 5, a source of white-blue light can be observed in the RGB map towards the south, and when contrasted with the CCT map, it is evident how this light mixes with the natural brightness of the sky. This phenomenon indicates a degradation in sky quality, resulting in the inability to perceive objects in deep space, the Milky Way, and even stars.

Clouds play a crucial role in the propagation and impact of light pollution, as they reflect and scatter artificial light toward the ground, amplifying its effects and degrading the quality of the night sky, making it difficult to observe celestial objects (Kyba et al. 2011; Jechow et al. 2017). In Colombia, where skies are covered by clouds most of the year due to their geographical location, all-sky measurements are essential to estimate the state of the sky and visualize cloudy areas, thus understanding their interaction with ALAN. This understanding is vital for developing effective light pollution mitigation strategies and ensuring better sky quality for both ecological and astronomical purposes. Therefore, prolonged studies, conducted over months or years, are suggested to more accurately characterize the interaction between clouds and light pollution, implementing measures that protect the night sky and promote sustainable astronomical observation. By enhancing our knowledge in this area, we can better advocate for preserving the night sky for future generations.

Conducting studies on ALAN is crucial for understanding its impact on biodiversity. ALAN alters the natural behaviors of many species, including their reproductive, foraging, and migration patterns (Davies et al. 2014; Hölker et al. 2021; Mayer-Pinto et al. 2022). This disruption can lead to significant population declines and affect entire ecosystems. Additionally, light pollution influences plants, since artificial light can interfere with their growth and flowering cycles, which in turn impacts the species that depend on them (Singhal et al. 2019; Meravi & Kumar Prajapati 2018). By quantifying light pollution and identifying its sources, we can develop strategies to mitigate its effects, helping to preserve the rich biodiversity found in Colombia, and more specifically in the BBG. These studies are essential for creating policies that balance the needs of human development with the conservation of natural habitats.

Our data represent an initial step in understanding the ALAN phenomenon and will serve as a foundation for future studies on its evolution. All the sites studied are either ecologically important or in proximity to protected areas. The presence of endemic fauna in these locations allows for studies of numerous animal and plant species, making them areas of significant conservation and preservation value.

In future research, we plan to monitor the sites studied in this work to investigate possible seasonal or annual changes in the quality of the night skies. Additionally, we intend to expand our study to include more sites of astronomical and ecological interest. This will enable us to obtain a more comprehensive understanding of the evolution of light pollution and its effects on different ecosystems. We will also seek collaborations with local and regional entities to raise awareness about the importance of preserving the night sky and reducing light pollution in these areas.

The authors would like to thank the referee for helpful comments and suggestions that improved the manuscript. The authors also express their gratitude for all the logistical management carried out by the directors of each site: Dr. Edwin Andrés Quintero at AOUTP, Professor Javier Rua at TD, and María Liliana Perdomo at BBG. They also thank all the support received in the selection of the sites from the technical staff at each location. JPUT acknowledges the financial support of the National Agency for Research and Development (ANID) Scholarship Program/Doctorado Nacional/2021-21210732 and the

PhD Program in Astronomy at the University of La Serena. M.J.A. acknowledges the financial support of DIDULS/ULS through project PR2353855.

REFERENCES

Aceituno, J., Sánchez, S. F., & Aceituno, F. J. 2011, PASP, 123, 907, https://doi.org/10.1086/661918

Aguilera Camargo, J. N. 2012, Evaluacin e impacto de la contaminacin lumnica en Bogot, Tesis, Universidad de los Andes, Facultad de Ingeniera, Uniandes, http://hdl.handle.net/1992/25111

Alarcon, M. R., Serra-Ricart, M., Lemes-Perera, S., & Mallorquín, M. 2021, AJ, 162, 1, https://doi.org/10.3847/1538-3881/abfdaa

Andrade-C, M. G. 2011, Revista De La Academia Colombiana De Ciencias Exactas, Físicas Y Naturales, 35, 137, https://doi.org/10.18257/raccefyn.35(137).2011.2424

Angeloni, R., Uchima-Tamayo, J. P., Jaque Arancibia, M., et al. 2024, AJ, 167, 2, https://doi.org/10.3847/1538-3881/ad165c

Arbeláez-Cardona, D., Silva-Villa, E., Galvez, J., Martínez, A., & Cuartas-Restrepo, P. 2020, IJRS, 41, 14, https://doi.org/10.1080/01431161.2020.1727051

Aubé, M., Fortin, N., Turcotte, S., et al. 2014, PASP, 126, 1068, https://doi.org/10.1086/679227

Aubé, Kocifaj, M., Zamorano, J., Solano Lamphar, H. A., & Sánchez de Miguel, A. 2016, JQSRT, 181, 11, https://doi.org/10.1016/j.jqsrt.2016.01.032

Bará, S., Tapia, C. E., & Zamorano, J. 2019, Senso, 19, 6, https://doi.org/10.3390/s19061336

Bará, S. & Falchi, F. 2023, 378, 1892, https://doi.org/10.1098/rstb.2022.0352

Barentine, J. C. 2022, NatAs, 6, 10, https://doi.org/10.1038/s41550-022-01756-2

Benítez García, L. M. 2016, Eficacia de la reglamentación para la prevención y la disminución de la contaminación lumínica en Colombia, en el período 2010-2016, Tesis, Repositorio - Universidad Libre, https://hdl.handle.net/10901/10198

Bertolo, A., Binotto, R., Ortolani, S., & Sapienza, S. 2019, Journal of Imaging, 5, 56, https://doi.org/10.3390/jimaging5050056

Bohórquez-Alfonso, I. A. 2008, Cuadernos de Vivienda y Urbanismo, 1, 1, https://revistas.javeriana.edu.co/index.php/cvyu/article/view/5485

Bonilla Romero, J. 2011, Revista de Topografía AZIMUT, 3, https://revistas.udistrital.edu.co/index.php/azimut/article/view/4055

Bonilla Romero, J., Bustos velazco, E. H., & Reyes, J. D. 2017, Revista Científica, Numero Especial, https://doi.org/10.14483/udistrital.jour.RC.2017.27.a15

Cadena-Vargas, C. E., Sánchez Callejas, S. D., & Morales Pisco, A. F. 2020, Revista Facultad de Ciencias Básicas, 15, 2, https://doi.org/10.18359/rfcb.4382

Cadena-Vargas, C. E., Sánchez Callejas, S. D., & Velásquez Niño, J. 2021, Biota colombiana, 22, 2, https://doi.org/10.21068/c2021.v22n02a10

Cao, C. & Bai, Y. 2014, Remote sensing, 6, 12, https://doi.org/10.3390/rs61211915

Chang, Moon-Hwan, Das, Diganta, Varde, P. V., & Pecht, M. 2012, Microelectronics Reliability, 52, 762, https://doi.org/10.1016/j.microrel.2011.07.063

Chaparro Molano, G., Ramírez Suárez, O. L., Restrepo Gaitán, O. A., & Martínez Mercado, A. M. 2017, PASP, 129, 105002, https://doi.org/10.1088/1538-3873/aa83fe

Cho, Y., Ryu, S., Lee, B. R., et al. 2015, Chronobiology International, 32, 1294, https://doi.org/10.3109/07420528.2015.1073158

Cho, J., Park, J. H., Kim, J. K., & Schubert, E. 2017, LPRv, 11, 2, https://doi.org/10.1002/lpor.201600147

Cinzano, P., Falchi, F., Elvidge, C. D., & Baugh, K. E. 2000, MNRAS, 318, 3, https://doi.org/10.1046/j.1365-8711.2000.03562.x

Cinzano, P. 2005, ISTIL Internal Report, 9, 1

C-Sánchez, E., Sánchez-Medina, A. J., Alonso-Hernández, J. B., & Voltes-Dorta, A. 2019, Sensor, 19, 13, https://doi.org/10.3390/s19132840

Davies, T. W., Duffy, J. P., Bennie, J., & Gaston. J. K. 2014, Frontiers in Ecology and the Environment, 12, 6, https://doi.org/10.1890/130281

Deprato, A., Maidstone, R., Cros, A. P, et al. 2024, BMC medicine, 22, 67, https://doi.org/10.1186/s12916-024-03291-5

Deverchère, P., Vauclair, S., Bosch, G., et al. 2022, NatSR, 12, 1, https://doi.org/10.1038/s41598-022-21460-5

Dill, H. G., Andrei, B., Sorin-Ionut, B., et al. 2020, Catena, 194, 104696, https://doi.org/10.1016/j.catena.2020.104696

Duriscoe, D. M. 2016, JQSRT, 181, 33, https://doi.org/10.1016/j.jqsrt.2016.02.022

Durmus, D. 2022, Lighting Research & Technology, 54, 363, https://doi.org/10.1177/14771535211034330

Falchi, F., Cinzano, P., Elvidge, C. D., Keith, D. M., & Haim, A. 2011, JEnvM, 92, 2714, https://doi.org/10.1016/j.jenvman.2011.06.029

Falchi, F., Cinzano, P., Duriscoe, D., et al. 2016, SciA, 2, 6, https://doi.org/10.1126/sciadv.1600377

Falchi, F. & Bará, S., 2021, NatSc, 1, 2, https://doi.org/10.1002/ntls.10019

Falchi, F., Ramos, F., Bará, S., et al. 2023, MNRAS, 519, 1, https://doi.org/10.1093/mnras/stac2929

Flórez, M. T., Parra, L. N., Jaramillo, D. F., & Jaramillo M. J. M. 2013, Revista De La Academia Colombiana De Ciencias Exactas, Físicas Y Naturales, 37, 143, https://doi.org/10.18257/raccefyn.6

Gabriel, K. M. A., Kuechly, H. U., Falchi F., Wosniok, W., & Hölker, F. 2017, IJBm, 61, 11, https://doi.org/10.1007/s00484-016-1187-y

Gallaway, T., Olsen, R. N., & Mitchell, D. M. 2010, EcoEc, 69, 658, https://doi.org/10.1016/j.ecolecon.2009.10.003

Galvis, H. D., Galeano, D., & Quintero Salazar, E. A., 2019, SunGe, 14, 2, https://doi.org/10.31401/SunGeo.2019.02.10

García Sierra, J. H. & Ramírez Cardona, J. L., 2011, Luna Azul, 32, https://revistasojs.ucaldas.edu.co/index.php/lunazul/article/view/1242

Garzón Díaz, F. A., 2014, Revista latinoamericana de bioética, 14, 1, https://doi.org/10.18359/rlbi.498

Gaston, K. J, Bennie, J., Davies, T. W., & Hopkins, J. 2013, BioRv, 88, 812, https://doi.org/10.1111/brv.12036

Góez Therán, C. & Vargas Domínguez, S. 2021, RMxAA, 57, 1, https://doi.org/10.22201/ia.01851101p.2021.57.01.03

Hänel, A., Posch, T., Ribas, S. J. et al. 2018, JQSRT, 205, 278, https://doi.org/10.1016/j.jqsrt.2017.09.008

Henderson, D. 2010, Environmental Philosophy, 7, 1, https://www.jstor.org/stable/26168027

Hölker, F., Moss, T., Griefahn, B., & Kloas, W. 2010, EcSoc, 15, 4, https://www.jstor.org/stable/26268230

Hölker, F., Bolliger, J., Davies, T., et al. 2021, FREEv, 9, 767177, https://doi.org/10.3389/fevo.2021.767177

Hung, Li-Wei, Anderson, S. J., Pipkin, A., & Fristrup, K. 2021, JEnvM, 292, https://doi.org/10.1016/j.jenvman.2021.112776

Iglesias, F. A., Francile, C., Lazarte-Gelmetti, J., et al. 2023, SolPhys, 298, 46, https://doi.org/10.1007/s11207-023-02139-0

Jechow, A., Kolláth, Z., Ribas, S. J., et al. 2017, NatSR, 7, 6741, https://doi.org/10.1038/s41598-017-06998-z

Jechow, A., Hölker, F., & Kyba, C. C. M. 2019, NatSR, 9, 1391, https://doi.org/10.1038/s41598-018-37817-8

Jiménez-Alvarado, J. S., Moreno-Díaz, C., Alfonso, A. F., et al. 2017, Mammalogy Notes, 4, 1, https://doi.org/10.47603/manovol4n1.37-41

Jiménez Villariaga, S., Quintero Salazar, E. A., & Aguirre Galvis, J. A. 2017, TEC-CIENCIA, 12, 23, https://doi.org/10.18180/tecciencia.2017.23.6

Kolláth, Z. 2010, JPhCS, 218, 1, https://doi.org/10.1088/1742-6596/218/1/012001

Kolláth, Z., Cool, A., Jechow, A. et al. 2020, JQSRT, 253, 107162, https://doi.org/10.1016/j.jqsrt.2020.107162

Krisciunas, K., Semler, D. R, Richards, J. et al. 2007, PASP, 119, 687, https://doi.org/10.1086/519564

Kyba, C. C. M., Ruhtz, T., Fischer, J., & Hölker, F. 2011, PloS one, 6, 3, https://doi.org/10.1371/journal.pone.0017307

Kyba, C. C. M., Kuester, T., Sánchez de Miguel, A. et al. 2017, SciA, 3, 11, https://doi.org/10.1126/sciadv.1701528

Kyba, C. C. M., Altintas, Y. O., Walker, C. E., et al. 2023, Science, 379, 6629, https://doi.org/10.1126/science.abq7781

Longcore, T. & Rich, C. 2004, FREEv, 2, 4, https://doi.org/10.1890/1540-9295(2004)002[0191:ELP]2.0.CO;2

Luo, W., Kramer, R., Kompier, M., et al. 2023, BuEnv, 231, https://doi.org/10.1016/j.buildenv.2022.109944

Mander, S., Alam, F., Lovreglio, R., & Ooi, M. 2023, SusCS, 92, https://doi.org/10.1016/j.scs.2023.104465

Marín Gómez, O. H. 2022, Animal, 12, 8, https://doi.org/10.3390/ani12081015

Masana, E., Carrasco, J. M., Bará, S., & Ribas, S. J. 2021, MNRAS, 501, 4, https://doi.org/10.1093/mnras/staa4005

Masana, E., Bará, S., Carrasco, J. M., & Ribas, S. J. 2022, International Journal of Sustainable Lighting, 24, 1, https://doi.org/10.26607/ijsl.v24i1.119

Mayer-Pinto, M., Jones, T. M, Swearer, S. E. et al. 2022, UCL Open Environment, 4, https://doi.org/10.14324/111.444/000103.v1

Mejía, M. P. 2006, Fronteras de la Historia, 11, https://www.redalyc.org/articulo.oa?id=83301108

Meravi, N. & Kumar Prajapati, S., 2018, BioRR, 51, 7, https://doi.org/10.1080/09291016.2018.1518206

Meza, C. A. 2008, Revista Colombiana de Antropología, 44, 2, https://www.redalyc.org/articulo.oa?id=105012451007

Mills, P. R, Tomkins, S. C. & Schlangen, L. J. 2007, Journal of circadian rhythms, 5, https://doi.org/10.1186/1740-3391-5-2

Mitchell, D. M. & Gallaway, T., 2019, Tourism Review, 74, 4, https://doi.org/10.1108/TR-10-2018-0146

Montealegre Vega, A. & Garavito González, L. 2022, TURPADE. Turismo, Patrimonio y Desarrollo, 1, 17, https://revistaturpade.lasallebajio.edu.mx/index.php/turpade/article/view/65

Montes, C., Silva, C. A., Bayona, G. A., et al. 2021, FrEaS, 8, https://doi.org/10.3389/feart.2020.587022

Müller, A., Wuchterl, G. & Sarazin, M. 2011, RMxAA, 41, https://www.redalyc.org/articulo.oa?id=57120784014

Nair, G. B. & Dhoble, S. J., 2015, Luminescence, 30, 8, https://doi.org/10.1002/bio.2919

Plauchu-Frayn, I., Richer, M. G., Colorado, E., et al. 2017, PASP, 129, 973, https://doi.org/10.1088/1538-3873/129/973/035003

Posh, T., Binder, F. & Puschnig, J. 2018, JQSRT, 211, 144, https://doi.org/10.1016/j.jqsrt.2018.03.010

Poveda, G., Álvarez, D. M., & Rueda, O. A. 2011, ClDy, 36, 2233, https://doi.org/10.1007/

s00382-010-0931-y

Riegel, K. W., 1973, Sci, 179, 1285, https://doi.org/10.1126/science.179.4080.1285

Rodríguez Ramos, N. B. 2015, Plan de Gestión Ambiental del acuífero de la formación Guadalupe y de los cerros orientales como zona de recarga a partir de la evaluación del índice de escasez de aguas subterráneas, Tesis de maestría, Repositorio Universidad Javeriana, http://hdl.handle.net/10554/17958,doi:10.11144/Javeriana.10554.17958

Rueda-Espinosa, K. J, Guerrero-Guio, A. F., Vargas-Dominguez, S., Vinasco-Téllez, M., & Giez-Therán, C. 2023, Revista de la Academia Colombiana de Ciencias Exactas, Físicas y Naturales, 47, 183, https://doi.org/10.18257/raccefyn.1867

Rueda Esteban, N. R, 2017, PASOS Revista de Turismo y Patrimonio Cultural, 15, 1, https://www.pasosonline.org/Publicados/15117/PASOS51.pdf\#page=87

Sánchez-González, K., Aguirre-Obando, O., & Ríos-Chelén, A. A. 2020, EtEcE, 33, 4, https://doi.org/10.1080/03949370.2020.1837963

Singhal, R. K., Kumar, M., & Bose, B. 2019, Russian Journal of Plant Physiology, 66, 2, https://doi.org/10.1134/S1021443719020134

Svechkina, A., Portnov, B. A., & Trop, T. 2020, Landscape Ecology, 35, 8, https://doi.org/10.1007/s10980-020-01053-1

Tsao, J., Saunders, H. D., Creighton,J. R., Coltrin, M. E., & Simmons, J. S. 2010, JPhD, 43, 35, https://doi.org/10.1088/0022-3727/43/35/354001

Tovmassian, G., Hernandez, M., Ochoa,J. L. et al. 2016, PASP, 128, 961, https://doi.org/10.1088/1538-3873/128/961/035004

Urrego Guevara, G. A. 2016, Análisis de los niveles de luz artificial de 13 puntos en los límites del Jardín Botánico para la especialización de la contaminación lumínica en el circuito general, Tesis, Facultad de Ingeniería, Bogotá, Repositorio - Universidad Libre, https://hdl.handle.net/10901/8897

Varela Perez, A. M. 2023, Sci, 380, 6650, https://doi.org/10.1126/science.adg0269

Verheijen, F. J. 1985, Experimental biology, 44, 1

Vierdayanti, K., Kunjaya, C., Herdiwijaya, D., et al. 2024, JPhCS, 2773 1, https://doi.org/10.1088/1742-6596/2773/1/012020

Walker, M. F., 1970, PASP, 82, 672, https://doi.org/10.1086/128945

Zamorano, J., García, C., Tapia, C. et al. 2016, International Journal of Sustainable Lighting, 18, 1, https://doi.org/10.26607/ijsl.v18i0.21

Zielinska-Dabkowska, K. M. 2019, PASP, 1, 4, https://doi.org/10.4324/9780367814588-2

Zielinska-Dabkowska, K. M., Xavia, K. & Bobkowska, K. 2020, Sust, 12, 12, https://doi.org/10.3390/su12124997

Rodolfo Angeloni: Gemini Observatory, NSF's NOIRLab, Av. J. Cisternas 1500 N, 1720236, La Serena, Chile (rodolfo.angeloni@noirlab.edu).

Cristian Goez Theran: Oficina de Olimpiadas Colombianas, Universidad Antonio Nariño, Calle 58a # 37 - 94, Bogotá, Colombia (cristian.goez@uan.edu.co).

Marcelo Jaque Arancibia & Juan Pablo Uchima-Tamayo: Departamento de Astronomía, Universidad de La Serena, Av. R. Bitrn 1305, La Serena, Chile (marcelo.jaque, juan.uchima@userena.cl).

Marcelo Jaque Arancibia: Instituto Multidisciplinario de Investigación y Postgrado, Universidad de La Serena, Av. R. Bitrn 1305, La Serena, Chile.

Javier Fernando Rúa Restrepo: Observatorio Astrosur, Km 8 desierto de la Tatacoa, Villavieja, Colombia (astrosur@yahoo.com).

Revista Mexicana de Astronomía y Astrofísica, **61**, 155–171 (2025)

https://doi.org/10.22201/ia.01851101p.2025.61.01.11

CHARACTERIZATION OF A DOUBLE WOLLASTON MODULE FOR POLARIMETRY IN ASTROPHYSICS

A. García-Pérez[1], A. Luna[1], J. Castro-Ramos[1], E. O. Serrano-Bernal[1], and S. Medina[2]

Received April 4 2024; accepted February 24 2025

ABSTRACT

The Wedge Double Wollaston (WeDoWo) or "double Wollaston" module is a device capable of displaying four images of a single field of view (FOV); each image corresponds to a different polarization angle (0°, 45°, 90°, and 135°), providing enough information for the Stokes I, Q, and U parameters calculation and the linear polarization angle and fraction values retrieved from the source observed, in this case, an astronomical source, in a single exposure (single-shot). In this paper, we present the design of a SiO2 (Crystalline Silica) WeDoWo module, describe the characterization process carried out in the laboratory and the subsequent calibration. Likewise, we show the application of this module for imaging astronomical polarimetry using the 1.0-meter telescope of the National Astronomical Observatory from Tonantzintla, Puebla (OAN-TNT), and illustrate the advantages and limitations of this technique and the optimal performance of this module.

RESUMEN

El módulo Wedge Double Wollaston (WeDoWo) o "doble Wollaston" es un dispositivo capaz de desplegar 4 imágenes de diferente ángulo de polarización (0°, 45°, 90°, 135°), permitiendo calcular los parámetros de Stokes I, Q y U, así como el grado y ángulo de polarización lineal de la fuente observada en una sola exposición. En este artículo presentamos el diseño de un módulo WeDoWo en SiO_2 (Sílice Cristalina) y describimos la caracterización realizada en laboratorio a distintas longitudes de onda y su posterior calibración. De igual manera mostramos la aplicación de este módulo para polarimetría astronómica utilizando el telescopio de 1 metro del Observatorio Astronómico Nacional de Tonantzintla, Puebla (OAN-TNT); exponemos las ventajas y limitaciones que presenta esta técnica y el rendimiento óptimo que se puede lograr.

Key Words: instrumentation: polarimeters — methods: observational — polarization — techniques: polarimetric

1. INTRODUCTION

Polarization at visible and near-infrared (NIR) wavelengths gives us fundamental information about the scattering of light produced by various physical phenomena that occur in astronomical objects; one of them is the interaction of the light with the circumstellar medium (CSM) that surrounds the stars, produced during their evolution. Polarimetric measurements allow us to understand light interaction with the CSM better, to identify the point of origin of the light, and to constrain other parameters of the dust distribution. In some instances, the polarization angle is related to a magnetic field, where the longer axis of dust particles acquires preferential orientation, with the media acting as a dichroic. Polarimetric phenomena can occur in reflection nebulae, star-forming regions, (Tinbergen 1996; Clarke 2009), supernova remnants (Ritacco 2016), stars, and planetary nebulae (Scarrott & Scarrott 1994; Gledhill et al. 2001; Serrano-Bernal et al. 2020; Devaraj et al. 2018), and they can be caused by dichroic extinction from dust grains whose position is associated to local magnetic fields (Hiltner 1949; Lazarian & Hoang 2007), by the presence of synchrotron radiation or

[1]Instituto Nacional de Astrofísica, Óptica y Electrónica. Luis Enrique Erro #1, Sta. María Tonanzintla, 72840, San Andrés Cholula, Puebla, México.

[2]Tyndall National Institute. Lee Maltings Complex Dyke Parade, Cork, Cork, T12 R5CP, Ireland.

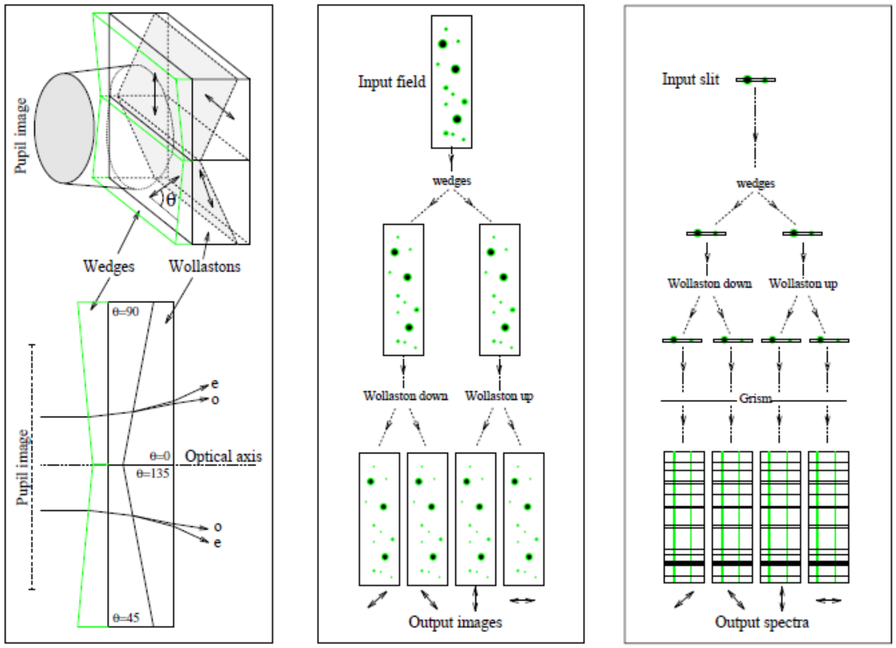

Fig. 1. *Left*: Schematic representation of the WeDoWo module and its behavior. To prevent the field's cross-talk, the Wedge's angles are calculated to split the field into four. *Center*: Illustration of how the system makes four polarized images of a stellar field. *Right*: Illustration of how the system with an additional dispersive component can take four polarized spectra of two stars (Oliva 1996). The color figure can be viewed online.

by thermal emission of the dust (Ritacco 2016; Tinbergen 1996; Clarke 2009).

Nowadays, there are several instruments capable of measuring image polarization of astronomical objects and phenomena at different wavelengths. Some designs contain mechanical elements, such as a rotating half-wave plate (HWP), a useful component for wide-field observations. Examples of this kind of instrument are POLICAN, SIRPOL, and MIMIR in the NIR band or NIKA in the submillimeter waveband (Devaraj et al. 2018; Ritacco 2016). However, because of the long exposures needed, the HWP may introduce instabilities in the system or be sensitive to the change in the sky quality. A solution is to remove the rotating component using a birefringent material capable of splitting the light into its ordinary and extraordinary components, which allows recovery of the polarization of the light. One proposed solution to the rotation problem was the Wollaston prism, which splits the light into two orthogonal components, but requires an HWP to fully measure the entire linear polarization. Oliva (1996) proposed a new design using a double Wollaston. Each one gives the ordinary and extraordinary components of the incident light: paired at 0° and 90° angles for the first Wollaston, 45° and 135° for the second. It contains an entrance "Wedge", which helps split the FOV and redirect it to each Wollaston. This design is called the "Wedge Double Wollaston" (WeDoWo). Figure 1 shows the design developed by Oliva (1996). This device is already implemented in some polarimeters (Helhel et al. 2022; Pernechele et al. 2012), and they are focused on performing observations of small astronomical sources (i.e., small solar system bodies or stars). The principal difference concerning polarimeters using a rotating optical element is that the WeDoWo class of polarimeters can retrieve enough information to make a polarization analysis of the observed FOV within a single exposure, which represents an advantage in reducing the noise and the uncertainties caused by the mechanical and optical components.

In this paper, we present the design of the WeDoWo module and its application to imaging astronomical polarimetry. We perform simulations using specialized software for optical design (Ansys®Zemax OpticStudio) and perform tests in the laboratory and on a 1.0-meter telescope. In § 2 and 3, we present the current design of the WeDoWo module, the considerations that must be taken into account to perform the laboratory tests, and the results of the characterization and calibration. In § 4, we show the performance of the WeDoWo on astronomical observations focusing on the polarimetric

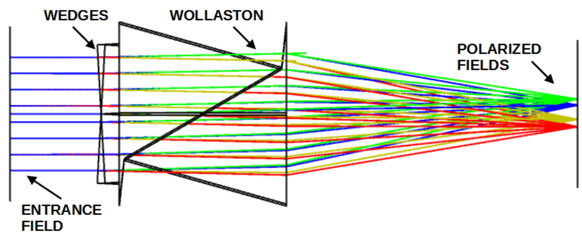

Fig. 2. Final optical design of the WeDoWo module implemented in Zemax *OpticStudio*. Each color represents a polarized field. Green: Vertical polarization, blue: horizontal polarization, yellow: 45° polarization, red: 135° polarization. This schematic is only for illustrative purposes, and the structure of the built WeDoWo is shown in Figure 3. The color figure can be viewed online.

Fig. 3. Final assembly of the WeDoWo module. This takes into account the considerations exposed in § 2 and its behavior is shown in Figure 2. The color figure can be viewed online.

standard stars and extended sources like Frosty-Leo, a pre-planetary nebulae with an angular size $\leq 1'$. Finally, the conclusions of this work are presented in § 5.

2. THE WEDOWO MODULE

As described in § 1 and illustrated in Figure 1, the WeDoWo module is designed to display simultaneously four images of the same FOV, allowing to compute the Stokes Q and U parameters related to the linear polarization fraction and angle. § 2.1 describes the Stokes parameters more profoundly.

In this case, the WeDoWo module was initially designed for the 2.1-meter telescope of the Guillermo Haro Astrophysical Observatory (OAGH) by Medina (2020) for a one-shot polarimeter specialized for observing minor bodies in the Solar System. Designed and manufactured on SiO_2 following the Oliva (1996) considerations, the lack of chromatic difference between two or more elements and the relatively high Abbe number ($V_d = 70.132$ for the crystalline silica) ensure that the performance of the WeDoWo, described in Figure 1 can be achieved. The Wedges and the Wollaston have an angle of $\alpha = \pm 3.2°$, and $\beta = \pm 60°$, respectively. Figure 2 shows the simulation performed in OpticStudio for a collimated wavefront and an ideal convergent lens at the module's output to show the ideal performance and field distribution; further description of this design is reported by Medina (2020). It's important to consider the different configurations of the Wedges and the Wollaston surfaces related to the values of α and β to model the WeDoWo performance correctly. Figure 3 shows the WeDoWo module, built by Bernhard Halle Nachft. § 3 describes the different tests performed once the module was in INAOE's laboratory.

2.1. *Stokes Parameters and Polarization of the WeDoWo Module*

2.1.1. *Stokes Parameters and Polarization*

The Stokes parameters are quantities that describe the polarization fraction and angle of the incident light. For an instrument with a WeDoWo module as a main polarimetric device, the Stokes parameter expressions for the linear polarized incident light are enunciated in equation 1 (Helhel et al. 2022; Tinbergen 1996; Shurcliff 1962):

$$\begin{aligned} I &= I_{0°} + I_{90°} \quad or \quad I_{45°} + I_{135°}. \\ Q &= I_{0°} - I_{90°}. \\ U &= I_{45°} - I_{135°}. \end{aligned} \tag{1}$$

The analysis of the Stokes I parameter can come out separately for each Wollaston, i.e., $I_{W1} = I_{0°} + I_{90°}$, and $I_{W2} = I_{45°} + I_{135°}$, which allows a precise analysis of the polarization fraction by normalizing the Stokes parameters $q = Q/I_{W1}$ and $u = U/I_{W2}$. The linear polarization fraction and angle can be obtained with the following equations 2 and 3:

$$P = 100\sqrt{q^2 + u^2}. \tag{2}$$

$$A = \frac{1}{2}\arctan\left(\frac{u}{q}\right). \tag{3}$$

These relations allow us to determine the fraction and angle of linear polarization, regardless of whether the light comes from an astronomical object or a controlled source in the laboratory.

2.1.2. *Linear Polarization Debiasing*

The measurement corresponding to the different polarization angles carry some statistical uncertainties, and error propagation can be carried out with

DOI: https://doi.org/10.22201/ia.01851101p.2025.61.01.11

standard techniques (Bevington & Robinson 2010; Serrano-Bernal 2021):

$$\sigma_x^2 = \sigma_u^2 \left(\frac{\partial x}{\partial u}\right)^2 + \sigma_v^2 \left(\frac{\partial x}{\partial v}\right)^2 + \sigma_w^2 \left(\frac{\partial x}{\partial w}\right)^2. \quad (4)$$

Equation 4 considers the contribution of error for a parameter X depending on the variables u, v and w, i.e., $X = f(u, v, w)$. The nature of the uncertainties depends on the measurement instrument. In the case of imaging astronomy, the most common devices are the charge-couple devices (CCDs). The corresponding uncertainties are related to the readout noise and the system gain (Howell 2006) and can be described with equation 5 as follows:

$$\sigma_{ADU} = \sqrt{\frac{F}{G}}. \quad (5)$$

The Analog Digital Units (ADUs) are the analog readout from the CCD transformed into digital units. F is the value of each pixel of the detection matrix, and G is the gain of the CCD's system. The statistical uncertainties of each field and polarization angle are represented as $\sigma_{0^\circ}, \sigma_{45^\circ}, \sigma_{90^\circ}$, and σ_{135°. The propagation through the Stokes I, Q, and U parameters can be calculated with equations 6, 7 and 8 as follows:

$$\sigma_I = \sqrt{\sigma_{0^\circ}^2 + \sigma_{90^\circ}^2} \quad or \quad \sqrt{\sigma_{45^\circ}^2 + \sigma_{135^\circ}^2}. \quad (6)$$

$$\sigma_q = \frac{2}{I^2}\sqrt{\sigma_{0^\circ}^2 I_{90^\circ}^2 + \sigma_{90^\circ}^2 I_{0^\circ}^2}. \quad (7)$$

$$\sigma_u = \frac{2}{I^2}\sqrt{\sigma_{45^\circ}^2 I_{135^\circ}^2 + \sigma_{135^\circ}^2 I_{45^\circ}^2}. \quad (8)$$

σ_q and σ_u are the error propagation related to the Q and U normalized Stokes parameters. Statistical errors of $P(\sigma_P)$ and $A(\sigma_A)$ are related to the error propagation of the Stokes elements under the relations described in equations 9 and 10 as follows:

$$\sigma_P = \frac{100^2}{P}\sqrt{q^2 \times \sigma_q^2 + u^2 \times \sigma_u^2}. \quad (9)$$

$$\sigma_A = \frac{100^2}{2P^2}\sqrt{u^2 \times \sigma_q^2 + q^2 \times \sigma_u^2}. \quad (10)$$

The error propagation of the Stokes parameters is contained in the quadratic sum related to the polarization fraction expression (equation 2); the statistical error makes a positive contribution to the measurement of polarization, introducing a bias value that is necessary to subtract. Equation 11 is the expression of the polarization difference between the average of the observed $\langle P \rangle$ and the real polarization fraction P_0.

$$\Delta P = \langle P \rangle - P_0. \quad (11)$$

The debiasing of the polarization fraction is performed by the *Ricean* correction, described in equation 12:

$$P_0 = \sqrt{P^2 - \sigma_P^2}. \quad (12)$$

Bias correction is necessary even for the case of high signal-to-noise ratio (SNR) values where the polarization values are small and σ_P and ΔP are similar (Patat & Romaniello 2004). Equations 7 and 8 represent a threshold value in the future polarimetric data analysis to keep the relevant information of the observed source in an imaging analysis.

2.2. *A Non-Ideal Wollaston Prism: Effects and Considerations*

2.2.1. *Parameter-t*

The WeDoWo module comprises two Wollaston prisms with a different linear polarization angle orientation. In an ideal case, the Wollaston prism splits incoming unpolarized light into identical fractions, i.e., intensities in the ordinary and extraordinary axes are equal to $I/2$, where I represents the total intensity of the incident light (Helhel et al. 2022; Patat & Romaniello 2004). But in the case of non-ideal Wollaston prisms, we need to introduce the parameter-t or the transmission parameter (Helhel et al. 2022; Patat & Romaniello 2004). Equation 13 gives the intensity of each polarized field.

$$\begin{aligned} I_0 &= t_1 I. \\ I_{90} &= (1 - t_1)I. \\ I_{45} &= t_2 I. \\ I_{135} &= (1 - t_2)I. \end{aligned} \quad (13)$$

Here t_1 and t_2 are the parameters-t of each Wollaston and, in an ideal scenario, both are equal to 1/2 (Helhel et al. 2022; Patat & Romaniello 2004). If we derive equation 13, we can replace the total intensity with the real intensity of each field. Equation 14 represents the real fluxes of each polarized field:

$$\begin{aligned} I'_0 &= I_0/(2t_1). \\ I'_{90} &= I_{90}/(2(1 - t_1)). \\ I'_{45} &= I_{45}/(2t_2). \\ I'_{135} &= I_{135}/(2(1 - t_2)). \end{aligned} \quad (14)$$

The importance resides in the fact that once we know the real values of the parameter-t of each Wollaston, it is possible to correct the fluxes of each field and make the first polarimetric correction (Helhel et al. 2022; Patat & Romaniello 2004).

DOI: https://doi.org/10.22201/ia.01851101p.2025.61.01.11

2.2.2. *Instrumental Polarization*

Any optical system could introduce some instrumental polarization values related to its configuration, so it is necessary to consider this to recover the actual incident polarization degree. The description of instrumental polarization can be performed by the Mueller matrix represented by the equation 15 as follows:

$$\mathbf{M_i}(x,y) = \frac{1}{(1+p)} \begin{bmatrix} 1 & p\cos 2\theta & p\sin 2\theta \\ p\cos 2\theta & 1-p\sin^2 2\theta & ps\cos 2\theta \\ p\sin 2\theta & p\sin 2\theta\cos 2\theta & 1-p\cos^2 2\theta \end{bmatrix}. \tag{15}$$

The matrix of equation 15 corresponds to an ideal Mueller matrix of polarization, where $p = p(x,y)$ and $\theta = \theta(x,y)$ are the instrumental polarization fraction and angle across the FOV, making it possible to estimate the instrumental Stokes parameters Q_i and U_i which can be represented by the system described in equation 16 as follows:

$$\begin{aligned} I_i(1+p) &= I_0 + Q_0 p\cos 2\theta + U_0 p\sin 2\theta. \\ Q_i(1+p) &= I_0 p\cos 2\theta + Q_0(1-p\sin^2 2\theta) + U_0 p\sin 2\theta\cos 2\theta. \\ U_i(1+p) &= I_0 p\sin 2\theta + Q_0 p\sin 2\theta\cos 2\theta + U_0(1-p\cos^2 2\theta). \end{aligned} \tag{16}$$

Here I_0, Q_0, and U_0 are the incident Stokes parameters. For an unpolarized source, equation 16 is simplified, and $p(x,y)$ and $\theta(x,y)$ can be derived immediately. The problem becomes more complicated with an incoming polarized light beam. Still, in this case, the system can be simplified assuming that $p \ll 1(100\%)$ and $P \ll 1(100\%)$, since instrumental polarization is typically less than a few percent (Patat & Romaniello 2004), equation 16 can be rewritten as follows:

$$\begin{aligned} I_i &\simeq I_0. \\ Q_i &\simeq Q_0 + I_0 p\cos 2\theta. \\ U_i &\simeq U_0 + I_0 p\sin 2\theta. \end{aligned} \tag{17}$$

Equation 17 represents a set of approximate expressions useful to evaluate the instrumental polarization, provided that the input polarization is known and the observed source covers a large fraction of the FOV. Solving equation 17 for $p(x,y)$ and $\theta(x,y)$ yields:

$$p_1 \simeq \frac{Q_i - Q_0}{I_0\cos 2\theta}, \tag{18}$$

$$p_2 \simeq \frac{U_i - U_0}{I_0\sin 2\theta}, \tag{19}$$

$$\theta \simeq \frac{1}{2}\arctan\frac{U_i - U_0}{Q_i - Q_0}, \tag{20}$$

where p_1 and p_2 are two independent estimates of $p(x,y)$ and can be averaged to increase the accuracy due to the non-polarized nature of the source and the value of the instrumental polarized related to the optical system (Patat & Romaniello 2004).

2.2.3. *The Transmittance Ratio R*

Due to the possible difference of transmission between the two Wollaston that compose the module, it is possible to introduce the transmittance ratio (R) value, represented by the ratio of the two intensity expressions of equation 1 as follows:

$$R = \frac{I_{45} + I_{135}}{I_0 + I_{90}}. \tag{21}$$

The transmittance ratio could be applied to the instrumental Stokes parameters correction as follows, Helhel et al. (2022):

$$\begin{bmatrix} I \\ Q \\ U \end{bmatrix} = \begin{bmatrix} I_i \\ R \times Q_i \\ U_i \end{bmatrix}. \tag{22}$$

The application of the transmittance ratio requires, for the computation of the polarization fraction, the implementation of the second intensity expression of equation 1 (i.e., $I = I_{45} + I_{135}$) considering the respective error propagation.

2.3. *Final Description of the WeDoWo Module*

Taking into account the considerations enumerated in the previous sections, a WeDoWo-based instrument can be cataloged as a four-intensity polarimeter, i.e., the four intensities can be measured simultaneously (Compain et al. 1999), and can be described by the following expression:

$$\begin{bmatrix} I_1 \\ I_2 \\ I_3 \\ I_4 \end{bmatrix} = \mathbf{AS}. \tag{23}$$

Here $\mathbf{A}$ is the characteristic matrix of the polarimeter, and $\mathbf{S}$ is the input Stokes vector. The WeDoWo module can only work with linear polarized incident emission; so in this case, the structure of the equation 23 is represented by:

$$\begin{bmatrix} I_1 \\ I_2 \\ I_3 \\ I_4 \end{bmatrix} = \begin{bmatrix} t_1 & t_1\cos 2\theta_{o_1} & t_1\sin 2\theta_{o_1} \\ t_{11} & t_{11}\cos 2\theta_{e_1} & t_{11}\sin 2\theta_{e_1} \\ t_2 & t_2\cos 2\theta_{o_2} & t_2\sin 2\theta_{o_2} \\ t_{21} & t_{21}\cos 2\theta_{e_2} & t_{21}\sin 2\theta_{e_2} \end{bmatrix} \begin{bmatrix} I_{in} \\ Q_{in} \\ U_{in} \end{bmatrix}. \tag{24}$$

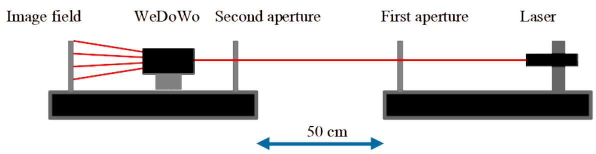

Fig. 4. Schematic representation of the alignment process of the optical system on the test-bench. The color figure can be viewed online.

Here, θ_{o_1}, θ_{o_2}, θ_{e_1} and θ_{e_2} are the orientation angles for the ordinary and extraordinary transmission axis for the first and the second Wollaston respectively. t_1, t_{11}, t_2 and t_{21} are the parameter-t values, described previously in § 2.2.1, for the first and second Wollaston of the module, where $t_{11} = (1 - t_1)$ and $t_{21} = (1 - t_2)$. If $\theta_{o_1} = 0°$, $\theta_{e_1} = 90°$, $\theta_{o_2} = 45°$ and $\theta_{e_2} = 135°$, the expressions from equation 1 can be easily derived taking account the following:

$$\mathbf{S} = \mathbf{A}^{-1}[I_1, I_2, I_3, I_4]^T. \tag{25}$$

Equation 24 is a variation of the polarimeter characteristic matrix exposed by Compain et al. (1999), with the main change in the matrix size due to the lack of capability to detect circularly polarized incident emission. Also, the representation changes; in this case, we consider the orientation angles related to the ordinary and extraordinary transmission axis instead of the ellipsometric angles considered by Compain et al. (1999). However, both representations are equivalent, and equation 24 can be represented with the ellipsometric angles, with their respective considerations.

3. LABORATORY CHARACTERIZATION

The previous modeling and simulation made in OpticStudio, shown in Figure 2, demonstrates that the performance of the designed WeDoWo module can satisfy the requirements for which it was intended. The laboratory test aims to prove the reliability of the simulations and find the actual characteristics of a non-ideal WeDoWo module in terms of the location of the polarized fields, which describes the configuration of each Wollaston, and the response of the module to an incident polarized light beam. In the following, we describe the characterization process in the laboratory and the results of these experiments.

3.1. *Characterization Process*

For a successful characterization process, plenty of considerations must be taken about the position of the different optical elements. First of all, it is necessary to align the optical components properly. Figure 4 shows a schematic representation of the proper alignment of the elements of the WeDoWo module. Figures 5 and 6 show the implementation of the previous schematic diagram. Second, the entrance pupil must be controlled to avoid the crosstalk between polarized intensities, constraining the effective FOV. In the following, we enumerate the optical components involved in this characterization process:

1. Optical tables and support elements and tools for the WeDoWo and the optical elements. For this purpose, a special mount was developed for the WeDoWo, which consists of a couple of CPVCs of 1 inch in diameter (2.56 cm).

2. Newport 20LP-VIS-B linear analyzer installed on a Newport RSP-2T rotational coupler. This element is necessary to find the position of each field.

3. Biconvex optic lens with a focal distance of $f =$ 13.62 cm. Useful for the focus of the polarized fields.

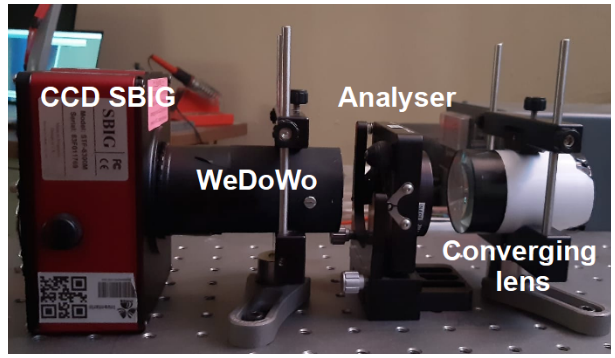

Fig. 5. Final distribution of the test-bench with the Newport analyzer. The color figure can be viewed online.

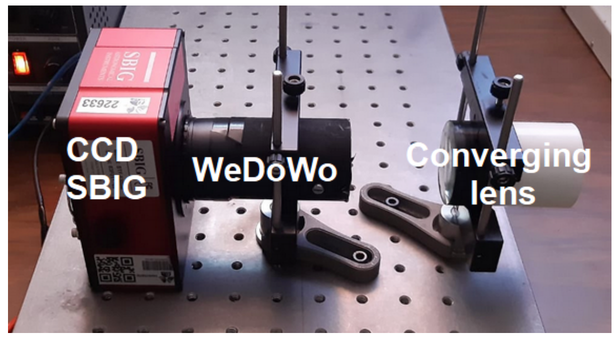

Fig. 6. Final distribution of the test-bench without the analyzer. The color figure can be viewed online.

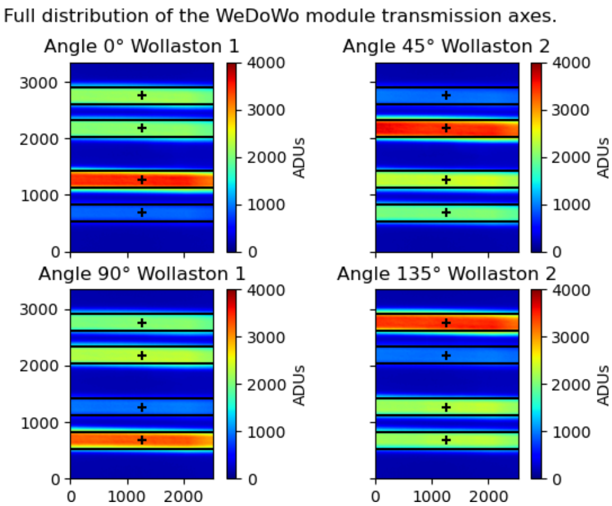

Fig. 7. Four polarized fields plotted each one by a position of the linear analyzer, matching the transmission axis of each Wollaston. Black frames highlight the fields, and the field corresponding to the analyzer's transmission angle shows the maximum value of the color bar reported for each image. The color figure can be viewed online.

4. "SBIG STF-8300" Optical CCD with a detection matrix of 3352×2532 pixels and a saturation level of 65536 ADUs, with its respective CCD RGB filters.

5. Newport Fabry-Perot laser module $\lambda = 635\,n\mathrm{m}$.

6. Blank field positioned and illuminated by reflection to generate the low-polarized light source.

For the low-polarized source emission, we use an emission light diode (LED) and a blank field, causing the reflection of the LED's light to the optical system. Saito et al. (2022) enunciate that LED devices have the characteristic of emitting low-polarized light related to the material that surrounds the chip (the epoxy resin) and the orientation of the LED's emission to the optical system. Still, in the case of emission coming from the top of the LED's structure, the polarization fraction is minimum but not zero, i.e., $0-9\%$. The low-polarized source will aid us in constraining the location of the fields and performing an initial polarimetric analysis to show the capabilities of the WeDoWo module to produce quality polarimetric data.

Once the alignment of the optical components is performed and the entrance field is appropriately controlled, we need to make a location for each field to find its transmission axis orientation angle. In this instance, a linear analyzer device is crucial; the task is to match the polarizer transmission axis with the

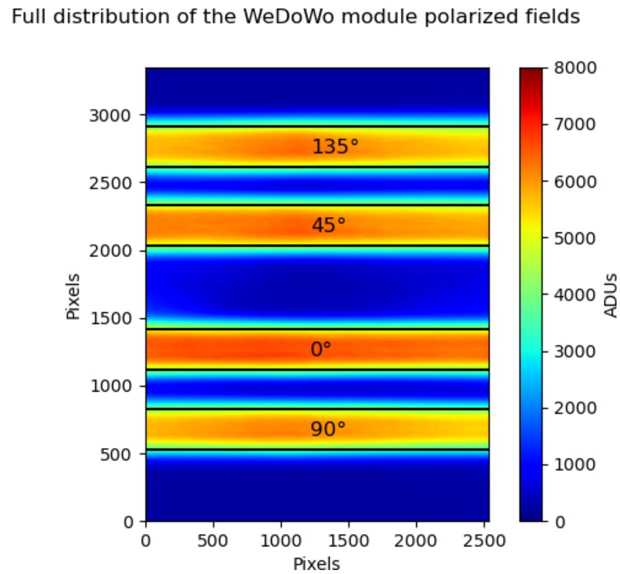

Fig. 8. Distribution of each polarized field for a flat blank field in the detector. The color figure can be viewed online.

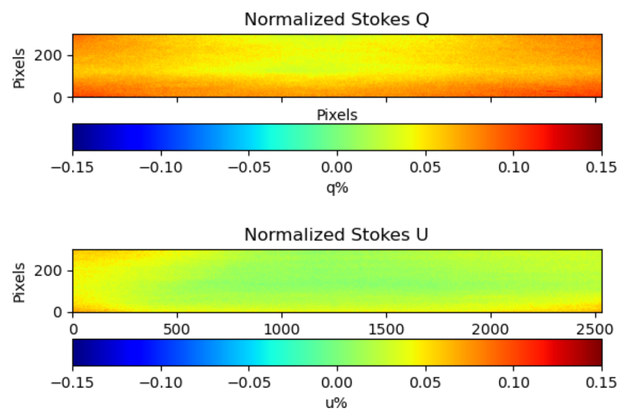

Fig. 9. *Top:* Normalized Q Stokes. *Bottom:* Normalized U Stokes imaging fields, obtained by the trim and calculation of the blank field observation shown in Figure 8 using equation 1 described in § 2. The color figure can be viewed online.

different transmission axes that compose the module. Theoretically, the transmission axes angle distribution is $\theta_{o_1} = 0°$, $\theta_{e_1} = 90°$, $\theta_{o_2} = 45°$ and $\theta_{e_2} = 135°$ for the first and second Wollaston respectively, but is necessary to locate the position of the fields before any polarimetric analysis. Figure 5 shows the position of the analyzer in the system, and Figure 7 shows the results of these tests, showing that $\theta_{o_1} = 0°$, $\theta_{e_1} = 90°$ corresponds to the bottom location of the image, and $\theta_{o_2} = 45°$ and $\theta_{e_2} = 135°$ corresponds to the top.

With the proper location of the fields, the analyzer is withdrawn from the optical system. Then,

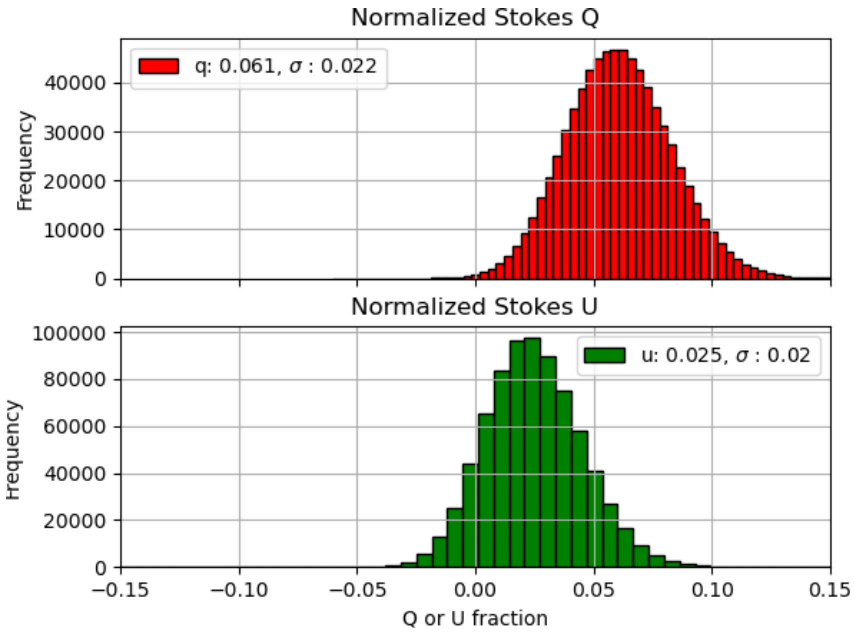

Fig. 10. *Top:* Normalized Q Stokes. *Bottom:* Normalized U Stokes distribution values, obtained by the trim and calculation of the blank field observation shown in Figure 8 using equation 1 described in § 2. The color figure can be viewed online.

we perform several data acquisition of the FOV for the polarimetric analysis. We trim each polarized field from the observed data, as shown in Figure 8, and analyze it following the equation 1 expressions.

The maps corresponding to the normalized Stokes Q and U parameters are shown in Figure 9, with their respective histogram that shows the value distribution across the observed FOV (Figure 10). The calculation of the polarization fraction and angle is performed with equations 2 and 3, respectively. Figures 11 and 12 show the spatial distribution and the value distribution of the polarized fraction obtained from the blank-field observations. The average values for the normalized Stokes parameters Q and U are $\langle q \rangle = 0.060 \pm 0.022$ and $\langle u \rangle = 0.024 \pm 0.020$, and the average polarization fraction and angle values are $\langle P \rangle = 6.8\% \pm 2.35\%$ and $\langle A \rangle = 79.5° \pm 9.558°$, retrieved from the observational data, with the sigma values containing the product of the error propagation computed and the statistical uncertainties analyzed within the polarization fraction and angle values. The values reported for the blank-field observations resemble the values reported by Saito et al. (2022) about the polarization fraction value for an LED, aided with a reflection surface that introduces an extra polarization fraction value for our measurement. With these results, we can conclude that the WeDoWo module can display four fields of the observed FOV with enough information for the computation of the Stokes parameters of the linear polarization emission and the polarization fraction and angle values. As aforementioned in § 2.2.2, the values related to the instrumental polarization are a few percentage (i.e., $\langle P_{inst} \rangle \ll 100\%$) and, for the configuration of the optical system, the only element that can introduce instrumental polarization values is the biconvex optic lens.

To conclude, the laboratory tests helped find the characteristics of the double Wollaston module in terms of the transmission axis of each Wollaston and their angle orientation, the location of the fields related to each transmission axis, and finally, calibrating how the polarimetric data from the WeDoWo observations must be computed for obtaining satisfactory processed data.

4. APPLICATION TO ASTRONOMICAL OBSERVATIONS

Once the laboratory tests have been performed, the next step is to prove the capabilities of the WeDoWo module in making astronomical polarimetric observations. For this, an experimental instrument was implemented in the 1.0-meter telescope of the National Astronomical Observatory of Tonantzintla, Puebla (OAN-TNT), which is an instrument with optical characteristics that allow one split of the fields on its detection matrix; this means that it is possible to recover information on the astronomical

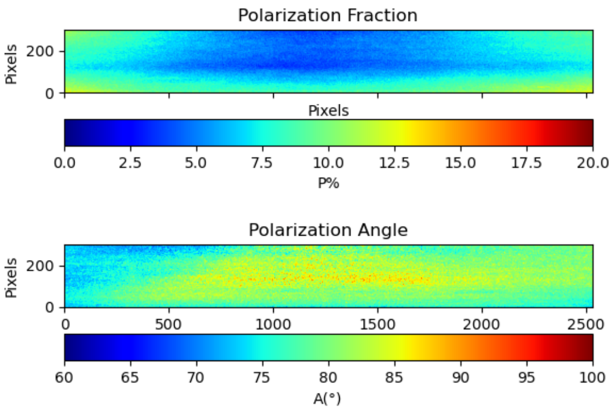

Fig. 11. *Top:* Polarization fraction. *Bottom:* Polarization angle imaging fields, obtained by the trim and calculation of the blank field observation shown in Figure 8 using equation 1 described in § 2. The color figure can be viewed online.

sources observed and to carry on polarimetric analyses of them via one-shot observations.

4.1. *Telescope Overview*

The OAN-TNT 1.0 meter telescope is of Cassegrain type, with an equatorial mount and an effective focal distance of $f_{eff} = 15240$ mm, meaning that it is an $f/15$ telescope and has a plate scale of $PS = 13.53$ arcsecs/mm. The "CCD STL-1001E (SBIG)", the optical detector of the telescope, has a detection matrix of 1024×1024 pixels, with a pixel size of 24×24 μm^2. The plate scale of this system is 0.325 arcsecs/pixel, and the total recovered field is 5.5×5.5 arcmin^2. This CCD detector incorporates a Johnson filter wheel, which is essential for polarimetric observations at different wavelengths. Table 1 shows the various characteristics of the Jonhson filters.

Since the WeDoWo polarimeter is mounted on a telescope that does not match its original design parameters and has no correction lenses (as reported by Medina 2020), small optical aberrations might affect our images. However, we did not notice any evidence of such aberrations in our results. Therefore, we conclude that the WeDoWo module is useful for studying the polarization of point sources and small extended objects.

4.2. *Experimental Polarimeter*

Several simulations were performed to find the best implementation of the WeDoWo module in the telescope. In this case, without any other corrective lenses, the WeDoWo module must be positioned at a distance of 200 mm from the CCD detector to obtain a satisfactory split and distance between the fields and to avoid cross-talk between them, Figure 13 shows a schematic of the distribution on the CCD detector of the four fields and also shows the analysis performed to get the optimal position of the WeDoWo module. Figure 14 shows the physical design implemented to hold the WeDoWo module on the telescope. One of the primary considerations of the implementation (besides the four fields display) is the implementation that attached the CCD to the telescope with no changes to the original structure.

TABLE 1

LIST OF THE JOHNSON FILTERS SYSTEM

Filter	λ_c (Å)	FWHM $\Delta\lambda$ (Å)
U	3400	600
B	4200	1100
V	5400	1200
R	6000	700
I	8500	3000

Figure 15 shows the installation of the holder in the telescope mechanism and the optical CCD of the OAN-TNT. To better display the four fields, we rotated the WeDoWo 45° in a counter-clockwise direction, giving us a rotation of the transmission axes obtained in the four fields. Figure 16 describes graphically the critical features for the further polarimetric analysis of the target astrophysical sources.

Figure 17 shows the observations performed at the OAN-TNT corresponding to the schematic diagram of Figure 16. The first stage of the implementation was successfully done; the observed FOV with the astrophysical source has been divided into four fields, each corresponding to a different transmission axis orientation and, consequently, to a different polarization angle, allowing a polarimetric analysis using only a single exposure. The next stage was to test the system's performance and capability to recover the actual polarization fraction and angle. The laboratory tests, exposed in § 3, ensemble the path of the data reduction that must be performed for the observational astrophysical data.

4.3. *Calibration*

The first step of the calibration process is to observe a non-polarized standard star to find the approximate values of the parameter-t, described in § 2.2.1, instead of the intrinsic possible bias caused by the instrumental polarization; it is possible to make an initial correction of the parameter-t values of each Wollaston that could reveal the true value of the instrumental polarization. Once this correction is performed, the instrumental polariza-

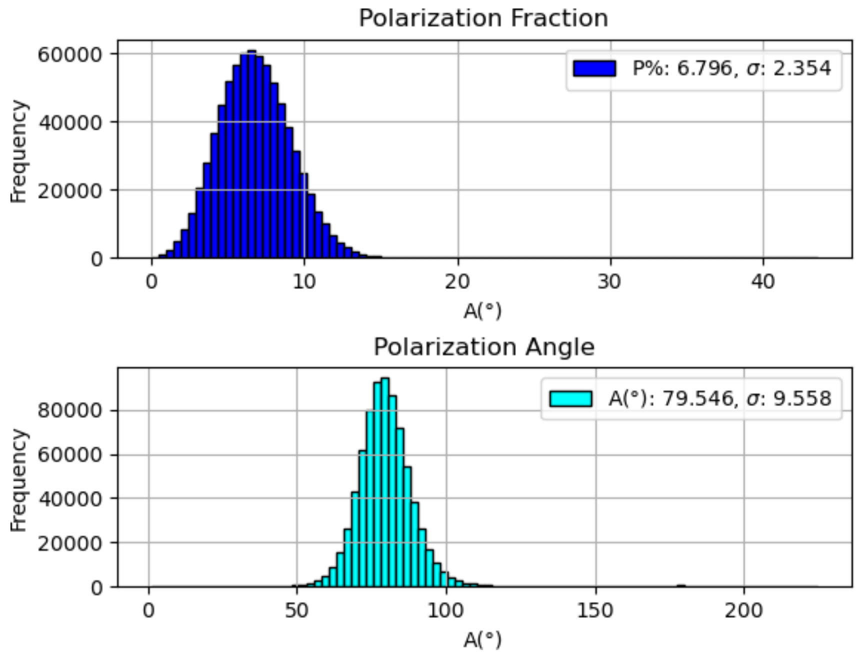

Fig. 12. *Top:* Polarization fraction. *Bottom:* Polarization angle distribution values, obtained by the trim and calculation of the blank field observation shown in Figure 8 using equation 1 described in § 2. The color figure can be viewed online.

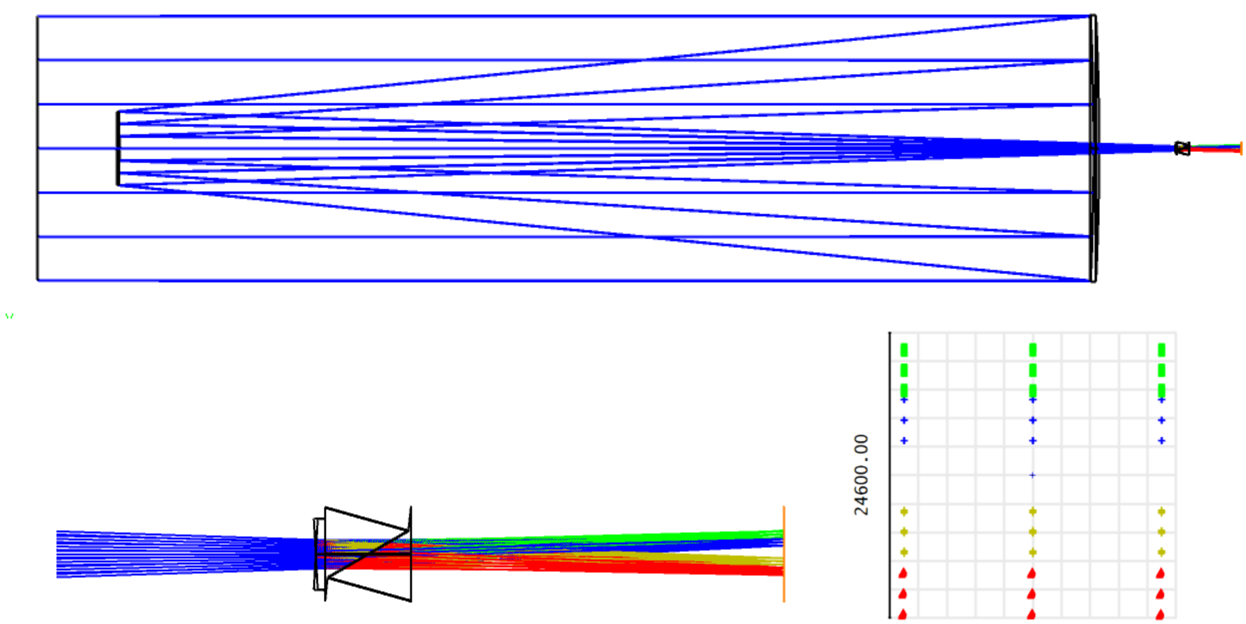

Fig. 13. *Top:* Simulation at the 1 meter OAN-TNT telescope of WeDoWo position. *Bottom left:* Zoom in from the top image, focusing on the weDoWo module's position that shows the splitting of the fields. *Bottom right:* Distribution of the polarized field over an area replicating the CCD detector's dimensions. The left number on the diagram is the CCD dimensions in μm. The color of the fields, as shown in Figure 2, corresponds to a polarized field. The color figure can be viewed online.

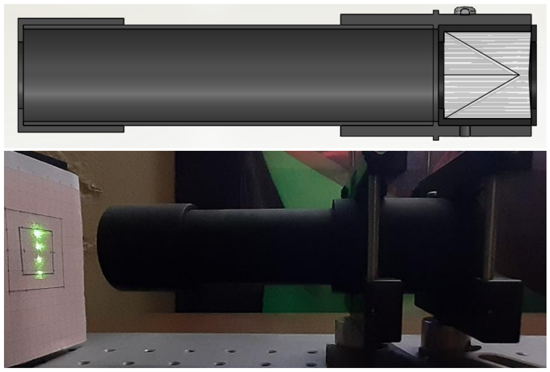

Fig. 14. *Top:* Transversal view of the WeDoWo module holder designed. *Bottom:* Implementation of the holder in the laboratory. The WeDoWo module lies inside. The color figure can be viewed online.

Fig. 15. *Left:* Mount of the WeDoWo holder inside the structure that attaches the optical CCD to the telescope. The design takes into consideration this structure. *Right:* CCD structure properly attached to the telescope, the WeDoWo holder is already inside. The color figure can be viewed online.

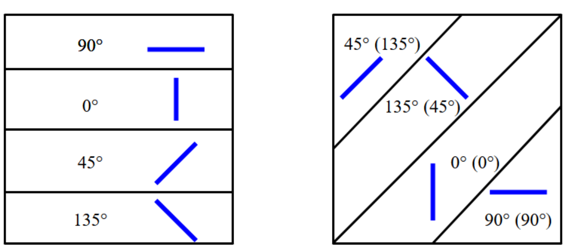

Fig. 16. *Left:* Original distribution of the polarized field. *Right:* 45° rotated WeDoWo distribution. The polarized fields change as a function of the rotation. This consideration must be taken account in the polarization analysis of the observations. The color figure can be viewed online.

tion and the polarization bias correction can be performed using equation 12, showing the true value of the non-polarized sources, in this case, an average

Fig. 17. *Left:* HD 109055, non polarized source. *Right:* HD 154445, polarized source. Both were observed with the 1.0-meter OAN-TNT telescope and the WeDoWo module.

TABLE 2

LIST OF THE SOURCES OBSERVED IN THE CALIBRATION STAGE

Source	Kind	No. of Observations
HD109055	Unpolarized	40 (10 Obs $BVRI$)
HD154892	Unpolarized	40 (10 Obs $BVRI$)
HD154445	Polarized	40 (10 Obs $BVRI$)
HD161056	Polarized	40 (10 Obs $BVRI$)

value of $\langle P \rangle \approx 0\%$. For the validation stage, we perform observations for polarimetric standard calibration sources, focusing on retrieving the reported value of polarization fraction and angle. Table 2 enumerates the observed polarimetric standard stars chosen for the instrument calibration and validation, two non-polarized standard stars (HD 109055 and HD 154892), and two polarized standard stars (HD 154445 and HD 161056). The star's polarimetric information is taken from the Poidvein (2023) database.

For data analysis, we perform the same strategy that is described in § 3, modifying the analysis tool to focus on trimming a section of the field where the astronomical object appears, using standard techniques of aperture photometry, i.e., the sum of the values within a circular aperture, minus the average value of an external annular ring section for the sky subtraction and the possible correction for effects of the background in the polarimetric calculus (Patat & Romaniello 2004; Tinbergen 1996). For an accurate polarimetric analysis, the aperture radius must be big enough to include all of the star emission; to test that, we perform some growth curves to find an aperture value where the cumulative flux of the source reaches a stable value (O'Connor et al. 2020). Figure 20 shows this task, performed for the

TABLE 3

PARAMETER-t AND NORMALIZED Q AND U STOKES PARAMETERS MEAN VALUES WITH THEIR RESPECTIVE UNCERTAINTIES PER JOHNSON FILTER.*

Johnson filter	t_1	$1-t_1$	t_2	$1-t_2$	q	σ_q	u	σ_u
I	0.515	0.485	0.495	0.505	-0.03	±0.001	-0.011	±0.011
R	0.512	0.488	0.501	0.499	-0.024	±0.001	0.001	±0.009
V	0.513	0.487	0.502	0.498	-0.026	±0.011	0.005	±0.007
B	0.525	0.475	0.497	0.503	-0.051	±0.004	-0.006	±0.006

*Results before the correction procedure.

TABLE 4

PARAMETER-t AND NORMALIZED Q AND U STOKES PARAMETERS MEAN VALUES WITH THEIR RESPECTIVE UNCERTAINTIES PER JOHNSON FILTER.*

Johnson filter	t_1	$1-t_1$	t_2	$1-t_2$	q	σ_q	u	σ_u
I	0.5	0.5	0.5	0.5	0.0	±0.001	0.0	±0.011
R	0.5	0.5	0.5	0.5	0.0	±0.001	0.0	±0.009
V	0.5	0.5	0.5	0.5	0.0	±0.011	0.0	±0.007
B	0.5	0.5	0.5	0.5	0.0	±0.004	0.0	±0.006

*Results after the correction, procedure.

TABLE 5

RESULTS OF THE POLARIZED SOURCES OBSERVATIONS

Object	filter	$P(\%)$	$P_{lit}(\%)$	$A(°)$	$A_{lit}(°)$
HD154445	I	2.975 ± 0.5	3.06	92.679 ± 1.68	91
	R	2.988 ± 0.3	3.6	93.6 ± 1.63	90.1
	V	2.994 ± 1.3	3.72	82.858 ± 2.07	90.3
	B	1.612 ± 0.6	3.44	99.293 ± 4.55	90.1
HD161056	I	3.782 ± 0.8	3.578	71.04 ± 1.41	69.08
	R	4.593 ± 0.6	3.846	75.97 ± 1.12	68.2
	V	4.54 ± 1.01	4.048	60.568 ± 1.52	68.61
	B	4.5 ± 0.8	3.771	68.8 ± 2.0	68.71

HD 101656 observations, where we found that the cumulative relative fluxes of the four fields become stable after an aperture radius of 10 arc seconds.

Table 3 enumerates the original parameter-t values and their effects on the Q and U-normalized Stokes parameters. After the calibration, Table 4 shows that once the parameter-t values are corrected, the Q and U Stokes parameters have a value close to zero (or zero in some cases). Figures 18 and 19 complement the material shown in the tables with the distribution of the parameter-t values and the instrumental normalized Q and U Stokes values before and after the correction procedure. The values of the parameter-t and the Q and U Stokes parameters seem centered on zero and 0.5. Still, the uncertainty of the value causes an instrumental polarization value to reach $\approx 1\%$.

After the calibration and correction procedure, with the same strategy, we perform the validation polarimetric analysis with the set of polarized standard stars. The comparison between the retrieved values with the reported values on the Poidvein (2023) database is contained in Table 5 and shows that the retrieved polarization fraction and angle values are close enough to the database values, validating the performance of the WeDoWo module for astronomical polarimetric observations in a single-shot technique.

4.4. *Observations*

To perform the observations, the astronomical sources must span a field of view of 1×1 arcmin^2 to avoid cross-talk between fields. This implies that our polarimeter is suitable for studying small objects, like stars (as shown in the previous section to

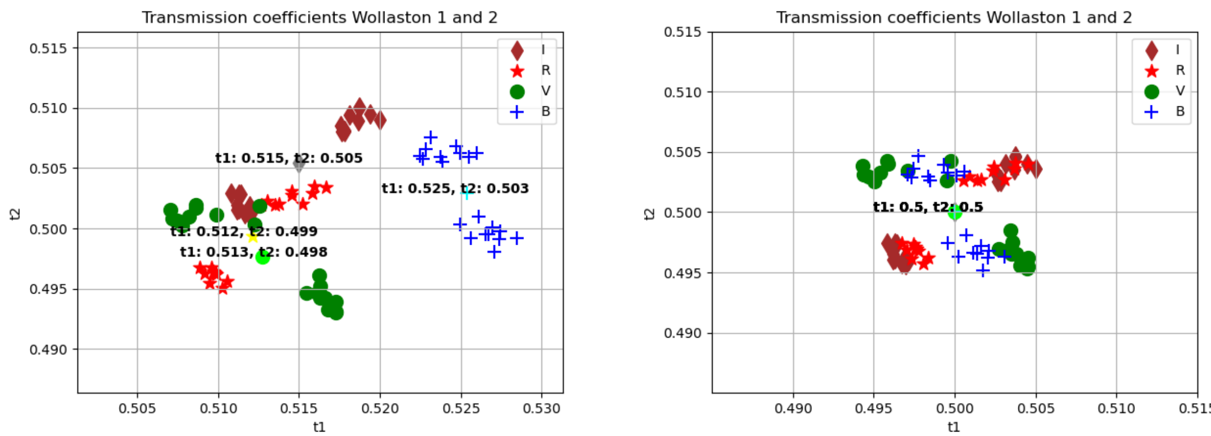

Fig. 18. *Left:* Plot of parameter-t of each Wollaston without the calibration procedure. *Right:* Plot of parameter-t of each Wollaston, calibration procedure implemented. In both cases, the colors represent the measurements in the Johnson filter system. The values in bold font represent the average values of the measurements. The color figure can be viewed online.

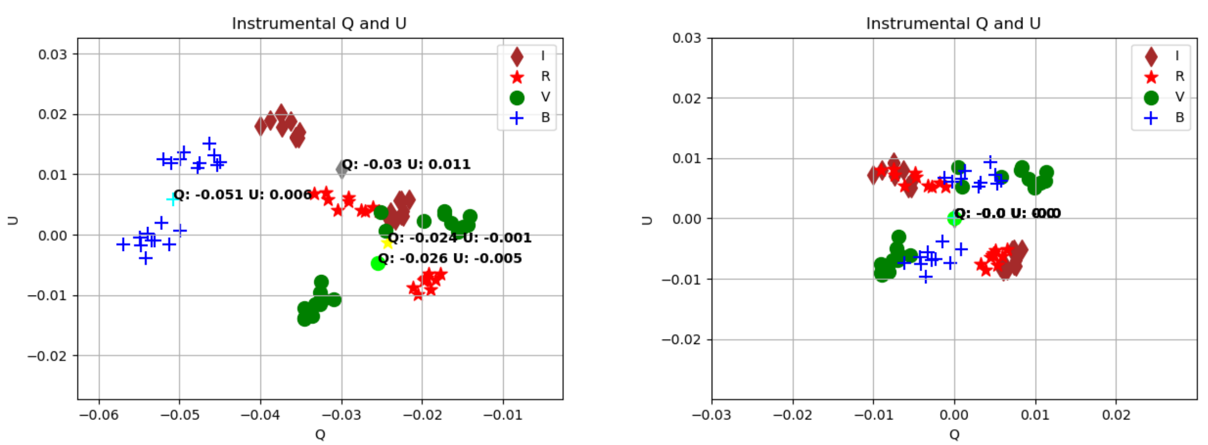

Fig. 19. *Left:* Plot of the Q and U normalized Stokes parameters without the calibration procedure. *Right:* Plot of the Q and U normalized Stokes parameters, calibration procedure implemented. In both cases, the colors represent the measurements in the Johnson filter system. The values in bold font represent the average values of the measurements. The color figure can be viewed online.

perform the calibration procedure on a telescope), asteroids, and compact extended objects, e.g., planetary nebulae.

We observed the Frosty Leo nebula (IRAS 09371+1212) in the full $BVRI$ range to show WeDoWo's performance for extended emission astronomical objects. Exploring the observations, I-band data showed the best results in the way that the SNR of the nebular extended emission was better recovered. The polarization fraction and angle were computed pixel by pixel for extended sources, as described in Devaraj et al. (2018) and Serrano-Bernal et al. (2020). The results of these observations are shown in Figure 21, where we also compare them against near-infrared polarization data from Serrano-Bernal et al. (2020).

As shown in Figure 21, the polarization vectors in the nebula's central region show a centrosymmetric pattern in both the optical (WeDoWo at I-band) and the near-infrared (POLICAN at J-band Serrano-Bernal et al. (2020)). The centrosymmetric pattern of the polarization vectors is caused by the nature of the circumstellar medium, which is described as optically thin. The center of the pattern indicates the location of the primary emission source, and the scattered emission of the extended envelope is lin-

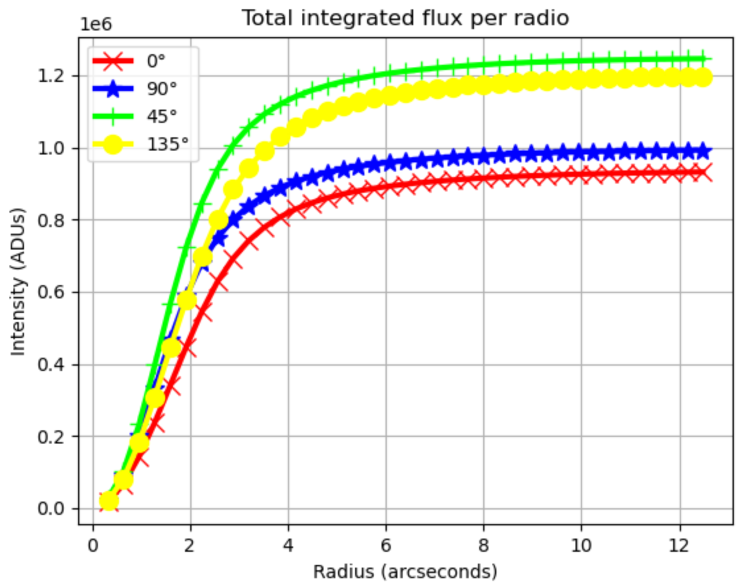

Fig. 20. Growth curve of the flux retrieved for the HD 161056 observation. This task aids us in properly computing the polarization fraction and angle values of an observed source. This is implemented in all of the polarimetric standard stars analyses. The color figure can be viewed online.

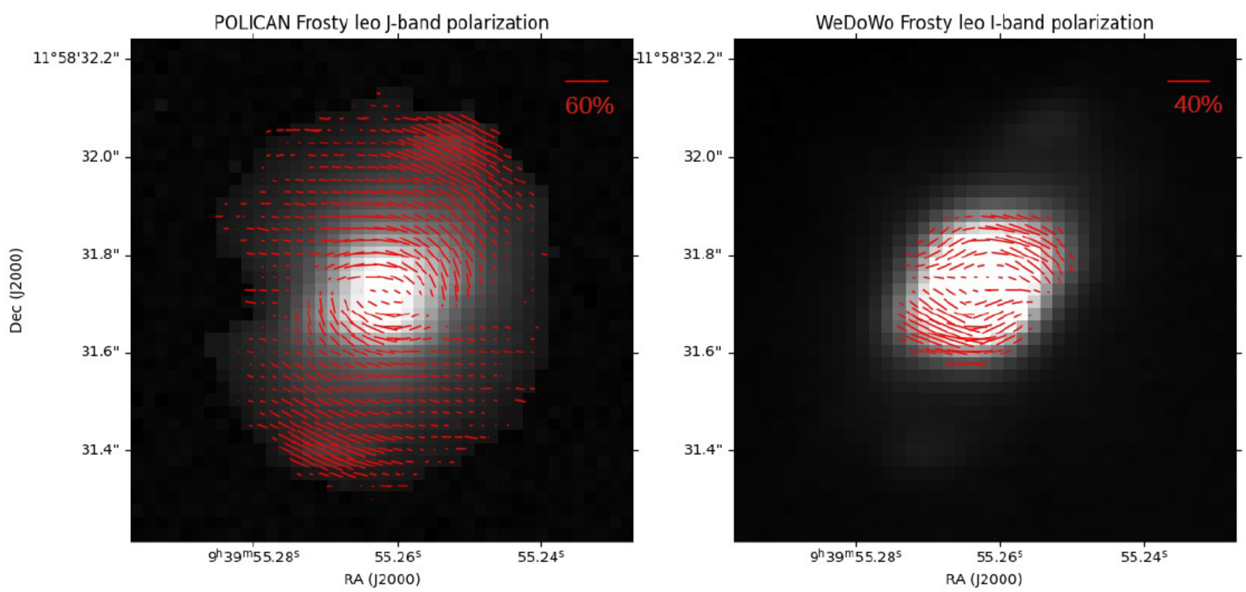

Fig. 21. *Left:* Total intensity results from the Frosty Leo observation in the J-band with the polarization vectors over plotted. Performed by the OAGH polarimeter POLICAN as described by Serrano-Bernal et al. (2020). *Right:* Total intensity results from Frosty Leo observation in the I-band with the polarization vectors over plotted. Performed by the WeDoWo module on the OAN-TNT telescope. The color figure can be viewed online.

early polarized (Gledhill et al. 2001; Serrano-Bernal et al. 2020).

In Figures 22 and 23, we compare the results of the polarization analysis obtained from Frosty Leo's observations by POLICAN and the WeDoWo module. Figure 22 shows the polarization fraction maps, illustrating the extended structure distribution near the central system and in the north and

DOI: https://doi.org/10.22201/ia.01851101p.2025.61.01.11

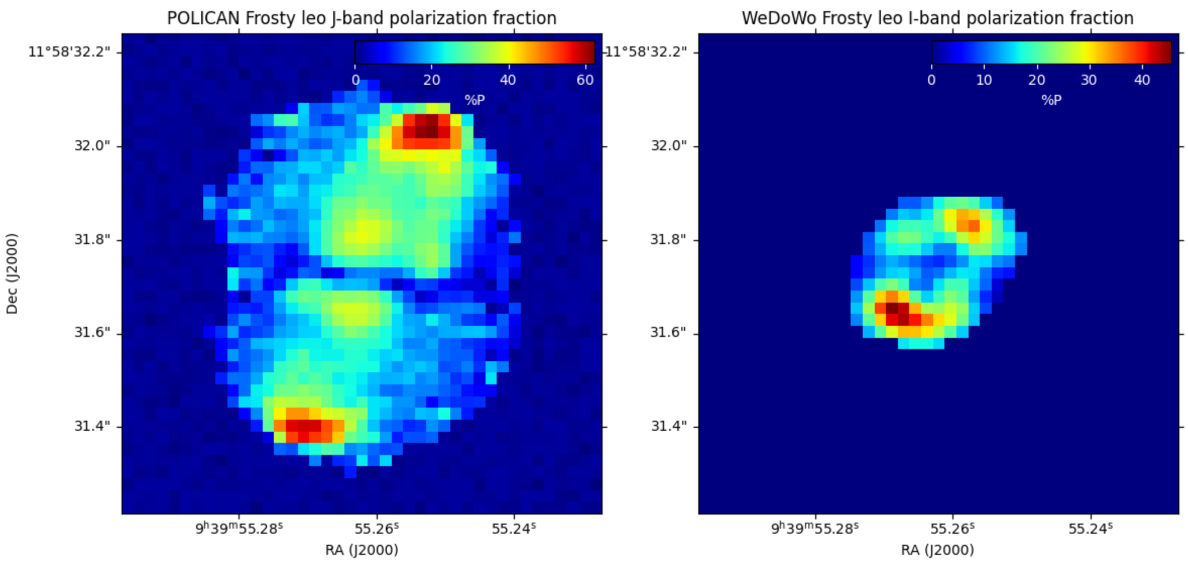

Fig. 22. *Left:* Polarization fraction results from the Frosty Leo observation in the J-band. Performed by the OAGH polarimeter POLICAN as described by Serrano-Bernal et al. (2020). *Right:* Polarization fraction results from Frosty Leo observation in the I-band. Performed by the WeDoWo module on the OAN-TNT telescope. The color figure can be viewed online.

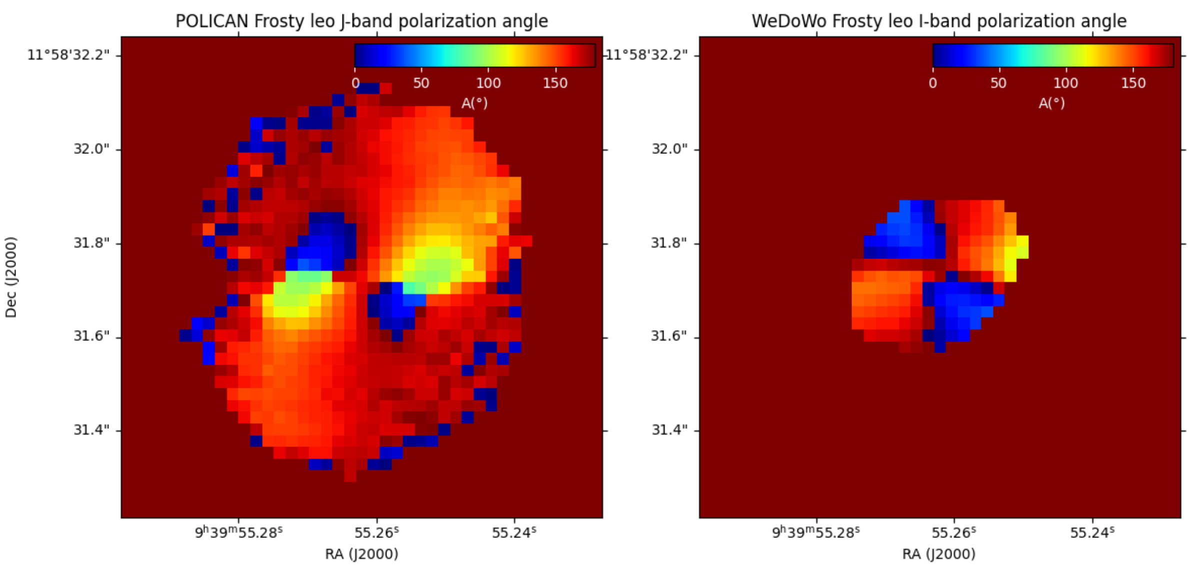

Fig. 23. *Left:* Polarization angle results from the Frosty Leo observation in the J-band. Performed by the OAGH polarimeter POLICAN as described by Serrano-Bernal et al. (2020). *Right:* Polarization angle results from Frosty Leo's observation in the I-band. Performed by the WeDoWo module on the OAN-TNT telescope. The color figure can be viewed online.

south regions. In the case of WeDoWo's result, we can retrieve the extended structure distribution near the central system, where the centrosymmetric pattern lies. Compared with the POLICAN results reported by Serrano-Bernal et al. (2020), polarimetric observational results performed with the WeDoWo module show the structure of the extended envelope product of the scattered emission in the I-band. Figure 23 shows the similarities between polarization angle results for corresponding regions.

These results exposed in Figures 21, 22 and 23 also resemble the distribution of the polarization fraction and angle reported by Scarrott & Scarrott (1994). However, it is necessary to perform more profound observations in the full $BVRI$ to recover the polarization fraction and angle for the faint extended emission located to the north and south of the object, where the ansae structures reside and, according to Serrano-Bernal et al. (2020), the multiple scattering is the primary emission process in these regions, giving information about the extension of the dusty circumstellar medium that surrounds the system.

5. CONCLUSIONS

This paper presents the design of a WeDoWo module developed for the 2.1-meter telescope in OAGH for a one-shot polarimeter. We tested this module and described the steps and preliminary considerations needed to obtain the required parameters for a full characterization and calibration. These procedures allowed us to retrieve Stokes parameters of the linear polarization radiation and the observed sources' fraction and angle of polarization. The laboratory's description of the calibration helped us understand WeDoWo's behavior in a controlled environment. With this preliminary information, it was possible to better plan the calibration procedures that must be taken with the telescope. The 1.0-meter telescope of the OAN-TNT gave us an excellent chance to test the WeDoWo capability to make astronomical observations. Despite the lack of an accurate optical system to correct the multiple optical aberrations that could be present, the results obtained via our observations proved that an instrument with these characteristics can perform polarimetric studies of astronomical sources. The only considerations that must be taken into account are that the observed sources must be small enough to avoid cross-talk between the polarized fields, and the need to use use filters to reduce the possible chromatic aberration when using a birefringent material.

The conclusion of this work is that the WeDoWo module can perform astronomical polarimetric observations. The one-shot technique was satisfactorily implemented, producing the observatory's first polarimetric results. Frosty Leo's observations and results had the main objective of showing the capabilities of the WeDoWo module to retrieve the polarization fraction and angle values in extended sources with size ≤ 1 arcmin, which encourages us to continue the extended source investigations at the full $BVRI$ bands for this kind of astronomical objects.

We express our special thanks to Claudio Pernechele for his advice about the design of the WeDoWo module and the polarimeter reported in Medina (2020). Also, we express special thanks to the National Astronomical Observatory of Tonantzintla (OAN-TNT) Puebla, Mexico, for support on the testing and observations in the 1.0-meter telescope and to the technical personnel of the Schmidt camera located at INAOE for the laboratory material provided for the characterization of the WeDoWo module. The authors thank CONAHCYT for supporting the following students: A. Garca-Prez (CVU 1080875) and S. Medina (CVU 905889). E. O. Serrano-Bernal acknowledges CONAHCYT for the postdoc grant (CVU 480840) and support from the project CB-2016-01-281948. We also would like to thank the support for the following projects: 301917 "Actualizacin de la infraestructura cientifica del Observatorio astrofsico Guillermo Haro" and A1-S-54450 "Campos magnticos en el medio interstelar". Finally, we thank INAOE for using the licenses associated with the OpticStudio and Solidworks programs.

REFERENCES

Bevington, P. R. & Robinson, D. K., 2010, Data reduction and error analysis for the Physical Sciences (Boston: McGraw-Hill)

Clarke, D. 2010, Stellar Polarimetry, (John Wiley & Sons, Ltd.)

Compain, E., Poirier, S., & Drevillon, B. 1999, ApOpt, 38, 3490, https://doi.org/10.1364/AO.38.003490

Devaraj, R., Luna, A., Carrasco, L., et al. 2018, PASP, 130, 055002, https://doi.org/10.1088/1538-3873/aaab3f

Gledhill, T. M., Chrysostomou, A., Hough, J. H., & Yates J. 2001, MNRAS, 322, 321. https://doi.org/10.1046/j.1365-8711.2001.04112.x

Helhel, S., Khanitov, I., Kahya, G., et al. 2015, ExA, 39, 595, https://doi.org/10.1007/s10686-015-9468-8

Hiltner, W. A. 1949, ApJ, 109, 471, https://doi.org/10.1086/145151

Howell, S. B. 2006, Handbook of CCD Astronomy (United Kingdom: CUP)

Lazarian, A. & Hoang, T. 2007, MNRAS, 378, 910, https://doi.org/10.1111/j.1365-2966.2007.11817.x

Medina S. 2020, Polarímetro óptico para estudios de cuerpos menores del Sistema Solar, Tesis (México: INAOE), http://inaoe.repositorioinstitucional.mx/jspui/handle/1009/1995

O'Connor E. G. P., Harvey, . J., Devaney, N., Steele, I. A., & Varas, R. 2022, SPIE 12148, Galway Liverpool Imaging Polarimeter - GLIP: design and prototype status, 121847T, https://doi.org/10.1117/12.26229283

Oliva E. 1996, A&AS, 123, 589, https://doi.org/10.1051/aas:1997175

Patat F. & Romaniello M. 2004, PASP, 118, 146, https://doi.org/10.1086/497581

Pernechele, C., Abe, L., Bendjoya, P., et al. 2012, SPIE 8446, A single-shot optical linear polarimeter for asteroid studies, 84462H-1, https://doi.org/10.1117/12.925933

Poidvein, F. 2023, Departamento de Astronomia, http://astroweb.iag.usp.br/~polarimetria/padroes/index.html

Ritacco, A. 2016, Polarimetry at millimeter wavelengths with the NIKA and NIKA2 instruments, Thesis (France: Université Grenoble Alpes)

Saito, T., Sunati, T., Kiyono, K. & Oikawa, T., 2022, JPhCD, 012009, https://doi.org/10.1088/1742-6596/2149/1/012009

Scarrott S. M. & Scarrott R. M. J. 1994, MNRAS268, 615, https://doi.org/10.1093/mnras/268.3.615

Serrano-Bernal E. 2021, The Near-Infrared Polarimeter of Cananea, POLICAN: Optimization, Observations, and Results, Ph. D. Thesis (México: INAOE)

Serrano-Bernal E., Sabin L., Luna A., et al. 2020, MNRAS, 495, 2599, https://doi.org/10.1093/mnras/staa1291

Shurcliff, W. A. 1962, Polarized Light: Production and Use, Harvard University Press, https://doi.org/10.4159/harvard.9780674424135

Tinbergen, J. 1996, Astronomical Polarimetry, (UK: CUP)

J. Castro-Ramos, A. García-Pérez, A. Luna, and E. O. Serrano-Bernal: Instituto Nacional de Astrofísica, Óptica y Electrónica. Luis Enrique Erro #1, Sta. María Tonanzintla, 72840 San Andrés Cholula, Puebla, México (alexgp, aluna, jcastro, arthas@inaoep.mx).

S. Medina: Tyndall National Institute. Lee Maltings Complex Dyke Parade, Cork, Cork, T12 R5CP, Ireland (s.medina-rangel@mycit.ie).